USE OF STEEL FIBER REINFORCED CONCRETE IN STRUCTURAL MEMBERS WITH HIGHLY COMPLEX STRESS FIELDS

by

TARUN PAREEK

Presented to the Faculty of the Graduate School of
The University of Texas at Arlington in Partial Fulfillment
of the Requirements
for the Degree of

MASTER OF SCIENCE IN CIVIL ENGINEERING

THE UNIVERSITY OF TEXAS AT ARLINGTON
December 2011

ACKNOWLEDGEMENTS

First of all, I would like to express my gratitude to my advisor, Assistant Professor Dr. Shih-Ho Chao. Without his expertise and guidance I would not have been able to complete this study. I would like to extend my acknowledgement to Hanson Pipe & Precast Inc. and Maccaferri Inc. for donating materials required for this study.

I would also like to thank the staffs at CELB at the University of Texas at Arlington for their advice and technical support throughout my testing program: Jorge Fortez, Oleh Kinash, and Paul Shover.

In addition, I would like to express my appreciation to my friends and colleagues who have helped me throughout my Masters degree, both inside and outside the lab: Dr. Dipti Sahoo (now Assistant Professor at Indian institute of Technology, Delhi), Dr. Xuejian Liu, Sanputt Simasathien, Jae-Sung Cho, Netra Karki, Regina Waweru, Chatchai Jiansinlapadamrong.

Finally, I would like to give my heartfelt thanks to my mother Nidhi Pareek and father Vijay Pareek for their constant help, support and encouragement.

November 3, 2011

ABSTRACT

USE OF STEEL FIBER REINFORCED CONCRETE

IN STRUCTURAL MEMBERS WITH HIGHLY

COMPLEX STRESS FIELDS

Tarun Pareek, M.S

The University of Texas at Arlington, 2011

Supervising Professor: Shih-Ho Chao

Reinforced concrete (RC) members with significant geometric discontinuities and complex stress distributions under loading require considerable analyses and usually complicated reinforcement detailing. RC members with large openings are one of the examples. These large openings may interrupt the load transfer by direct concrete struts and cause substantial decrease in strength and unpredictable failure modes. The reinforcement detailing of these concrete members based on strut-and-tie models (STMs) is generally complicated and very often, these models cannot predict the failure mechanism due to localized damages. The actual stress fields in such members are typically very different from that predicated by STMs, as evidenced by many experimental investigations. This study investigates the influence of highly complex stresses on the mechanical behavior of deep beams. One RC and three steel fiber reinforced concrete (SFRC) deep beams with two large openings were monotonically loaded up to failure. A simple design approach based on elastic finite element analysis (FEA) was also proposed for the reinforcement detailing of the SFRC specimens. Experimental results indicated that, although the complex reinforcement detailing as per STM was not used, the

SFRC specimens with 1.5% and 1% volume fraction of steel fibers reached much higher strength than the design load and exhibited ductile mode of failure.

TABLE OF CONTENTS

LIST OF ILLUSTRATIONS

LIST OF TABLES

NOTATION

A_s = area of reinforcement (in^2, mm^2)

B = width of specimen (in, mm)

D = depth of specimen (in, mm)

d = diameter (in, mm)

E = Young's modulus (ksi, MPa)

f_b = bending stress (ksi, MPa)

f'_c = cylinder compressive strength of concrete (psi, MPa)

f_{ct} = tensile strength of concrete (psi, MPa)

f_p = flexural bending strength.

$f_{150, 0.75}$ = residual strength – the stress value obtained from $P_{150, 0.75}$

$f_{150, 3.0}$ = residual strength – the stress value obtained from $P_{150, 3.0}$

f_y = yield strength of reinforcement (psi, MPa)

h = beam height (in, mm)

I = moment of inertia (in^4, m^4)

M = moment (kip-ft, kN-m)

MOR = modulus of rupture (psi)

L = span length (in, mm)

l_d = development length (in, mm)

P = load (kip, kN)

$P_{150, 0.75}$ = residual load corresponding to a net deflection equal to 1/600 of the span or 0.75 mm- (0.03in) using a specimen with a width and depth of 150 mm (6 in.) and span of 20 in

$P_{150, 3.0}$ = residual load corresponding to a net deflection equal to 1/150 of the span or 3.0 mm- (0.12in) using a specimen with a width and depth of 150 mm (6 in.) and span of 20 in.

P_u = load at failure (kip, kN)

P_y = load at yield (kip, kN)

V = shear (kip, kN)

ϕ = strength reduction factor

υ = angle between axis of strut and tension chord

α = angle between axis of strut and reinforcing bars

γ_c = unit weight of concrete (lb/ft^3)

ν = Poisson's ratio

δ = deflection, displacement (in, mm)

δ_p = peak-load deflection (in, mm)

δ_1 = first peak deflection (in, mm)

ε = material strain (in/in, mm/mm)

σ = standard deviation

CHAPTER 1

INTRODUCTION

Sufficient plastic redistribution of internal forces is essential for a structure to sustain expected and unexpected loads, and to fail in a ductile manner if over-loaded. In RC members, due to the brittle nature of concrete, this redistribution primarily relies on the steel reinforcing bars and their layouts, in which bars are placed at locations where the concrete is overly stressed beyond its cracking strength. For typical concrete members with simple and regular geometries, those locations can be easily predicted by classical elastic theory. It is well known, however, that the stress pattern is highly non-linear and deviates considerably from the classical elastic theory for RC members with significant geometric discontinuities. One such example is RC deep beams/walls with large web openings used as structural member in buildings.

A typical example is deep beams with large openings. Deep beams can also be classified as deep walls when they extend entire height of the floor. These beams/walls have very small slenderness ratio. The most effective load-carrying system in these beams/walls is by arch mechanism (Muttoni, 2011) with a tie at bottom (see **Figure 1.1**), if the supports are at lower edge of the beam/wall and if span to depth ratio is approximately less than three. These structures are very often provided with openings for doors and windows, or for passing a duct (see **Figure 1.2**). These openings, if located between the loading point and support, will disrupt the flow of force transfer, and usually significantly reduce the load-carrying capacity. Most advantageous position for these openings will be in the center of the structure as it would not interfere with load transfer mechanism, i.e., the compression arch (see **Figure 1.3**). However, if these utility provisions are located near supports intersecting this compression arch (see **Figure 1.4**), it is necessary to use an alternative load transfer mechanism

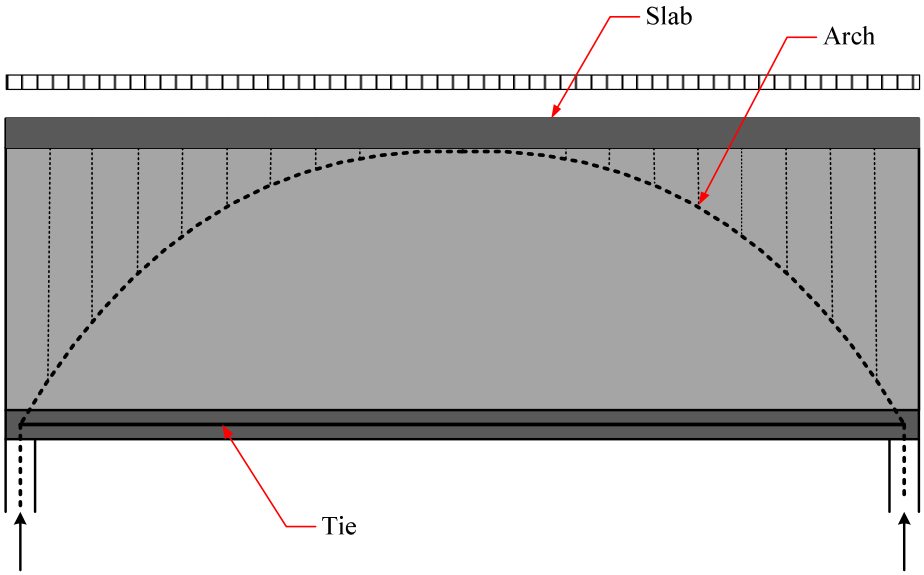

Figure 1.1 Load carrying system in deep beam (Muttoni, 2011)

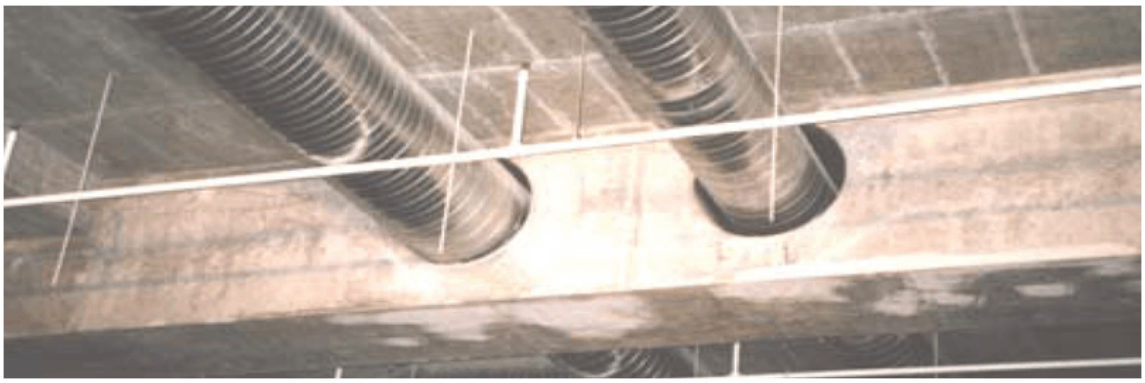

Figure 1.2 Concrete beam with large circular openings (Amiri, 2011)

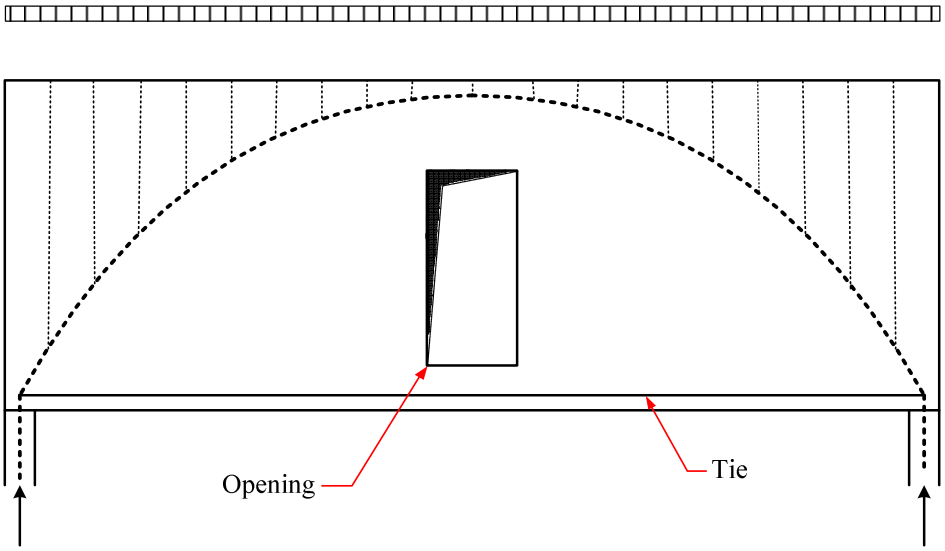

Figure 1.3 Structurally optimum position for opening (Muttoni, 2011)

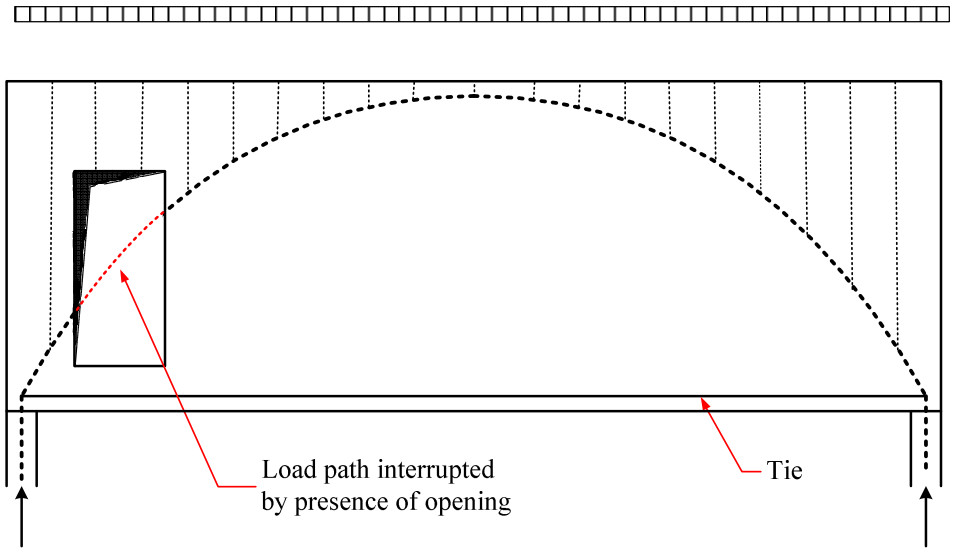

Figure 1.4 Interrupted load carrying system of deep beam due to presence of opening near support (Muttoni, 2011)

This compression arch mechanism becomes more efficient if these beams/walls extent to multiple floors. Generally these walls are connected monolithically to the horizontal parts of the construction which are generally formed by concrete slabs, this contributes in carrying compressive and tensile forces in horizontal direction. In case of multiple stories there is even bigger arch formed with tie at bottom (see **Figure 1.5**). In the **Figure 1.5** a single arch is formed within the beams/walls and tie is positioned within the lower slab. This system is a perfect solution if the requirement is to keep open space in ground floor. In such case few available columns in the structure needs to be dimensioned so as to resist all the forces, also braces can be inserted on the ground floor in order to transmit any horizontal forces from wind and seismic activity. Efficiency of these structures is based on large effective depths, which allows them to carry remarkable loads and span over very large distances (Muttoni, 2011).

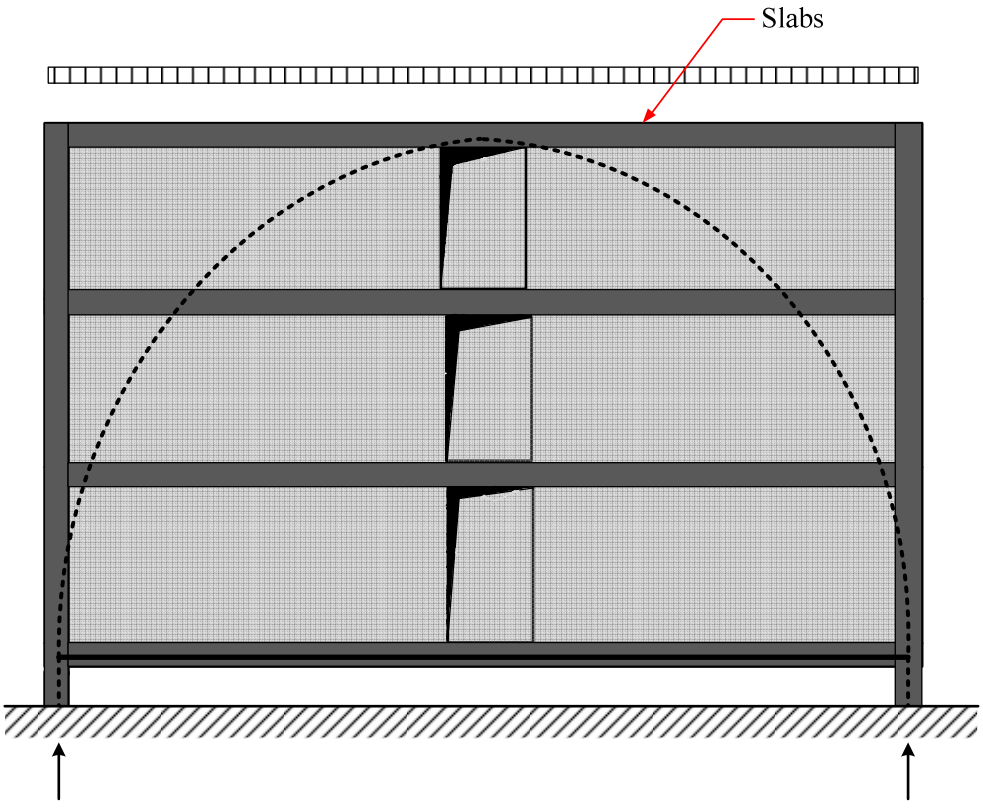

Figure 1.5 Deep walls on multiple levels to cover a large open span on ground floor (Muttoni, 2011)

These members with significant geometric discontinuities and complex stress distributions under loading require considerable analysis and usually complicated reinforcement detailing. The reinforcement detailing of these concrete members based on STMs, is generally complicated and very often, these models cannot predict the failure mechanism due to localized damages. Also, the actual stress fields in such members are typically very different from that predicated by STMs, as indicated by many experimental investigations. It should be noted that the concept of STMs were originally developed based on plastic truss analogy, in which the structure is assumed sufficiently ductile. However, due to the fact that concrete has a limited capacity to sustain plastic deformation, along with the complex stress field after cracking, those members deigned based on STM generally have limited post-peak ductility.

1.1 Motivation and Objectives

In the past deep beams were designed based on empirical formulas which were based on experimental data. These empirical-based approaches as specified in the codes, however, do not address the design of D-regions with openings. Recently, strut-and-tie model has been expensively used for designing these discontinuous regions. The ACI Building Code (ACI 318-11, 2011) does not give any explicit guidance for designing these elements with openings. Several past studies (Kuchma and Park 2007; Tan and Zhang 2007; Maxwell and Breen 2000; Chen et al. 2002; Breña and Morrison, 2007; Kuchma et al. 2008) have been done on deep beams with different configuration and location of openings to validate the effectiveness of strut-and-tie models. These experiments showed that the strut-and-tie model gives consistent and conservative results in terms of ultimate strength. However, some tests have shown that large differences occur between calculated forces from strut-and-tie model and instrumented experimental specimens (Breña and Morrison 2007).

Another difficulty in using strut-and-tie model is anchorage and congestion of reinforcement bars. Recently, there have been concerns and investigations in performance of

structural members with complex D-regions under service loads using strut-and-tie model. A poorly selected and detailed strut-and-tie model can lead to the member cracking and damage and having limited ductility under service loads (Kuchma et al., 2008). Moreover from past research it is seen that these members generally failed in brittle mode due to severe localized damage (Breña and Morrison, 2007; Flores, 2009; Sahoo, Flores and Chao, 2011).

Steel Fiber Reinforced Concrete (SFRC) has gained increased popularity in construction industries in past years. Tests have shown that SFRC is tougher and more ductile (ACI 544-96, 1996). Shear tests on steel fiber reinforced concrete (SFRC) beams without stirrups have shown that if the fiber dosage is sufficient no other transverse reinforcement is necessary to achieve the desired shear capacity (Parra-Montesinos, 2006). Furthermore, SFRC beams show a more ductile behavior and have reduced crack widths (Dupont, et al. 2003). Prior testing on deep beams with single large opening showed that the fiber bridging effect limits crack width and mitigates or eliminates the brittle failures encountered in previous experiments (Flores, 2009; Sahoo, Flores and Chao, 2012).

The objectives of this research are (a) to investigate the performance of steel fiber reinforced concrete used in deep beam members with highly complex stress field due to presence of large openings; (b) to investigate the extent of accuracy to which non-linear computer programs available currently can predict the strength and failure patterns/modes of reinforced concrete and steel fiber reinforced deep beam members with large openings; (c) to develop an alternative and reliable design method in order to improve the performance of these members with highly complex stress fields.

1.2 Overview of Study Program

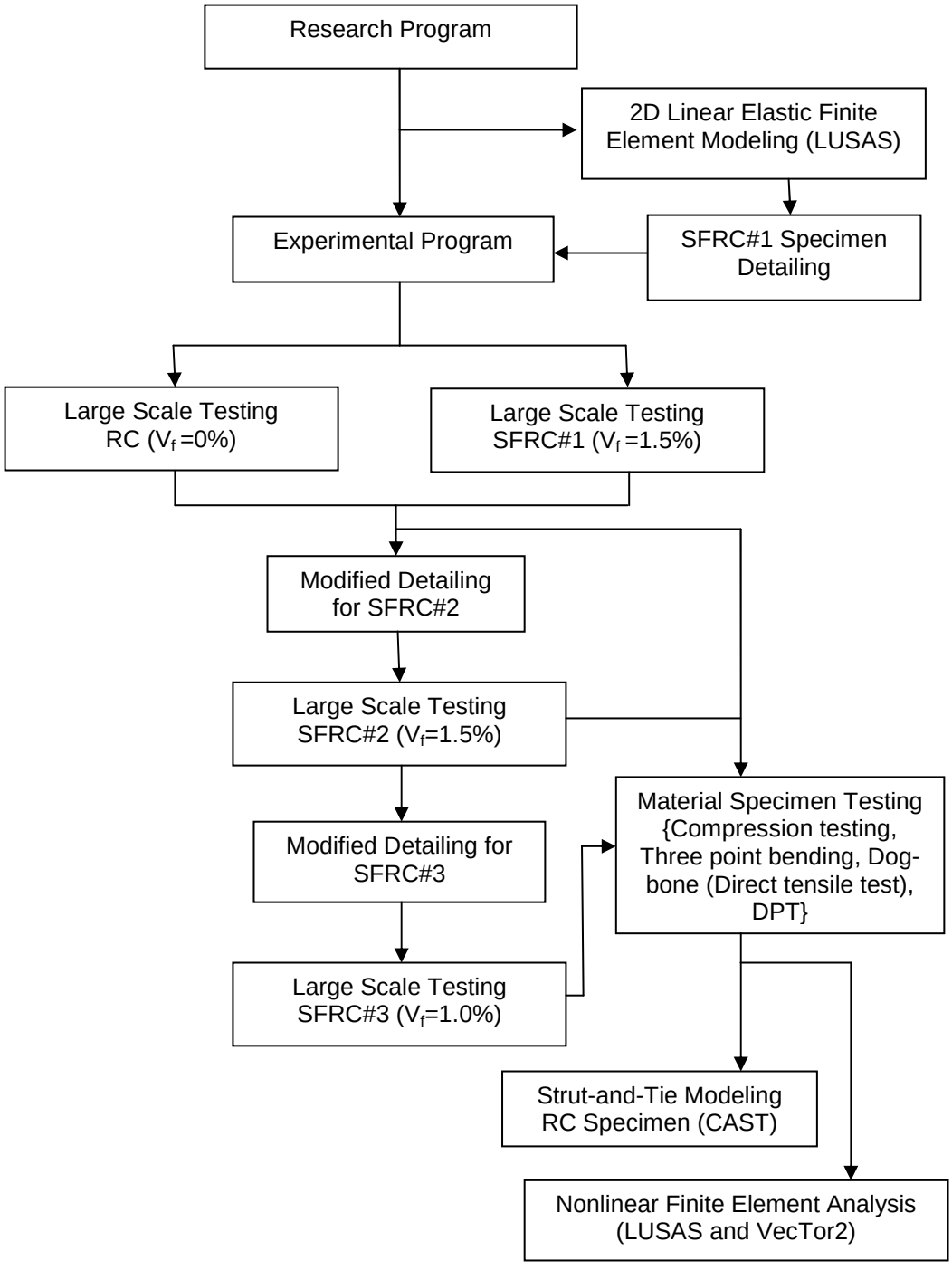

Figure 1.6 Flow of research program

This study investigates the performance of one reinforced concrete (RC) and three steel fiber reinforced concrete (SFRC) deep beams with two large openings, all of them had same geometries and were tested under monotonically increased loads until failure. Complex reinforcement detailing as per STM for the RC specimen was not used for the SFRC specimens. The feasibility of using SFRC in the members with complex stress fields is based on the assumption that, if breakdown of the most stressed locations are prevented by steel reinforcing bars, the greater plastic deformation capacity of SFRC will allow considerable internal force redistribution, thus increasing the ultimate load-carrying capacity.

1.3 Organization of Thesis

The present chapter, as discussed above, motivates this research project and complements the previously publications on this study. Chapter 2 presents the backgrounds of strut-and-tie model, fibers, deep beams and effect of opening in these structures. It also reviews previous publications on these members with and without fibers. Chapter 3 discusses the testing of materials used in the experimental program. Material testing was conducted following appropriate American Standard for Testing and Material (ASTM) standards, with the exception of Direct Tensile Test and Double Punch Test (DPT) as there are no ASTM standards available for these tests. Chapter 4 summarizes in detail the results from large scale testing of all four specimens. Chapter 5 summarizes the results form finite element analysis carried out by both LUSAS and VecTor2. In addition, a strut-and-tie analysis for the RC specimen was performed by Computer Aid Strut and Tie (CAST) program and the results are summarized. The conclusions of this research are presented in Chapter 6. This chapter also gives recommendation for future work. In addition, Appendix A, B and D contains the detailed procedure for construction of models on LUSAS, CAST and VecTor2 respectively, where as Appendix C contains design output results from CAST analysis.

CHAPTER 2

LITERATURE REVIEW

The ACI Building Code (ACI 318-11, 2011) Sections 10.7.1 and 11.7.1 define deep beams as those beams where the clear span from face-to-face of support (l_n) is equal to or less than four times the overall member depth, or beams with concentrated loads within a distance equal to or less than two times the beam depth from the face of support. Traditionally, these members were designed based on empirical equations that were based on experimental data, however these equations are not universally applicable (Breña and Morrison, 2007). Deep beams are commonly designed by using a method called “truss analogy”. This method was first described by Ritter (1899) and Mörsch (1909). One of its forms (strut-and-tie model) is being widely used today to design regions of structural concrete members with geometric or loading discontinuities. The use of strut-and-tie models (STMs) have been increased significantly since its inclusion in design codes (ACI Committee 318, 2002; CSA, 1994; AASHTO, 1998). In strut-and-tie method a member is divided into D-regions and B-regions (discussed later). In addition, for strut-and-tie method to apply the deep beams must be loaded so that compression struts can be developed between loads and supports.

2.1 B- and D- Regions in Deep Beams

In selecting appropriate design approach for structural concrete, it is useful to classify portions of the structure as either B-(Beam or Bernoulli) regions or D-(Distributed or Discontinuity) regions. B-regions are those in which Bernoulli’s hypothesis applies. Bernoulli hypothesis states that: *Plane sections remain plane after bending*”. Bernoulli's hypothesis facilitates the flexural design of reinforced concrete structures by allowing a linear strain

distribution for all loading stages, including ultimate flexural capacity (Section 10.2.2, ACI 318-11, 2011). However, Bernoulli's principle does not apply to members with discontinuities or D-regions where discontinuity of stress trajectories occurs. D-regions include portions near abrupt changes in geometry (geometric discontinuities) or concentrated forces (force discontinuities) (see **Figure 2.1**). **Figure 2.1** illustrates examples of discontinuity with resulting D-regions shaded in the members. D-regions are located at a distance of (*h*) from forces and geometric discontinuity, all the other portions of the member outside the D-regions are B-regions (Appendix A, ACI 318-11, 2011). As discussed earlier in B-regions stresses can be determined according to sectional methods whereas in D-regions shear strains dominate the behavior, and beam theory cannot be used to determine the internal state of stress.

Due to the presence of these regions stress distribution in the structure can vary significantly. From St. Venant's principle it is clear that the stress due to axial load and bending approach a linear distribution at a distance approximately equal to the maximum cross-sectional dimension of a member, *(h)*, in both directions, away from a discontinuity. **Figure 2.2** shows an illustration of St. Venant's principal. The empirical-based formulas however, do not address issues regarding detailing of D-region.

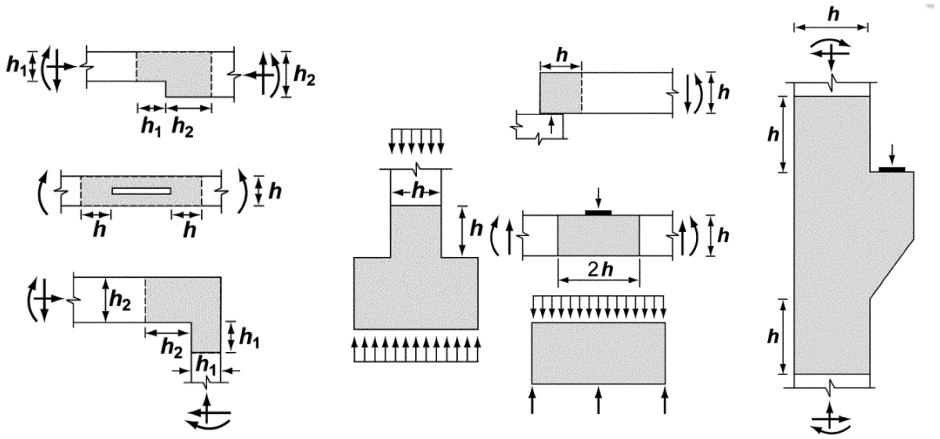

Figure 2.1 Examples of D-regions (ACI 318, 2011)

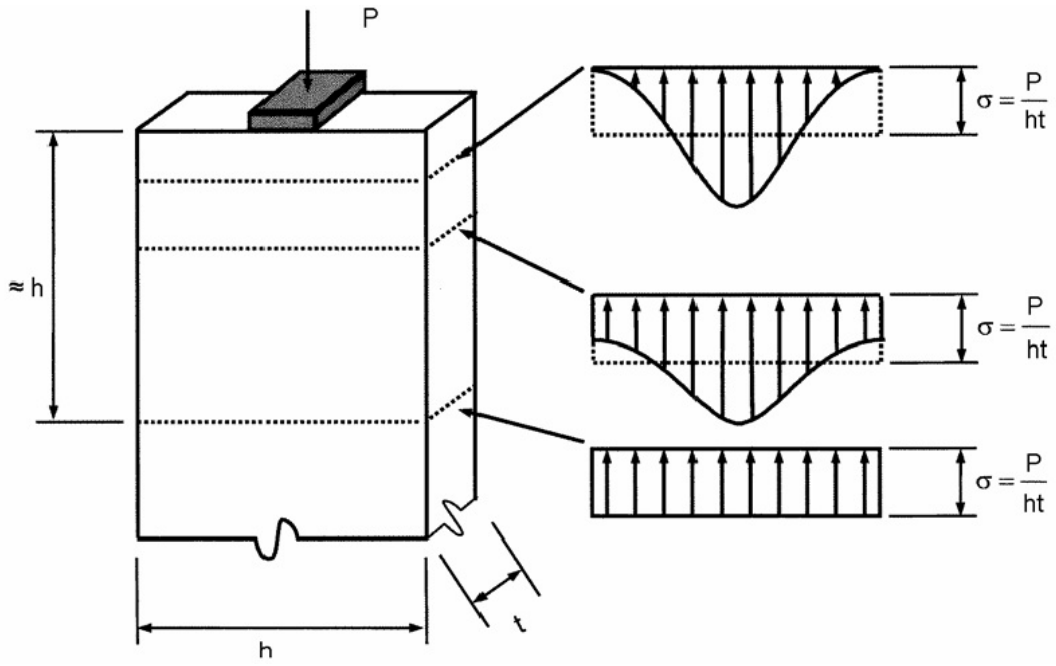

Figure 2.2 St. Venant's principle (Brown et al., 2006)

For this reason discontinuities are assumed to extend a distance (*h*) from the section where the load or change in geometry occurs. **Figure 3.2** illustrates examples of discontinuities with the resulting D-regions shaded. Most design practices for B-regions are based on model for behavior for example design for flexural is based on conventional beam theory while the design for shear is based on parallel chord truss analogy. In contrast most common type of D-region in deep beams, corbel, pile caps are still designed by empirical approaches. The strut-and-tie method is emerging as a code worthy methodology for design of all types of D-regions in structural concrete.

2.2 Strut-and-Tie Model (STM)

The use of STMs has increased significantly since publication of paper by Schlaich et al. (1987) that led to inclusion and implementation of the method in design codes (Breña and

Morrison, 2007). Although strut-and-tie models have been used in practice for a significant number of years in Europe and Canada, their widespread use in the U.S. began with the publication of Appendix A of the ACI 2002 "Building Code Requirements for Structural Concrete and Commentary" (ACI Committee 318-2002) and the 1998 *AASHTO LRFD Specifications* (AASHTO, 1998)

The strut-and-tie method can be used for the design of Disturbed regions (D-regions) of structures where the basic assumption of flexure theory, namely "*plane sections remains plane before and after bending"*, does not hold true. The strut-and-tie method of design is based on the assumption that the D-regions in concrete structures can be analyzed and designed using hypothetical pin-jointed trusses consisting of struts and ties interconnected at nodes.

Furthermore, STM reduces complex states of stress within a D-region of a reinforced concrete member into a truss comprised of simple, uniaxial stress paths. Each uniaxial stress path is considered a member of the STM. Members of the STM which are subjected to tensile stresses are called ties and represent the location where reinforcement should be placed, where as members subjected to compression are called struts. The intersection points of struts and ties are called nodes. Knowing the forces acting on the boundaries of the STM, the forces in each of the truss members can be determined using basic truss theory. With the forces in each strut and tie determined from basic statics, the resulting stresses within the elements themselves must be compared with permissible values. Through the use of this approach, an estimation of strength of a structural element can be made and hence can be appropriately detailed. Unlike the sectional methods of design, the strut-and-tie method does not lend itself into a cook book methodology and therefore requires the application of engineering judgment.

One of the benefits of using strut-and-tie model over empirical code procedures is that they provide solutions for problems where traditional design equations are not applicable (Maxwell and Breen, 2000). STM has been used effectively to design elements commonly encountered in practice such as corbels, post-tensioning anchorage zones, dapped-ends of

prestressed beams, pile caps, or deep beams (Breña and Morrison, 2007). In these applications, widely accepted strut-and-tie models have been developed and can be applied directly by designers. The development of an efficient strut-and-tie model for non-traditional design situations however is not straightforward. Geometrical discontinuities in the structure such as large openings which are required for utility purpose are one of the examples of these non-traditional situations.

2.3 Beams/Walls with Openings

Openings are frequently required in web area of reinforced concrete beams/walls (see **Figure 2.3**) to facilitate essential services such as conduits, network system access, or even movement from one room to another. Based on ultimate load theory a number of investigators studied the problem of deep beam with solid webs and put forward certain empirical and semi-empirical equations for predicting their load capacity (Rogowsky and MacGregor, 1986). However, studies on deep beams with web openings are very limited (Maxwell and Breen 2000; Chen et al. 2002; Kuchma and Park 2007; Tan and Zhang 2007; Ley et al. 2007; Breña and Morrison 2007; Kuchma et al. 2008) and there is no design procedure as such which can be used specifically for designing these members. Also ACI 318-11 does not address this issue, as a result of which engineers today are not equipped with lawful methodology to design these members.

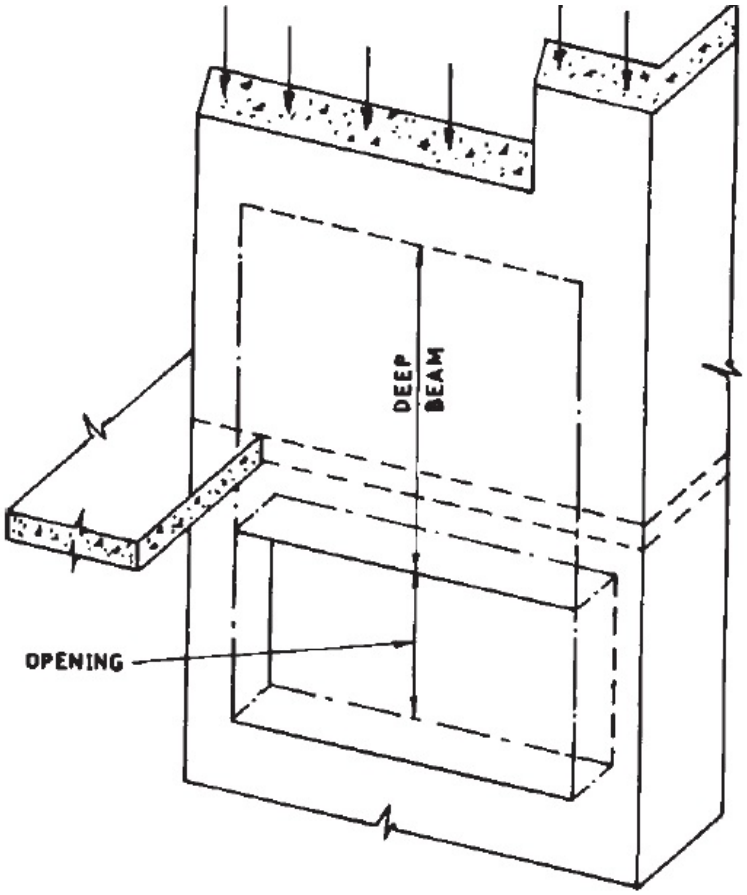

Figure 2.3 Deep beam with rectangular web opening (Ray, 1980)

Kong and his associates in 1973 at the universities of Nottingham Cambridge and Newcastel studied at length the problems of deep beams and presented semi-empirical formulae for predicting the ultimate strengths of both solid beams and beams with web openings. The CIRIA deep beam design guide (Arup and Partners, 1984) dealing with the design and detailing of web openings was mainly based on published literature, insightful feel for the forces and constructional experiences. However there is no legal document available till date giving detailed design guidelines. Therefore there is a definite need for extensive research and understanding particularly the behavior and strength of these concrete structural members.

2.3.1 Problems with Openings

These openings often interrupt direct load transfer from loading points to supports thus interfering with concrete strut and can cause a sharp decrease of strength and serviceability of deep beam. Although the strength evaluation and reinforcement details around openings in the deep beam are essential consideration, there are very few published data on such members (Breña and Morrison, 2007; Ruiz and Muttoni, 2007; Breen and Maxwell, 2000; Tan and Mansur, 1996). Maximum crack width at failure will be greater if the opening centre is located in the path of load transfer than at any other position (Kong, 1990). So location of the opening centre is undoubtedly the most important factor and governs the strength of the beam. It is recommended that the opening should not be brought too close to the vertical edge and inner and outer soffits of the beam, because at higher loads secondary cracks might appear and cause failure of the beam (Kong, 1990). The strength of the beam increases when the opening is located away from the concrete strut and vice-versa (Ray and Reddy, 1979; Ray, 1982). For the beams in which openings are located completely outside the concrete strut region, may be assumed to be a solid web beam (Ray, 1982). The location of the web opening is therefore a major factor influencing the strength of the beam.

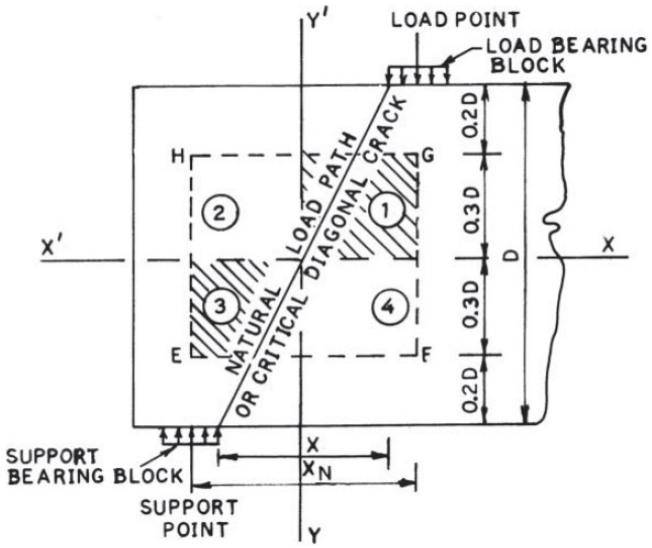

Figure 2.4 Practical regions for web openings (Ray, 1982)

2.3.2 Shear Zone or Practical Region for Web Opening by (Ray and Reddy, 1989)

Shear zone or practical region for web opening are the zone or region bounded by the verticals from the center of support point, center of load point and the horizontals at 0.2*D* and 0.8*D* from top of the beam (see **Figure 2.4**). The region marked EFGH in **Figure 2.4** represents the practical region. This region is divided into four equal quadrants by axes XX' and YY' passing through the center of the plane of rupture (natural load path). It is not advisable to position any opening within the 0.2*D* width regions at the top and bottom soffits of the beam. Ray and Reddy concluded that if the opening in the structure is located in the quadrants marked 1 and 3 in **Figure 2.4** then it will affect the strength of the structure to a greater extent as compared to if the opening is located in quadrant marked 2 and 4. From their conclusion it is evident that if the opening is located in between the load transfer path i.e. near the loading point and support block the strength of the beam is adversely affected. They also specified maximum allowable size of opening and was calculated based on equation 2-1. Based on the dimension of the specimen adopted in this study the maximum allowable area was 169 in^2, however the

area of the opening provided in the specimen was of 225 in^2 exceeding the area limit by 56 in^2.

$$\frac{X_N}{2} \times \frac{0.6D}{2} \qquad \textbf{Equation 2-1}$$

2.3.3 Stress State in RC members with Openings

Reinforced concrete (RC) members with significant geometric discontinuities and complex stress distributions under loading require considerable analysis and usually complicated reinforcement detailing. RC members with large openings are one of the examples. As discussed earlier these large openings may interrupt the load transfer by direct concrete struts and cause substantial decrease in strength and unpredictable failure modes. The actual stress fields in such members are typically very different from that predicated by STMs, as evidenced by past experimental investigations (Ruitz and Muttoin, 2007).

So far, only few studies have been conducted on systematic procedures for the development of stress fields (Despot 1995; Muttoni 1997; Vecchio 2000; Ruitz and Muttoin 2007). Although a well-established theoretical basis exists, a range of discontinuous stress fields can be proposed for a structural member subjected to a given and load combination. Therefore, the development of stress fields remains mainly based on perception and experience. A general method for developing stress fields has been proposed by Muttoni et al. (1997) including the serviceability behavior.

This method is based on the selection of a load-carrying mechanism for the structure and also on the role of the openings in developing cracks in critical regions. Although the method is completely general, it requires a trial-and-error procedure that is complicated to implement in a general way and also requires a certain level of experience for the choice of the load-carrying mechanisms. Despot (1995) has also proposed a finite element approach to the

problem with promising results. This approach combines the results of a linear-elastic analysis with a set of self-induced state of stresses to tackle the condition of plasticity in the elements. Ruitz and Muttion (2007) concluded that obtaining the stress field from nonlinear FE analysis done by applying reasonable values of physical parameters provides a step forward in developing a truss model for the structure.

2.4 Problems with Using STMs

It should be noted that the concept of STMs were originally developed based on plastic truss analogy, in which the structure is assumed sufficiently ductile. However, due to the fact that concrete has a limited capacity to sustain plastic deformation, those members deigned based on STM generally have limited post-peak ductility. That is, the envisioned STM structures do not behave as plastic trusses (Kuchma, et al, 2008).

With STM, it is not possible to determine the actual failure mode. Ideally the steel ties must yield, but the possibilities of brittle failures due to improper detailing are not discarded. Previous studies have shown that even though the ultimate loads were much higher than the design load, full strength of reinforcement bar was not utilized as most of the ties did not yield (Breña and Morrison, 2007; Carlos, 2009 Chao, 2011). Other; structural elements with D-regions such as beam-to-column joints designed with STM might exhibit brittle behavior if subjected to cyclic loading such as in an earthquake where ductility is of major concern. Researchers have shown that brittle failures are more pronounced for elements where higher concrete strength is used (Kuchma, et al., 2007). This is of prime importance because usually concrete suppliers aim for superior strengths than that specified by the designers to be on the safer side, not knowing the harmful effect of using higher compressive strength.

The choice of a strut-and-tie model is vital for design of reinforced concrete structures, especially for those containing discontinues regions. Several authors have recommended using elastic stress fields to set location of elements in strut-and-tie model for design (Schlaich et al.,

1987; MacGregor, 1997). Muttoni et al. (1997) have suggested identifying stress fields compatible with boundary conditions as a mechanism to construct strut-and-tie model. However the directions of principal stress might change significantly after concrete cracks. Hence, there is no unique strut-and-tie model to design a particular discontinuous structure. It is possible that a designer may end up with several models and face dilemma of using the correct one. Inexperienced designers might have doubts about their selected model. This is because no single model is the correct one for a given structure. In fact, two designers can come up with completely different models, yet both can be statically admissible. Hence, both are adequate based on current design methods. Also, tests have shown that large differences occur between calculated forces from STM and actual instrumented experimental specimens (e.g. Breña and Morrison, 2007). This implies that the model does not behave as designed.

Moreover the “truss analogy” as discussed by Ritter and Mörsch assumes that the concrete between the model is neglected. In a way it can be said that the material is wasted. As there is continuous increase in concerns of energy consumption, ozone layer depletion and recycling all over the world, advancements in “green material” is becoming more important. Today materials which can be recycled, consume less energy and are more durable are preferred more over materials that do not provide these advantages. Now the question which arises here is that weather conventional concrete used in day to day construction is really a green material. Answer to this question is “no” as cracks can be easily formed due to environmental action loading effect (Chao, 2008). Another aspect of green materials is its long-term performance when exposed to the environment. “Green” concrete has superior serviceability characteristics, and requires less rehabilitation and gives infrastructure longer service life (Chao, 2008). It is precisely said “A sustainable (or green) concrete structure is one that is constructed so that the total societal impact during its entire life cycle is minimal” (Niak, 2008).

2.5 RC Member with Complex Stress Field

Sufficient plastic redistribution of internal forces is essential for a structure to sustain expected and unexpected loads, and to fail in a ductile manner if over-loaded. In RC members, due to the brittle nature of concrete, this redistribution primarily relies on the steel reinforcing bars and their layouts, in which bars are placed at locations where the concrete is overly stressed beyond its cracking strength. For typical concrete members with simple and regular geometries, those locations can be easily predicted by classical elastic theory, It is well known, however, that the stress pattern is highly non-linear and deviates considerably from the classical elastic theory for RC members with significant geometric discontinuities.

2.5.1 In-Span Hinges in RC Box-Girder

Hinges are typically used to accommodate the longitudinal expansion and contraction of the structure and to allow independent vibrations of two adjacent bridge frames. In-span hinges have very complex internal stress distribution due to the geometries of the seat and discrete bearing locations, as well as the geometric discontinuities when utility openings exist. These utility openings allow human access from the interior of the box girder to the seat of in-span hinges. These members with significant geometric discontinuities and complex stress distributions under loading require considerable analyses and usually complicated reinforcement detailing. The reinforcement detailing of these concrete members based on STMs, is generally complicated and very often, these models cannot predict the failure mechanism due to localized damages. Also, the actual stress fields in such members are typically very different from that predicated by STMs, as indicated by many experimental investigations

Hube and Mosalam (2009) addressed the issues with in-span hinges. They carried out extensive research to understanding the load path, the failure modes, and the strength of typical

in-span hinges designed and constructed in California. They also investigated the influence of openings on behavior and strength of in-span hinges.

Figure 2.5 In-span hinges in RC box-girder bridges (Interstate 580 connector, San Rafael)

They reported that these opening reduces the load carrying capacity by 5% and are critical for the behavior, ductility and failure modes these structures. These members require considerable pre and post analysis. They concluded that designing of these members using standard procedures such as those in ACI 318, which is simplified analytical and design procedure lead to inefficient detailing because they do not take into account the expected failure modes (Hube and Mosalam, 2009). Also resulting detailing of these members with significant geometric discontinuities and complex stress distributions under loading require considerable analysis and usually complicated reinforcement detailing.

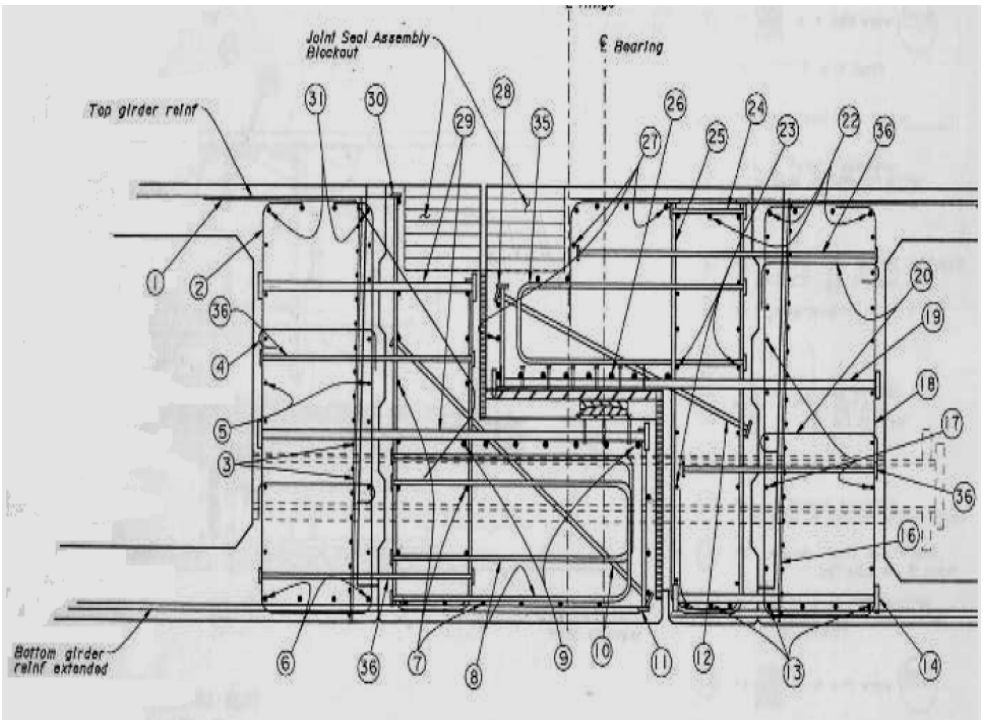

(a)

(b)

Figure 2.6 Reinforcement congestion of in-span hinge of prestressed box-girder bridge (a) section view (b) On site view (Hube and Mosalam, 2009)

2.5.2 Deep Beam with Large Openings by Breña and Morrison

Breña and Morrison performed series of experiments on deep beams with geometric discontinuities. The focus of their research was to identify and quantify the sources affecting the strength of the elements designed using strut-and-tie model. Experimental testing conducted by previous researches has indicated that the design based on strut-and-tie are typically conservative (Maxwell and Breen, 2000; Chen et al. 2002). They tested four deep beams, two with single opening and two with dual openings. The location and size of these openings were so selected so as to interfere with direct load paths than were suspected to potentially form between loading point and supports (Breña and Morrison, 2007). The strut-and-tie model used by them is shown in **Figures 2.8; 2.9**, these models were developed by approximately following the elastic principal stress distribution shown in **Figure 2.7**, dark arrows in the figure represent direction of principal compressive stress and principal tensile stress are perpendicular to principal compressive stress. Stress flow analysis showed that in the specimen with single opening the load is directly transferred from the loading point to support through bottle-shaped strut, but opening at left corner impairs this transfer and stress seems to flow around the opening. In case of the specimen with two openings more careful observation was required in order to determine the load transfer path (Breña and Morrison, 2007). Two strut-and-tie models were developed for each type of specimen (see **Figures 2.8; 2.9**), struts are represented by dashed lines where as ties are represented by solid lines. Reinforcement steel bars (10M) was layed in two layers along the thickness of the beam.

Their test showed that measured strength of the specimens was significantly higher than what was calculated from design strut-and-tie model. The ratio of measured to calculated load was approximately 3.2 for specimen shown in **Figure 2.8** and 1.7 for specimens shown in **Figure 2.9**. All their specimens failed at much higher loads than those associated with critical tie yielding. It is important to note that the development of strut-and-tie model is based on plasticity theory, based on this the all ties are supposed to yield at failure; however this was not

the case as observed from there testing as only few ties yielded at ultimate loads. Concrete crushing was observed in the regions of high stress i.e. near support and region between opening and edge of beam (see **Figures 2.10, 2.11**). Moreover completely different failure modes were observed for same specimen designed using different strut-and-tie model, also they did not comply with the failure mode based on the strut-and-tie model analysis done by them on software developed by Tjhin and Kuchma (2002). They concluded that occurrence of these failure modes emphasizes the need to carefully the detail regions of structure where strut-and-tie model do not adequately capture the actual stress conditions and also the detrimental effect of support restrains on the failure modes of the structure needs vigilant observation as well as proper detailing since they are not explicitly addressed by ACI 318-11, Appendix A (Breña and Morrison, 2007).

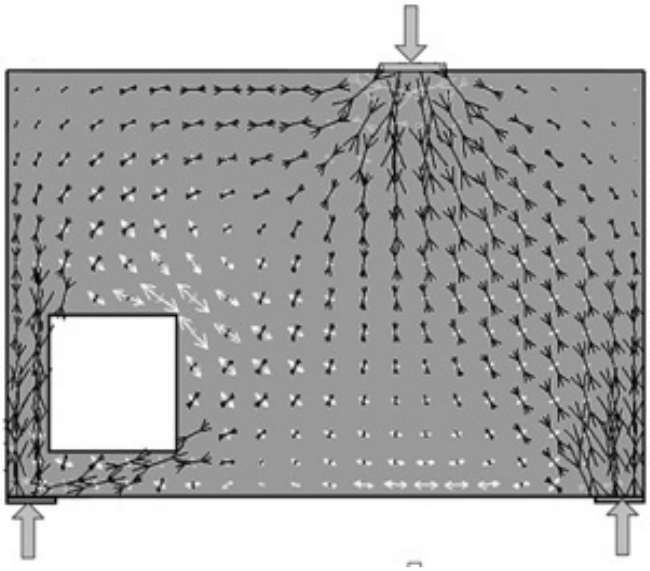

(a)

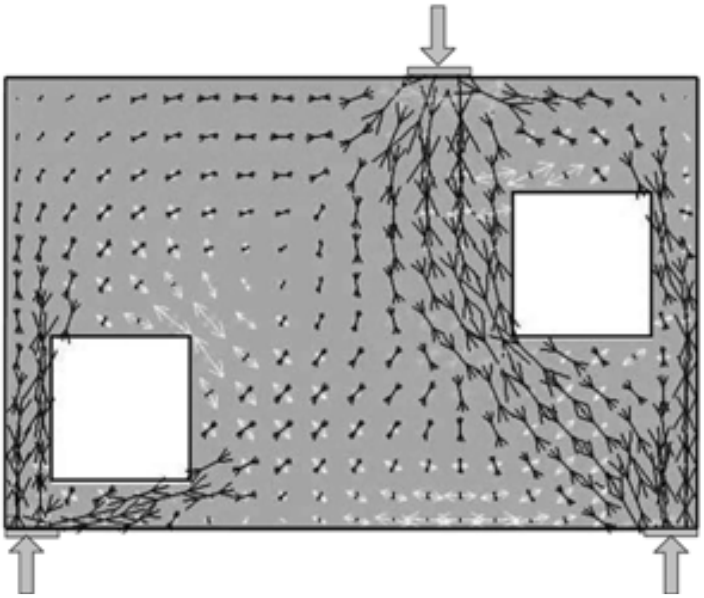

(b)

Figure 2.7 Principal stress direction (a) beam with single opening (b) beam with dual opening (Breña and Morrison, 2007)

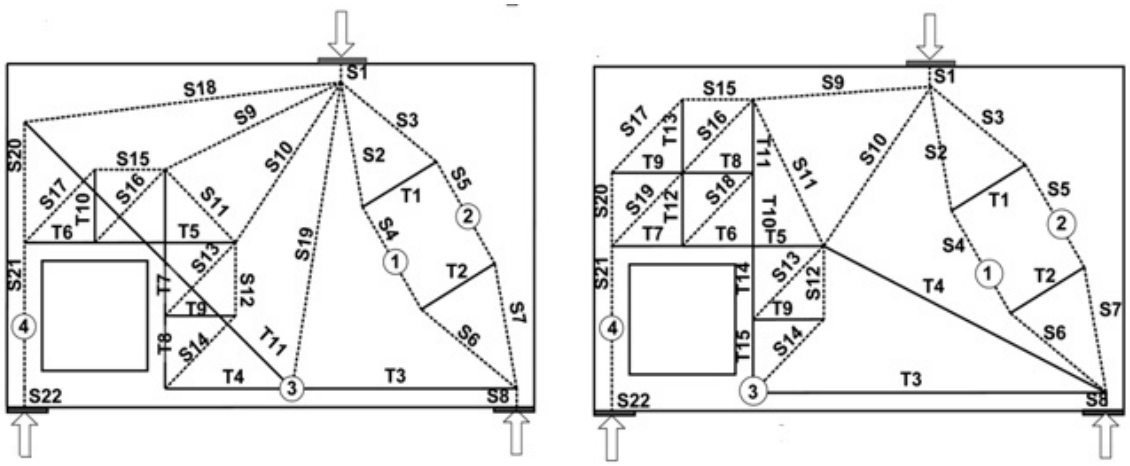

Figure 2.8 Design Strut-and-tie models based on principal stress field in **Figure 2.7**(a) (Breña and Morrison, 2007)

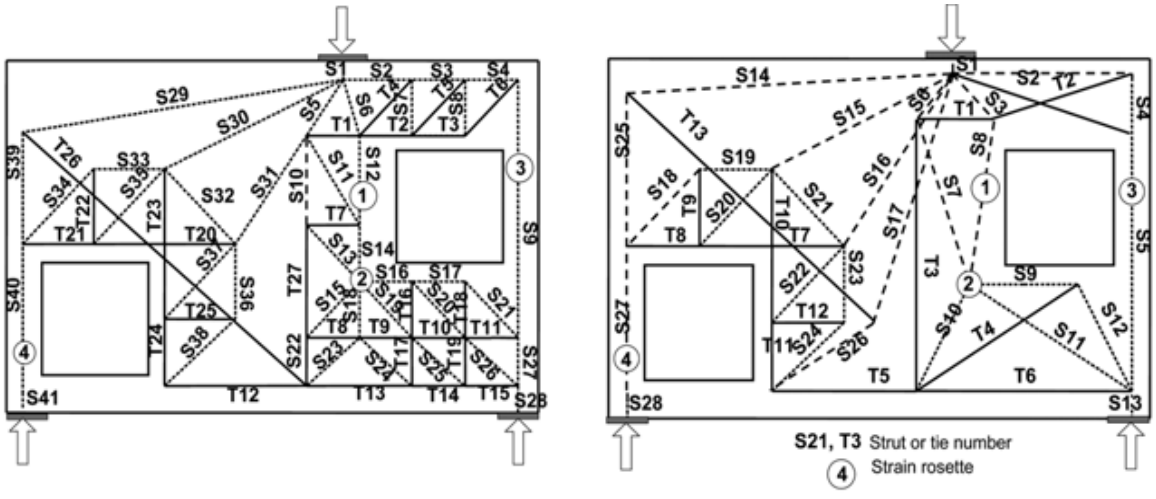

Figure 2.9 Design Strut-and-tie models based on principal stress field in **Figure 2.7**(b) (Breña and Morrison, 2007)

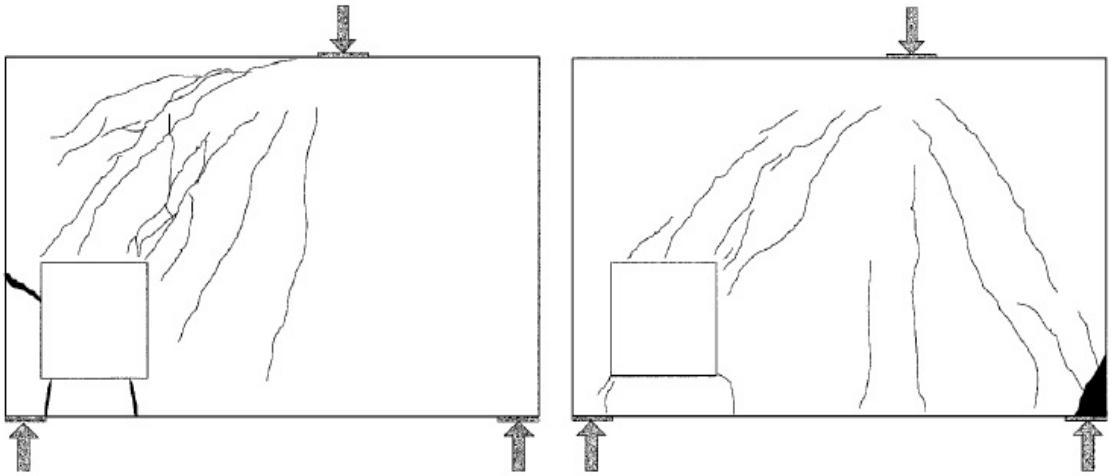

Figure 2.10 Observed cracking pattern for beam designed based on **Figure 2.8**
(Breña and Morrison, 2007)

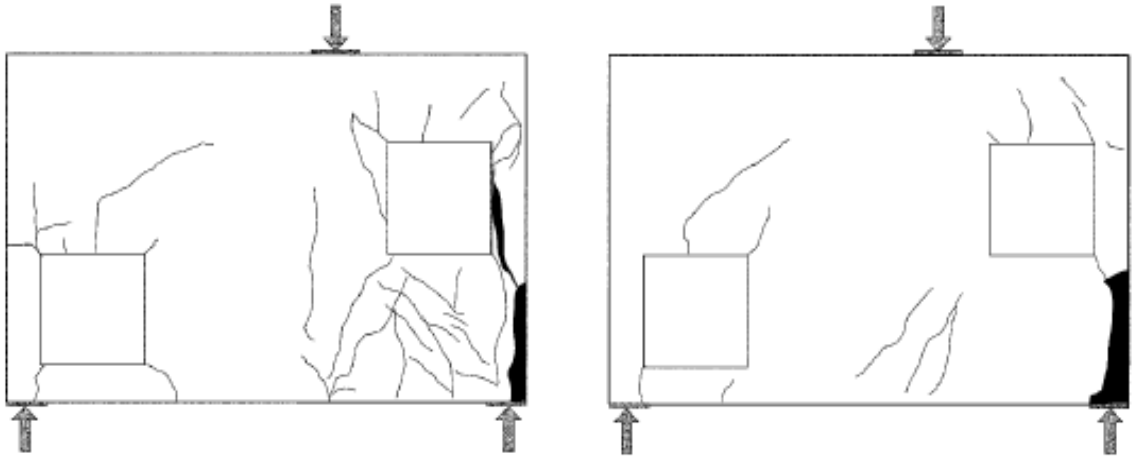

Figure 2.11 Observed cracking pattern for beam designed based on **Figure 2.9**
(Breña and Morrison, 2007)

2.6 Fiber Reinforced Concrete

The next question which arises is that how all the issues discussed above regarding strut-and-tie model, concrete strength, its brittle nature can be addressed. To address these issues fiber reinforced concrete was used in this research.

The concept of using small, discrete fibers as reinforcement for brittle materials has been known from thousands of years. There is evidence that the ancient Egyptians used straw to improve the cracking behavior of the sun-dried mud brick used in construction (Mansour et al., 2007). However, Romualdi and Batson began the modern development of fiber reinforced concrete (FRC) with a publication in 1963, which was followed by more work by Romualdi and Mandel in 1964 (Romualdi and Batson, 1963; Romualdi and Mandel, 1964). These works demonstrated the feasibility of using fibers to improve the ductility and tensile strength of concrete. Research has also shown that shrinkage and temperature reinforcement can be reduced, and in many cases eliminated, with the addition of fibers to the concrete (Susetyo, 2009). Also addition of fibers reduces the labor cost for construction as there are minimal to no conventional reinforcement to place and tie (Johnston, 2001). For non-fibrous concretes, these improved cracking characteristics have to be obtained by providing additional shrinkage reinforcing bars, which in turn also increase the concrete cover required. Steel fibers can be used to eliminate or at least significantly reduce the transverse shear reinforcing bars in beams while maintaining the required shear resistance (Parra-Montesinos, 2006).

2.6.1 Types of Fibers

The effectiveness of fibers made from a variety of materials has been investigated extensively over the years. The fibers range from natural fibers (such as wood cellulose, grass, and bamboo), to synthetic fibers (such as nylon, polyester, polyethylene, aramid and carbon), to glass and steel fibers. Natural fibers have low modulus of elasticity, susceptibility to alkali

attack, and their high absorption capabilities which allow for excessive shrinkage and swelling (Johnston, 2001).

Carbon and aramid fibers had excellent material properties, but were relatively expensive (Johnston, 2001). Steel fibers have a relatively high modulus of elasticity and can have high tensile strength as well. These fibers are alkali resistant; in fact steel embedded in concrete develops an iron-oxide film in the alkaline environment which is corrosion-resistant, provided that crack widths are not excessively large (Mehta and Monteiro, 1993). As a result of above mentioned properties, steel fibers outperform most other fibers in terms of crack control. For these reasons, along with the fact that they are the most widely used fiber in industry today, steel fibers were chosen for this research program.

Steel fibers are available in a variety of shapes and lengths. These include straight, end-hooked, crimped, twisted polygonal, cone-ended, and flattened-end fibers. Deformed fibers provide superior mechanical anchorage, which increases the bond stress and thus the internal force in the fiber, allowing for a more efficient use of the material. This enhanced mechanical anchorage has the supplementary effect of reducing the crack spacing and widths of the SFRC over those which contain straight fibers. The tensile strength of steel fibers may be as low as that of mild steel, or approximately 350 MPa (Daniel, 1991). However, most modern steel fibers are typically available in two strength ranges; moderate strength (approximately 1000 MPa) and high-strength (2000 MPa and more).

2.6.2 Parameters Affecting SFRC

There are several parameters that affect the behavior of SFRC. These include the volumetric content (V_f), length (l), aspect ratio (l/d), tensile strength and orientation of the fibers as well as the strength of the concrete matrix. The amount of fibers added to a concrete mix is expressed as a percentage of the total volume of the composite (concrete and fibers), termed volume fraction (V_f). Aspect ratio (l/d) is calculated by dividing fiber length (l) by its diameter (d).

Fibers with a non-circular cross section use an equivalent diameter for the calculation of aspect ratio. If the modulus of elasticity of the fiber is higher than the matrix (concrete or mortar binder), they help to carry the load by increasing the tensile strength of the material.

Shah and Rangan (1971) observed that the flexural toughness, enclosed area under the load-deflection curve, could be increased to five to fifteen times that of plain concrete when fiber contents of 0.5 to 1% were used, respectively. They also found that an increase in fiber content from 0.5% to 1.0% has been found to increase the direct tensile strength from 1.1 to 1.3 times that of plain concrete, and to increase the direct tension toughness from 1.8 to 2.7 times that of plain concrete. The compressive toughness is also found to improve with the increase in the fiber content. For example, increase in the fiber content from 1.0% to 2.0% has been found to increase the compressive toughness from 2.3 to 2.8 times that of the equivalent plain concrete (Fanella and Naaman, 1985). However, increasing the fiber content does not seem to have a significant effect on the peak compressive strength of the concrete (Fanella and Naaman, 1985; Hsu and Hsu, 1994). Conversely, an increase in fiber content also reduces workability, because the addition of fibers reduces the paste volume fraction available for the free movement of aggregates and fibers (Deluce, 2011).

The fiber length has a significant effect on the performance of the composite. Fibers of a greater length have greater bond resistance before entirely pulling out, extending the range of crack widths and deformations that are affected by the improvement in behavior caused by fiber inclusion (Deluce, 2011). However, it should be noted that for a particular application, the fiber length may need to be limited as they “ball” in the mix and create workability problems. This is also important in order to fit the fibers into small spaces between reinforcement bars and formwork while allowing a proper dispersion of the fibers in two- or three-dimensional space while concrete poring.

2.6.3 SFRC Provisions in ACI 318

Since its introduction in the mid-1990s in national building code, (ACI 544-96, 1996) SFRC has gained popularity and are being preferred in many applications over conventionally-reinforced concrete. According to the report published by ACI Committee 554 the total energy absorbed in fiber debonding as measured by the area under the load-deflection curve before complete separation of a beam is at least 10 to 40 times higher for fiber-reinforced concrete than for plain concrete.

Despite of extensive laboratory demonstrations on usefulness of fibers in various structural applications, the actual use of fibers in construction industries is still limited. Among many reasons lack of design methods and specifications are prime factors making it difficult for the designers to adopt SFRC as a medium for constructing structural elements. However due to the increasing evidence from previous research results, the 2008 ACI Building Code allowed engineers to use steel fiber reinforced concrete (SFRC) to replace the conventional shear reinforcement (i.e. steel stirrups) even if the design shear force was greater than half of the concrete shear strength. Though the new ACI provisions, marked a significant transfer from research to practice, it restricts the beams constructed of steel fiber reinforced concrete to have a minimum amount of steel fibers of 0.75% in volume (100 pounds per cubic yards) and compressive strength not greater than 6 ksi.

2.7 Research on Deep Beam with Openings Using SFRC

Sahoo, Flores and Chao, (2012) carried out various lab experiments on these reinforced concrete structures. They emphasized the need to evaluate the performance of STMs in order to obtain consistent and reliable results from these models in terms of ultimate strength and failure mechanism prediction. To address this issue they proposed the use of steel fiber reinforced (SFRC) as a material to construct these structures. Their selection of SFRC as a material solution was backed by past researches (e.g., Narayana and Darwish, 1986; Mansur

and Ong, 1991) from which increase in strength, enhanced deformation capacities and better crack control in deep beams was observed.

There test specimen represented approximately one fourth scale models of beams originally considered by Schlaich et al. (1987). Geometrically similar specimens were tested in laboratory during past (Maxwell and Breen, 2000; Breña and Morrison, 2007). The location of opening in these specimens was selected so as to directly interfere with the load transfer path (Breña and Morrison, 2007).

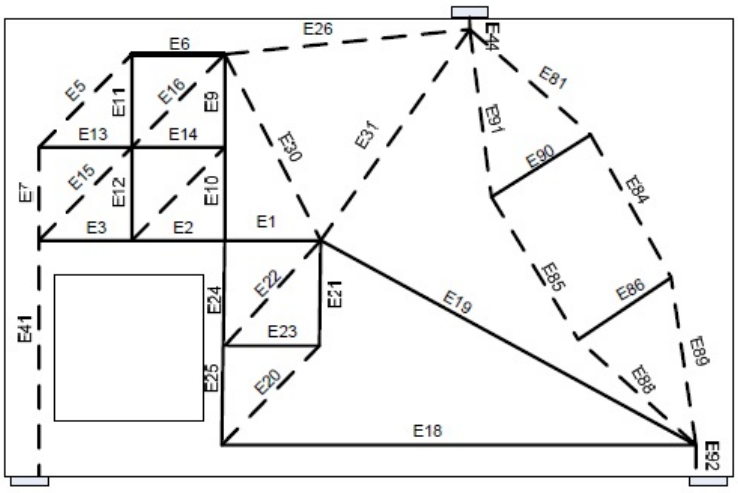

Figure 2.12 Design strut-and-tie model - Solid lines represents tie and dashed line strut (Sahoo, Flores and Chao, 2012)

As discussed earlier their main focus was to eliminate conventional reinforcement and secondary reinforcement detailing required by STMs, by mixing steel fibers in concrete. They tested two RC specimens (see **Figure 2.14**) designed based on STM (see **Figure 2.13**) under monotonically increased load and their behavior was compared with two geometrically similar SFRC specimens with 1.5% volume fraction of fibers under same loading conditions.

Failure mode and ultimate strengths of these beams was compared with those predicted by model. As mentioned earlier their RC specimens was detailed based on STM and had very

complicated detailing (see **Figure 2.14**) as compared to the SFRC specimens which had just flexural reinforcement as a means of conventional reinforcement, which not only simplified the design but also expedited the construction process compared to RC specimen.

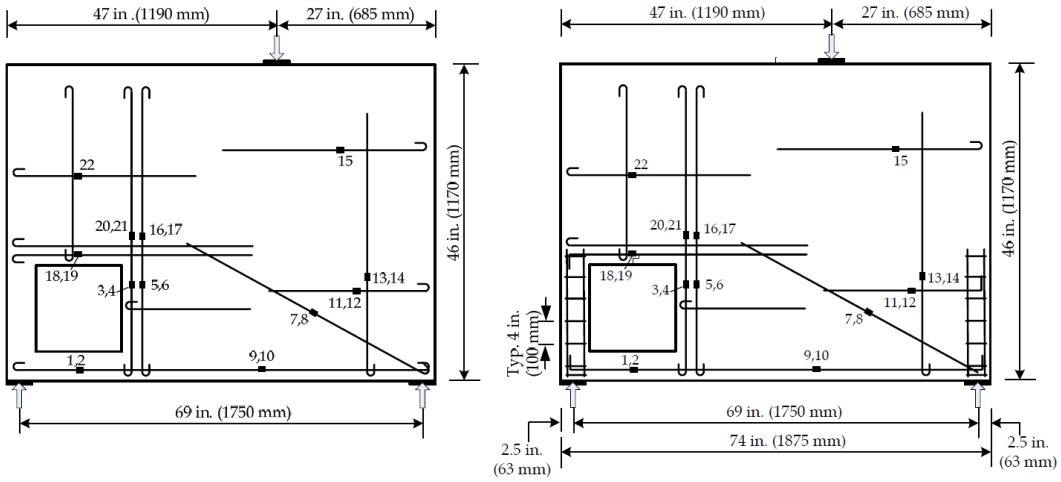

Figure 2.13 Dimension and reinforcement layout with strain gauge for RC specimens (Shaoo, Flores and Chao, 2012)

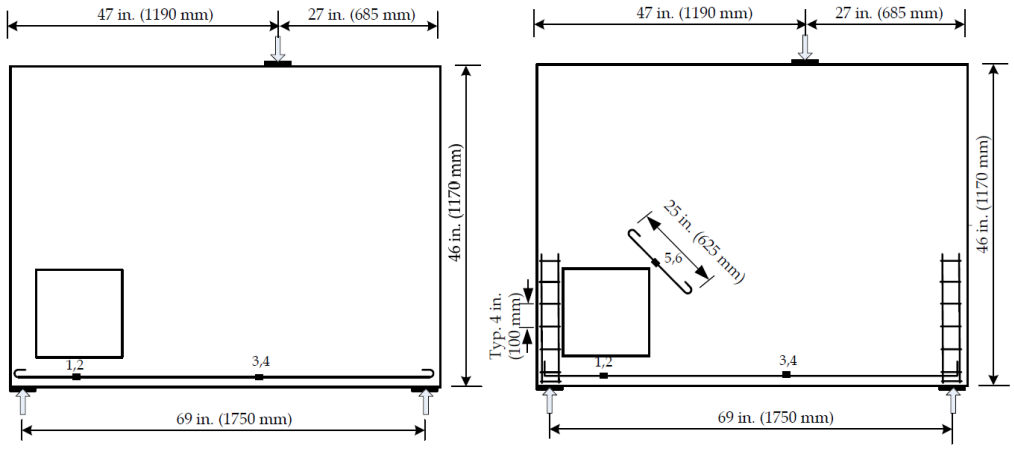

Figure 2.14 Dimension and reinforcement layout with strain gauge for SFRC specimens (Shaoo, Flores and Chao, 2012)

From their testing it was observed that the individual members designed based on STM exhibited greater strength than expected, this was apparent as RC specimen designed based on STM carried nearly 3.3 times the design load. Also use of SFRC proved to be beneficial as the specimens reinforced with fibers reached almost three times the design strength limit for RC specimens even though reinforcement bars was not used except for bottom tie. Concrete crushing was observer in localized regions (near support) due to high axial stress. These failure locations are not predicted by STM as no special detailing is in these regions provided based on STM (Sahoo, Flores and Chao, 2012).

The ratio of maximum value of load carried by SFRC specimen to nominal strength of RC specimen was 2.35. This indicates that steel fiber can significantly enhance the performance of deep beams with large openings (Sahoo, Flores and Chao, 2012). Further they concluded that fibers inhibits the widening of cracks and also increases the number of cracks in the specimen, thus helping to redistribute the forces in the specimen, even if conventional reinforcement bars are not present (Sahoo, Flores and Chao, 2012)

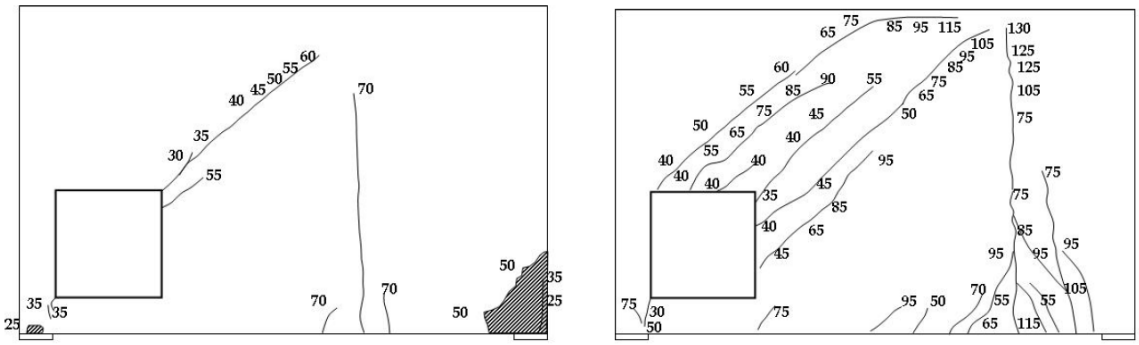

Figure 2.15 Observed cracking in RC specimens corresponding to reinforcement layout shown in **Figure 2.13** (Sahoo, Flores and Chao, 2012)

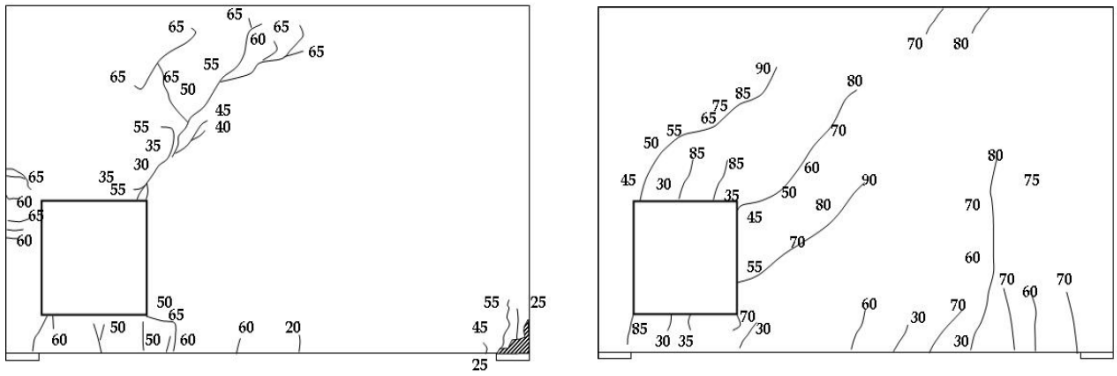

Figure 2.16 Observed cracking in SFRC specimens corresponding to reinforcement layout shown in **Figure 2.14** (Sahoo, Flores and Chao, 2012)

CHAPTER 3

MATERIAL TESTS

3.1 Introduction

It is necessary to determine the material properties of test specimens used in the experiment in order to evaluate the performance of the materials used, to compare or check the consistency between different concrete mixes and also to stimulate nonlinear finite element analysis. Several material specimens for were casted for each material tests along with large scale specimen in order to obtain reliable average data. **Figure 3.1** shows the oiled large-scale formwork and material molds before casting. In this study four testing method was employed for each concrete mixture.

Compressive Strength Test

Compressive strength of the concrete mix in terms of stress was determined in accordance of ASTM C39-11 by testing six cylinders of size 4 x 8 in. (102 x 203 mm) for each large scale specimen. Capping of these cylinders was also done in accordance to ASTM C 617-11.

Three-Point Bending Test

This test method is used to evaluate the flexural performance of RC and SFRC mixtures by using parameters derived from the load-deflection curve obtained by testing a simply supported beam under third-point loading. The bending test setup used in this study was based on ASTM C1609 (ASTM, 2010), as shown in **Figure 3.7**. Specimens have a prism shape with a dimension of 6 x 6 x 20 in. (152.4 x 152.4 x 508 mm). A pair of LVDTs was mounted on

a jig based on the ASTM C1609 requirement to ensure accurate determination of the net deflection at the mid-span, exclusive of the effects of seating or twisting of the specimen on its supports. Tests were carried out by a closed-loop, servo-controlled machine with a loading rate as prescribed by ASTM C1609 (ASTM, 2010)

Double Punch Test

This test method uses an indirect approach to determine the tensile strength. This method was developed by Chen in 1970 and was used for steel as well as polymeric fibers. This method was found to be better than split-cylinder test for obtaining tensile strength of SFRC (Chen and Yuan, 1980). DPT specimens have a cylindrical shape with dimensions of 6 x 6 in. (152.4 x 152.4 mm). A pair of LVDTs was used to measure the vertical deformation of the specimen. Test was carried out on 60 kip (267 kN) Baldwin hydraulic testing machine.

Direct Tensile Test

This test type can identify the key properties of FRC such as strain-hardening or strain-softening, elastic modulus, and stress versus strain relationships under tension, which are the constitutive properties of FRC that are useful for modeling and design of FRC structural members (Naaman, et al., 2007). However currently there is no standard method for this test in the U.S., in part because it is difficult to provide a gripping arrangement which will not lead to specimen cracking at grips. Specimens used in this study were specifically designed so that a pin-pin loading condition is created at the ends (see **Figure 3.26**). Both ends are strengthened by the double dog-bone geometry and steel meshes were used to ensure that cracking would only occur at the central portion within the gauge length. The double dog-bone shape was used to mitigate the stress concentration resulted from the reduction of cross-section. The central portion of the specimen had a square cross-section with a dimension of 4 x 4 in. (102 x 102 mm). This dimension was selected to reduce the size effect (Naaman and Reinhardt, 2006) while maintaining a suitable weight for laboratory handling. The strains were measure by a pair

of LVDTs with a gauge length of approximately 7 in. (178 mm). Tests were carried out by a closed-loop, servo-controlled machine with a loading rate of approximately 0.05 mm/min (0.002 in. /min).

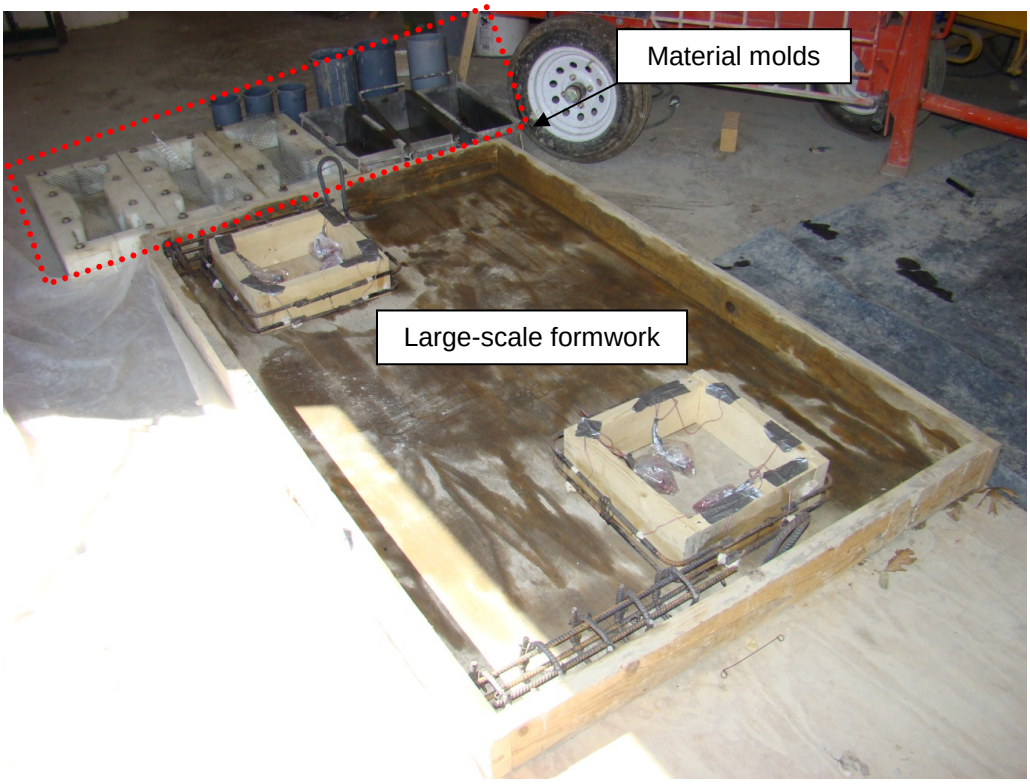

Figure 3.1 Oiled large-scale formwork kept with material molds before testing

3.2 Concrete Mixture Used for Plain and Fiber Reinforce Concrete

As there were mainly two types of mixtures one with fibers (SFRC mix) and one without fibers (RC mix), the mix design was optimize in order to use similar proportions for both mixes. The volume fraction of fibers in all SFRC specimens was 1.5% except that of SFRC#3

specimen in which 1% steel fibers was used. Chemical admixtures were not used in any specimens during this project.

Table 3.1 Concrete mixture composition in proportion by weight of cement for all four specimens

Material	RC Mix	SFRC#1 Mix V_f=1.5%	SFRC#2 Mix V_f=1.5%	SFRC#3 Mix V_f=1.0%
Portland Cement	1.0	1.0	1.0	1.0
Fly Ash (Class C)	0.50	0.50	0.50	0.50
Fine Aggregate (Sand)	1.70	1.70	1.70	1.70
Coarse Aggregate (3/8 in.)	1.0	1.0	1.0	1.0
Water	0.60	0.58	0.58	0.58
Steel Fiber	0	0.247	0.247	0.165

Note: Water to cementitious ratio (w/cm) is 0.4 for RC mix and 0.38 for SFRC mixes.

The sand used in this study was ASTM natural river sand with Fineness Modulus of 2.57. The maximum size of course aggregate used was 3/8 in. This size was selected to facilitate better mixing of fiber into concrete mix. The water to cementitious material ratio (w/cm) was changed from 0.4 in RC specimen to 0.38 in remaining specimens, this was done because during casting of RC specimen the concrete mixture seemed very flowable which may lead to bleeding or segregation of aggregate, therefore to ensure good mixture for the SFRC specimens the water to cementitious ratio (w/cm) was reduced to 0.02 for remaining specimens. The steel fibers used in the study was deformed hooked end fibers with measure length of 1.87

in. (47.5 mm) (see **Figure 3.2**) and tensile strength of 160 ksi as provided by manufacture. Detailed specification of this fiber is given in **Table 3.2**. The fiber percent in SFRC#3 specimen was reduced by 0.5%; this was done to see the effect of reduced fiber percentage on load carrying capacity, ductility, cracking control of the specimen.

Table 3.2 Mechanical Properties of Steel fiber

Fiber type	Length (L) in. (mm)[1]	Diameter (D) in. (mm)[1]	Aspect ratio (L/D)	Tensile strength ksi (MPa) [2]
Steel Hooked Fiber	1.87 (47.5)	0.031 (0.79)	60.3	160 (1100)

Note: [1] measured; [2] provided by manufacturer

Figure 3.2 Deformed hooked-end steel fibers used in study

3.3 Compressive Strength

Concrete cylinders were cured under the same environmental conditions (75 degree room temperature and 75% R.H.) as that of large-scale specimens. All specimens were covered with a sheet of polyethylene for twenty-four hours; this was done in order to prevent any shrinkage cracks. The cylinders were capped in accordance with ASTM C617, "Standard *Practice for Capping Cylindrical Concrete Specimens*", (ASTM, 2011). All cylinders were of same size of 4 x 8 in. (see Figure 3-3), in accordance to ASTM C39, "Standard *Test Method for Compressive Strength of Cylindrical Concrete Specimens*", (ASTM, 2011).

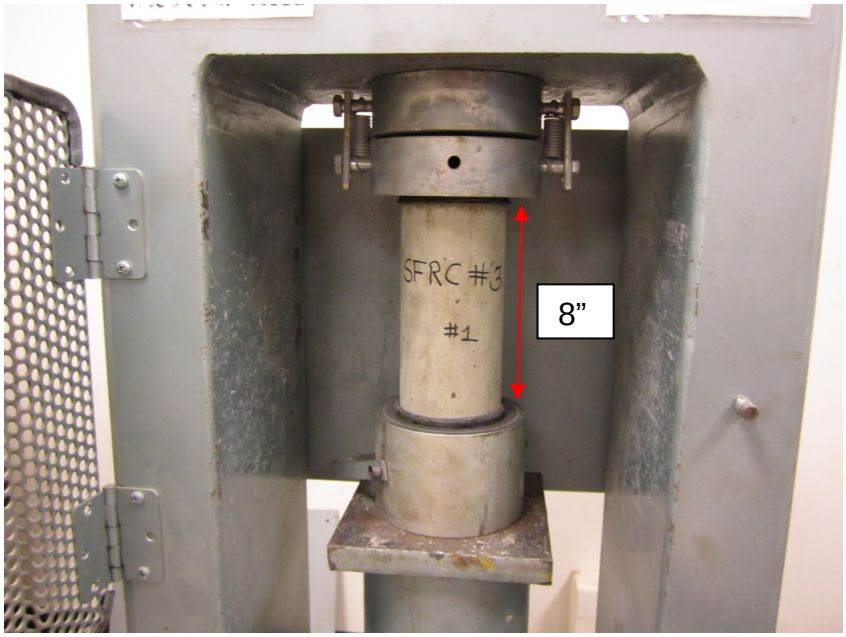

Figure 3.3 Capped steel fiber reinforced concrete cylinder before testing

The cylinders were tested on the same day when the large-scale specimen was tested. In total six cylinders were tested for one large-scale specimen, and average value of

compressive strength was obtained. **Tables 3.3** to **3.6** summarize the results of compression test. Compressive strength testing showed a brittle failure for the plain concrete cylinders. All cylinders had failure mode between Type “e” (columnar) and Type “b” (cone and split), as described by ASTM C39 (see **Figure 3.5**). The cylinders failed in an explosive way and were no longer able to resist load. Severe fracture was observed and concrete completely separated after the load was removed from the cylinders (see **Figure 3.4**).

Figure 3.4 Typical plain concrete cylinder after testing

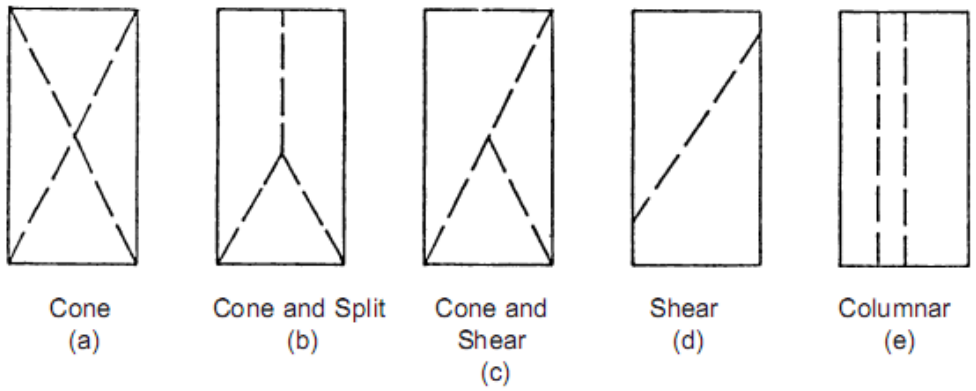

Figure 3.5 Sketch for Types of failure modes (ASTM C39, 2011)

The testing and capping procedure for SFRC was the same as that of plain concrete cylinders. Tests showed that there was severe concrete crushing at ultimate load. However none of the SFRC specimens had concrete separation even after the load was removed. The failure mode for all the SFRC cylinders was much more ductile as compared to that of plain concrete (**Figure 3.5**).

(a) (b)

Figure 3.6 Typical steel fiber reinforced concrete specimens (a) during testing (b) after testing

Table 3.3 Compressive test results for RC specimen (Specimen #1)

Sample No.	Load (lb)	Diameter x Height (in.)	Area (in^2.)	$f'_c = P/(\pi/4)d^2$(psi)
1	90920	4 x 8	12.56	7235
2	98860	4 x 8	12.56	7867
3	77540	4 x 8	12.56	6171
4	64150	4 x 8	12.56	5105
5	76810	4 x 8	12.56	6112
6	98140	4 x 8	12.56	7810
			Average f'_c	**6717**

Table 3.4 Compressive test results for SFRC#1 specimen (Specimen #2).

Sample No.	Load (lb)	Diameter x Height (in.)	Area (in^2.)	$f'_c = P/(\pi/4)d^2$(psi)
1	78560	4 x 8	12.56	6255
2	62780	4 x 8	12.56	4998
3	76960	4 x 8	12.56	6127
4	68280	4 x 8	12.56	5436
5	74850	4 x 8	12.56	5959
6	76550	4 x 8	12.56	6095
			Average f'_c	**5812**

Table 3.5 Compressive test results for SFRC#2 specimen (Specimen #3).

Sample No.	Load (kip)	Diameter x Height (in.)	Area (in^2.)	$f'_c = P/(\pi/4)d^2$ (psi)
1	78540	4 x 8	12.56	6250
2	78120	4 x 8	12.56	6217
3	87320	4 x 8	12.56	6949
4	83100	4 x 8	12.56	6613
5	71690	4 x 8	12.56	5705
6	84550	4 x 8	12.56	6728
			Average f'_c	**6410**

Table 3.6 Compressive test results for SFRC#3 specimen (Specimen #4).

Sample No.	Load (kip)	Diameter x Height (in.)	Area (in^2.)	$f'_c = P/(\pi/4)d^2$ (psi)
1	82270	4 x 8	12.56	6550
2	84680	4 x 8	12.56	6742
3	84880	4 x 8	12.56	6758
4	85350	4 x 8	12.56	6795
5	86784	4 x 8	12.56	6910
6	85684	4 x 8	12.56	6822
			Average f'_c	**6763**

3.4 Flexural Strength

As discussed earlier this test method covers the determination of the flexural strength of concrete by the use of a simple beam with third-point loading. All the specimens used for flexural testing had nominal dimensions 6 x 6 x 20 in. (152.4 x 152.4 x 508 mm) width, height and length, respectively, with a clear span length of 18 in. (see **Figure 3.7)**. The apparatus fixtures as shown in **Figure 3.7** were in accordance with ASTM C78, "*Standard Test Method for Flexural Strength of Concrete (Using Simple Beam with Third-Point Loading)*", (ASTM, 2010). However testing procedure for all the specimens were in accordance to ASTM C1609, "Standard *Test Method for Flexural Performance of Fiber-Reinforced Concrete (Using Beam with Third-Point Loading)*", (ASTM, 2010).

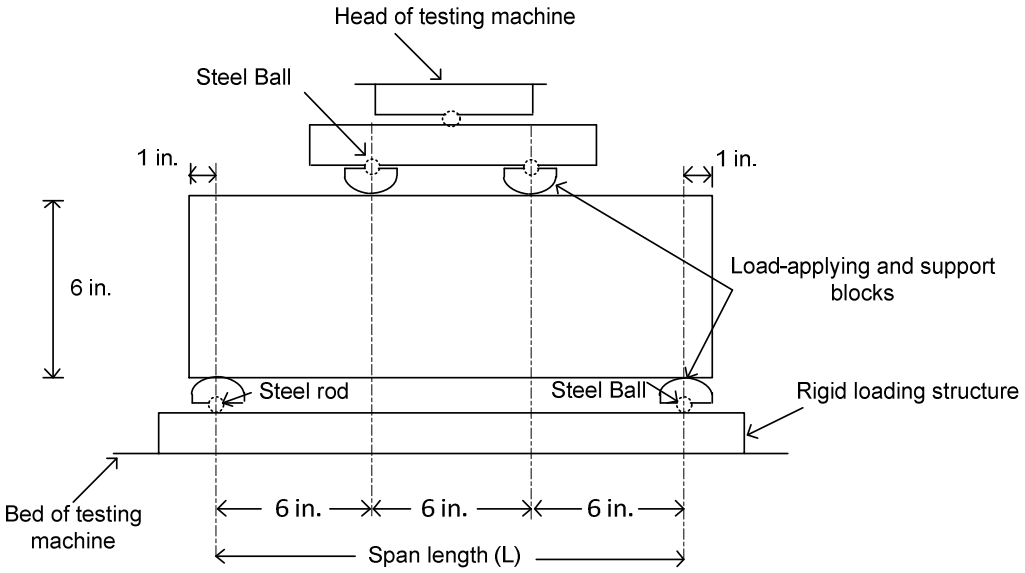

Figure 3.7 Diagrammatic view of apparatus for flexure test of concrete by Third-Point loading method

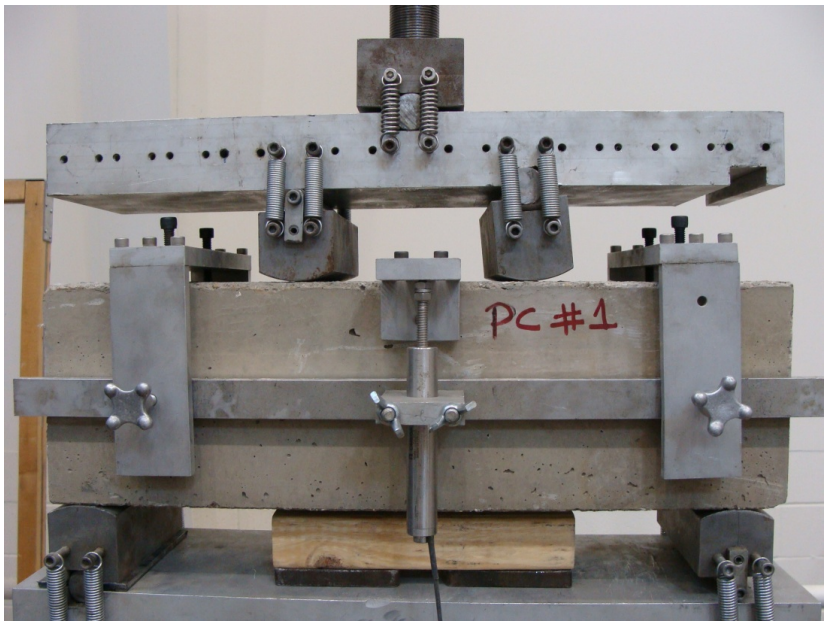

Figure 3.8 Test-setup for PC specimen by Third-Point loading method

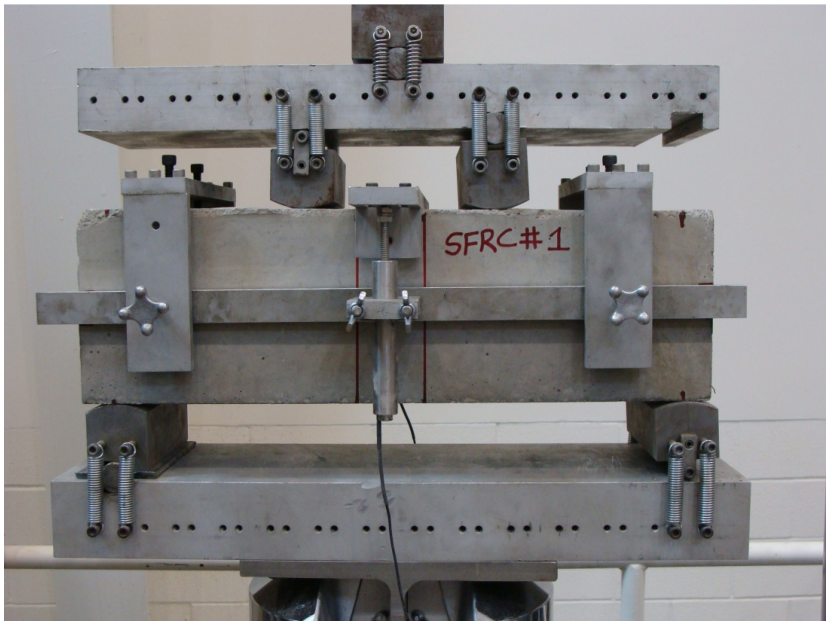

Figure 3.9 Test-setup for SFRC specimen by Third-Point loading method

Although the ASTM standards are different for RC and SFRC specimens, the instrumentation and testing procedure was carried out in accordance to ASTM C1609 (2010) for both the cases. This was done so that comparative study of results from different specimen can be done and for consistency purposes. It is important to note that ASTM C1609 (2010) allows using same apparatus fixtures as described in ASTM C78 (2010) with the qualification that the supporting rollers should be able to rotate freely and not offered any resistance.

The test-setup used in case of RC and SFRC specimens is shown in **Figures 3.8** and **3.9**. Two LVDTs were used to measured displacement, one of them were placed on either side of the beam along the thickness at midspan, so that an average displacement value can be taken. This arrangement of LVDTs ensured accurate determination of net deflection at mid span excluding the effects of seating or twisting of specimen at supports (ASTM C1609, 2010). Loading rate, as prescribed by ASTM C1609 (2010) standard was kept at 0.002 to 0.005 in. /min of net deflection up a total deflection of L/600. After this point, the loading rate was kept at 0.002 to 0.010 in. /min. until a deflection of L/150 was reached, or 0.12 in (as L = 18 in). Six specimens were casted for all SFRC beams and three specimens were casted for RC beam.

For most of the SFRC beams, peak load was greater than the first peak load (see **Figure 3.10**). These beams showed significant residual strength after reaching peak load. This was primarily due to crack retention properties of steel fibers in concrete. Also, smaller micro-cracks were developed from initial crack as the deflection increased from 0.3 in. (7.6 mm) to 0.12 in. (3 mm) (see **Figure 3.12 and 3.13**). Pull out of steel fibers from concrete was noticed at the failure stage (see **Figure 3.14**). In contrary RC beams showed failure due to propagation of large single crack and did not exhibit any residual strength (see **Figure 3.11**). First peak load, Peak load, Residual Strength at 0.3 in. and 0.12 in. deflections were calculated based on parameter calculations (**Figure 3.10**) were as Modulus of Rupture (MOR) was calculated based on **Equation 3-1** and results are summarized in **Tables 3.7** to **3.10**. Average load deformation curve was plotted for all specimens and are shown in **Figures 3.15** to **3.18.**

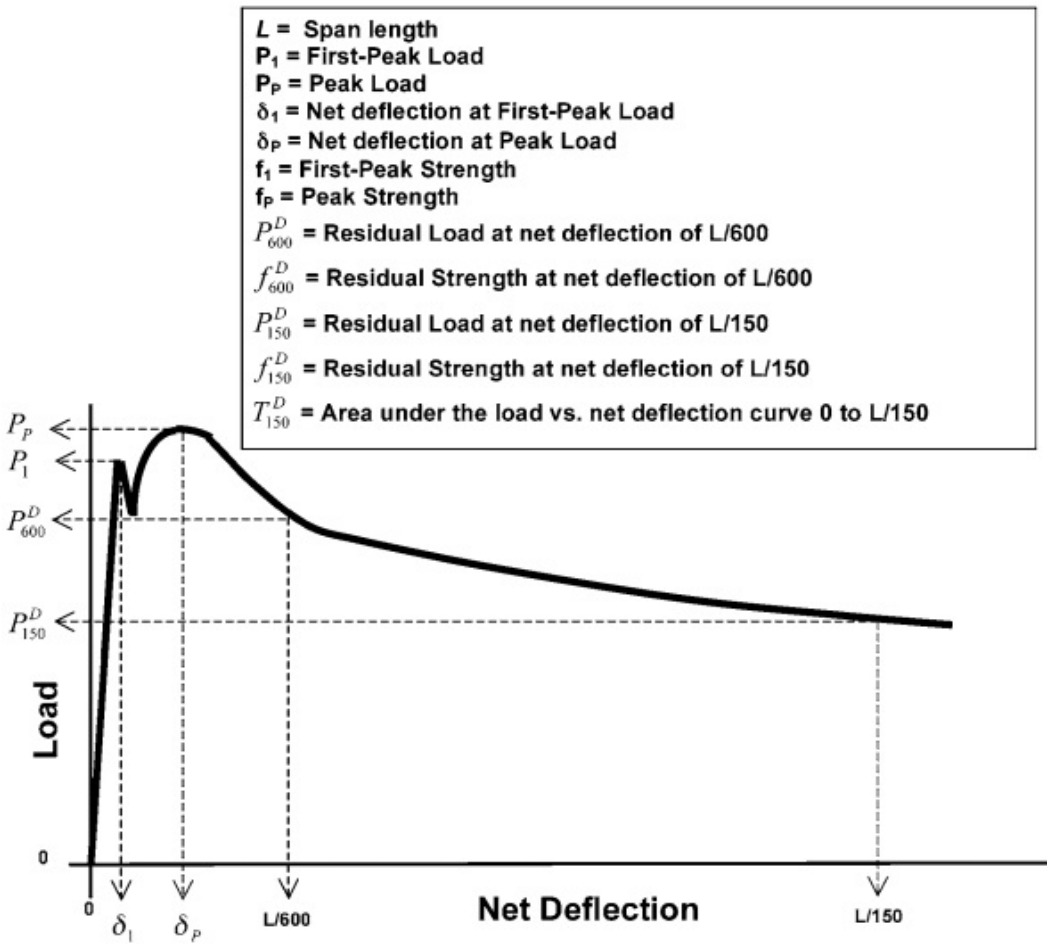

Figure 3.10 Example of parameter calculations when Peak load is greater than First-Peak load (ASTM C1609, 2010)

The modulus of rupture was calculated as follows:

$$MOR = \frac{PL}{bd^2} \qquad \textbf{(Equation 3-1)}$$

Where, MOR = modulus of rupture, psi

P = ultimate applied load, lb

L = specimen span, in

b =average width of specimen, in.

d = average depth of specimen, in.

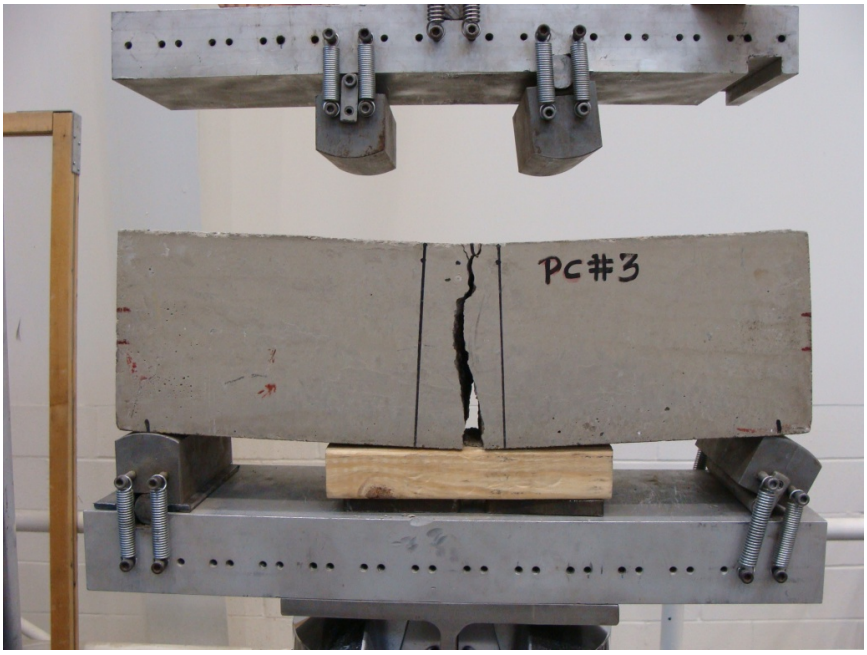

Figure 3.11 Failure mode of PC at peak load

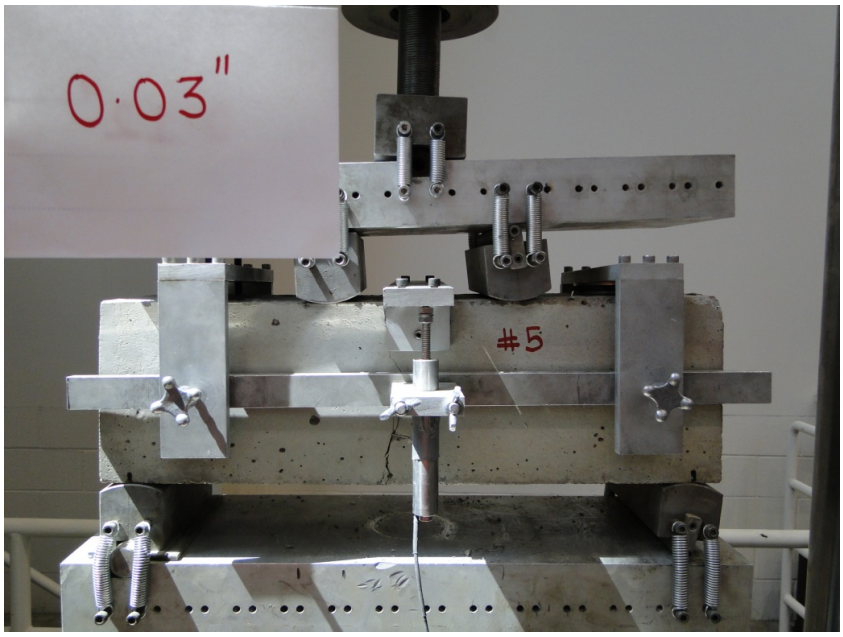

Figure 3.12 Failure mode of SFRC at 0.3” deflection

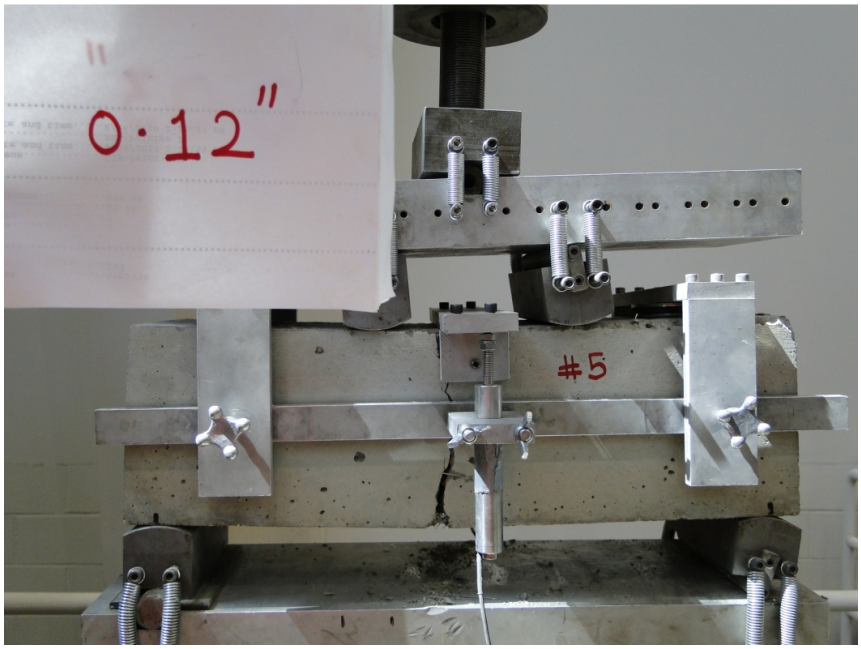

Figure 3.13 Failure mode of SFRC at 0.12” deflection

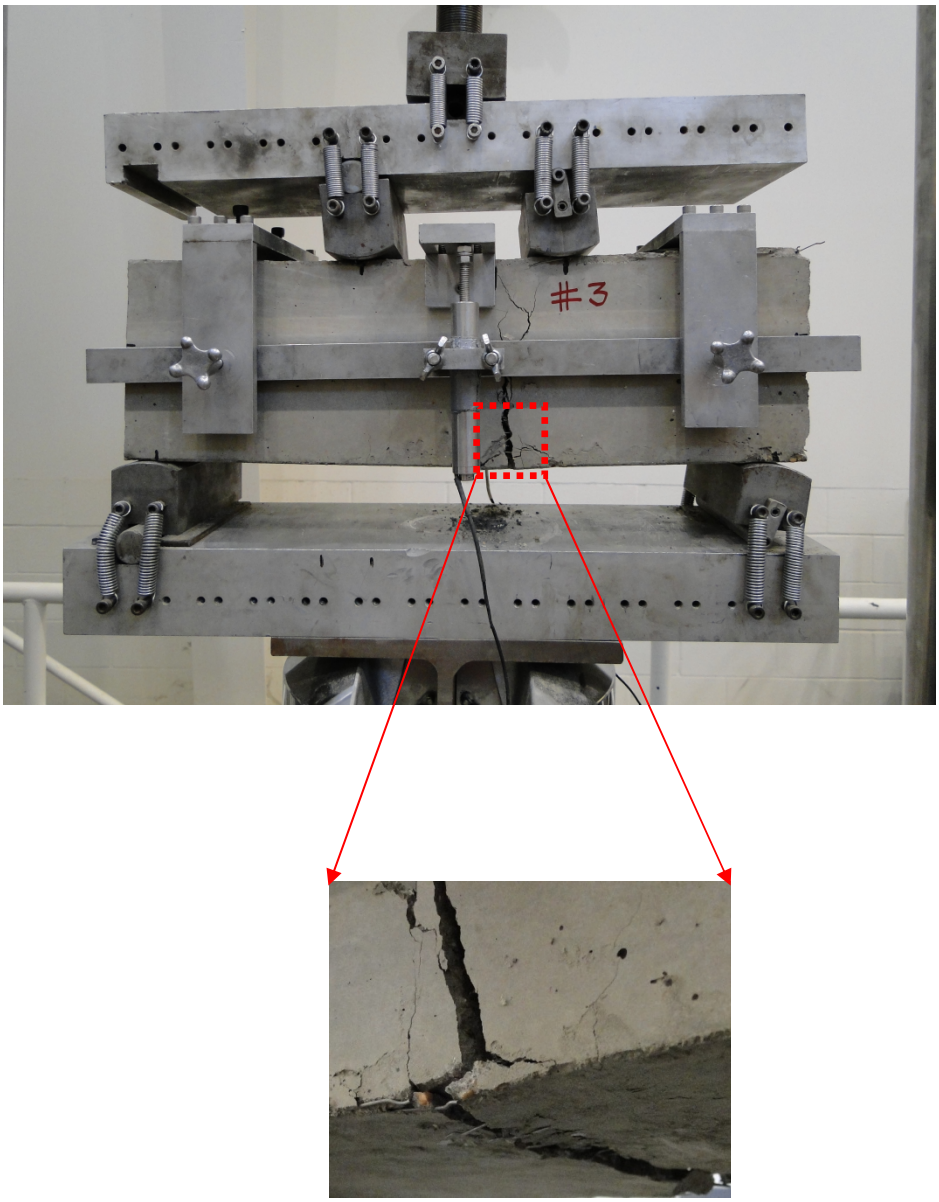

Figure 3.14 Cracks at the end of ASTM C1609 test in SFRC beam

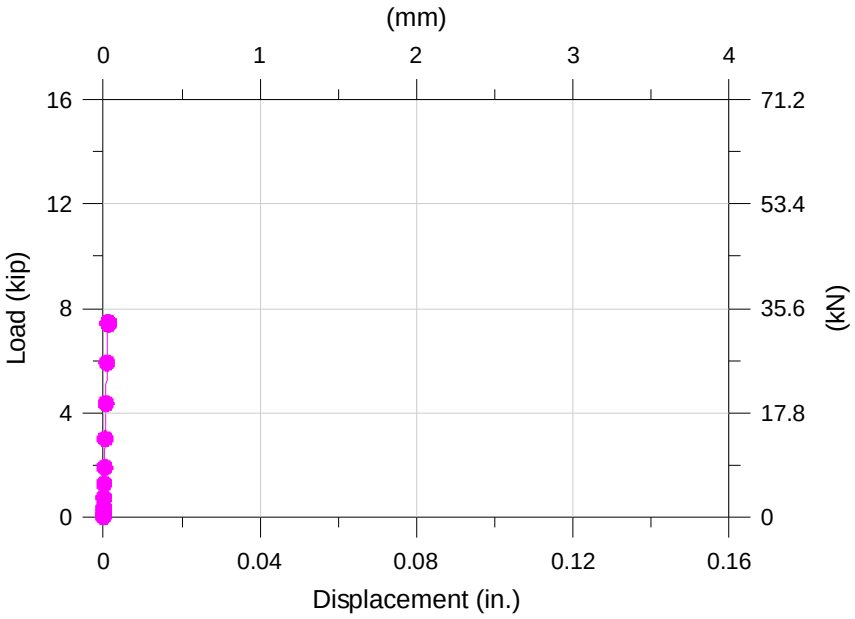

Figure 3.15 Average plot from Third-Point bending test – RC specimen

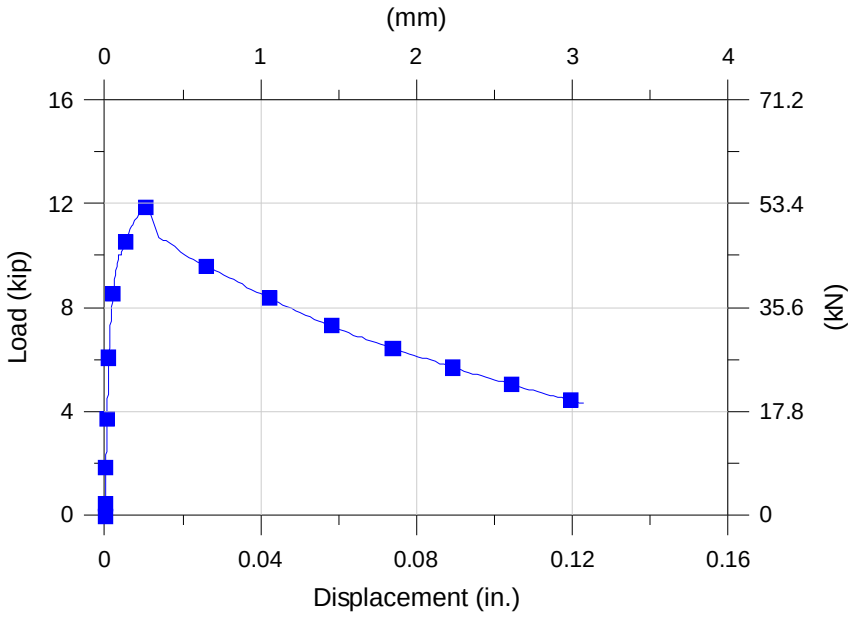

Figure 3.16 Average plot from Third-Point bending test - SFRC#1 specimen

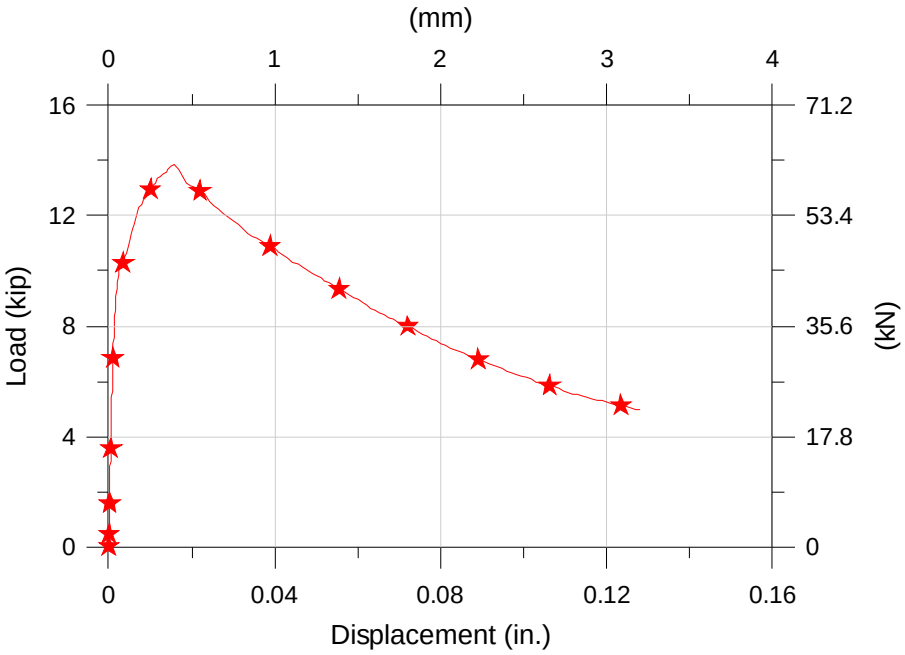

Figure 3.17 Average plot from Third-Point bending test - SFRC#2 specimen

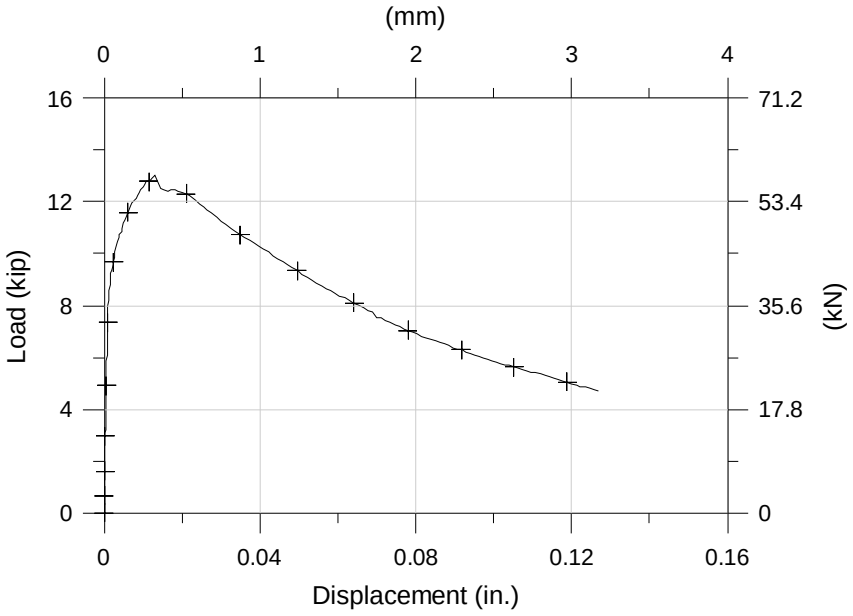

Figure 3.18 Average plot from Third-Point bending test - SFRC#3 specimen

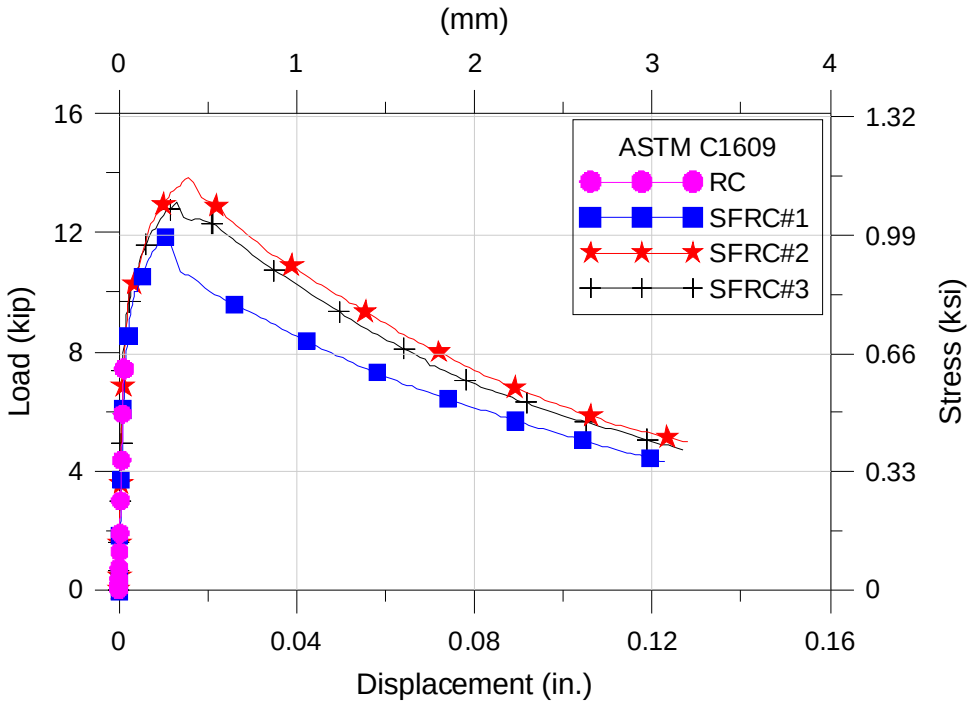

Figure 3.19 Average plots for flexural bending strength from Third-Point bending test for all specimens

Table 3.7 Third-Point bending test results - RC Specimen.

Test Specimen Summary for RC			
Specimen Number	**RC#1**	**RC#2**	**RC#3**
Span Length, **L** (in)	18	18	18
Modulus of Rupture, **MOR** (psi)	635	563	661
First Peak Load, $\mathbf{P_1}$ (lb)	n/a	n/a	n/a
Peak Load, $\mathbf{P_p}$ (lb)	7618	6757	7935
Peak-Load Deflection, $\boldsymbol{\delta_p}$ (in)	0.00095	0.00122	0.00142
First-Peak Deflection, $\boldsymbol{\delta_1}$ (in)	n/a	n/a	n/a
Peak Strength, $\mathbf{f_p}$ (psi)	n/a	n/a	n/a
First- Peak Strength, $\mathbf{f_1}$ (psi)	n/a	n/a	n/a
Residual Load at L/600, $\mathbf{P_{150,0.75}}$ (lb)	n/a	n/a	n/a
Residual Strength at L/600, $\mathbf{f_{150,0.75}}$ (psi)	n/a	n/a	n/a
Residual Load at L/150, $\mathbf{P_{150,3.0}}$ (lb)	n/a	n/a	n/a
Residual Strength at L/150, $\mathbf{f_{150,3.0}}$ (psi)	n/a	n/a	n/a

Table 3.8 Third-Point bending test results - SFRC#1 Specimen.

Test Specimen Summary for SFRC#1						
Specimen Number	**SFRC 1**	**SFRC 2**	**SFRC 3**	**SFRC 4**	**SFRC 5**	**SFRC 6**
Span Length, **L** (in)	18	18	18	18	18	18
Modulus of Rupture, **MOR** (psi)	1436	819	996	866	989	717
First Peak Load, $\mathbf{P_1}$ (lb)	17229	9828	11958	10393	11873	8607
Peak Load, $\mathbf{P_p}$ (lb)	18209	10014	11958	10393	12288	8857
Peak-Load Deflection, δ_p (in)	0.0176	0.0072	0.00483	0.00461	0.01432	0.01621
First-Peak Deflection, δ_1 (in)	0.116	0.0059	0.00483	0.00461	0.00362	0.00867
Peak Strength, $\mathbf{f_p}$ (psi)	1517	834	996	866	1024	738
First- Peak Strength, $\mathbf{f_1}$ (psi)	1436	819	996	866	989	717
Residual Load at L/600, $\mathbf{P_{150,0.75}}$ (lb)	15773	6803	7099	8088	10731	8149
Residual Strength at L/600, $\mathbf{f_{150,0.75}}$ (psi)	1314	567	591	674	894	679
Residual Load at L/150, $\mathbf{P_{150,3.0}}$ (lb)	6016	3183	4200	4145	4471	4230
Residual Strength at L/150, $\mathbf{f_{150,3.0}}$ (psi)	501	265	350	345	372	352

Table 3.9 Third-Point bending test results - SFRC#2 Specimen.

Test Specimen Summary for SFRC#2						
Specimen Number	**SFRC 1**	**SFRC 2**	**SFRC 3**	**SFRC 4**	**SFRC 5**	**SFRC 6**
Span Length, **L** (in)	18	18	18	18	18	18
Modulus of Rupture, **MOR** (psi)	n/a	857	1395	1523	768	976
First Peak Load, $\mathbf{P_1}$ (lb)	n/a	10285	16734	18285	9220	11717
Peak Load, $\mathbf{P_p}$ (lb)	n/a	11430	16734	18285	11125	11717
Peak-Load Deflection, $\boldsymbol{\delta_p}$ (in)	n/a	0.0150	0.0127	0.0174	0.0231	0.0104
First-Peak Deflection, $\boldsymbol{\delta_1}$ (in)	n/a	0.0029	0.0127	0.0174	0.0013	0.0104
Peak Strength, $\mathbf{f_p}$ (psi)	n/a	953	1395	1523	927	976
First- Peak Strength, $\mathbf{f_1}$ (psi)	n/a	857	1395	1523	768	976
Residual Load at L/600, $\mathbf{P_{150,0.75}}$ (lb)	n/a	10261	13575	15083	9702	10130
Residual Strength at L/600, $\mathbf{f_{150,0.75}}$ (psi)	n/a	855	1131	1257	809	844
Residual Load at L/150, $\mathbf{P_{150,3.0}}$ (lb)	n/a	4190	4483	6336	6485	4730
Residual Strength at L/150, $\mathbf{f_{150,3.0}}$ (psi)	n/a	349	374	528	540	394

Table 3.10 Third-Point bending test results - SFRC#3 Specimen.

Test Specimen Summary for SFRC#3						
Specimen Number	**SFRC 1**	**SFRC 2**	**SFRC 3**	**SFRC 4**	**SFRC 5**	**SFRC 6***
Span Length, **L** (in)	18	18	18	18	18	18
Modulus of Rupture, **MOR** (psi)	812	870	998	1154	1169	n/a
First Peak Load, $\mathbf{P_1}$ (lb)	9739	10441	11976	13853	14030	n/a
Peak Load, $\mathbf{P_p}$ (lb)	12049	12199	11976	14842	14030	n/a
Peak-Load Deflection, $\boldsymbol{\delta_p}$ (in)	0.0151	0.0169	0.0089	0.0120	0.0119	n/a
First-Peak Deflection, $\boldsymbol{\delta_1}$ (in)	0.0027	0.0050	0.0089	0.0076	0.0119	n/a
Peak Strength, $\mathbf{f_p}$ (psi)	1004	1017	998	1237	1169	n/a
First- Peak Strength, $\mathbf{f_1}$ (psi)	812	870	998	1154	1169	n/a
Residual Load at L/600, $\mathbf{P_{150,0.75}}$ (lb)	10868	11451	10493	11253	12104	n/a
Residual Strength at L/600, $\mathbf{f_{150,0.75}}$ (psi)	906	954	874	938	1009	n/a
Residual Load at L/150, $\mathbf{P_{150,3.0}}$ (lb)	4138	5487	5622	3744	6131	n/a
Residual Strength at L/150, $\mathbf{f_{150,3.0}}$ (psi)	345	457	469	312	511	n/a

Note: * Data not collected due to operator error.

3.5 Double Punch Test

A prospective material test method for FRC, the double punch test (DPT), was originally developed as an indirect tensile test method which was introduced by Chen (1970, 1975). It stood on the bases of the theory of plasticity. Chen and Yuan (1980) applied the DPT to steel as well as polymer fiber reinforced concretes, and compared those with the split-cylinder test. They concluded that the DPT was a better test method since a DPT specimen failed at weakest sections while a split-cylinder test specimen would fail at predetermined failure plane.

DPT specimen consisted of a cylinder with dimensions of 6 × 6 in. (152.4 × 152.4 mm), which was created by cutting half of 6 × 12 in. (152.4 × 304.8 mm) cylinder. Compressive load was applied through two steel punches, which had 1 in. (25.4 mm) height and 1.5 in. (38.1 mm) diameter, placed at the middle of top and bottom surfaces of the cylinder along its central axis (see **Figure 3.20**). For the double punch test a 60 kip (267 kN) Baldwin hydraulic testing machine was used. As discussed above a pair of LVDTs was used to measure the vertical deformation of the specimen (see **Figure 3.21**). The loading rate was 445 N (100 lb)/min prior to the first crack, and was kept three times faster during the post-cracking stage.

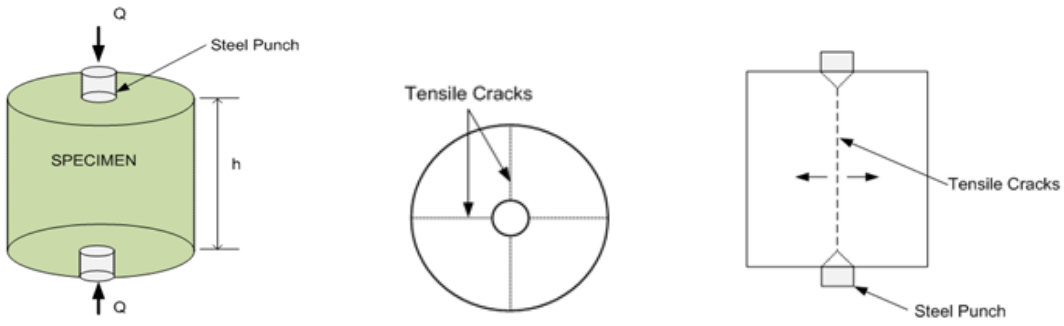

Figure 3.20 Schematic view of DPT specimen (Chao, 2011)

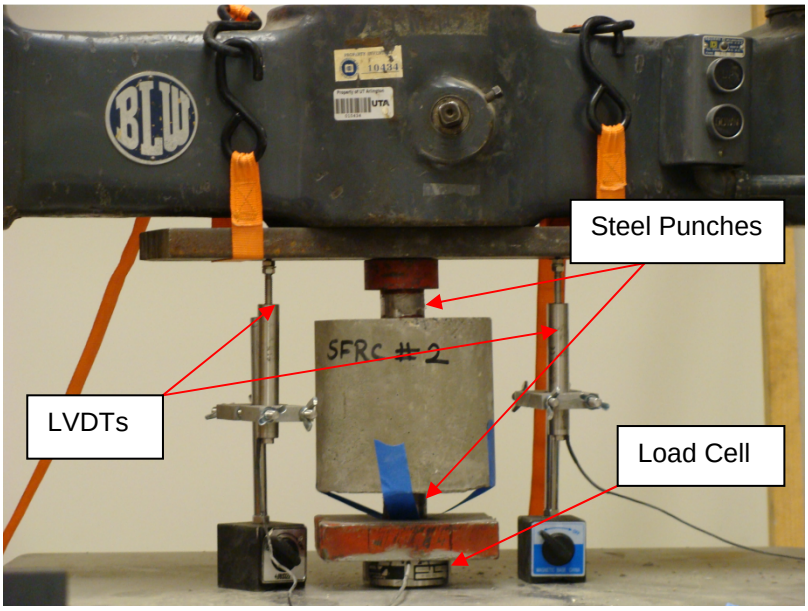

Figure 3.21 Testing setup for DPT testing

By applying compressive load on the specimen through the punches, uniform tensile stresses were generated over diametric planes, and tensile crack occurred along these diametric planes.

The equivalent tensile stress is calculated by (Chen, 1975):

$$f_t = \frac{Q}{\pi\left(1.20bh - a^2\right)} \qquad \textbf{(Equation 3-2)}$$

Where f_t is equivalent tensile stress, Q is the applied load, b is the radius of the cylinder, h is the height of the cylinder, and a is the radius of the punches. From testing it was observed that RC specimens exhibited very brittle failure and did not show any residual strength

after peak loading was reached, this was in contradiction to the SFRC specimens in which more controlled failure mode was observed. Load-deformation as well as equivalent tensile stresses is presented in **Figures 3.22** to **3.25** for all four specimens. The equivalent tensile stresses were estimated according to **Equation 3-2**. At deflection of 0.098 in. (2.5 mm) the equivalent tensile stress of SFRC#1, SFRC#2 and SFRC#3 was 1.44 MPa, 4.1 MPa and 3.4 MPa respectively. Low tensile strength of SFRC#1 is attributed to inconsistent mixture of concrete, as it was observed to be much more flowable during casting than other mixtures. However SFRC#2 had 1.5% volume fraction of fibers and exhibited greater tensile strength than SFRC#3 which had only 1% fibers justifying the effect of reduced fiber volume fraction.

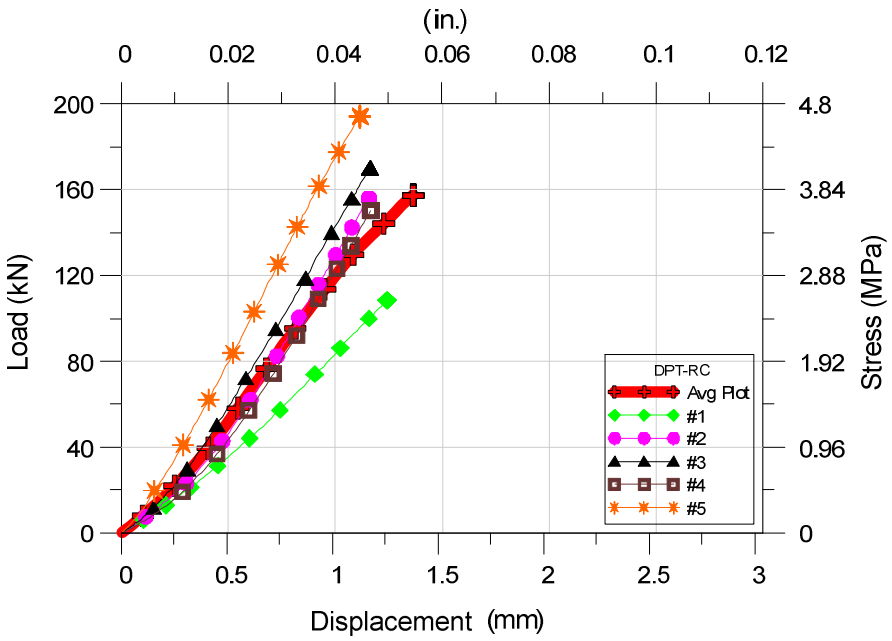

Figure 3.22 Load versus deformation curves for DPT (RC specimen)

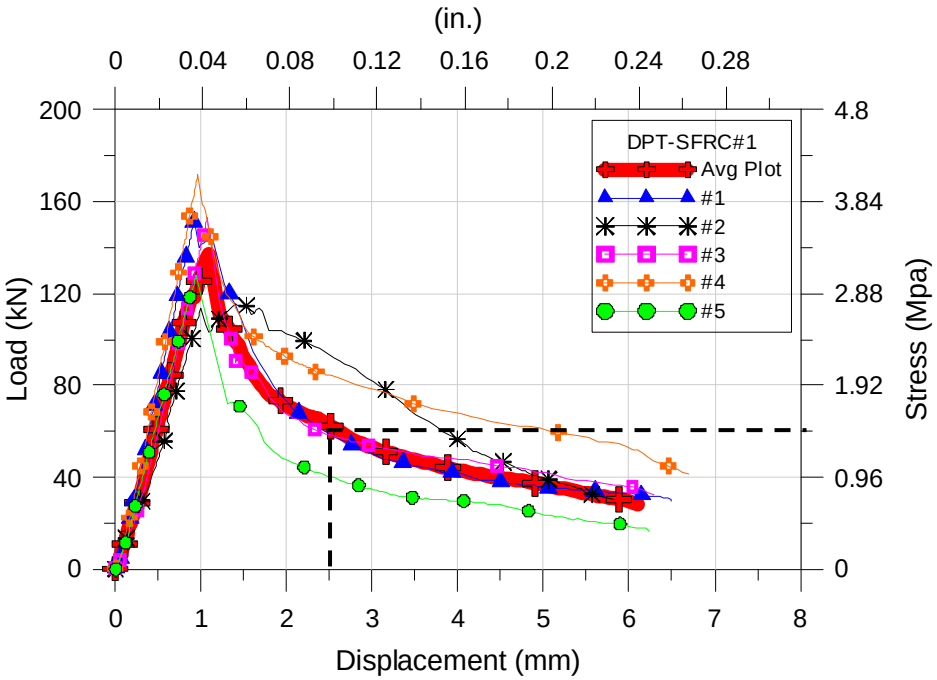

Figure 3.23 Load versus deformation curves for DPT (SFRC#1 specimen)

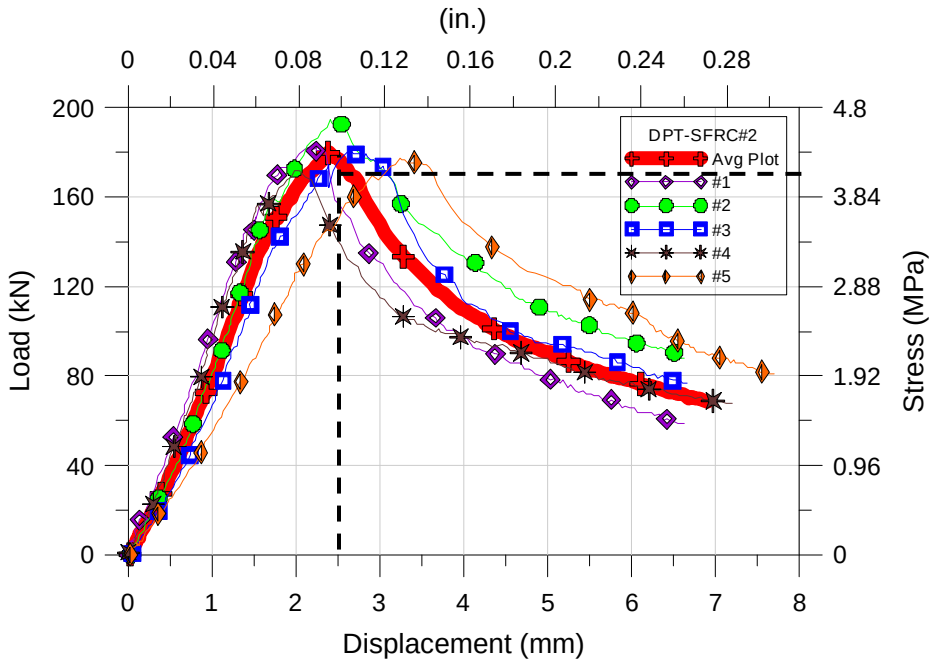

Figure 3.24 Load versus deformation curves for DPT (SFRC#2 specimen)

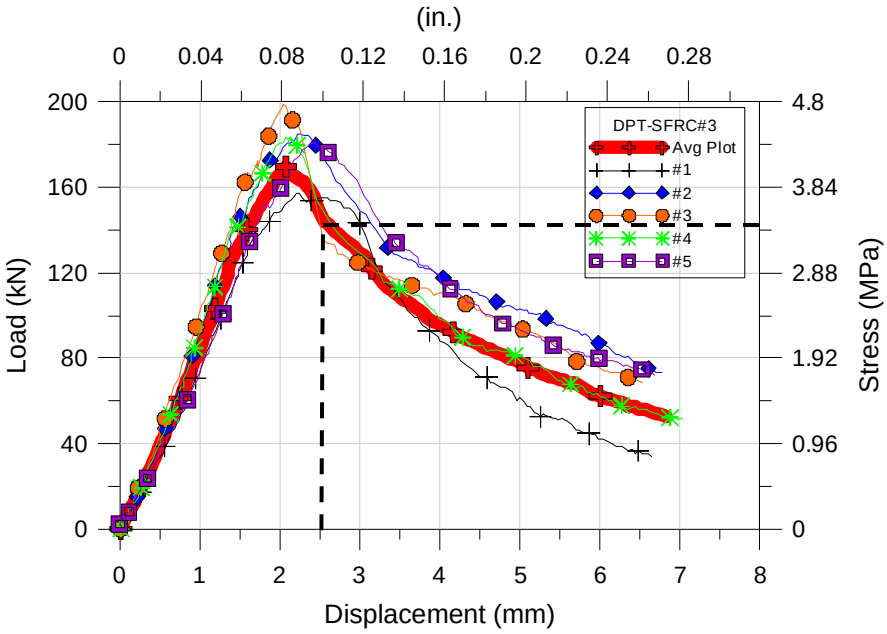

Figure 3.25 Load versus deformation curves for DPT (SFRC#3 specimen)

3.6 Direct Tensile Test

The primary focus of this testing program was to determine the behavior of SFRC when subjected to direct tension. It was necessary to determine the behavior of the concretes used in the study when they were subjected to tensile loads so as to better understand the results from large scale testing and also for modeling purposes. As discussed earlier specimens used in this study were specifically designed so that a pin-pin loading condition is created at the ends. Due to adopted end conditions pure axial load is applied as any additional end moment is minimized also ends of the specimen are not required to be fixed to the test-setup by adhesive (Chao, 2011). Both ends of the specimen were strengthened by the double “dog-bone” geometry and steel meshes to ensure that cracking would only occur at the central portion within the gauge length. The double dog-bone shape was used to mitigate the stress concentration resulted from the reduction of cross-section. The central portion has a square cross-section with a dimension

of 4 x 4 in. (102 x 102 mm). Detailed dimension of specimen is shown in **Figure 3.26**. These dimension were selected to reduce the size effect (Naaman and Reinhardt, 2006) while maintaining a suitable weight for laboratory handling.

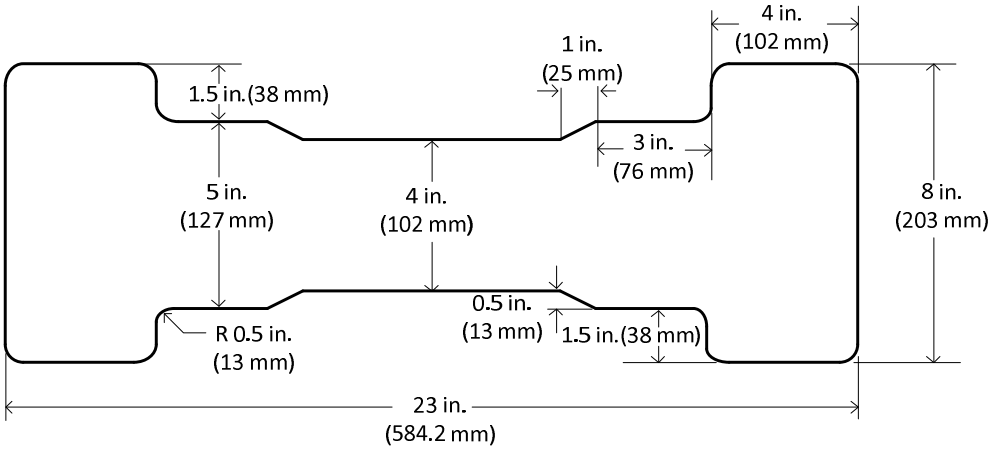

Figure 3.26 Dimension of dog-bone specimen

Six dog-bone specimens were cast for each SFRC mixture type. These specimens were cast in four lifts. Between the first, second, third and fourth lift, a steel mesh was inserted into the flared ends of each specimen at approximately mid-depth of each layer (see **Figure 3.27**) to help prevent cracks from occurring outside of the gauge length of the specimen (see **Figure 3.29**). These specimens were demoulded and stored next to their corresponding large scale specimens to ensure same environment for curing.

The applied load was monitored by the load cell of the testing machine and elongation was recorded by a pair of LVDTs attached to the specimen (see **Figure 3.29**), with a gauge length of about 7 in. (178 mm). It is noted that this type of direct tensile test has been extensively used previously to obtain tensile stress-strain responses in FRCCs with great success (Sujivorakul and Naaman, 2003; Chandrangsu and Naaman, 2003). The loading rate

was the same as that used in ASTM C1609 testing. It is important to note that data from only those specimens data can be used in which cracking takes within the gauge length (see **Figures 3.30**; **3.31**), hence for those in which cracking initiated outside the gauge length data was discarded.

Figure 3.27 Placement of wire mesh in end section of dog-bone specimen

Figure 3.28 Final touch given to dog-bone specimen after installing four layers of mesh

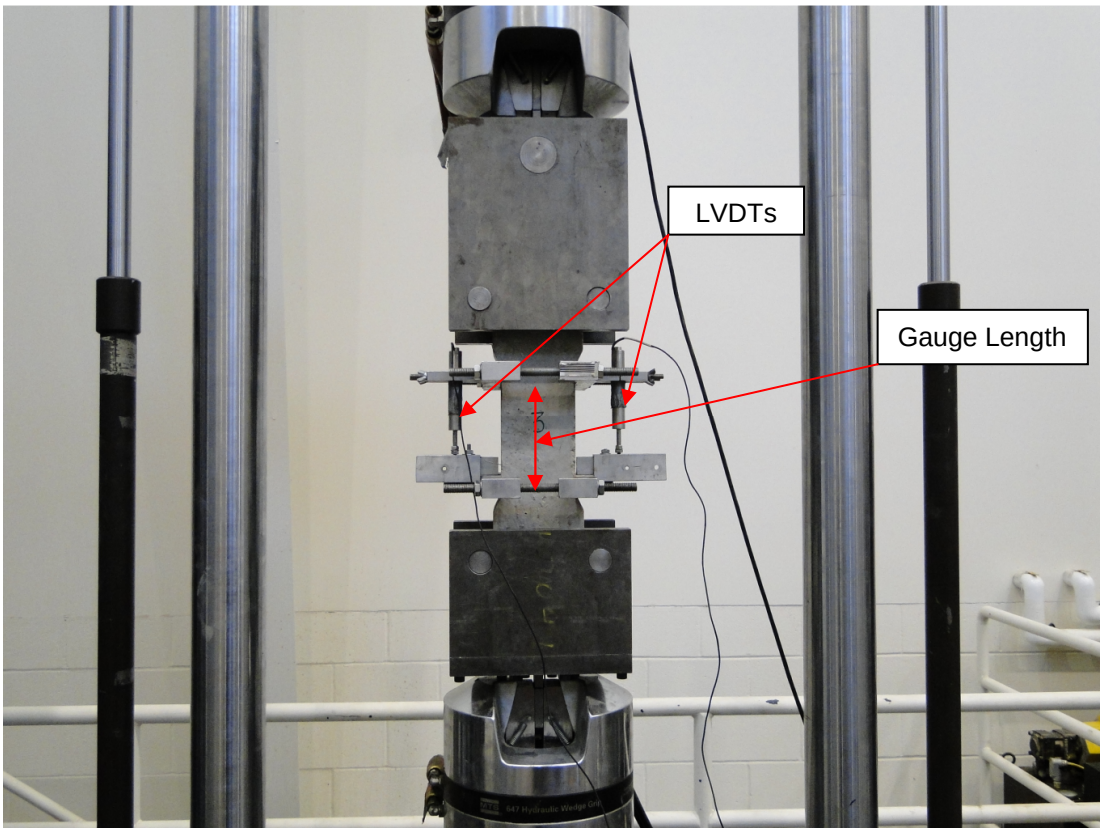

Figure 3.29 Test setup for dog-bone specimen (front view)

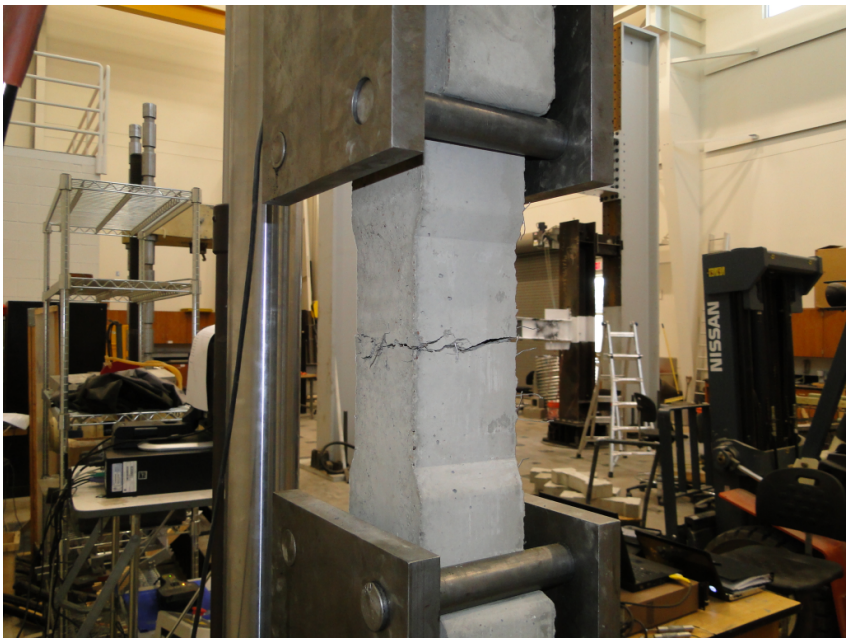

Figure 3.30 Test setup for dog-bone specimen (side view)

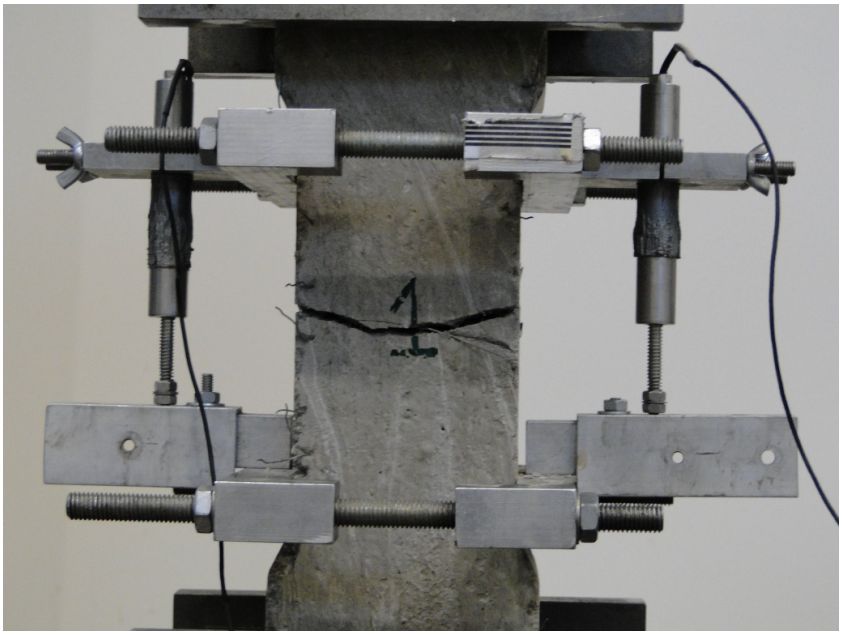

Figure 3.31 Observed failure along the gauge length of the dog-bone specimen

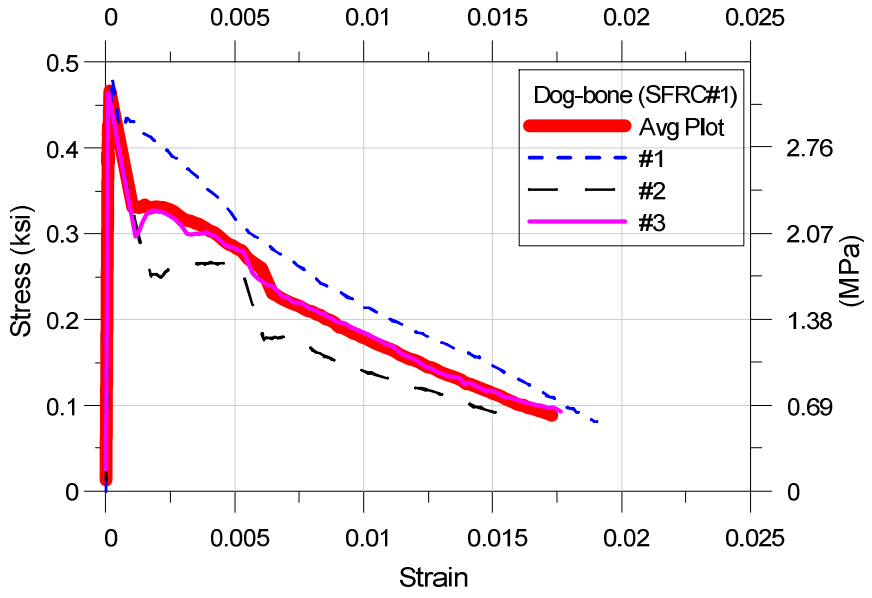

Figure 3.32 Average stress-strain curves for SFRC#1 specimen

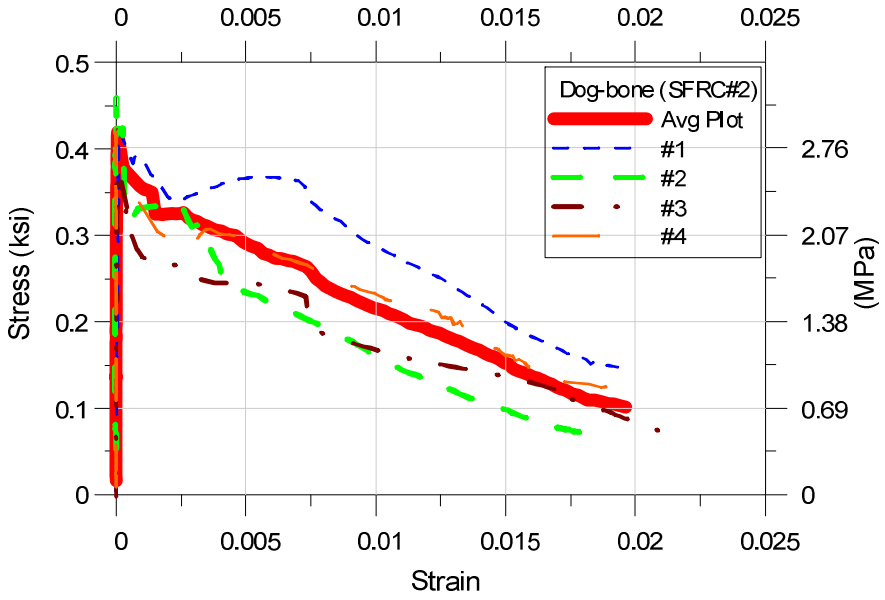

Figure 3.33 Average stress-strain curves for SFRC#2 specimen

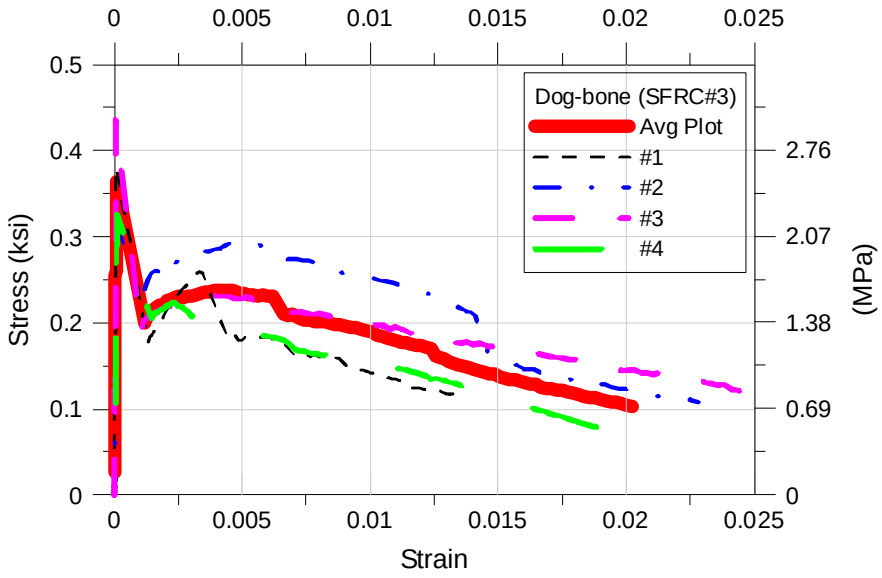

Figure 3.34 Average stress-strain curves for SFRC#3 specimen

All the dog-bone specimens for SFRC#1 and SFRC#2 specimen which contained 1.5% of fibers by volume and for SFRC#3 specimen containing 1% fibers exhibited very small strain hardening was observed. A residual stress of 0.60, 0.70 and 0.73 MPa was maintained at a deflection of 0.12 in. (3 mm) respectively (see **Figures 3.32**; **3.34**).

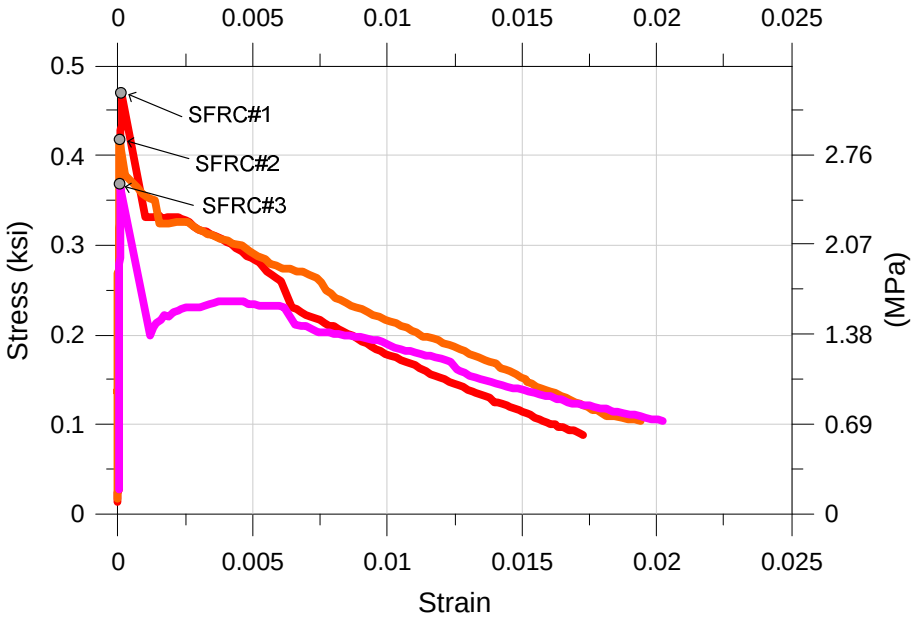

Figure 3.35 Average stress-strain curves for all specimens

CHAPTER 4

EXPERIMENTAL PROGRAM

4.1 Introduction

Schlaich et al. (1987) originally considered an example of deep beam with single large opening to evaluate the design procedure by using strut-and-tie model. This example was also used previously in other laboratory tests (Maxwell and Breen, 2000). Test specimens representing approximately 1/4-scale models of this beam have been studied by Breña and Morrison (2007) to investigate the over-strength factors in the design using strut-and-tie models. Position and size of the opening were selected to interfere with direct load paths that could potentially form between loading point and supports (Breña and Morrison, 2007).

4.2 Specimen Geometry and Reinforcement Detail

The four deep beam specimens investigated in this study had the same dimensions (see **Figure 4.1**) as the ones used by Breña and Morrison (2007). The span is 74 in. (1875 mm) long, height is 46 in. (1170 mm), the thickness is 4.4 in. (112 mm). It has two square openings: one in the left bottom corner and one in the right top corner. Both the openings are of size 15 x15 in (381 x 381 mm). Supports were positioned directly at specimen ends based on two considerations: 1) for consistency with the support location indicated by Schlaich et al. (1987) in their design example; and 2) so that support pins would line up with the centerline of the concrete region between the opening and edge of the specimens (Breña and Morrison, 2007). As discussed the geometry was kept exactly same as used by Breña and Morrison (2007).

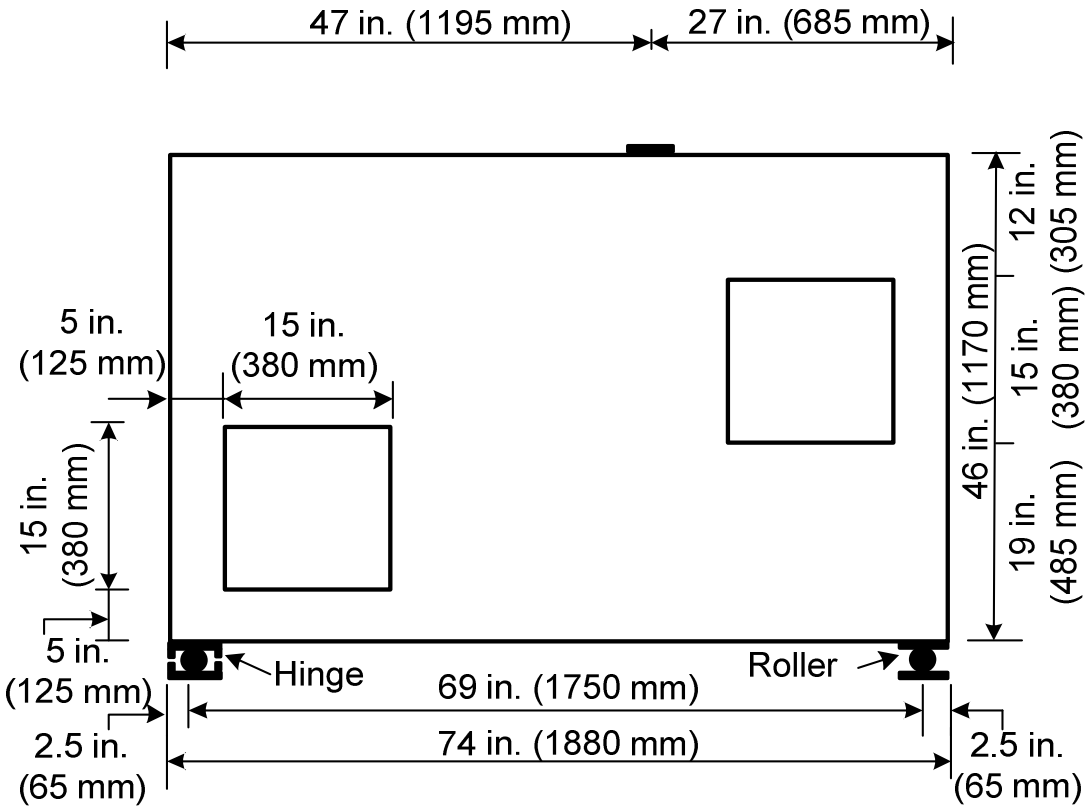

Figure 4.1 Specimen geometry with openings

There were a few modifications made: one being introduction of steel cages at the supports, which was included in order to prevent local damage as seen from previous testing (Breña and Morrison, 2007; Flores, 2009). These steel cages were formed by four longitudinal steel reinforcement bars at corners and transverse stirrups at a center-to-center spacing of 4 in. (100 mm). Another significant modification in this study was that secondary reinforcement (welded wire meshes) used for temperature and shrinkage cracking by Breña and Morrison (2007) in one of their specimens (beam with single opening) was not used in any of the specimens. This secondary reinforcement was not used as it was expected to increase the specimen load carrying capacity as observed by Breña and Morrison (2007).

4.3 Conventional Reinforced Concrete Specimen (Specimen#1)

The RC specimen had same reinforcement layout as used by Breña and Morrison (2007), with exception of steel cages as discussed above. Standard No. 3 rebar (Grade 60) having nominal area of 0.11 in^2 (2.8 mm^2) were used. These rebars were placed within the wood form leaving approximately 1 in. cover (from center of the bars to the form) on each side of the beam. Anchorage for all the bars was accomplished by using standard 180-degree hooks at their ends to avoid pullout (see **Figure 4.3**). This was based on the suggestion by Breña and Morrison (2007). The strut-and-tie model (**Figure 4.2**) adopted by them was also used for this study, as discussed earlier this model was developed by them to approximately follow the elastic principal stress distribution shown in **Figure 2.7(b)**. Bottom longitudinal reinforcing bars for the specimens extended into the right support and were anchored at the support by using standard 90-degree hooks. The bottom longitudinal reinforcement did not extend into the left support in strict compliance with the strut-and-tie models used for design. This allowed the examination of potentially detrimental effects of inadequate reinforcing details on load-carrying capacity of the specimen (Breña and Morrison, 2007).

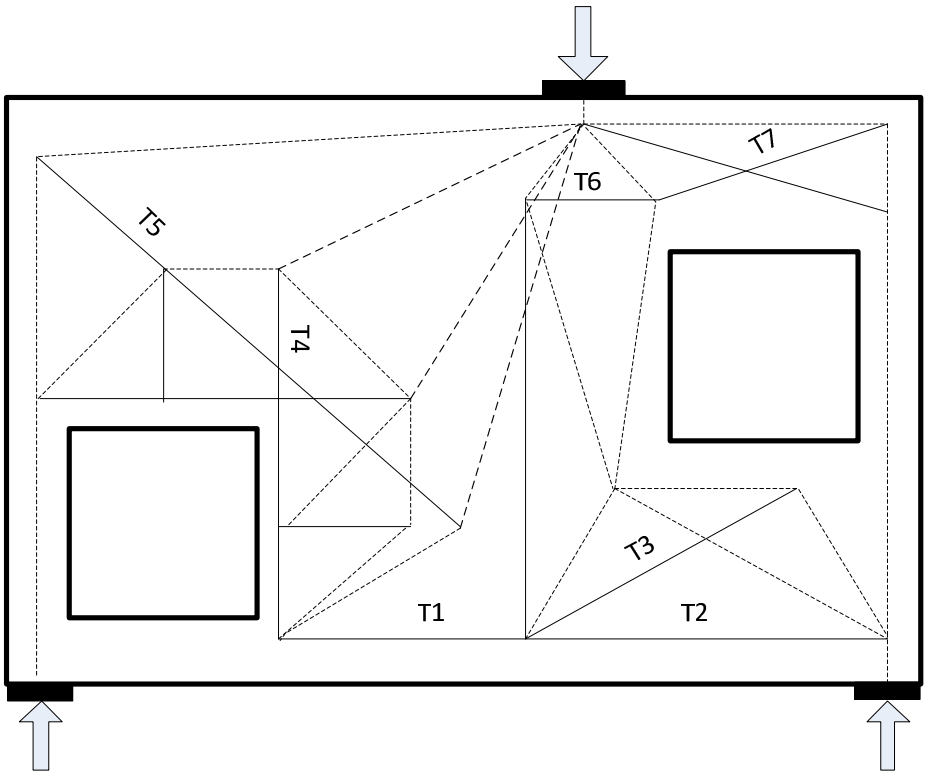

Figure 4.1 Design strut-and-tie model adopted in this study (solid lines represent ties and dashed lines represent struts, numbers indicate tie ID for those having strain gauges)

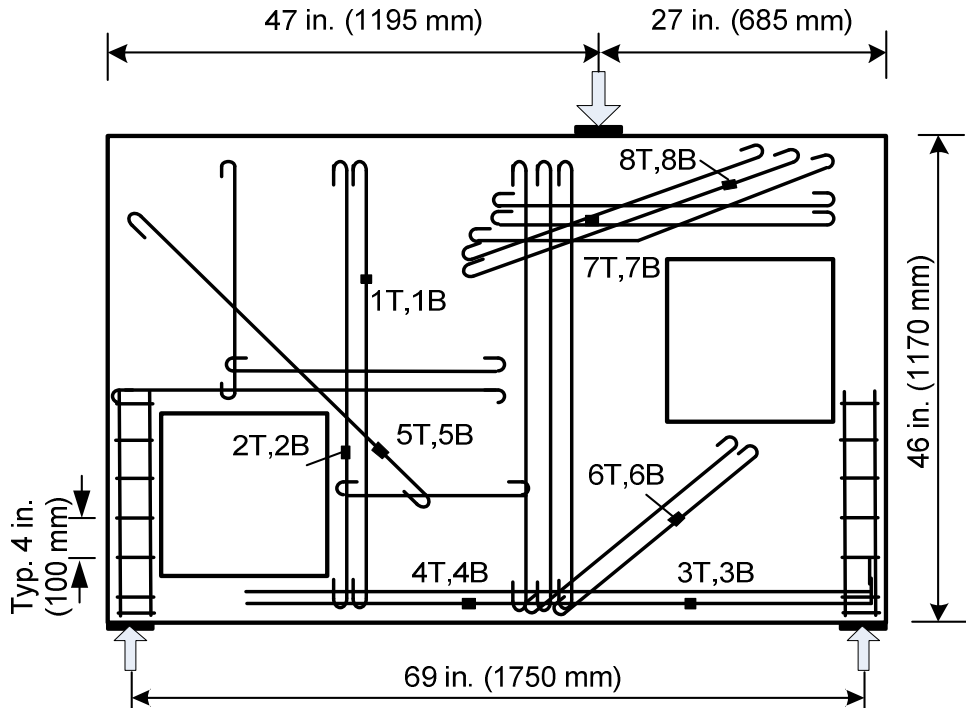

Figure 4.3 RC specimen reinforcement layout (Numbers on the bar indicate strain gauge number)

There were two layers of reinforcement, one top and other bottom side of the specimens (notations “top” and “bottom” used to identify the two layers of steel reinforcement). Both layers had approximately one-inch cover (from centre of bar to the formwork) along thickness of the beam. Steel cages at left and right supports were used to avoid any localized damage as was observed by Breña and Morrison (see **Figure 2.11**). Steel strain gauges were carefully installed on the surface of rebars to record the strains at certain location during testing. The locations of strain gauges are shown in **Figure 4.3** with small black box. At each location there were two strain gauges: one on each layer of the bars, therefore naming them “T” for top and “B” for bottom. In total there were 16 strain gauges installed. Two hooked rebar were placed one on either side of beam for lifting purpose (see **Figure 4.4**).

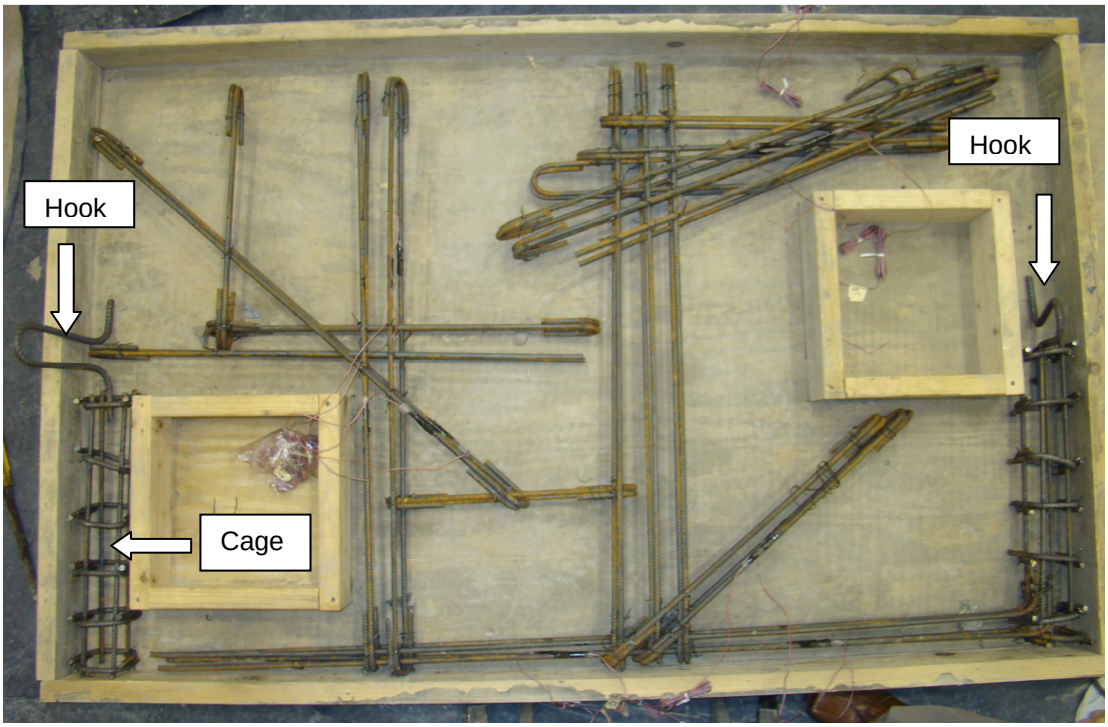

Figure 4.4 RC specimen before casting

The concrete mixture with a nominal 28-day expected compressive strength *f'*c equal to 5,000 psi (34.47 MPa) was used. The measured compressive strength was 6717 psi (46.3 MPa) at the day of testing, 38-days after casting. The maximum aggregate (crushed limestone) size used was 3/8 in. Concrete mixing was done using two nine cubic foot concrete mixers (see **Figure 4.5**). Two batches were mixed per mixer for each beam. Consolidation was accomplished using a concrete vibrator with a 9 in. (229 mm) head as concrete was poured in the form (see **Figures 4.6 and 4.7**). RC specimen and material specimens (ASTM beam, tensile specimens and concrete cylinders) after casting were covered with a sheet of polyethylene for 24 hours for curing. All material specimens were demolded after 24 hours.

(a)

(b)

Figure 4.5 Mixers used during casting (a) Mixer #1; (b) Mixer #2

Figure 4.6 Concrete pouring for RC specimen

Figure 4.7 Consolidation of concrete by vibrator

4.3.1 Instrumentation

Important aspect of any testing is to record and analyze the data letter. Several sensors were used to measure the response of all four test specimens at different load levels. A 600 kips (2670 kN) load cell was used at loading point to measure the magnitude of applied load (see **Figure 4.8**). Uniaxial strain-gauges (gauge length = 0.2 in. (5 mm)) were bonded to surface of steel reinforcements at specified locations to measure the tie forces at various load levels. **Figure 4.3** shows the locations and numbering of various strain gauges used in RC test specimens. Instrumentation and test setup for the specimen is shown in **Figures 4.9** and **4.10**. Four linear varying differential transformers (LVDTs) were mounted on the surface of test specimens to measure the deformation of concrete during testing. A linear potentiometer was used exactly below the load point to measure the deflection of test specimens. Two additional linear potentiometers were also used to measure the displacement or settlement of both supports, if any. Also Acoustic Emission (AE) sensors were used to identify internal crack formations that were not visible to the naked eye upon loading. All the instruments except AE were connected to data acquisition system which was connected to a computer for data storage. AE was connected to a separate laptop.

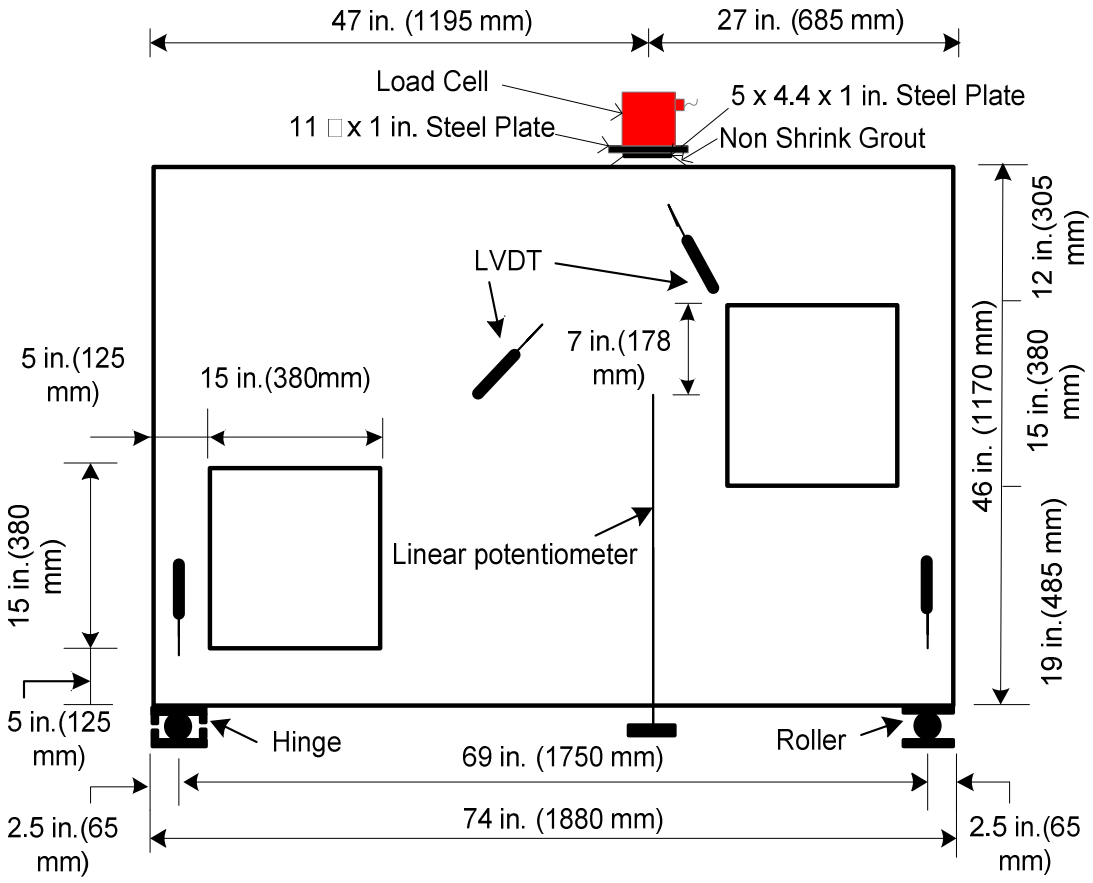

Figure 4.8 Test setup for specimen testing

(a)

(b)

(c)

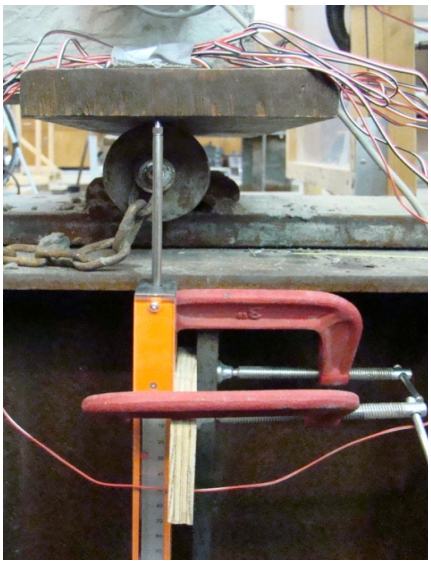

(d)

Figure 4.9 Instrumentation for test setup (a) Load cell (b) LVDT (c) Strain gauge (d) Support LVDT

(a)

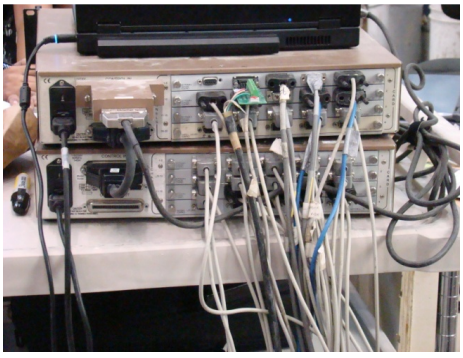

(b)

(c)

Figure 4.10 Test setup (a) Large scale specimen (b) Data acquisition box (c) AE acquisition box

4.3.2 Strain Gauge

Steel strain gauge having gauge length of 0.2 in. (5 mm) were carefully affixed to rebars. At first bars were grinded with a steel grinder (see **Figure 4.11(a)**) and later on they were smoothen using a sand belt (see **Figure 4.11(b)**). Careful observations were made so as not to grind too much such that steel area is significantly reduced. One important thing kept in mind during this procedure was to make sure that the surface remains straight and does not have any groove. After finishing grinding the surface small amount of degreaser was sprayed and the surface was made rough by using sand paper (see **Figure 4.11(c)**). This was done to make sure that when strain gauge was glued to the surface it is secured at its position; if the surface remains smooth there are chances it might slip. Once the surface was degreased then it was cleaned by using acid agent first (see **Figure 4.11(d)**) and then neutralized by using another neutralizing agent (see **Figure 4.11(f)**). Now a catalyzing agent was applied on the surface of the rebar, this is done to speed the gluing process. Finally glue was applied on the surface of strain gauge and its position was secured on rebar by using paper tape. Once it's affixed to the rebar coat A and B are applied on the strain gauge after 10 and 30 minutes respectively. Once the surface is dry it was covered by thick black rubber tape. Finally a liquid tape was applied so as to seal any air gaps left (see **Figure 4.11(h)**).

(a)

(b)

Figure 4.11 Material used for installation of strain gauge (a) Surface preparation materials (b) Installation materials

(a)

(b)

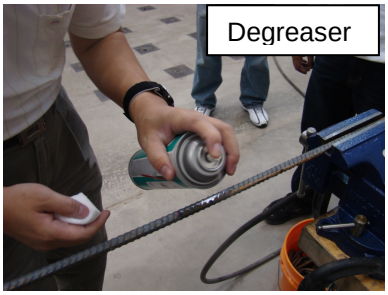

(c)

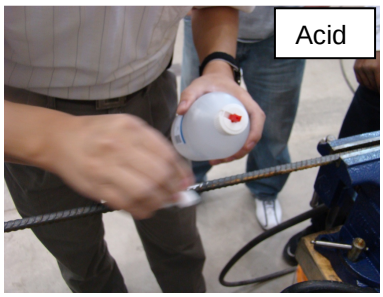

(d)

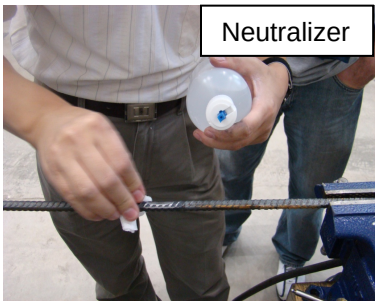

(e)

(f)

(g)

Figure 4.12 Strain gauge installation process (a) steel grinding (b) fine grinding (c) degreasing (d) acidifying (e) neutralizing (f) glued strain gauge (g) finished strain gauge

4.3.3 Linear Variable Differential Transformers (LVDTs)

LVDTs were installed on the specimen at various locations to measure the concrete deformation as monotonic load was applied. For the same reason two LVDTs were positioned in the concrete strut regions (see **Figure 4.21**). All LVDTs were connected to a data acquisition system which was in turn connected to computer for data storage. In total four LVDTs were installed on the surface of the specimen see **Figure 4.21** for LVDTs location and two support LVDTs were used to measure support settlement (see **Figure 4.9(d)**).

4.3.4 Acoustic Emission

Acoustic Emission (AE) is a non-destructive evaluation method which is widely used to measure internal crack propagation. Acoustic emission uses sensors that detect acoustic waves created during cracking. It serves as a very valuable tool, as it allows analysis of the energy dissipation in the form of crack formation, crack propagation and reinforcing slippage and yielding (Colombo, et. al, 2003). AE sensors were bonded with hot glue to the surface of all the four specimens before testing (see **Figure 4.9(c)**). A total of 7 sensors were used, each having a radius of influence of approximately 30 in. (762 mm), as determined by the so-called lead pencil break test (see **Figure 4.13**). This test consists of breaking a 0.012 in. (0.3 mm) lead in steps to determine the effective radius of influence. Beyond this radius of influence, the system does not detect signals. These sensors were connected to a central scanner box with in-line pre-amplifiers (See **Figure 4.10(c)**). The pre-amplifiers were set at 40 dB boost, which was determined before testing that this setting was most effective on eliminating unwanted noise associated with loading the concrete specimen.

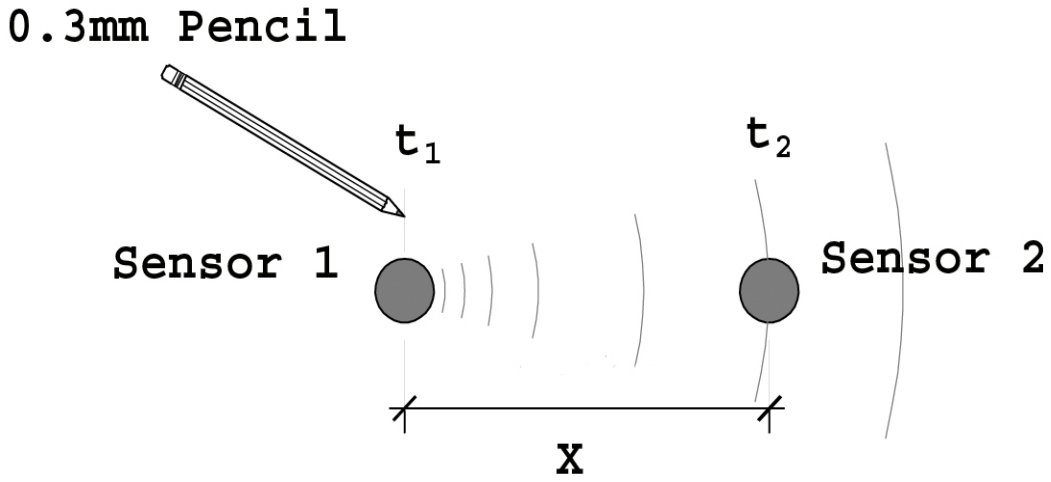

Figure 4.13 Method to determine shear wave velocity

For calculating shear wave velocity,

$$v = \frac{x}{\Delta t}$$

Where, v = shear wave velocity (ft/sec)

x = Distance in inches.

$$\Delta t = t_2 - t_1 \ (\mathrm{s})$$

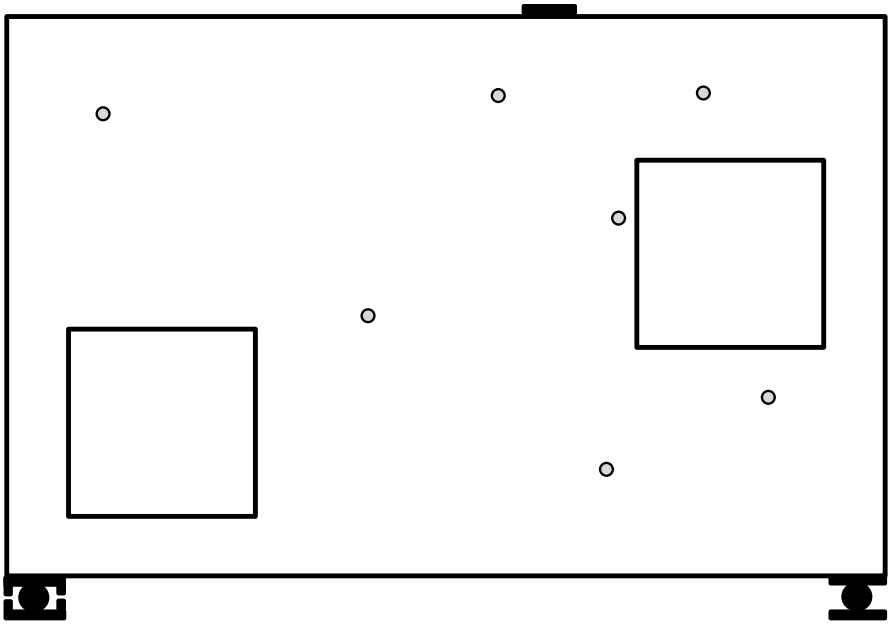

Figure 4.14 Location of AE sensors for RC specimen

AE sensors were installed on front face and LVDTs on the back face, this was done just for the convenience of connection to data acquisition system. Before affixing AE sensors the concrete surface was cleaned and made smooth by rubbing with metal brush.

The beam was demoded after 24 hours of casting and was placed horizontal for curing in natural environment inside lab. The STM was drawn on the front face and reinforcement layout on the back face of the specimen (see **Figure 4.10(a)**). The loading point consisted of an 11 in. (279 mm) diameter by 1 in. (25 mm) thick round steel plate on which load cell load cell was rested. The assembly of round plate and load cell bears onto a rectangular bearing plate of

dimension 5 in. (127 mm) by 1 in. (25 mm) thick which was grouted to the beam to ensure that there is no eccentricity, alignment and the surface is perfectly leveled (see **Figure 4.9(a)**).

Linear potentiometers were placed directly under the loading point, 20 in. (508 mm) from top of the beam to measure displacement under load. For this a quarter of an inches hole was drilled at location specified above and 8 in. (203 mm) threaded rod was glued inside this hole. Fish wire was tied to the rod at one end and to the linear potentiometer at other end. Large scale testing of the specimen was done using a 600 kips (2670 kN) universal testing machine (UTM) with monotonic load increments (see **Figure 4.15**). The test specimen was placed on top of a steel spreader beam that transferred the load to the base of the testing machine.

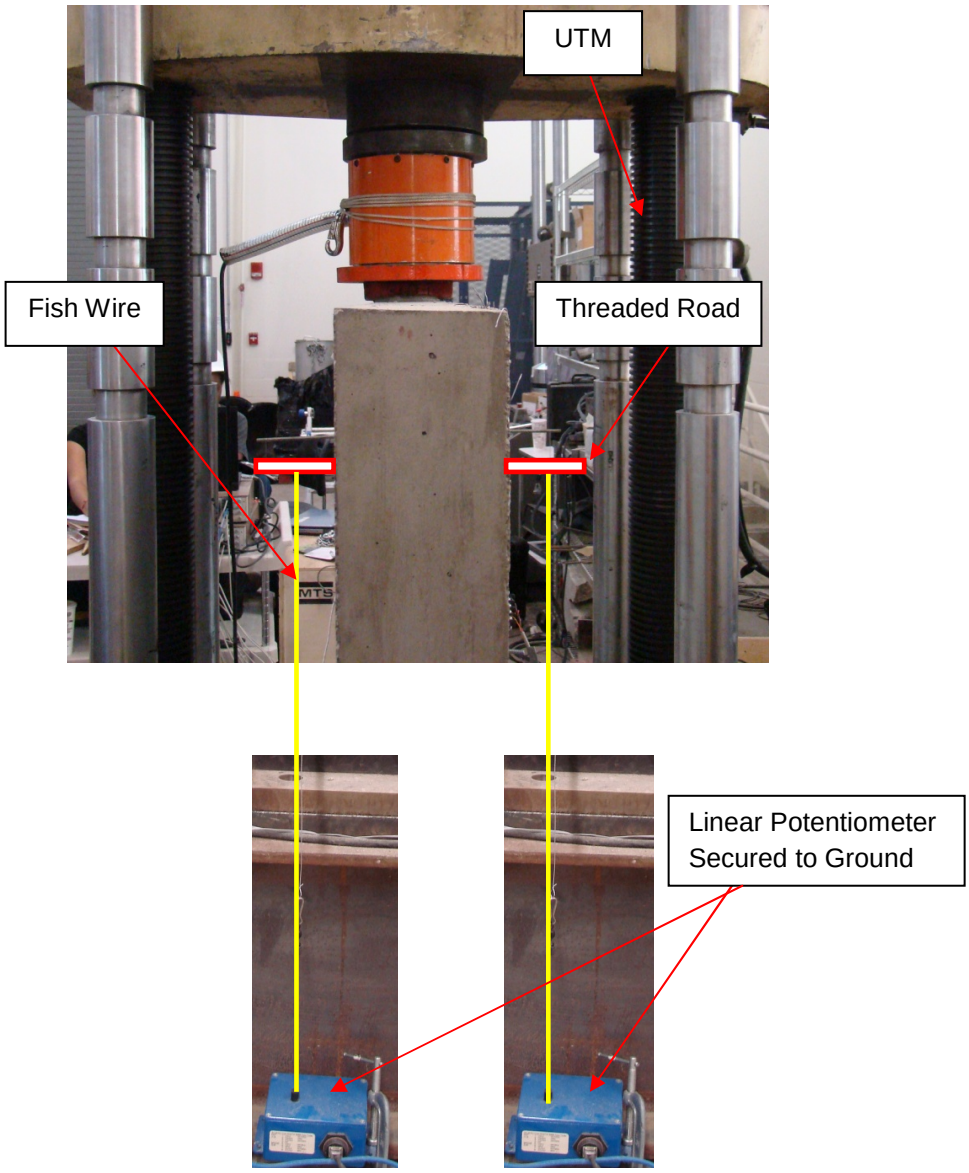

Figure 4.15 Typical linear potentiometer attached to threaded rod to measure vertical deformation

A steel roller of 2 in. (50 mm) diameter placed between two 1 in. (25 mm) thick plates were provided at the supports to avoid local crushing of the concrete and allow rotation of the plates (see **Figure 4.8**). Horizontal restraint was also provided on plates at the left support to

resemble ‘hinge’ condition, whereas roller at the right support represented ‘pin’ support. However, the effect of horizontal restraint at supports is negligible on strut-and-tie forces (Breña and Morrison, 2007).

4.3.5 Test results – RC Specimen (Specimen #1)

4.3.5.1 Observed Cracking During Testing

As mentioned earlier monotonic loading was applied at interval of 5 kips (22 kN) and at each interval cracking was observed and recorded. First crack started at 20 kips (89 kN) from lower corner of right window (see **Figure 4.16**). At next load step of 25 kip (111 kN) there were two new cracks, one at bottom fiber of beam and other at the top right corner of right window (see **Figure 4.16**). As the loading increased to 30 kips (133 kN) the cracks at bottom most fiber and at tip of windows started to elongate. Also there were few random cracks visible. At 35 kips (156 kN) loading crack at bottom fiber started changing its direction (see **Figure 4.17**). At 45 kips (200 kN) many new crack were seen along the corners of both windows and from bottom fiber of the beam.

As the loading was increased to 65 kips (289 kN) there were several visible cracks. One important thing to note was that there was no crushing or spalling of concrete on either support. This was primarily because of the presence of cages which helped to confine the concrete. In the beam tested by Breña and Morrison failure was because of spalling of a concrete wedge directly over the right support, as cages were not included. At 95 kips (423 kN) there were several cracks on the left side of the beam along the sides of window which extended almost to full height of the beam and they were propagating towards loading point.

As the loading reached 100 kips (445 kN) suddenly small portion of concrete from top right corner of the beam fell off (**see Figure 4.18**). It was very brittle and explosive failure with loud noise, testing was stopped at this stage. The ultimate failure of specimen was primarily due

to loss of concrete wedge near the top right opening. This was because there was, lack of confinement to the concrete under high axial forces.

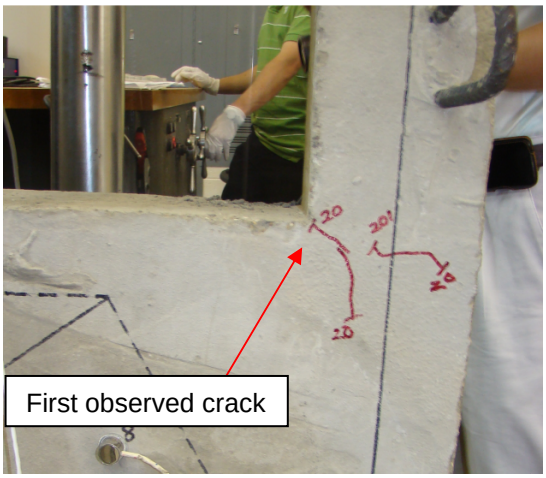

(a)

(b)

Figure 4.16 Observed cracking in RC specimen (a) First observed crack at 20 kips (89 kN) (b) Crack along thickness of beam at 25 kips (111 kN) load

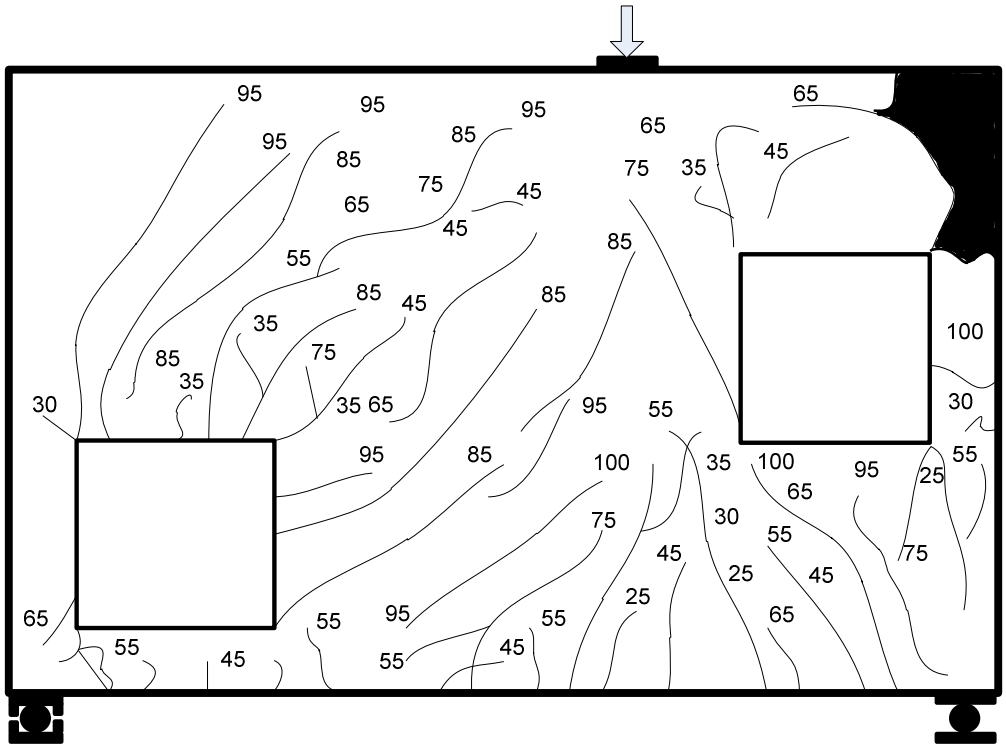

Figure 4.17 Overall observed cracking - RC specimen

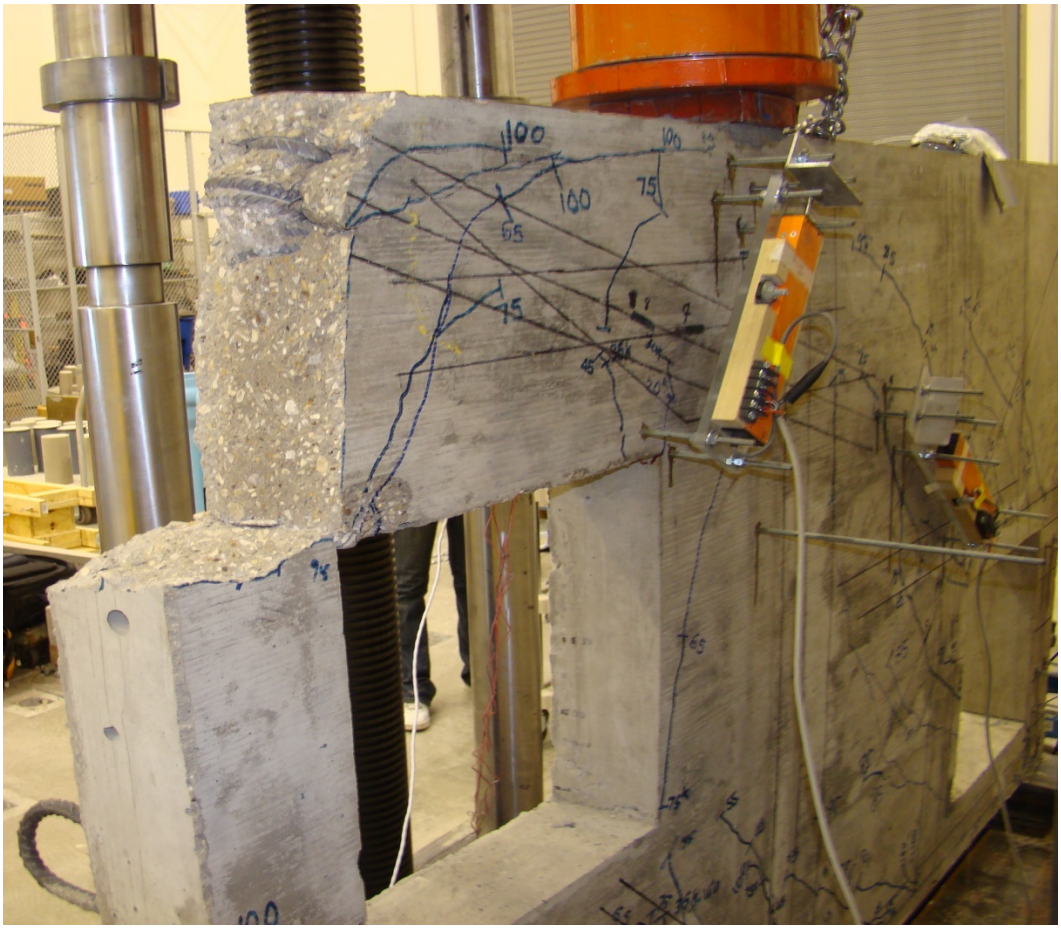

Figure 4.18 Top right corner of RC specimen at 100 kips

Figure 4.19 Overall state of specimen at failure stage – RC specimen

4.3.5.2 Load-Deflection Response

Failure of the RC specimens occurred at loads much higher than those causing yielding of the main tie in beam. The measured load-deflection response of the specimen (see **Figure 4.20**) corresponds to the total applied load and the deflection measured under the load point. The initial part of the curve is approximately linear indicating minimal cracking. Departure from this linear portion occurred at a load of approximately 45 kips (200 kN). Almost no post-yield strain-hardening behavior was observed; this was because the yielding of reinforcing bars in tension did not take place which was confirmed from the state of strains measured using uniaxial strain gauges. However specimen reached almost triple the design load of 34.1 kips (152 kN) predicted by SMT. The delaying of premature local failures near the supports due to presence of steel cages at the boundaries helped the specimen to reach higher load. There is a sudden drop in the curve at 100 kips (445 kN) load, this was because there was a localized brittle failure on the top right corner (see **Figure 4.18**) of the beam as a result of which testing was stopped.

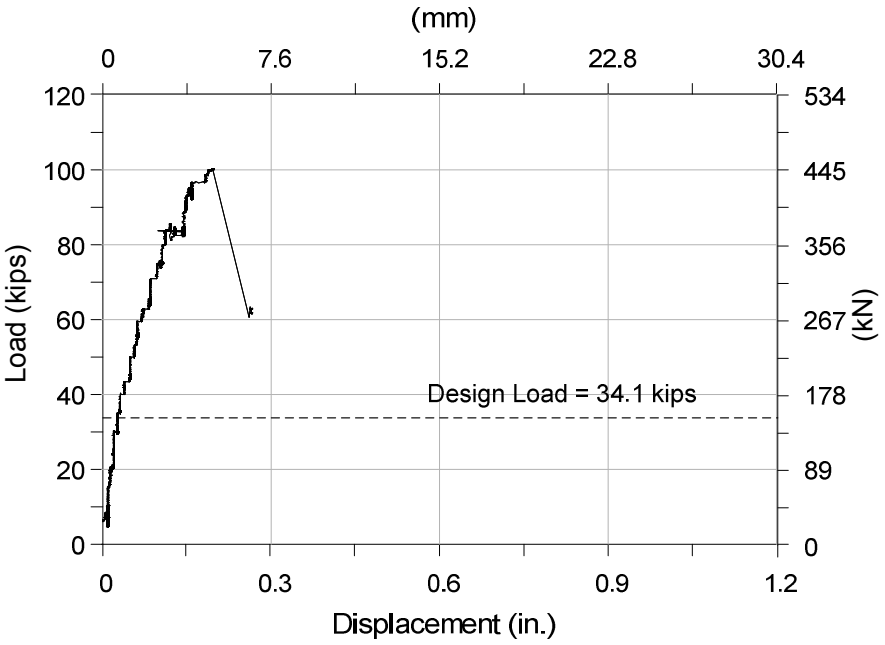

Figure 4.20 Gross Load-Deflection response of RC specimen

4.3.5.3 Concrete Strain Measured by LVDTs

Concrete strains recorded by all the LVDTs showed a linear behavior up to 10 kips. Concrete strain measured by LVDT 1 and 3 were -5.45×10^{-4} and -4.24×10^{-4} in./in. respectively (deformation measured/gage length) at ultimate. Both strains were negative as concrete was being stretched. LVDT 1 had positive strain of 0.3×10^{-4} in./in. till 82 kip, it suddenly became negative as there was sliding of roller. The strain measured by LVDT 4 discontinued the linear behavior from 10 kips and kept on increasing constantly. It had ultimate strain of 9.0×10^{-4} in./in.

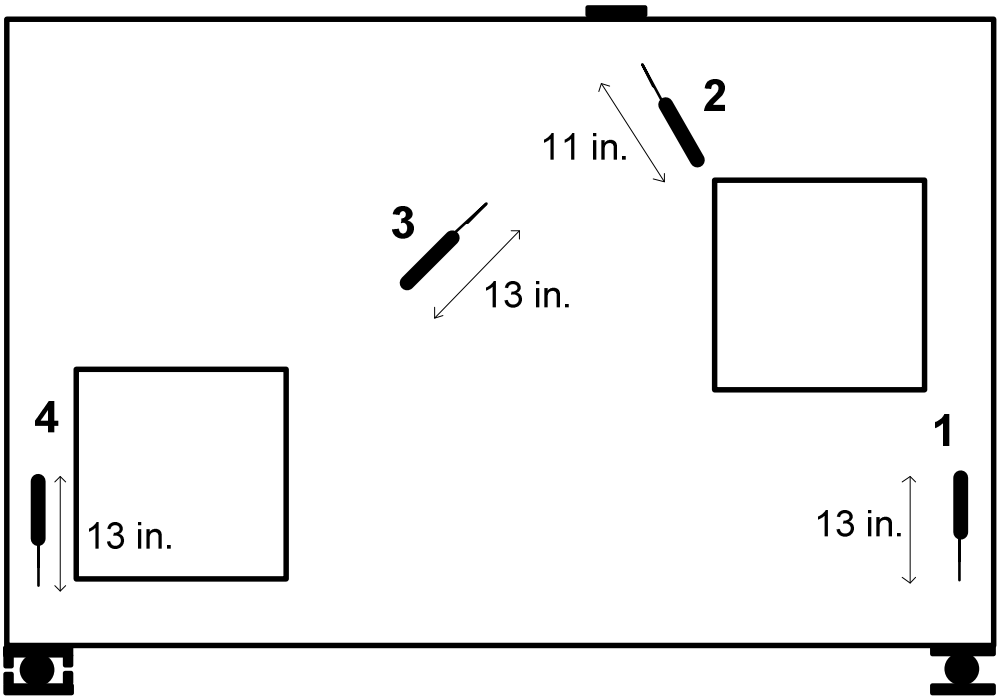

Figure 4.21 Location of LVDTs in RC specimen (Numbers indicate gauge length)

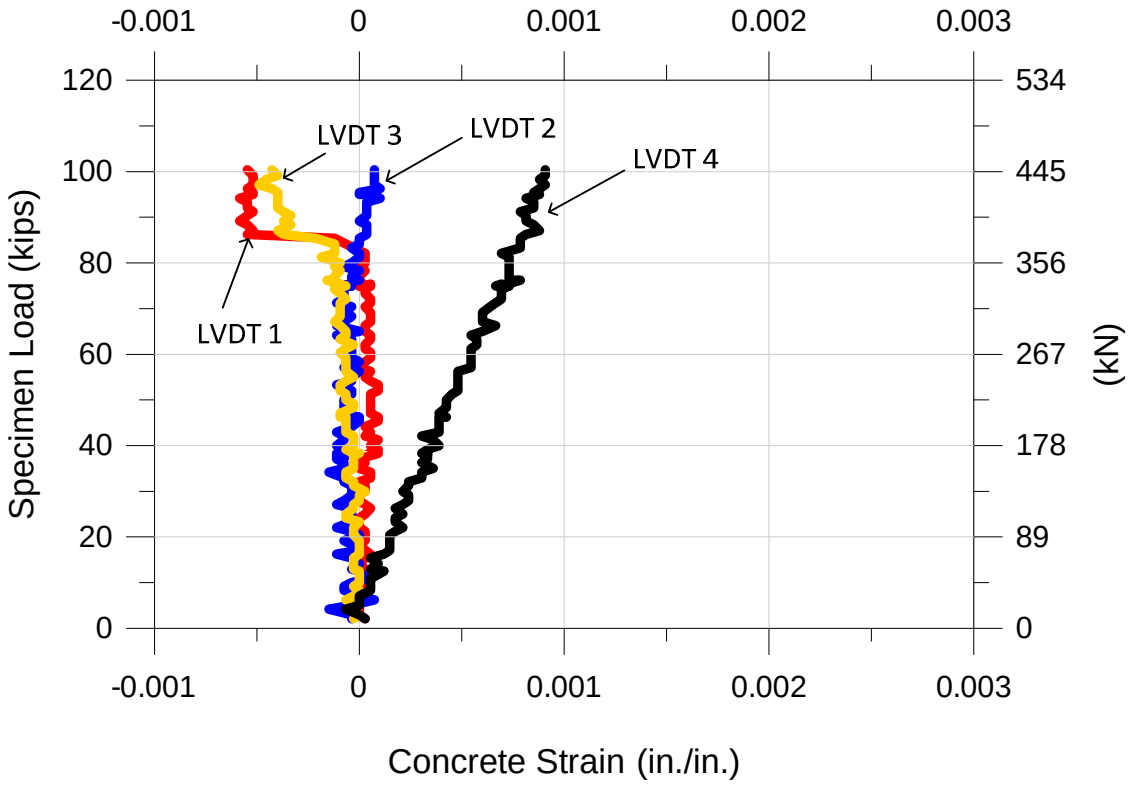

Figure 4.22 Plot of graph showing concrete stains in RC specimen (compression shown as positive, tension shown as negative)

4.3.5.4 Reinforcing Steel Strain

Determined strains were measured by using uniaxial strain gauge affixed on reinforcing bars placed in the specimen. The location of various ties in the design strut-and-tie model is shown in **Figure 4.2**. Strain gauges numbered “T” were installed on top layer of reinforcement and one marked “B” was installed on bottom layer (see **Figure 4.23**). The X and Y coordinated of strain gauge on top and bottom layers were kept same. This was done to see if weather the rebar at that location was sharing same force. Several strain gauges were located along the reinforcing bars corresponding to the same tie in the strut-and-tie model. The large strain

differences along reinforcement bars corresponding to a single tie (see strain in 2T and 2B in **Table 4.1**) in the model was due to the variation of bond stresses because of cracking in the concrete.

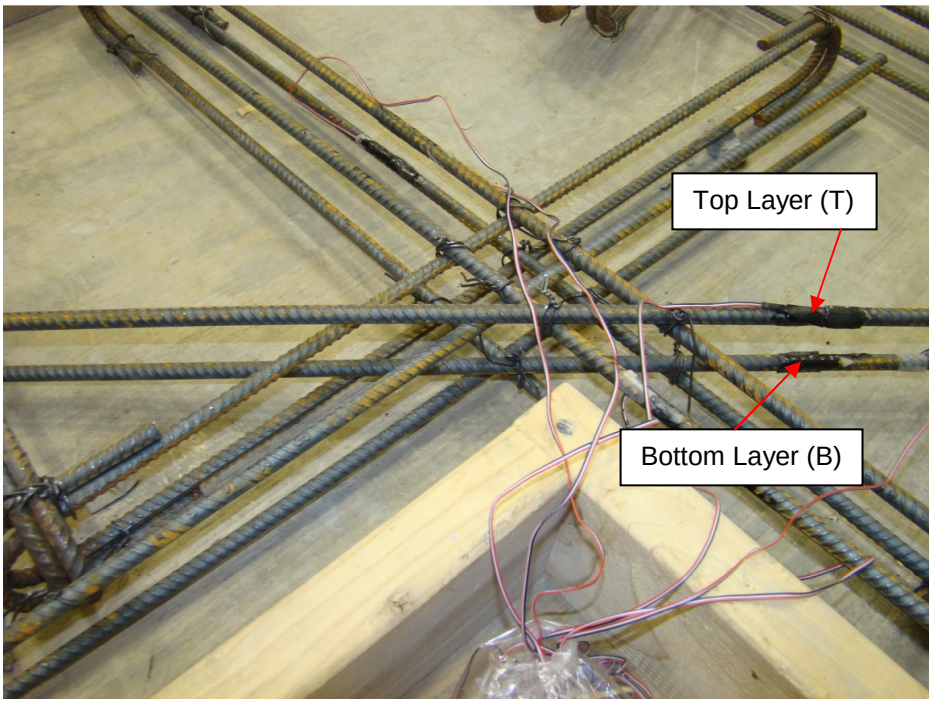

Figure 4.23 Strain gauge installed on top and bottom layer of reinforcement

All the strain gauges showed linear behavior till approximately 20 kips (89 kN). The bottom tie showed largest strain at ultimate. The strain in 3T and 3B suddenly increased after 95 kips, this was because crack at the bottom fiber widened and stressed the bar at that location. Strain in 4T and 4B (which are also located on bottom tie but left side of loading point) showed a sudden deviation from its linear behavior from 40 kips (178 kN) load, this was because bar started carrying greater force due to development of new crack and also because crack started increasing its width. There is a sudden drop in the strain at 100 kips (445 kN) in almost all strain

gauges this was because testing was stopped at this stages and specimen was unloaded owing to which strain in the bars was released suddenly.

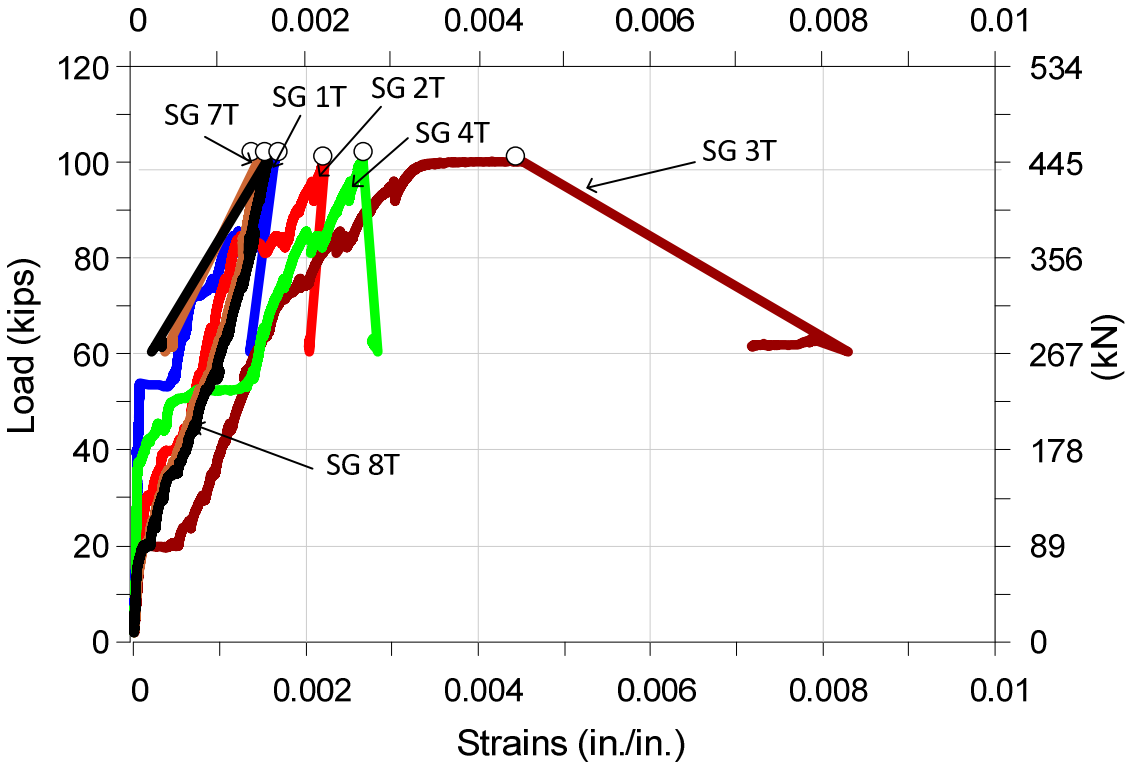

Figure 4.24 Reinforcement bar strain in top layer of RC specimen

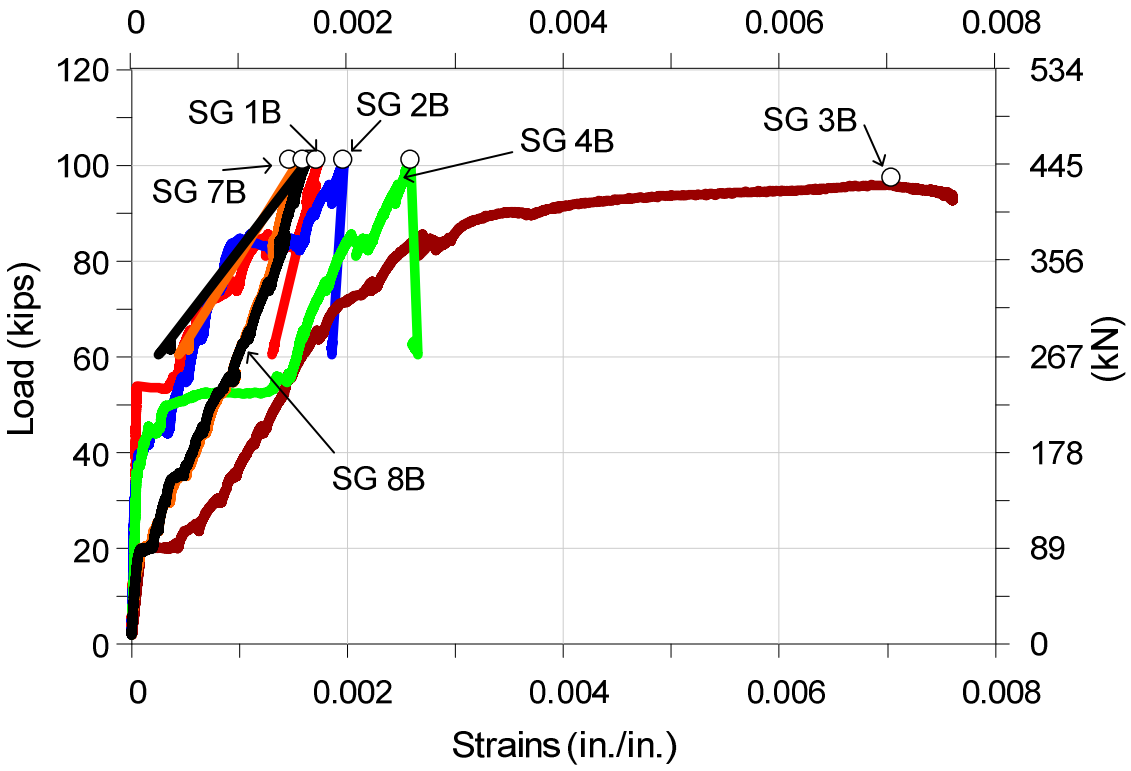

Figure 4.25 Reinforcement bar strain in bottom layer of RC specimen

It's important to note that most reinforcing bars deformed the same amount at the same location. Due to this strain gages in the top and bottom layer have nearly identical load-deformation curves (see **Figure 4.24 and 4.25**). However if they show different curves this phenomenon is due to unequal force sharing by the reinforcing bars as the crack forces bars on one layer of reinforcement to take larger forces than the other. In addition, there were several reinforcement bars which reached their yield strain limit of 2000 micro-strain at the ultimate load level of the specimen; they were 2T, 3T, 3B, 4T and 4B. As expected, the highest strains were recorded in the proximity of cracks and decreased rapidly with increase in distance from a crack. Although strut-and-tie models adequately identified the locations of critical ties (ties carrying maximum strains) in the specimens, they failed to capture the important role of anchorage bars in load-sharing mechanism, particularly if the vertical segments of the openings were

strengthened against premature local failures Breña and Morrison (2007). It should be noted that strain readings may be influenced by the proximity to cracks affecting the calculation of tie forces.

Tie forces were determined using measured strains of instrumented reinforcing bars in the specimens. To assess the performance of the design strut-and-tie models, measured tie forces at design load and ultimate loads were compared with tie forces calculated from the models. **Table 4.1** compares the forces measured in the specimen at the design load of 34.1 kips (152 kN) where as **Table 4.2** compares the measured forces in the specimen when testing was terminated at 100 kips to the predicted forces from analysis. The calculated tie forces listed in **Table 4.1** and **Table 4.2** correspond to those obtained using the design strut-and-tie model and a strength reduction factor of 1.00 by Breña and Morrison, expected strength predicted by them was 47.7 kips (212 kN). Since some ties were not instrumented with strain gages at every steel bar, the measured strain was assumed to be the same in the next adjacent bar.

Table 4.1 Tie forces at predicted design capacity of RC specimen

(1) Tie ID	(2) Tie Location	(3) Strain Gage	(4) Bar Area, in^2	(5) $Calc_0$:Tie Force from Analysis (kip)	Tie force at design capacity				
					(6) Strain (in/in)	(7) Stress (ksi)	(8) Force per bar (kip)	(9) Total $Force_0$ (kip)	(10) $Force_0/Calc_0$
T2	Bottom tie	3T	0.11	19	0.00089	21.601	2.37	4.83	0.254
		3B	0.11		0.00091	22.35	2.46		
T1	Bottom tie	4T	0.11	13.3	0.000039	0.902	0.099	0.248	0.0186
		4B	0.11		0.000049	1.360	0.149		
T5	Diagonal tie near left window	5T	0.11	7.2	Ï	-	-	-	-
		5B	0.11		Ï	-	-		
T3	Diagonal tie near bottom of right window	6T	0.11	10.34	Ï	-	-	-	-
		6B	0.11		Ï	-	-		
T6	Horizontal tie below loading point	7T	0.11	26.23	0.00036	8.629	0.949	2.075	0.079
		7B	0.11		0.00041	10.239	1.126		
T7	Diagonal tie near top right corner	8T	0.11	23.26	0.00039	9.795	1.077	2.026	0.087
		8B	0.11		0.00036	8.629	0.949		

Table 4.1 – *Continued*

T4	Vertical tie near bottom left window	1T	0.11	19.74	0.00004	1.193	0.131	0.262	0.013
		1B	0.11		0.00004	1.193	0.131		
		2B	0.11		0.000043	1.193	0.131		

Notes: Design load is 34.1 kips (152 kN) based on Berna and Morrison (2007)
Ï Damaged instrument (values not calculated), Ultimate load = 100 kips (445 kN)

Table 4.2 Tie forces at ultimate load of RC specimen

(1) Tie ID	(2) Tie Location	(3) Strain Gage	(4) Bar Area, in^2	(5) $Calc_0$:Tie Force from Analysis (kip)	Tie force at Ultimate Load				
					(6) Strain (in/in)	(7) Stress (ksi)	(8) Force per bar (kip)	(9) Total $Force_0$ (kip)	(10) $Force_0/Calc_0$
T2	Bottom tie	3T	0.11	19	0.00439	71.267	7.83	16.79	0.883
		3B	0.11		0.0076	81.520	8.96		
T1	Bottom tie	4T	0.11	13.3	0.00266	59.988	6.59	13.09	0.984
		4B	0.11		0.00259	59.086	6.5		
T5	Diagonal tie near left window	5T	0.11	7.2	Ï	-	-	-	-
		5B	0.11		Ï	-	-		
T3	Diagonal tie near bottom of right window	6T	0.11	10.34	Ï	-	-	-	-
		6B	0.11		Ï	-	-		
T6	Horizontal tie below loading point	7T	0.11	26.23	0.00144	34.878	3.83	7.89	3.00
		7B	0.11		0.00153	36.972	4.06		

Table 4.2 – *Continued*

T7	Diagonal tie near top right corner	8T	0.11	23.26	0.00154	37.444	4.11	8.37	0.359
		8B	0.11		0.00161	38.748	4.26		
T4	Vertical tie near bottom left window	1T	0.11	19.74	0.00163	39.761	4.37	8.97	0.454
		1B	0.11		0.00173	41.842	4.60		
T4	Vertical tie near bottom left window	2T	0.11	19.74	0.00222	52.455	5.77	10.93	0.553
		2B	0.11		0.00197	46.947	5.16		

Notes: Ï Damaged instrument (values not calculated)
Ultimate load = 100 kips (445 kN) - from testing.

From the tie forces tables, it can be observed that the tie forces at the predicted design load capacity based on STM are lower than calculated, hence all ratios of actual force/calculated are less than one (see column#10 in **Table 4.1**). At ultimate load capacity strain in all ties were lower than expected. However, the ratio of actual force to predicted force measured in tie T1 and T2 (bottom ties) was highest (see column#10 in **Table 4.2**). This corresponds to the observed crack at bottom fiber exactly below the loading point. This is because when the concrete is cracked large amount of force is transferred to the reinforcing steel. Also, strain gauges 3 and 4 reached yield limit of 2000 micro strain at ultimate load, although strain gauges 2 and 4 were expected to yield based on strut-and-tie model (Breña and Morrison, 2007). This is due to the fact that strain readings at discrete locations were strongly affected by proximity to cracks affecting the calculation of tie stresses and forces.

4.4 SFRC#1 (Specimen#2)

4.4.1 Specimen Geometry

It's hypothesized that SFRC has a higher shear capacity due to the superior performance in tension compared to plain concrete (ACI 544-96, 1996). As discussed earlier main objective of this research was to develop a more convenient design practice which result in much less complicated detailing. To achieve the target steel fiber reinforced concrete (SFRC) was used as a casting material. The use of SFRC is based on the assumption that, if breakdown of the most stressed locations are prevented by reinforcing bars, the greater plastic deformation capacity of SFRC will allow considerable internal force redistribution, thus also increasing the ultimate load-carrying capacity. Primary focus while deciding layout of SFRC specimens was to reduce the complexity of detailing and reinforcing only certain critical locations cited by two dimensional finite element analysis.

A linear elastic 2D finite element analysis of the specimen without any reinforcement rebars was carried out on software called LUSAS, based on the results of contour plot of principal tensile and compressive stress critical regions were cited and were reinforced using standard No 3 rebars. The regions having flexure bending strength f_p (see chapter 3) greater than or equal to 0.98 ksi (6.8 MPa) was designated as critical region. The resulting layout had two layers of closed square loops around the windows (see **Figure 4.26**). A clear cover of 1 in. (25 mm) was kept between the vertical and horizontal segment of the window and center of rebar. Form work was oiled before casting so that it could be easily demolded later, care was taken that the reinforcement bars do not come in contact with oil because otherwise it would create bond problems. Also two cages one at each support were used to prevent localized damage. In total 20 of strain gauges were used (see **Figure 4.26**).

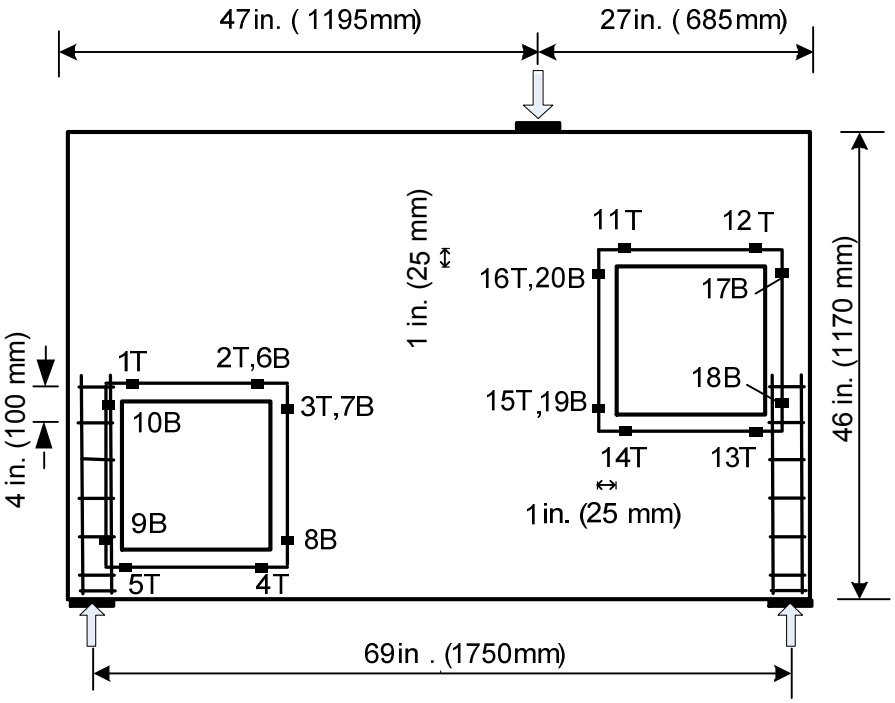

Figure 4.26 SFRC #1 specimen reinforcement layout (Numbers on the bar indicate strain gauge number and letter indicating type of layer “T”- top and “B”- bottom)

Figure 4.27 SFRC #1 specimen before casting

Figure 4.28 Square loops of reinforcement around the window, cage at support and anchor bar in SFRC #1 specimen

Figure 4.29 Steel fibers being mixed in the mixer during casting

Figure 4.30 Close up of concrete mix with fiber for SFRC #1 specimen

Figure 4.31 SFRC #1 test specimen during placing and consolidation of plastic concrete

In total four batches was prepared each with same ratio of materials and they were mixed in two mixers simultaneously. Fibers were added last during mixing. It was added in small quantities by hand (see **Figure 4.29**). Fibers used were deformed with hooked ends manufactured my Meccaferri (see **Figure 4.32**) with an aspect ratio of 60.3 (see Chapter 3 for detailed specification). A fiber volume fraction of 1.5% (or 200 lb. per cubic yard of concrete) was used. The procedure used to mix and consolidate the concrete was same as that used for casting specimen # 1 (see **Figure 4.31**). However after the mixing some cement and sand was found stuck in one of the concrete mixer which affected the actual water cementitious ratio, due to this the concrete mixture was observed to be much more flowable. Samples from each batch

were carefully observer and fibers were found to be oriented in different direction (see **Figure 4.30**).

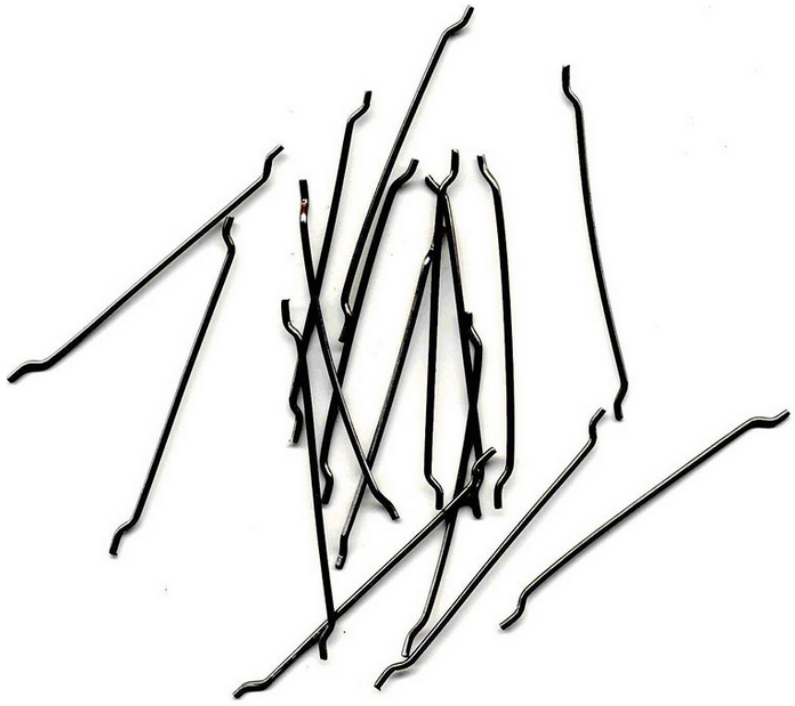

Figure 4.32 Deformed hooked end long (FF3) fiber used in SFRC specimens

4.4.2 Test Results

4.4.2.1 Observed Cracking

Cracks were drawn with blue marker on the front face and red on the back face to distinguish each side. Loading was increased in the intervals of 5 kips. At each interval cracks were observed, marked and recorded. A small portion of concrete was pre-crushed near left

support (see **Figure 4.33**), this occurred when the specimen was being demold. As expected first observed crack was flexural crack originating from bottom fiber of beam exactly below the loading point at 30 kips (133 kN) (see **Figure 4.34**). It was evident from the fact as there was no longitudinal reinforcement used. There was no other visible crack at this stage. In the next loading step i.e. at 35 kips (156 kN) the flexural crack propagated further to about 5 in. (127 mm) towards loading point. At this stage the width of crack measured was less than 0.004 in. (0.10 mm).

Figure 4.33 Pre-Crushing of concrete near the support of SFRC#1 specimen

During the next loading steps i.e. at 40 kips (178 kN) there were two new cracks formed both originating from the two opposite corners of top right window. The flexural crack propagated further and was increasing its length during each loading step. When the loading was increased to 50 kips (222 kN) there were several sudden cracks formed and the specimen looked unstable.

There was another flexural crack formed on the right side of the original one, it extended almost close to tip of right window (see **Figure 4.35**). There was another prominent crack formed on the top of right window propagating towards loading point (see **Figure 4.35**), observed width of this crack was less than 0.004 in. (0.10 mm). Another significant crack originated along the thickness of beam near right window at this loading stage (see **Figure 4.35**).

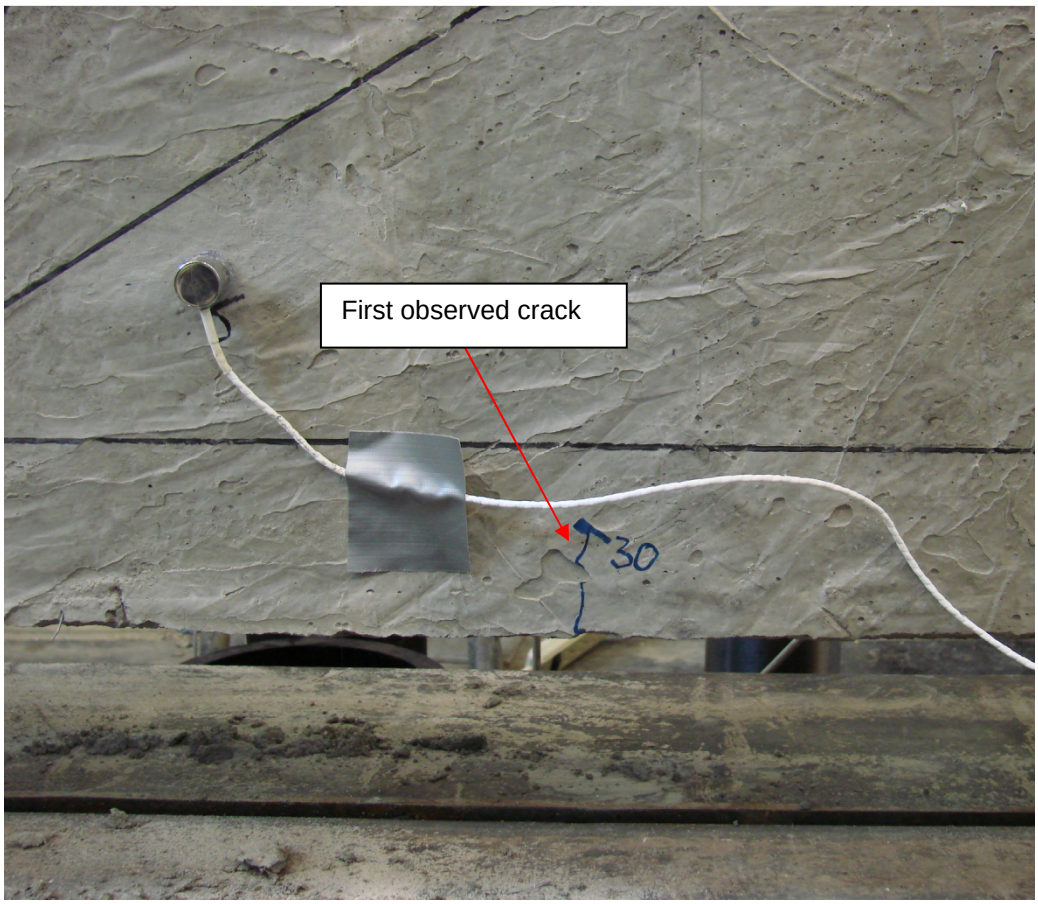

Figure 4.34 First observed crack in SFRC#1 specimen at 30 kips (133 kN) loading

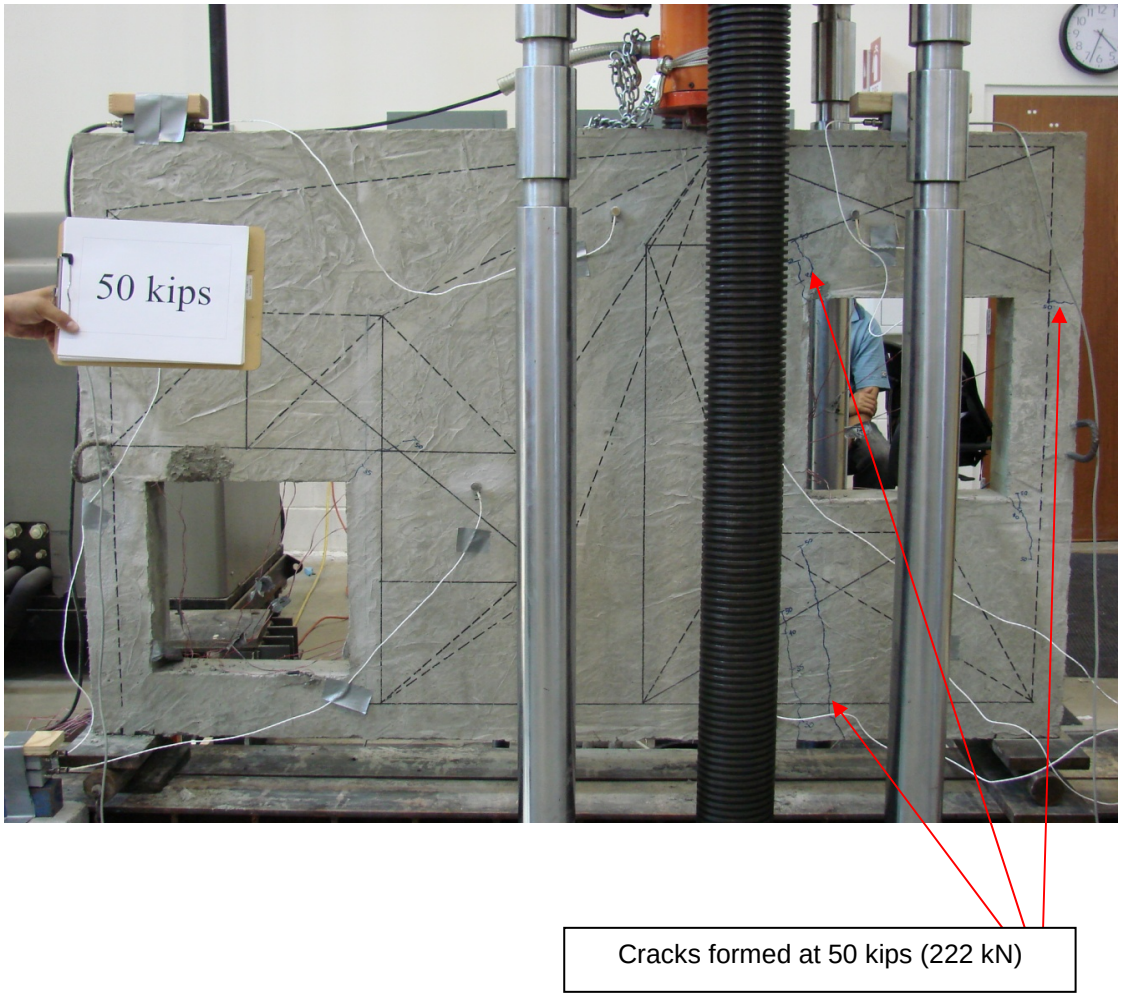

Figure 4.35 Crack formation in SFRC #1 specimen at 50 kips (222 kN) loading

As the loading was further increased there was sudden drop in loading after 53 kips (236 kN), this was because the flexural crack was wide open 0.07 in. (2 mm) and the beam was not taking any loading. At this stage the crack was being hold from opening by the fibers. The right window seemed to be deformed in shape due to formation of plastic hinges (see **Figure 4.37**).

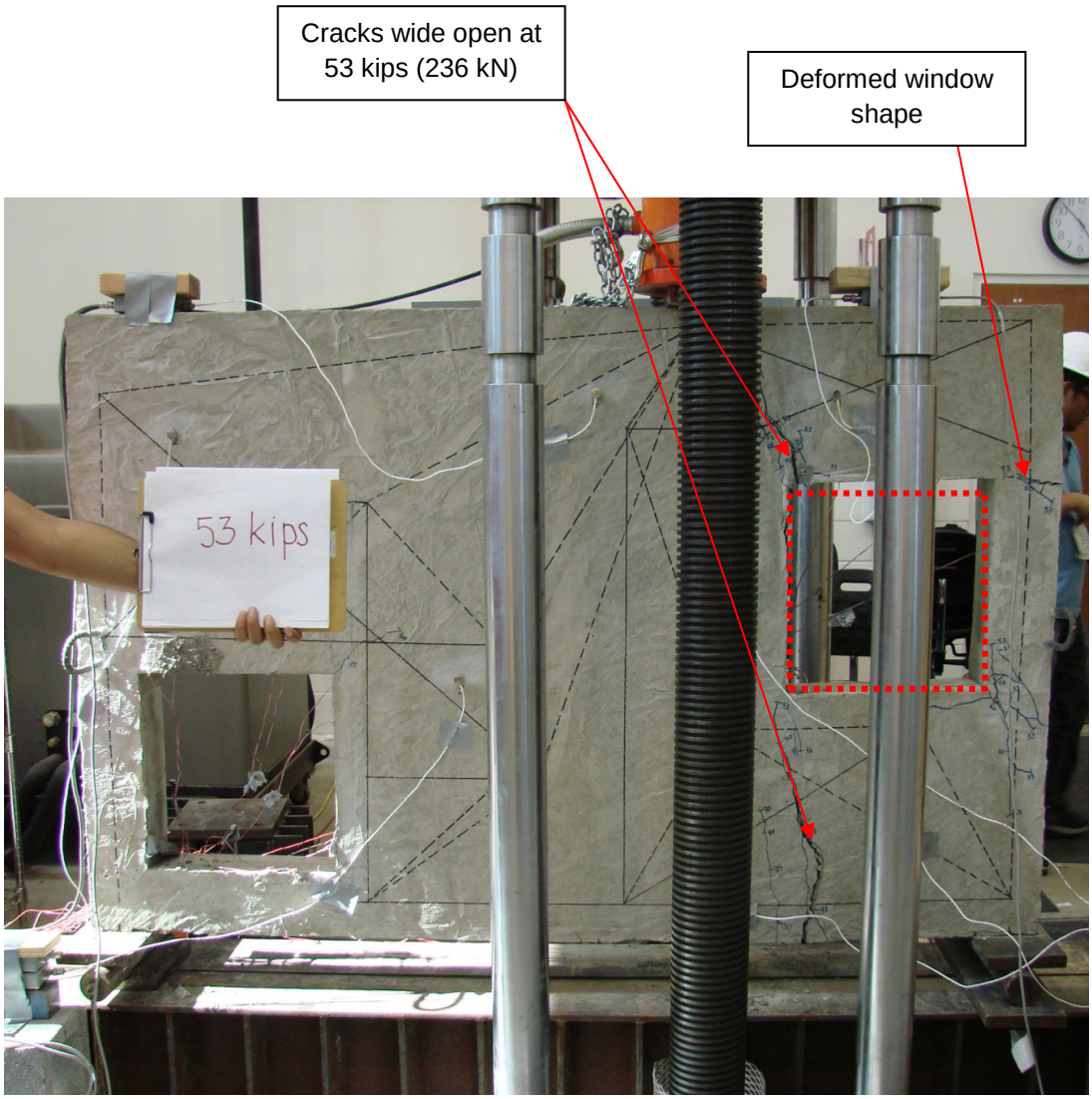

Figure 4.36 SFRC #1 test specimen at 53 kips (236 kN) loading

Loading was further increased which merely increased the deflection and widened the cracks, it was finally stopped at a deflection of 1.1 in. (28 mm). There was sever cracks along the sides of windows and fiber pull out was clearly visible (see **Figure 4.39**). Also a concrete

cover of 1 in. (25 mm) used for the bars around the window was found to be insufficient as there was debonding of rebar (see **Figure 4.38**); also it proved insufficient to stop the crack i.e. until the crack reached the bar the specimen already failed. Another main reason was because of small cover fibers were not able to sink in during casting as a result there were not enough fibers present between the reinforcement bar and the window.

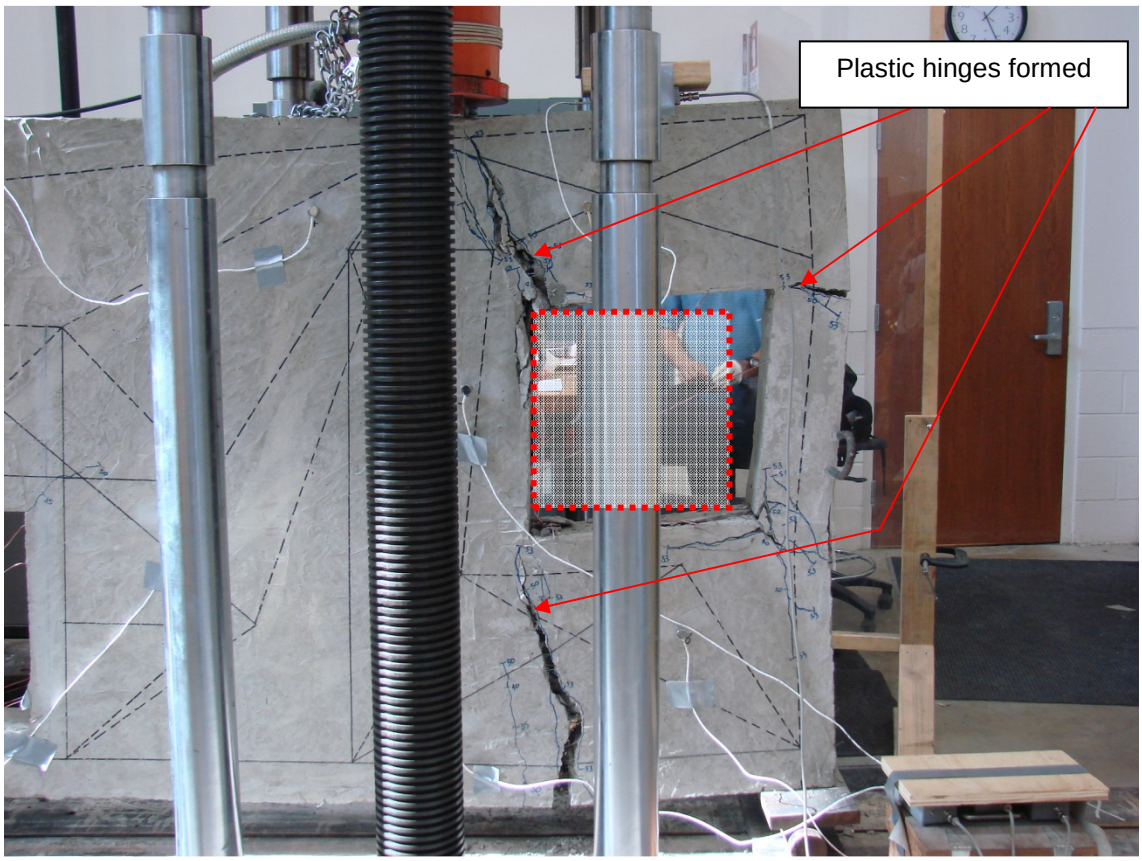

Figure 4.37 SFRC #1 test specimen at 1 in. (25 mm) deflection

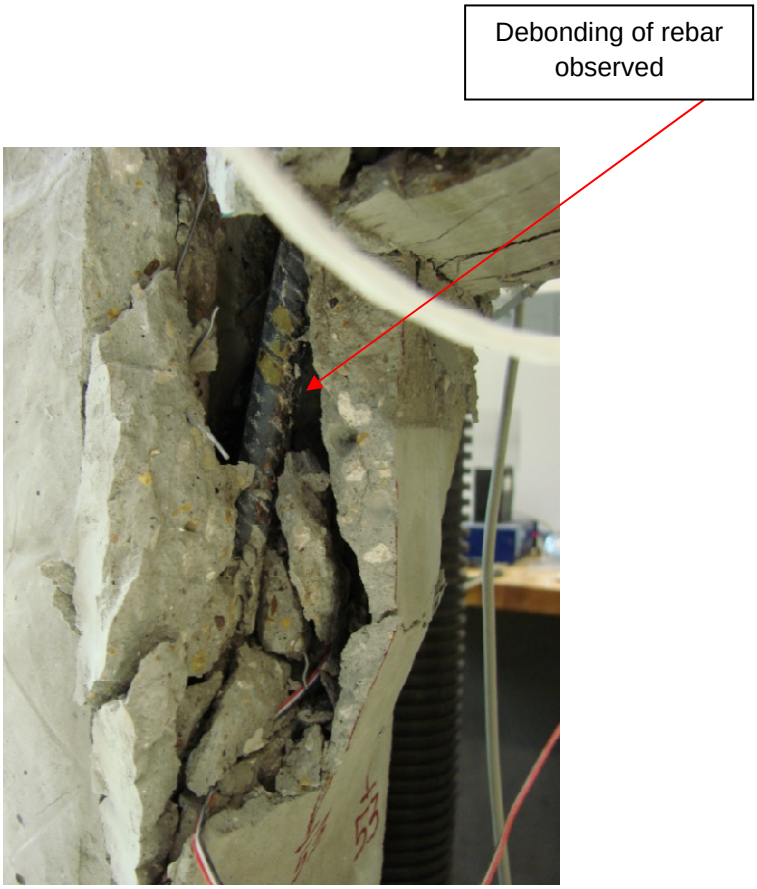

Figure 4.38 Observed debonding of rebar in SFRC #1 specimen

Figure 4.39 Fiber pull out at failure of SFRC #1 specimen

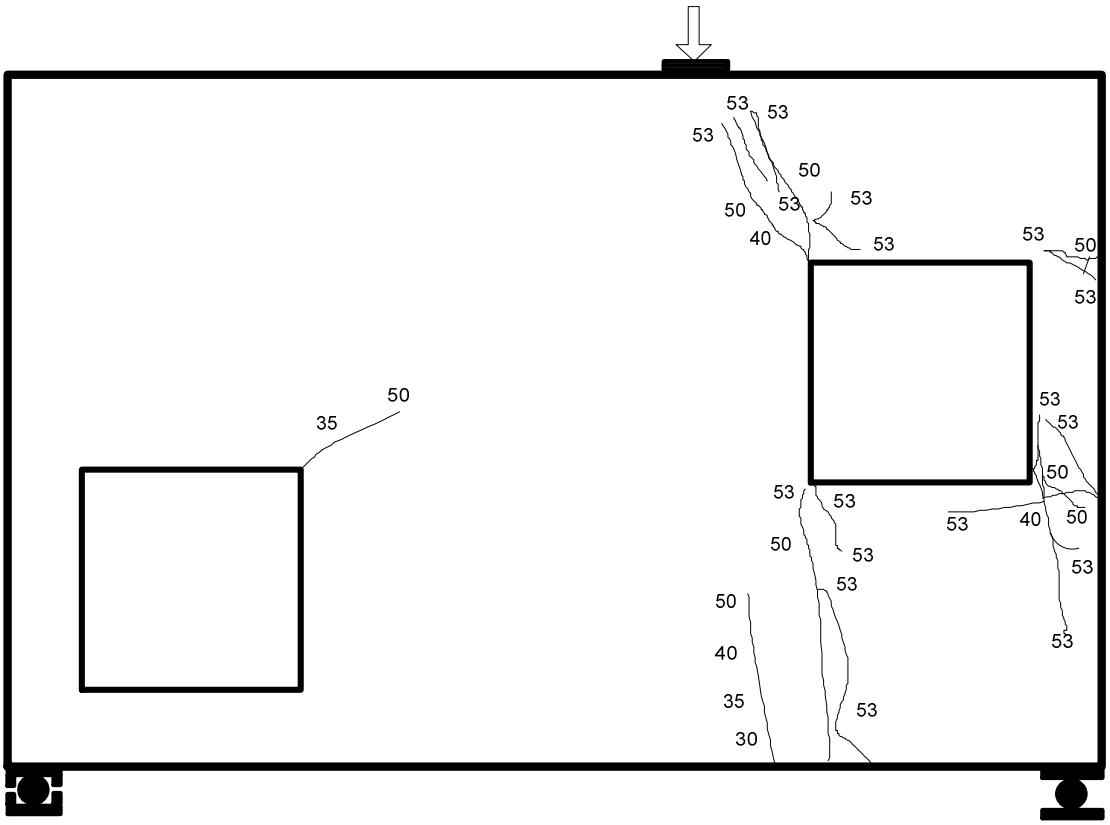

Figure 4.40 Overall cracking observed after testing of SFRC #1 specimen along front face (Numbers indicate load steps in kips)

Figure 4.41 Overall state of SFRC #1 specimen at final stage

Sever flexural cracking was observed and was identified as most critical region, it was concluded that if longitudinal rebar had been included the crack could have been delayed and specimen could have sustained higher load. Important to note was that the deformed shape complied with the elastic analysis done on LUSAS (see Figure 5-3); also critical areas were correctly cited. There was no brittle localized failure as in case of RC specimen on the contrary failure mode was more ductile.

4.4.2.2 Load-Deflection Response

The gross load-displacement plot under the loading point is presented here (see **Figure 4.35**). The method of obtaining load-displacement curve was same as used in RC specimen (specimen#1).The load-displacement plot of the SFRC#1 specimen shows a linear response up to 45 kips (200 kN). This agrees with the fact there were no major cracks observed until this loading stage and the specimen deformed proportionally to the load being applied. The maximum load reached was 53 kips (236 kN) and maximum deflection was 1.05 in. (27 mm).

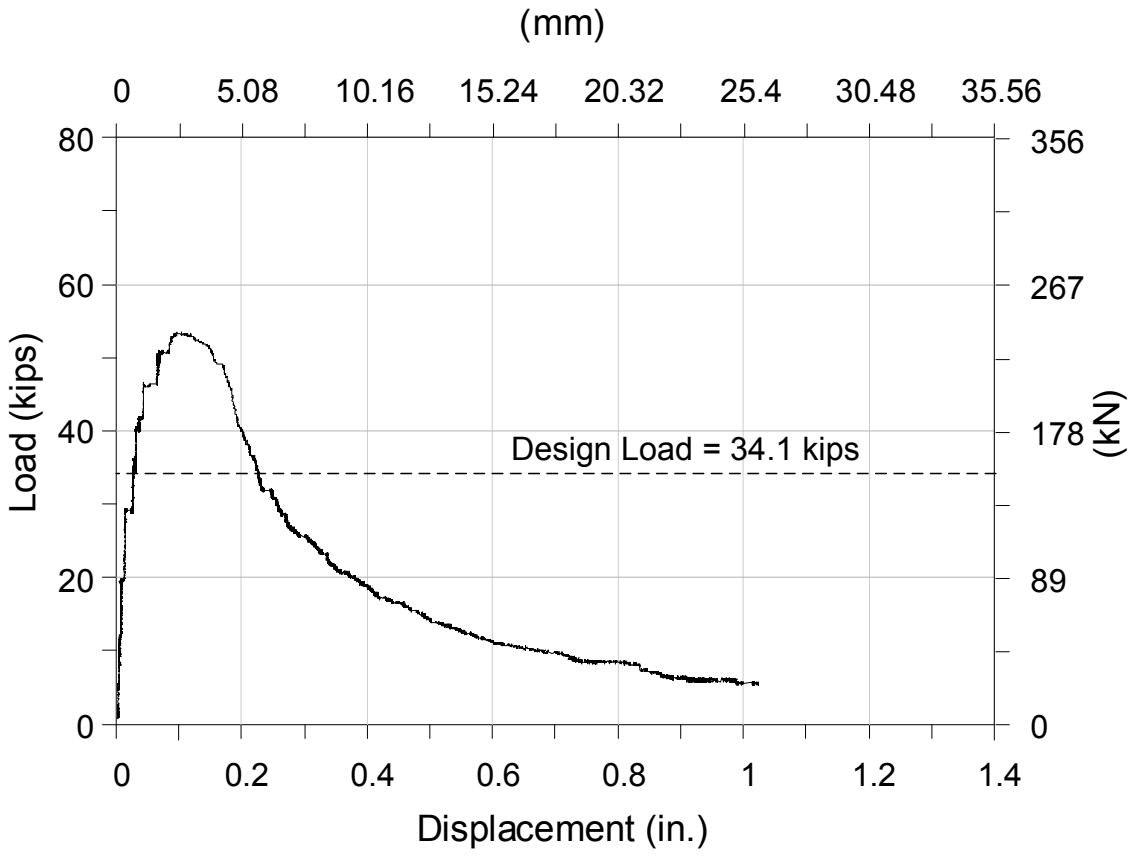

Figure 4.42 Gross load-displacement curve of SFRC#1 specimen

The comparison of the two plots shows similar load-displacement response for the applied load till 50 kips (222 kN) (see **Figure 4.43**). However SFRC#1 specimen deformed much more than the RC justifying the use of fibers, though it did not increase the capacity but it changed the failure mode from brittle to ductile.

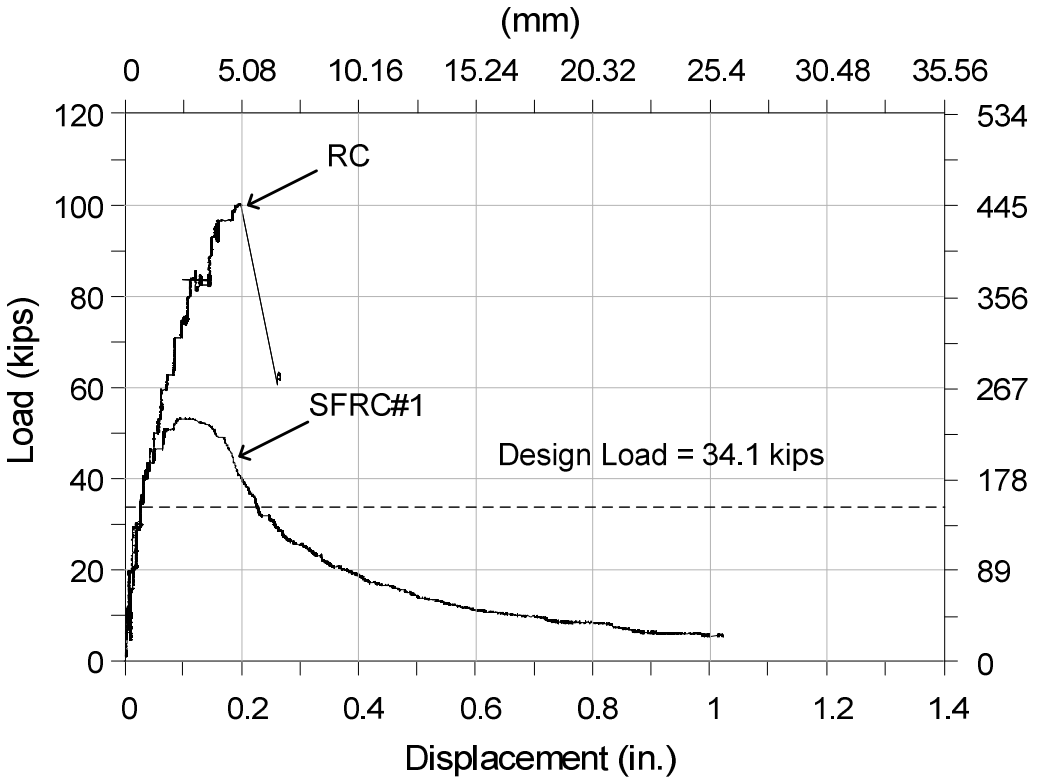

Figure 4.43 Gross load-displacement curve for RC and SFRC#1 specimen

However, both RC (specimen #1) and SFRC#1 (specimen #2) test specimens reached the design load of 34.1 kips (152 kN), it's important to note that in SFRC#1 specimen there were absolutely no steel reinforcement bars used as struts and ties as per strut-and-tie models. In addition, SFRC#1 specimen showed better post-peak falling branch as compared to the RC

specimens indicating significant contribution of steel fibers in residual strengths of the SFRC specimens.

4.4.2.3 Concrete Strains

Concrete strains were recorded using four LVDTs as discussed earlier. The positions of LVDTs were same as that used in RC (specimen #1). LVDT 2 and 3 measured very small deformations. These deformations were measured on axis with the compressive struts from the loading point. The response was linear; however, strains (deformation/gage length) measures at ultimate was -0.35×10^{-4} in/in and -0.60×10^{-4} in./in. respectively. Concrete near the left support compressed significantly more as compared to that near strut. The response of LVDT 4 was linear until 20 kip. Strain measured at ultimate load on the right and left support was 3.93×10^{-4} in./in. and 5.15×10^{-4} in./in. respectively (see **Figure 4.44**).

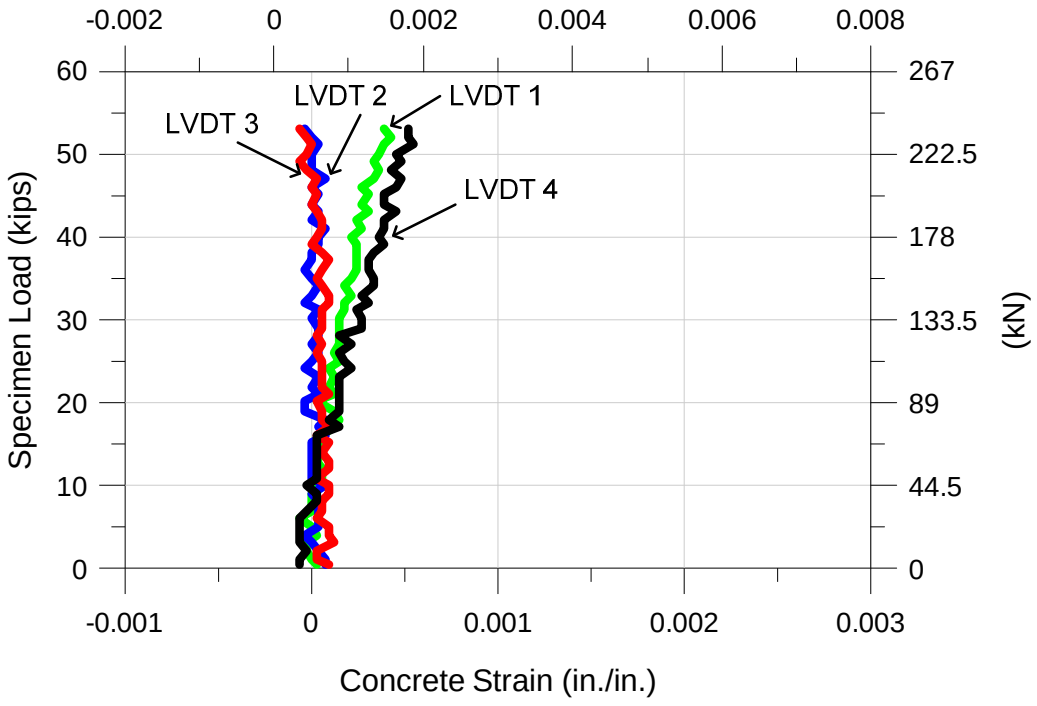

Figure 4.44 Concrete strain measured by LVDTs in SFRC #1 specimen

4.4.2.4 Reinforcing Steel Strain

The method of strain gauge installation was same as that mentioned earlier. In total 20 strain gauges were used (for location see **Figure 4.26**), the numbers in the figure indicate strain gauge number and letters “T” and “B” are used for top and bottom layers respectively. **Figure 4.45, 4.46** and **4.47** shows plot of strain vs specimen load. Only value till peak loading was plotted. None of the rebars yielded at the peak loading of 53 kip (236 kN). However few of them did yield at ultimate deflection of 1.05 in. (27 mm). Strains in strain gauge number 3T and 7B were not recorded as it was damaged during casting.

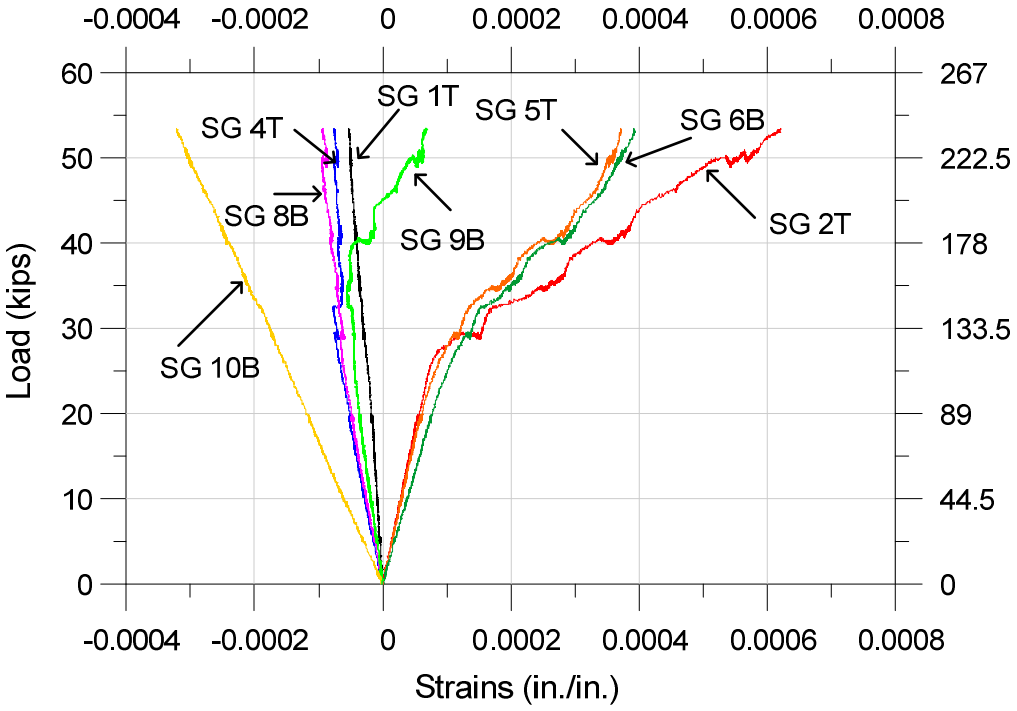

Figure 4.45 Reinforcing rebar strain for SFRC#1 specimen (strain gauge 1-10)

Strain gauges 1T, 4T, 8T had small value of strain at peak load it was 5 x 10^{-5}, 8 x 10^{-5}, 9 x 10^{-5} in./in. respectively. Strain in 10B varied linearly with increase in load, it was -0.0003 in./in. at ultimate. Strain in 6B, 2T varied linearly till 25 kips (111 kN). There was deviation from its linear behavior after 30 kips (133 kN), this was because of the cracking of concrete near the right top corner of left window. Strain measured at ultimate in these strain gauges was -0.00039 in./in. and 0.00062 in./in. Strain measured by strain gauge number 12T, 14T, 15T, 17B and 18B at peak loading were very small, they were -0.0002, -0.0004, -0.0003, -0.0006 and -0.0005 in./in. respectively.

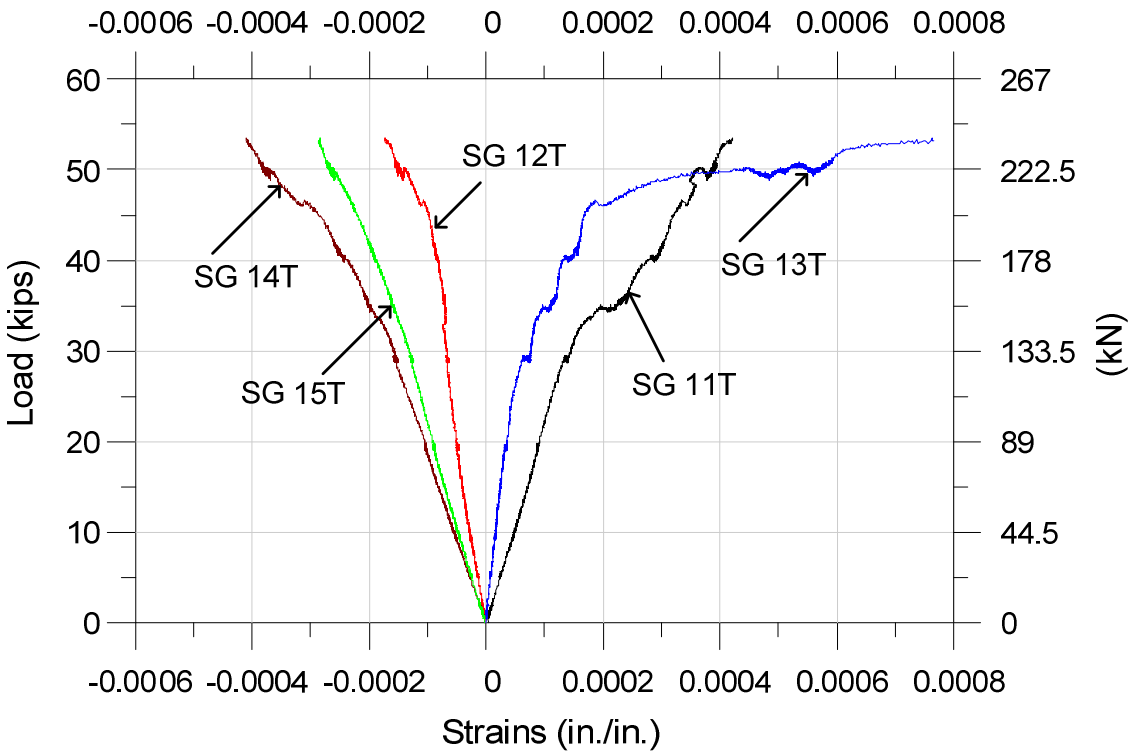

Figure 4.46 Reinforcing rebar strain for SFRC#1 specimen (strain gauge 11-15)

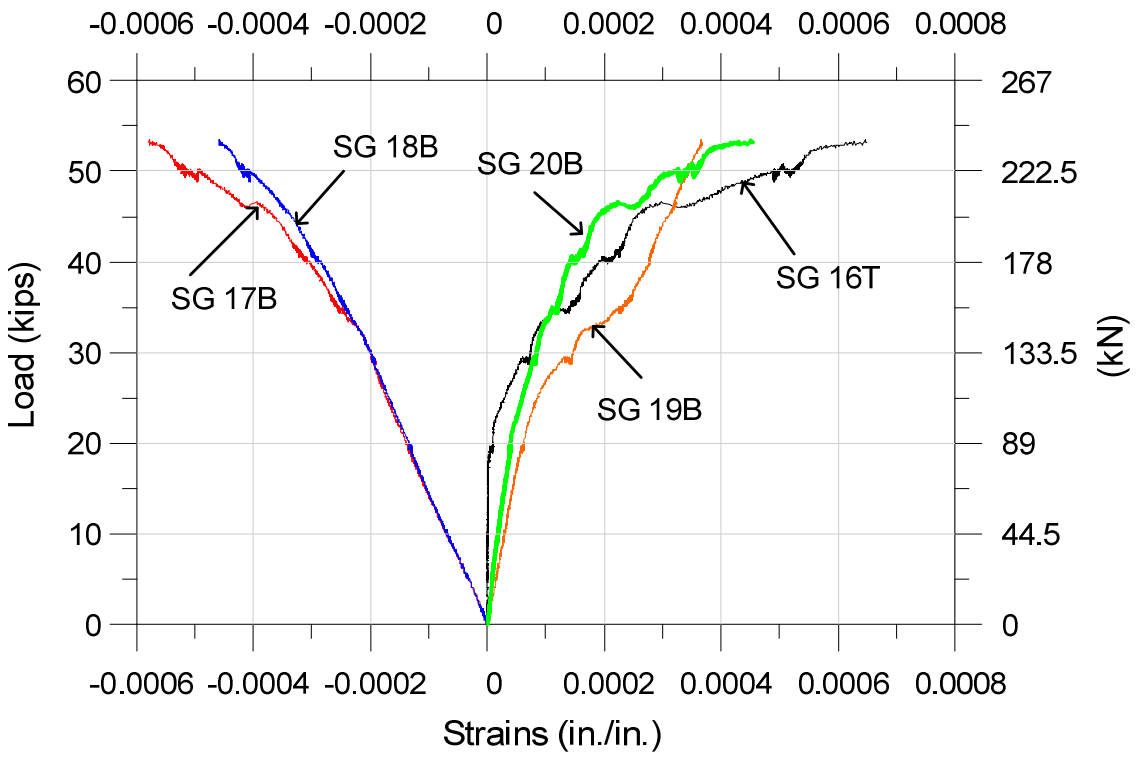

Figure 4.47 Reinforcing rebar strain for SFRC#1 specimen (strain gauge 16-20)

The reason that none of the bar yielded at peak load because failure occurred before full strength of the bars were used. However as the displacement was increased to 1.05 in. (27 mm) strain in 17B, 15T and 14T were greater than 2000 micro-strain indicating that respective bars reached their yield strain limit. Comparing to the STM, the reinforcement bar in SFRC was strained much less, indicating the higher force-resistance ability of fiber reinforced concrete. Considering fiber bridging effect, steel fibers were effective in transferring stress uniformly across the cross section of the beam. In the RC (specimen#1) the steel is effective in transferring stress, provided the crack occurs in the vicinity of the bar. Otherwise, it's likely that

since that there are large areas of plain concrete not confined by steel reinforcement, stress could not be transferred once the crack has occurred.

4.5 SFRC #2 (Specimen #3)

4.5.1 Specimen Geometry

SFRC#2 specimen had same dimensions and geometry as that of RC and SFRC#1 specimens. The main focus while deciding the layout of SFRC#2 specimen was on using minimum reinforcement and to reinforce only those critical regions cited from test results of SFRC#1 specimen (see **Figure 4.48**). The resulting reinforcement layout is shown in **Figure 4.50**. After analyzing the test results of SFRC#1 specimen it was clear that longitudinal reinforcement was critical and was required to restrict flexural crack. Also region near the corner of the windows were highly stressed.

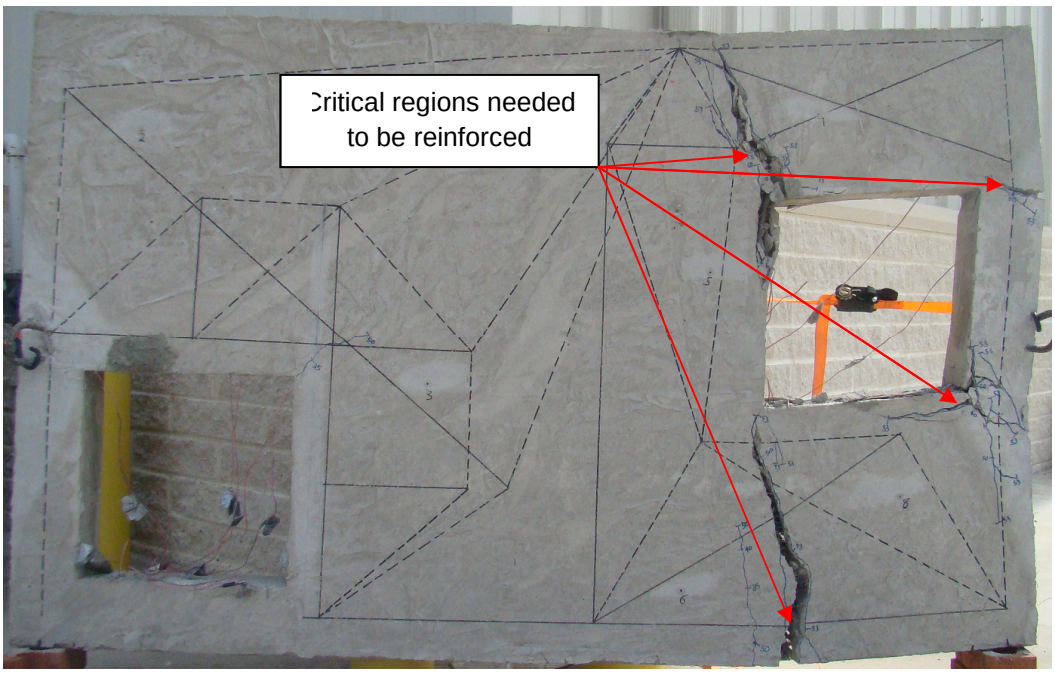

Figure 4.48 Critical regions considered for proposing reinforcement layout of SFRC#2 specimen

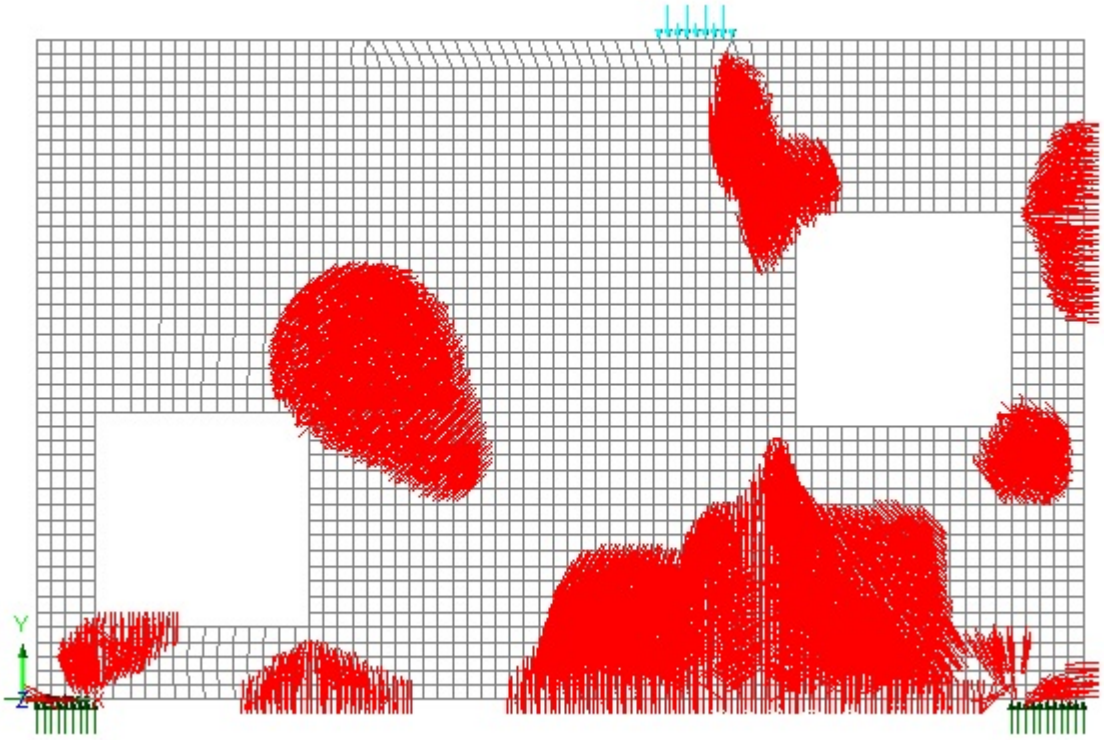

Figure 4.49 Cracking pattern result from elastic analysis done on LUSAS

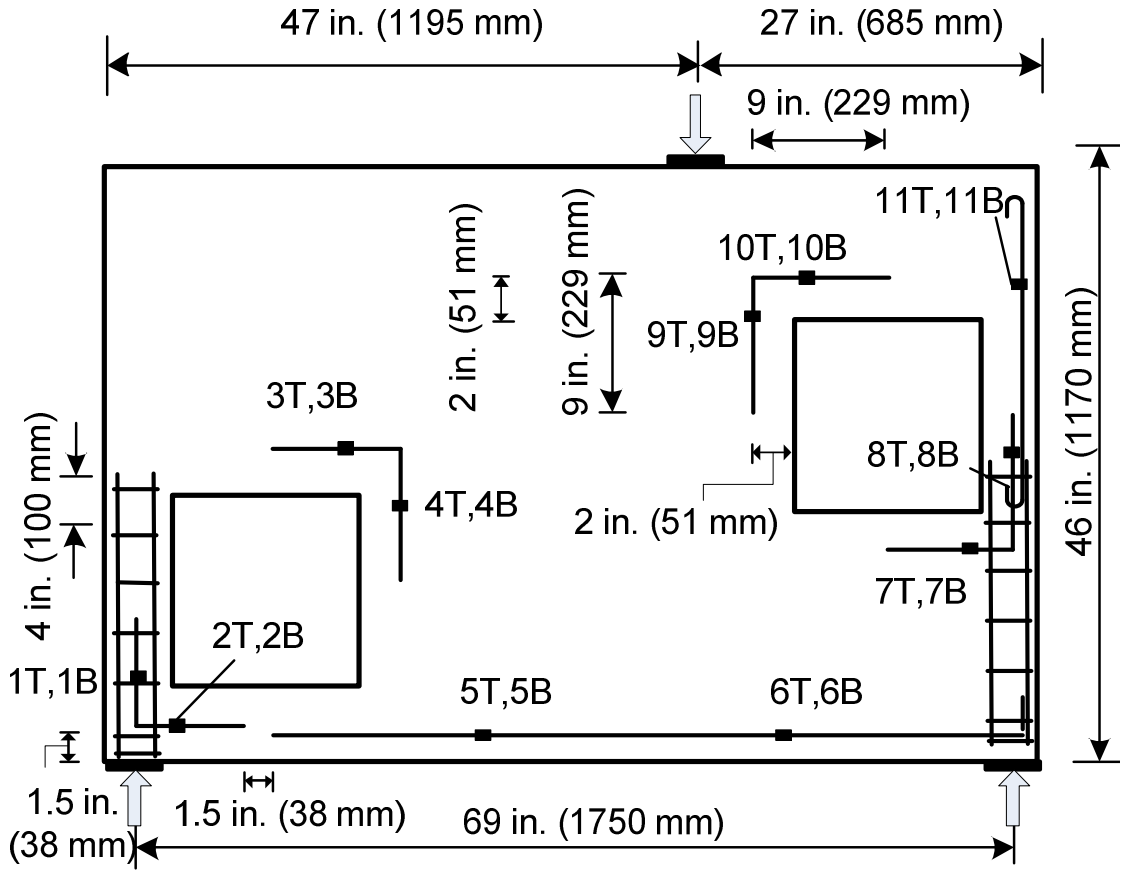

Figure 4.50 SFRC #2 specimen reinforcement layout (Numbers on the rebars indicate strain gauge numbers and letter indicating type of layer, “T”- top and “B”- bottom)

Among the few important modifications done in the reinforcement layout was the inclusion of longitudinal rebar (see **Figure 4.51**). This was done to delay the propagation of flexural cracking and hence increasing the ultimate load carrying capacity, clear cover was kept as 1 in. (25 mm). The longitudinal reinforcement was hooked to cage near the right support by a

90 degree hook and was terminated close to the mid span of the left window (see **Figure 4.51**), this was done in strict compliance to the strut-and-tie model which was adopted for this study. Also a vertical bar near right window extending from top of the beam to the end of the right window was included (see **Figure 4.51**). The reason because this bar was added was to stop the crack which originated along the thickness of beam in alignment to the top right corner of window (see **Figure 4.48**) as seen from the testing of SFRC#1 specimen. The clear cover for this bar was kept as 1 inch (25 mm) from extreme fiber of the beam in order to restrict the crack propagation at earlier stage.

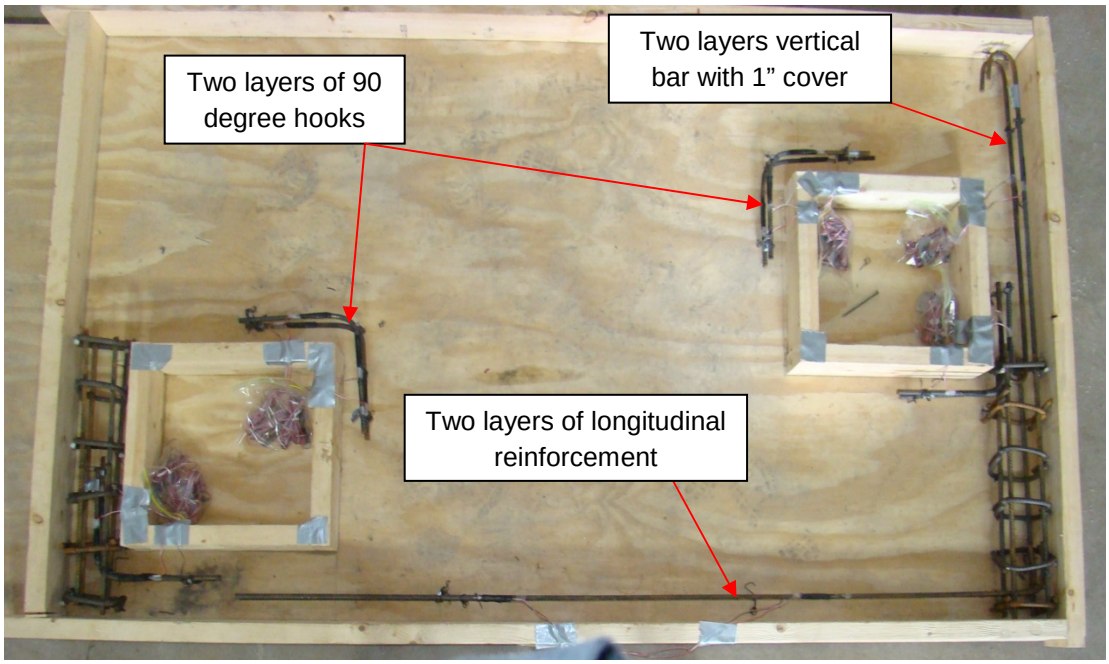

Figure 4.51 SFRC#2 specimen before casting

One more important modification was that only the corners of the windows along which load transfer occurs were reinforced with 90 degree bent hooks (see **Figure 4.52**). Clear cover (from centre of bar to form) was increased to 2 in. (50 mm), as from the testing result of SFRC#1 specimen it was seen that 1 in. (25 mm) cover was insufficient for fibers to penetrate during casting. In total 22 strain gages were used on top and bottom layers of reinforcement bars (see **Figure 4.50**).

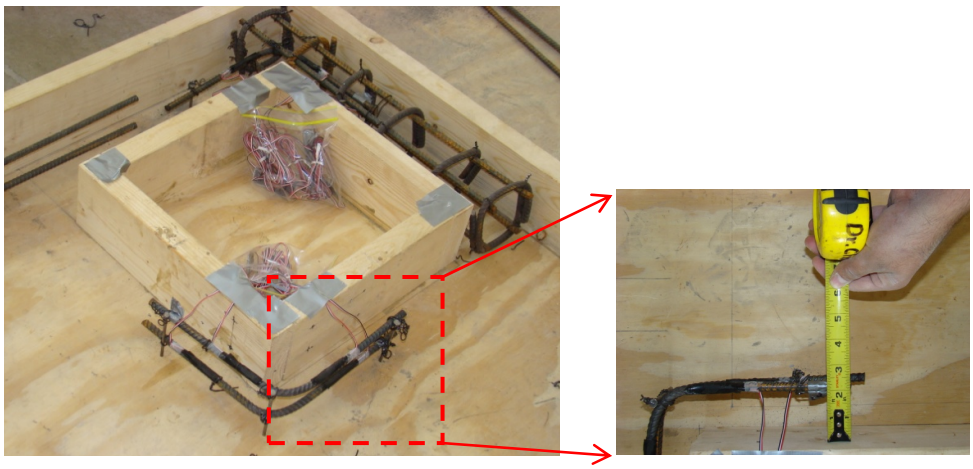

Figure 4.52 90 degree hooks used in SFRC #2 specimen

Also two cages one at each support was used to avoid any localized failure similar to earlier specimens. All reinforcement had two layers namely top and bottom layer. All bars were standard no 3 bars. Form work was oiled so that it could be easily demolded later, care was taken so as that the reinforcement bars do not come in contact with oil which otherwise would create bond issues.

Similar to the earlier specimens, four batches was prepared each with same ratio of materials; two batches were mixed in different mixers simultaneously. Fibers were added last

during casting in small quantities by hand to ensure that fibers are mixed properly. Same type and volume fraction of fibers were used in this specimen which was used for SFRC#1 specimen. The procedure used to consolidate was also kept same as used previously. Sample form each batch was carefully observed and fibers were found to be oriented in different direction conforming good mix (see **Figure 4.53**).

Figure 4.53 Close up of concrete mix for SFRC#2 specimen

Figure 4.54 SFRC#2 test specimen during placing and consolidation of plastic concrete

Figure 4.55 Finished SFRC#2 specimen and material specimens after casting

4.5.2 Test Results

4.5.2.1 Observed Cracking

Cracks were marked with blue marker on the front face and red on the back face to distinguish the two sides. Loading intervals were kept same as used previously i.e. 5 kips (22 kN). At each interval cracks were observed, marked and recorded. As expected, specimen developed more distributed cracks. Specimen developed several diagonal and flexural cracks up to failure point.

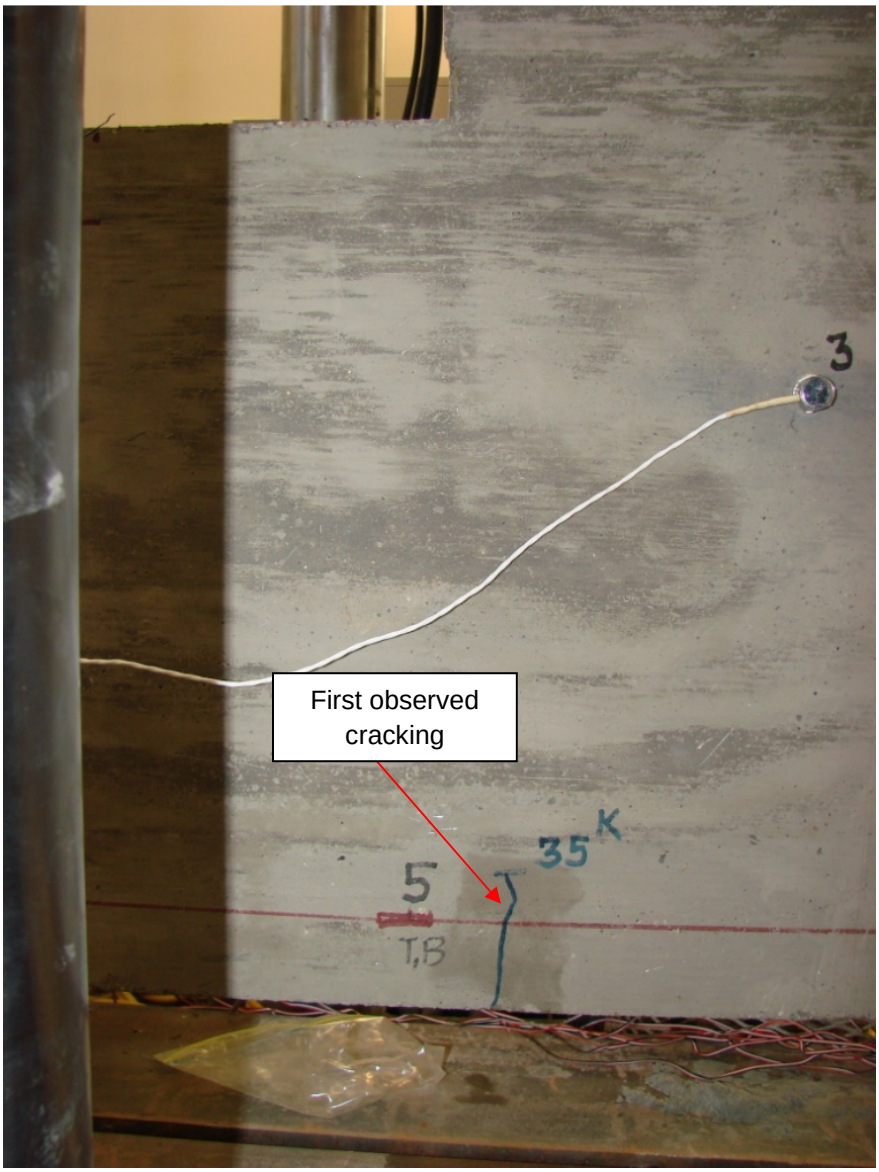

Figure 4.56 SFRC#2 specimen at 35 kips (156 kN) loading

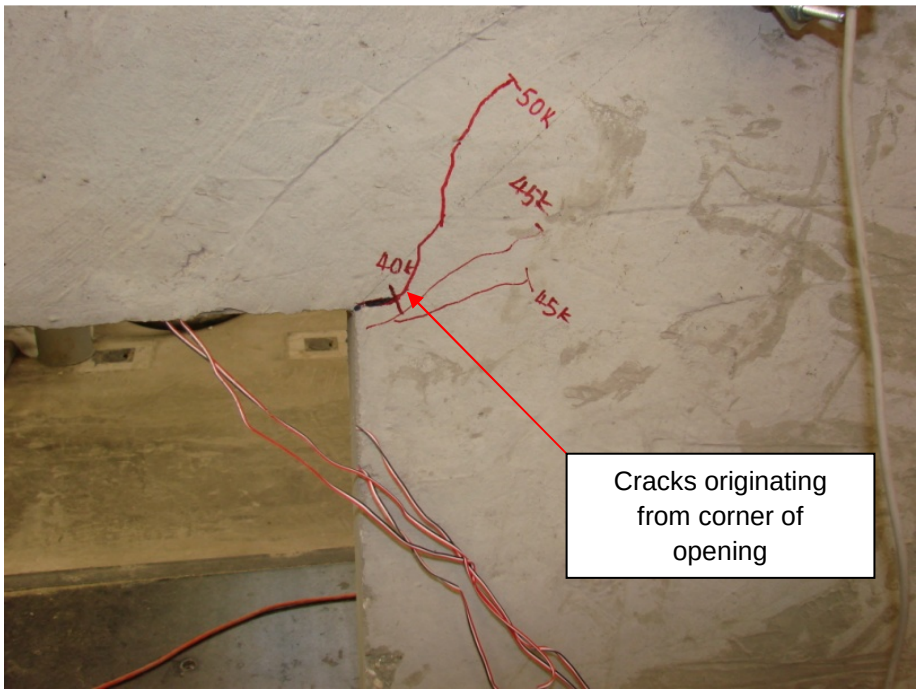

Figure 4.57 SFRC#2 specimen at 50 kips (222 kN) loading

There was no cracking observed till load step of 30 kips (133 kN). During the next load step i.e. at 35 kips (156 kN) first crack was observed, it was flexural crack originating from bottom fiber of the beam exactly below the loading point (see **Figure 4.56**) the width of crack observed was less than 0.004 in. (0.10 mm). Most diagonal cracks started around the opening at a load level of 40 kips (178 kN) and the maximum width of crack was 0.012 in. (0.3 mm). All diagonal cracks propagated further with the increase in magnitude of load levels. Beyond load level of 60 kips (267 kN), diagonal crack propagated horizontally towards load point due to width of compression block created at the top edge of the specimen near load point. At load level of 75 kips (334 kN), several flexural cracks were visible at the bottom fiber of the beam below the

loading point (see **Figure 4.58**) and the maximum width of crack was 0.03 in. (0.75 mm). Also at this stage there were several diagonal cracks seen along the mid height of the beam.

Figure 4.58 Flexural cracks in SFRC#2 specimen at 65 kips (289 kN) loading

Failure in the specimen was initiated by the loss of the portion of concrete located below the lower left opening. Concrete in the horizontal segment of these opening separated from the specimen because of the lack of continuity of bottom longitudinal reinforcement into the left support in the specimen, which led to the formation of crack at the termination point of the reinforcement at a load of approximately 80 kips (355 kN). This crack propagated throughout the entire 5 in. (125 mm) depth of concrete below the opening (see **Figure 4.59**). Also development

length of the 90 degree hooks was found to be insufficient as bond failure of these reinforcements was observed (see **Figure 4.61**). The diagonal crack running from below the loading point to the mid-height of the opening was wide open and fiber pullout was clearly visible (see **Figure 4.61**).

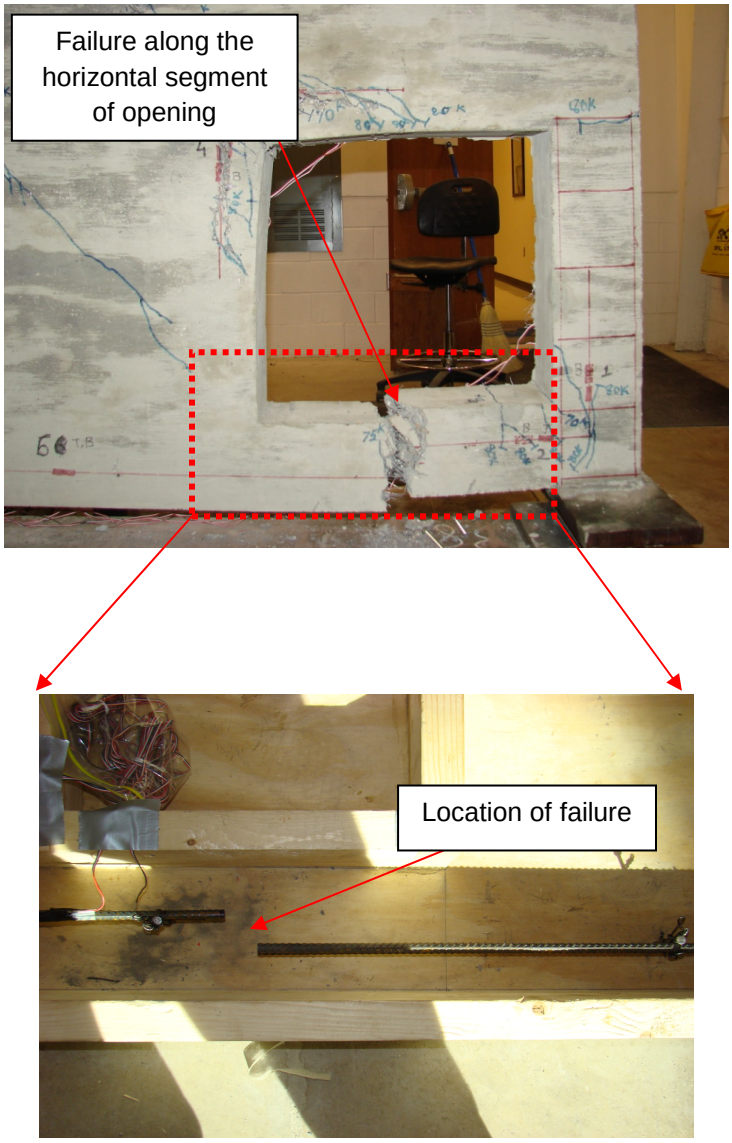

Figure 4.59 Failure along the horizontal segment of opening in SFRC #2 specimen at final stage

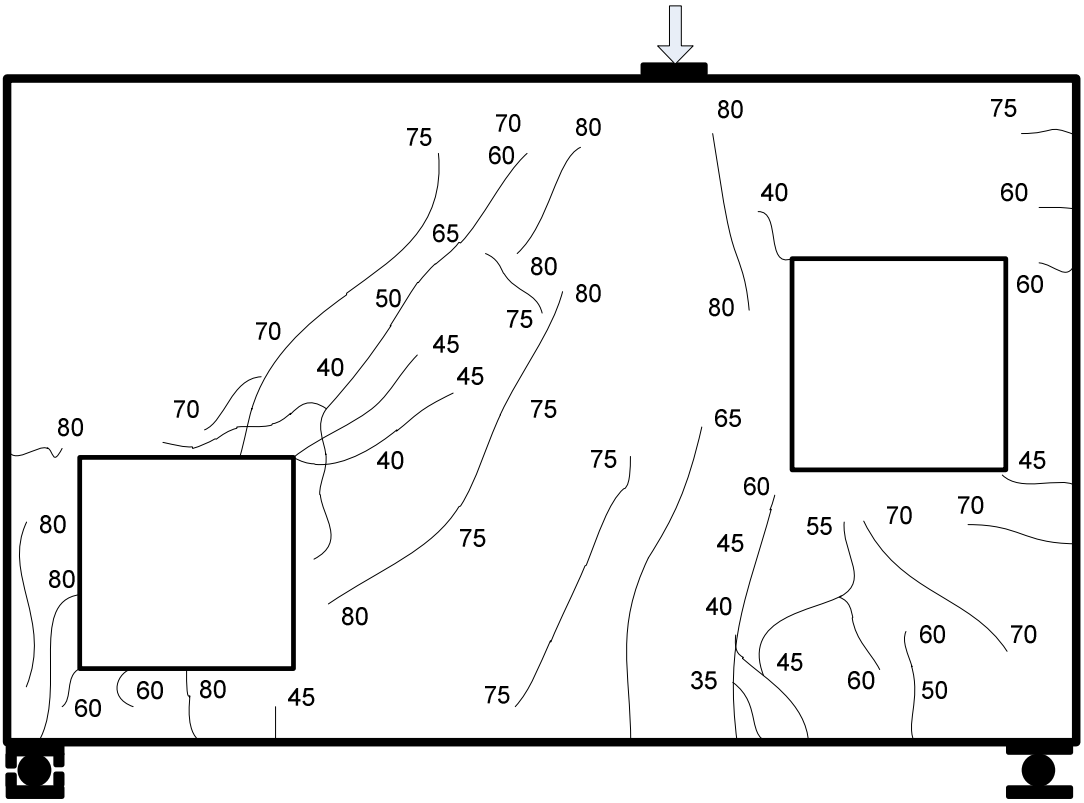

Figure 4.60 Overall cracking observed after testing of SFRC#2 specimen along front face (Numbers indicate load steps in kips)

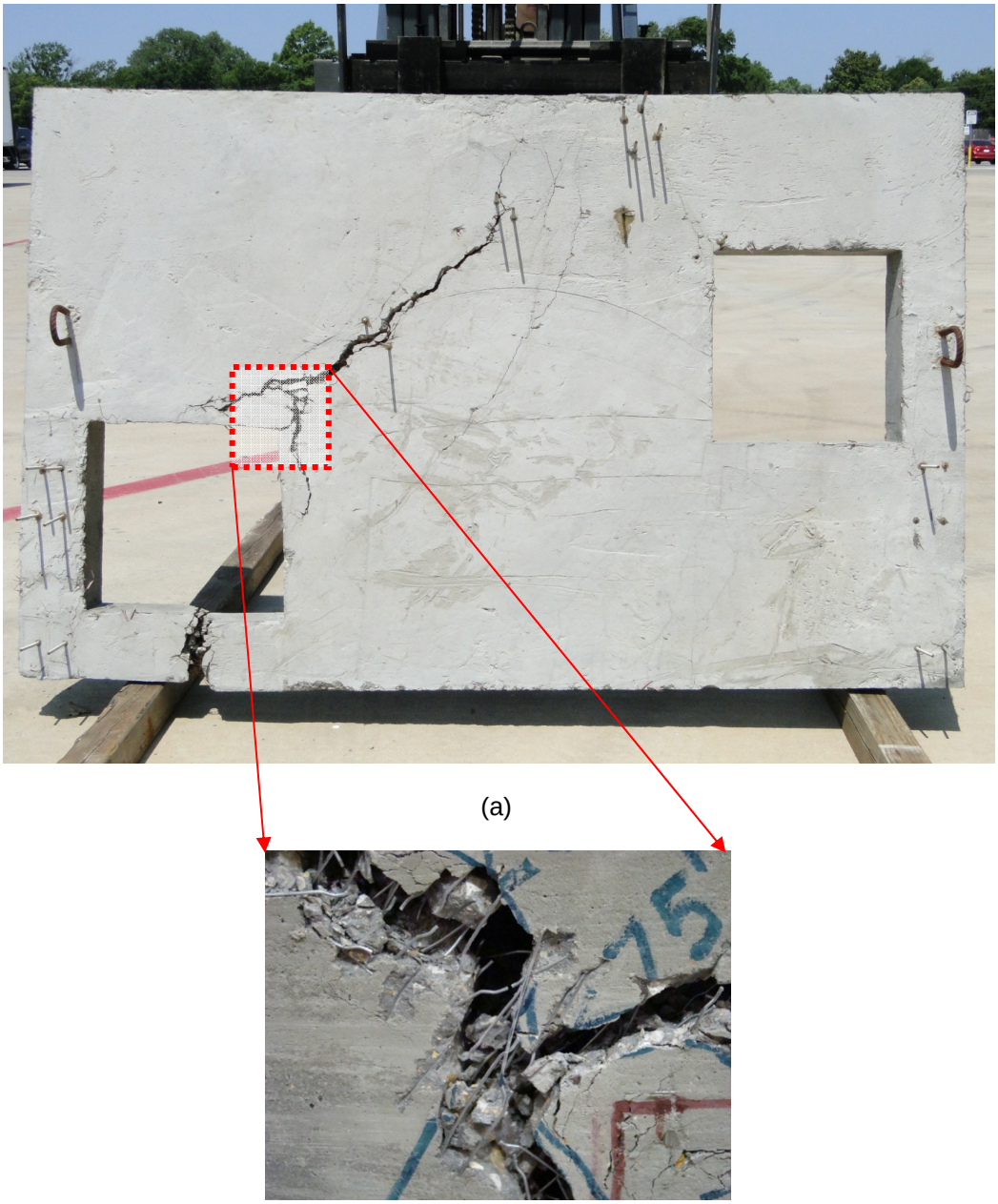

(a)

(b)

Figure 4.61 Mode of failure for SFRC#2 specimen (a) Overall state of specimen at failure stage (b) Fiber pull out and observed debonding

4.5.2.2 Load-Deflection Response

Failure of the specimen occurred at load much higher than those causing yielding of the main tie. The measured load-deflection response (see **Figure 4.62**) corresponds to the total applied load and the deflection measured under the load point. The load-displacement response showed nearly a linear behavior up to a load of 40 kips (178 kN). Since there were no major cracks observed between these loading stages, the specimen deformed proportionally to the load being applied. The SFRC #2 specimen exhibited higher displacement than the RC specimen indicating smaller elastic stiffness as compared to that of RC specimen.

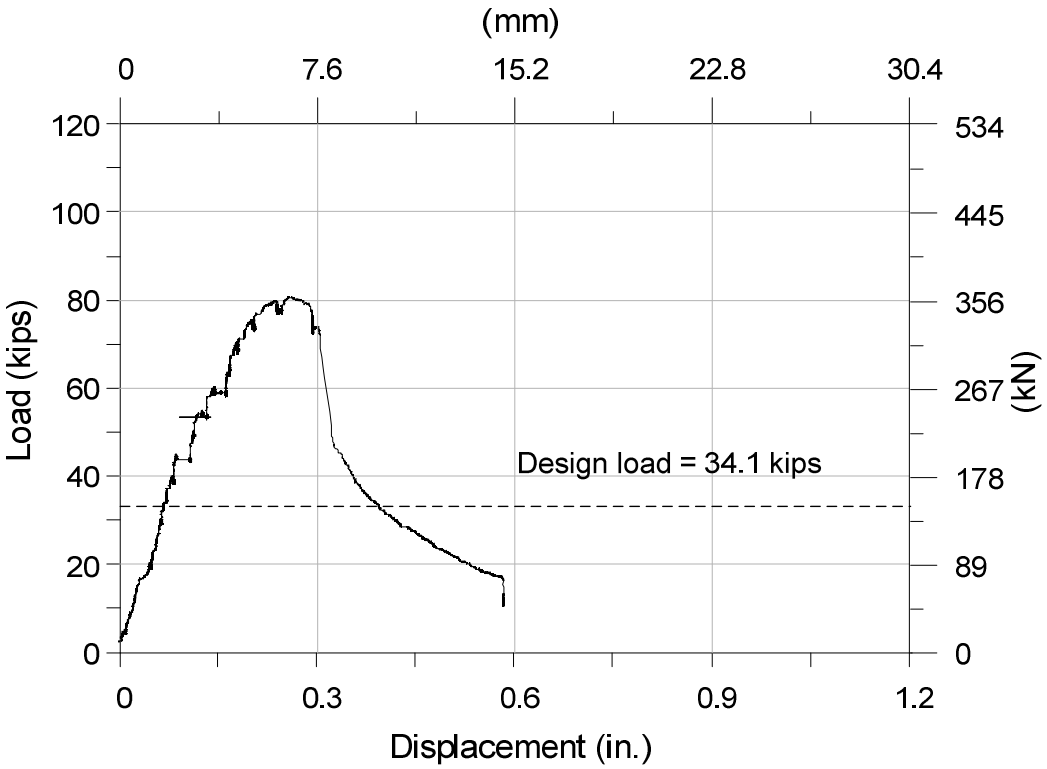

Figure 4.62 Load–Displacement response for SFRC#2 specimen

Departure from this linear portion occurred at a load of approximately 45 kips (200 kN), indicating specimen was cracked at various locations. However specimen reached a peak load of 80 kips (356 kN), which was more than twice the design capacity (see **Figure 4.63**) even though there were not much reinforcement used as per strut-and-tie model. SFRC specimens showed better post-peak falling branch (see **Figure 4.63**) as compared to the RC specimen indicating significant contribution of steel fibers in residual strengths of the SFRC specimens. Slightly greater displacement of the SFRC#2 specimen at the ascending branch was attributed to the local deformation near the opening.

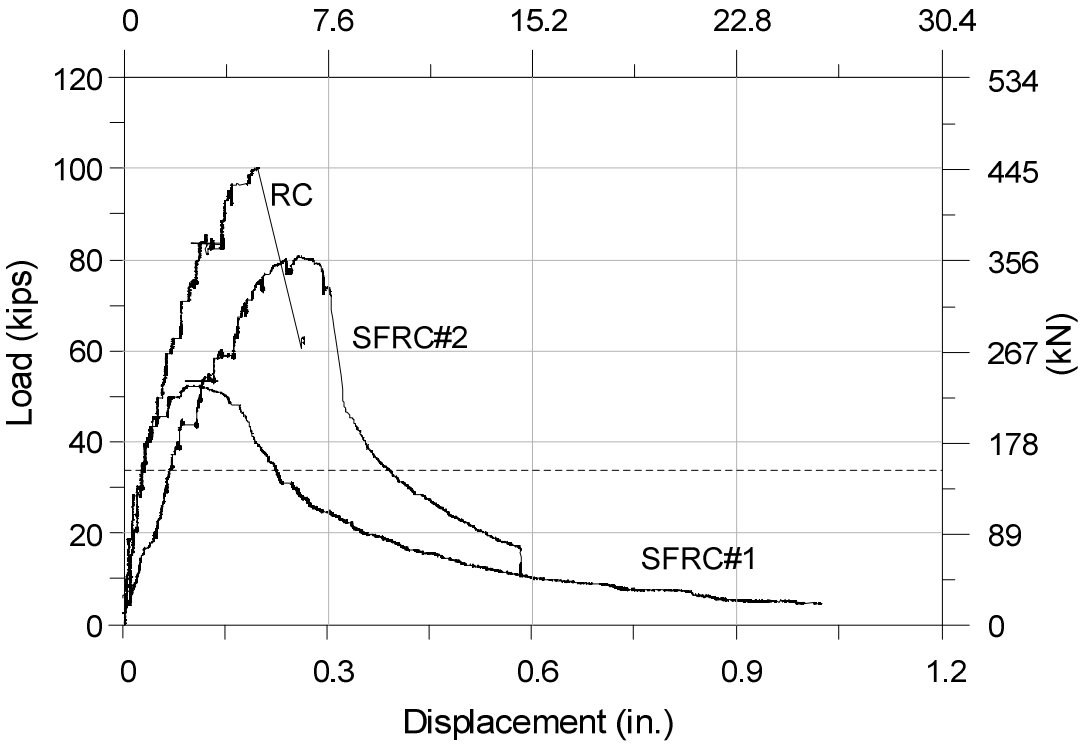

Figure 4.63 Load-Displacement response of RC, SFRC#1 and SFRC#2 specimens.

4.5.2.3 Concrete Strains

Four linear varying differential transformers (LVDTs) were installed on the surface of test specimen to measure the deformation of concrete during testing. LVDT 3 measured small deformation and the response was linear, however strain (deformation/gage length) measured at ultimate was 1.815×10^{-4} in./in. The response of the LVDTs 4 and 1 near support showed similar behavior, only difference was LVDT 1 was stretched (tension) and LVDT 4 was compressed (compression), however strains recorded at ultimate were -12.73×10^{-4} in./in. and 9.09×10^{-4} in./in. (-ve value indicating tension and positive compression).

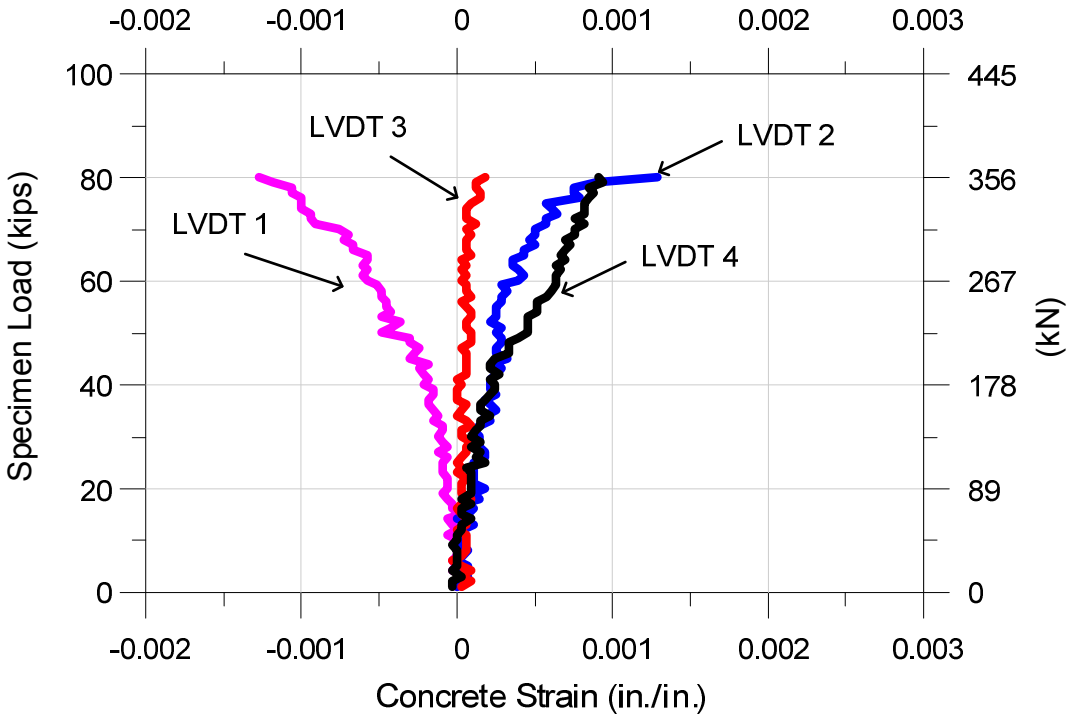

Figure 4.64 Concrete stains in SFRC #2 specimen (compression shown as positive, tension shown as negative)

4.5.2.4 Reinforcement Steel Strains

In total 22 strain gauges were used (for location see **Figure 4.50**). Figures 4.65, 4.66, 4.67, 4.68 show plot of strain vs specimen load, the numbers in the figure indicate strain gauge number and letters “T” and “B” are used for top and bottom layers respectively. None of the rebar yielded at the design load of 34.1 kips (152 kN), in fact the strain in the rebars were very low at this load. Strain in strain gauge number 1T, 1B, 4T, 10T, 3B, 8B and 9B were not recorded as they were damaged before testing. All the strain gauges showed linear behavior initially, and deviated from linear behavior as cracking started in the specimen. Strain gauge 6T and 6B were the first one to yield at 65 kips load, bars on top and bottom layers yielded at same time indicating both bars were carrying same force. Strain gauge 2B, 3T, 4B, 11T and 11B also reached their yield limit of 2000 micro strain as the specimen reached to its peak value.

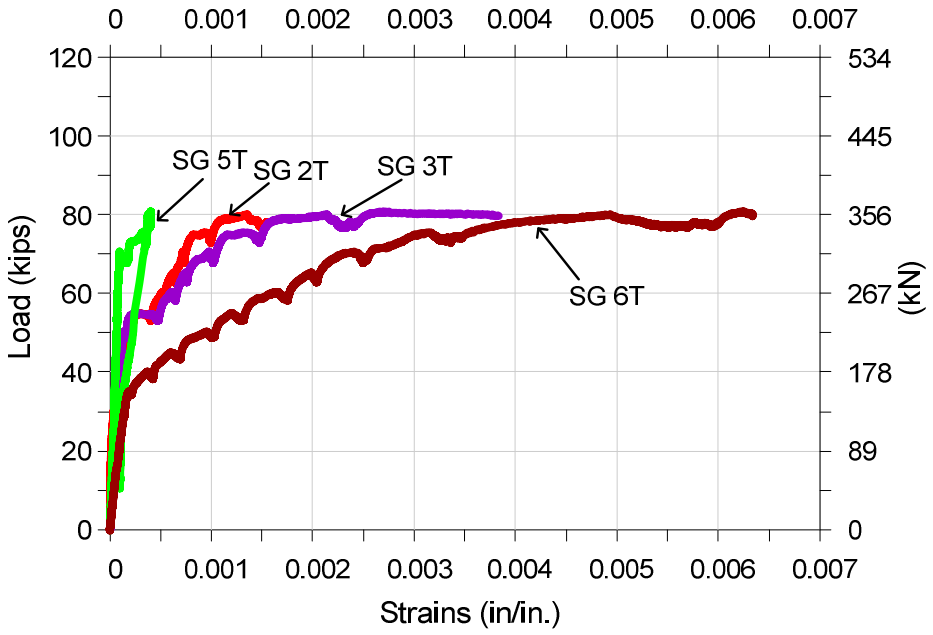

Figure 4.65 Reinforcing bar strain for SFRC #2 specimen (strain gauge 2T-6T)

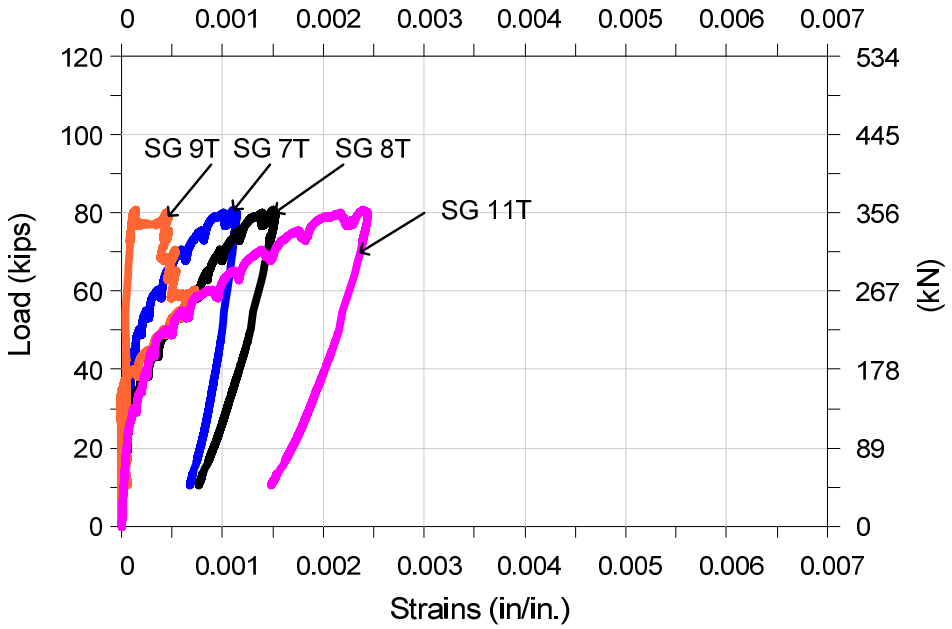

Figure 4.66 Reinforcing bar strain for SFRC #2 specimen (strain gauge 7T-11T)

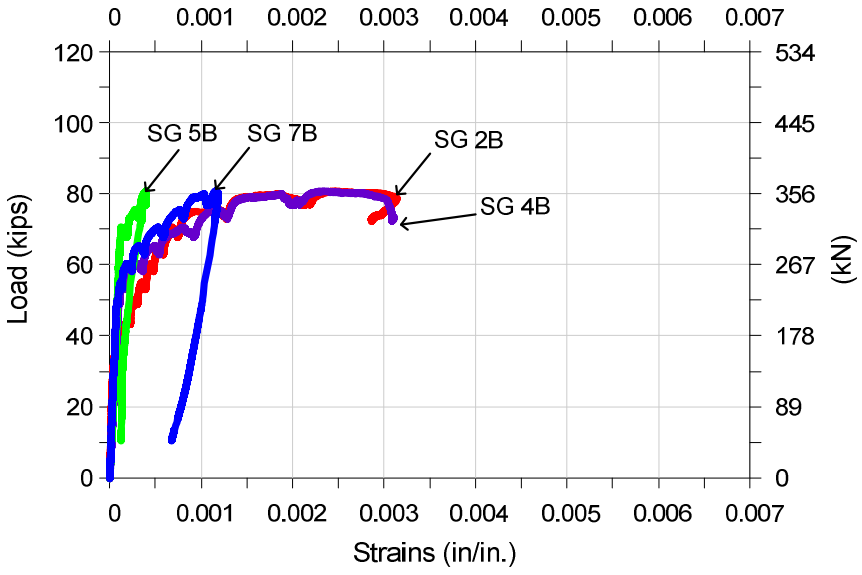

Figure 4.67 Reinforcing bar strain for SFRC #2 specimen (strain gauge 2B-7B)

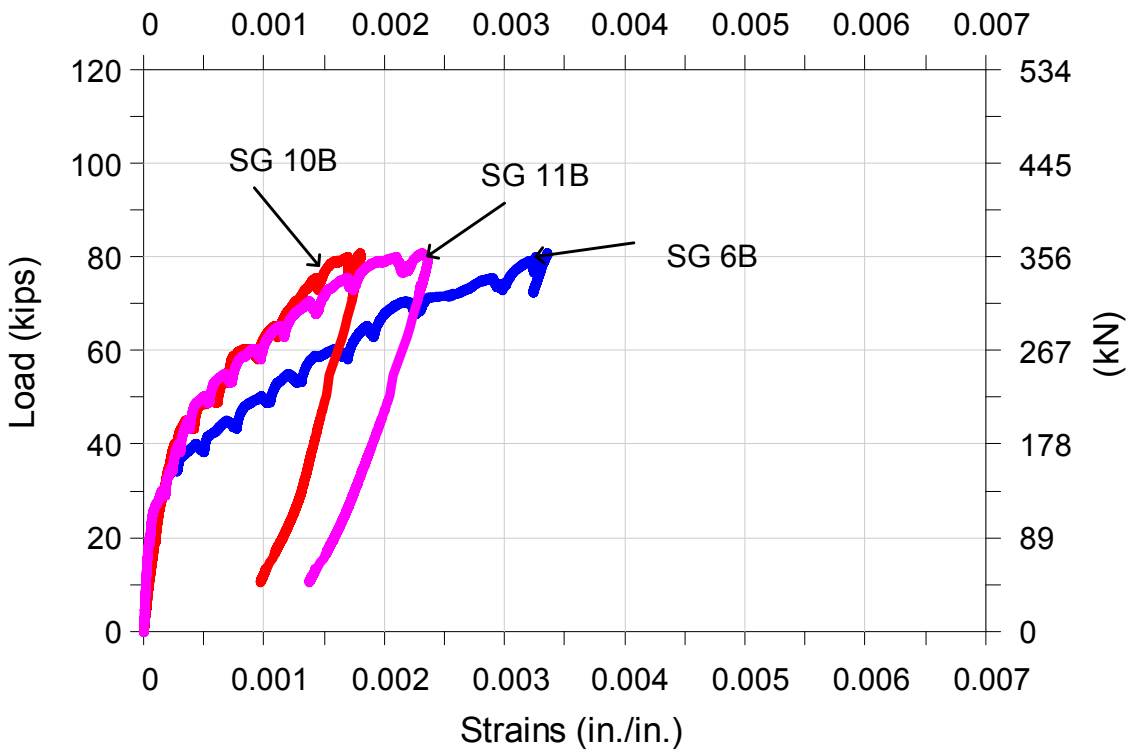

Figure 4.68 Reinforcing bar strain for SFRC #2 specimen (strain gauge 6B-11B)

4.6 SFRC#3 (Specimen #4)

4.6.1 Specimen Geometry

As mentioned earlier dimension and geometry for all the specimens were same. The chief intention while deciding the reinforcement layout for this specimen was on improve the performance based on addressing the issues cited from the testing of earlier specimens and also to minimize the amount of reinforcement steel used in order to avoid any complicated detailing.

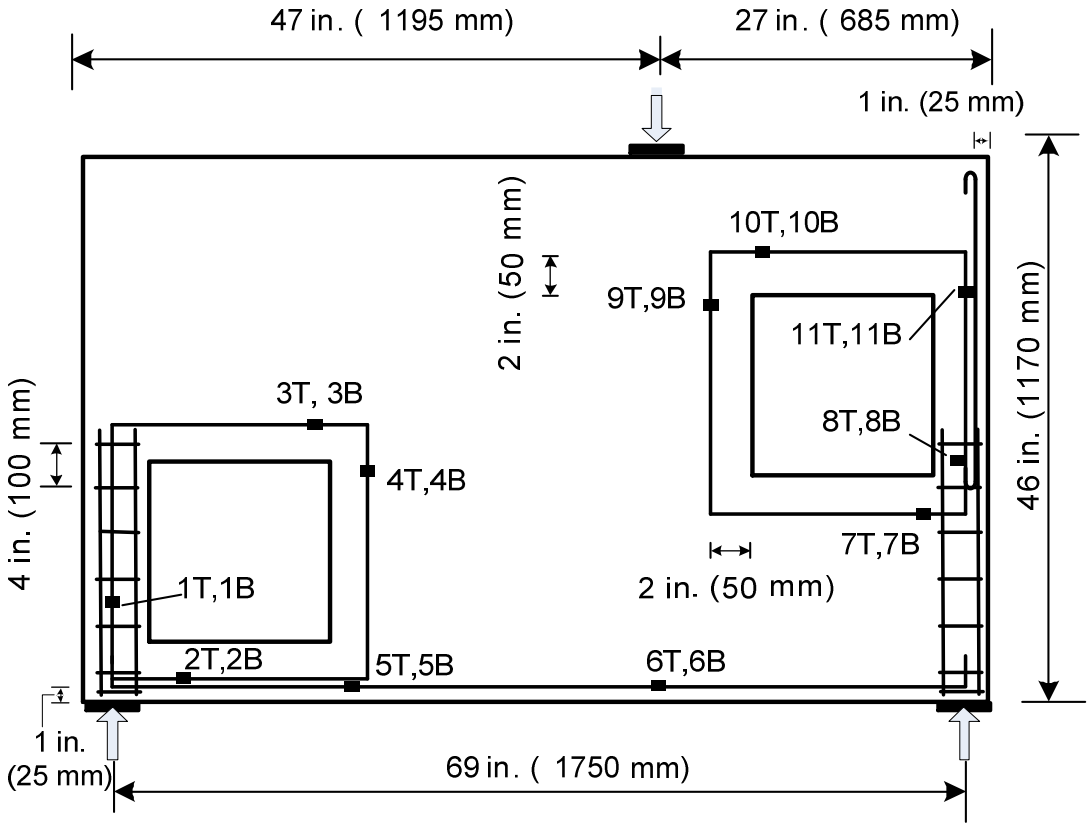

Figure 4.69 SFRC #3 specimen reinforcement layout (Numbers on the bar indicate strain gauge numbers)

The reinforcement layout for this specimen was basically a modification from the layouts of SFRC#1 and SFRC#2 specimens. Closed loops reinforcement used in SFRC #1 was used in this specimen but with clear cover of 2 in. (50 mm) from the sides of opening as compared to 1 in. (25 mm) used in SFRC#1 specimen (see **Figure 4.69**). This reinforcement configuration was mainly due to two reasons; closed loop layout was to avoid the bond failure observed in case of SFRC#2 specimen and increased cover to ensure that fibers pass through the given spacing while pouring concrete. A longitudinal reinforcement bar was placed at bottom and was hooked at both ends into the cages (see **Figure 4.69**). Also vertical reinforcement bar near the top right opening was used with clear cover of 1 in (25 mm) from bottom, top and sides. Two cages one

at each support were used to avoid support crushing. Also two hooks at to either ends of the specimen were used for lifting and placing purpose.

Total of 22 numbers of strain gauges were used in top and bottom layers combined (see **Figure 4.69**). The coordinates of the strain gauges on the top and bottom layer of reinforcement were kept same.

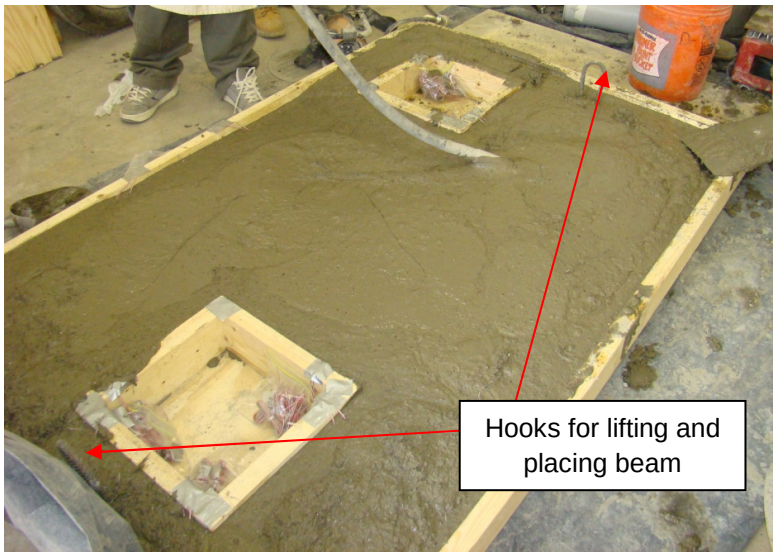

Figure 4.70 SFRC#3 specimen during placing and consolidation of plastic concrete

Four batches were prepared for mixing. Form work was oiled properly before casting so that it could be easily demolded later. From the test results of the previous beams it was seen that all of them were able to resist the design load of 34.1 kips (152 kN), so volume fraction of fiber used for this was reduced to 1% to see its effect on the load carrying capacity of the specimen.

4.6.2 Test Results

4.6.2.1 Observed Cracking

As expected steel fibers hindered the propagation and widening of cracks and also increased the number of cracks due to stress redistribution in the specimen as compared to the RC specimen**.** Initial cracking in the specimen occurred in the region of maximum elastic stress. First crack occurred at 35 kip (156 kN) and was a flexural crack. Loading steps were increased at an interval of 5kip (22 kN). Initially, vertical cracks were formed at the section corresponding to the point load and gradually developed into diagonal cracks that joined a diagonal crack emanating from the lower left corner of the right opening. At 60 kip (267 kN) there were several flexural cracks propagating towards the lower corner of the upper right opening. Also there were cracks propagating from top corner of the upper window towards the loading point reducing the depth of the compression zone (see **Figure 4.71**). At 60 kip (267 kN) loading minor crushing of concrete at right support was observed (see **Figure 4.72**).

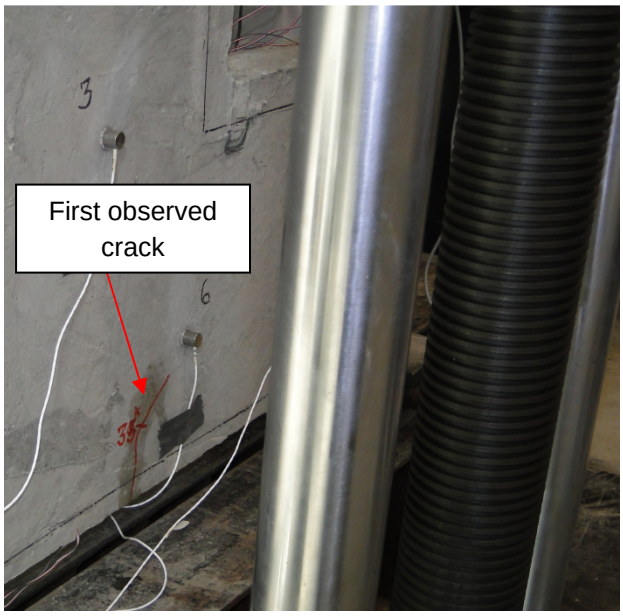

(a)

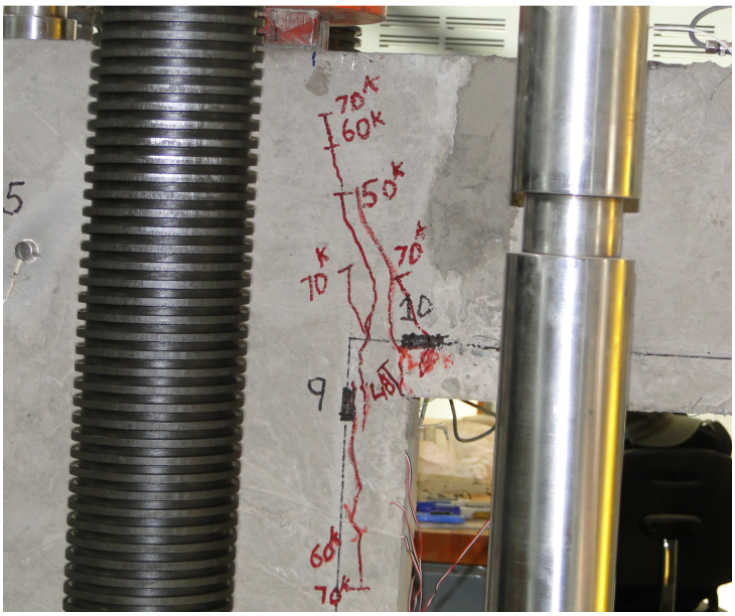

(b)

Figure 4.71 Observed cracking in SFRC#3 specimen (a) First observed crack (b) Diagonal cracks propagating from top left corner of window

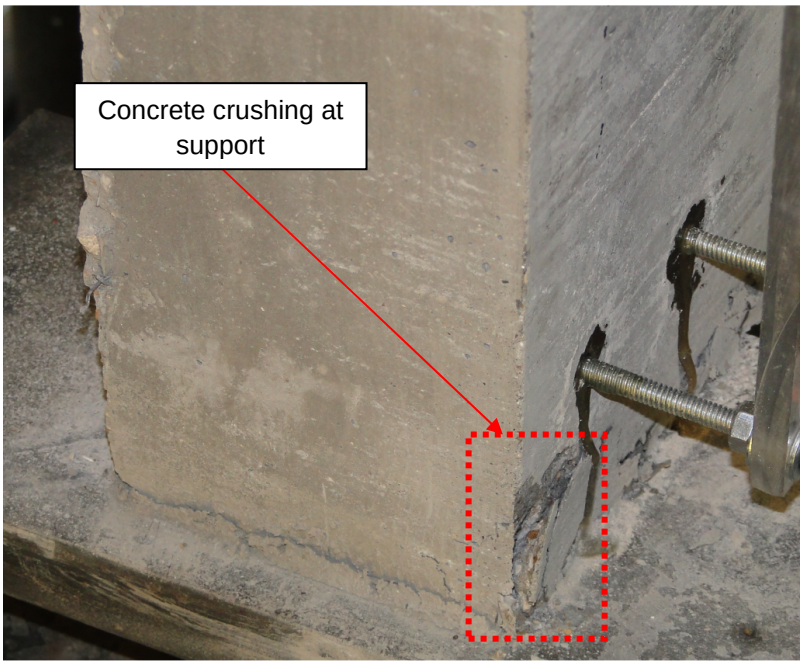

Figure 4.72 Concrete crushing at support in SFRC#3 specimen

Once the loading reached 80 kips (356 kN) there were sever cracking observed, existing cracks below the loading point started propagating towards loading point. Also there were several cracks along the vertical segment of the top right opening originating along the thickness (see **Figure 4.73**), vertical bar adjacent to the opening arrested these cracks and helped in delaying their propagation (see **Figure 4.73**).

The failure occurred at 87 kips (387 kN) due to excessive flexural cracking. At this stage the beam was not taking any load, but due to the presence of fibers it showed a ductile behavior and reached a deflection of 1.6 in. (41 mm). Testing was stopped at this deflection as beam seemed unstable, also cracks were wide open and fiber pull out was clearly visible. The right window seemed to be deformed due to formation of plastic hinges.

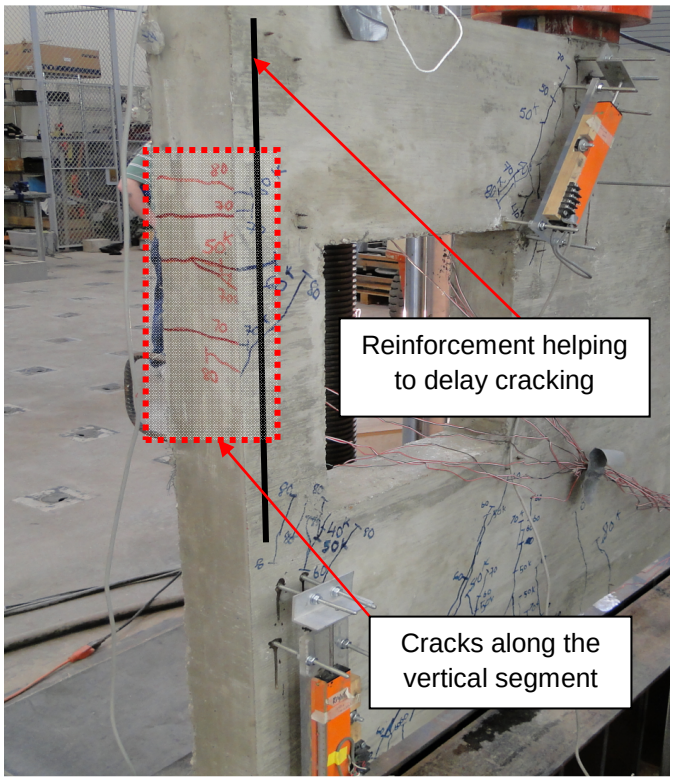

Figure 4.73 Cracking along the vertical segment at 80 kips (356 kN) loading in SFRC#3 specimen

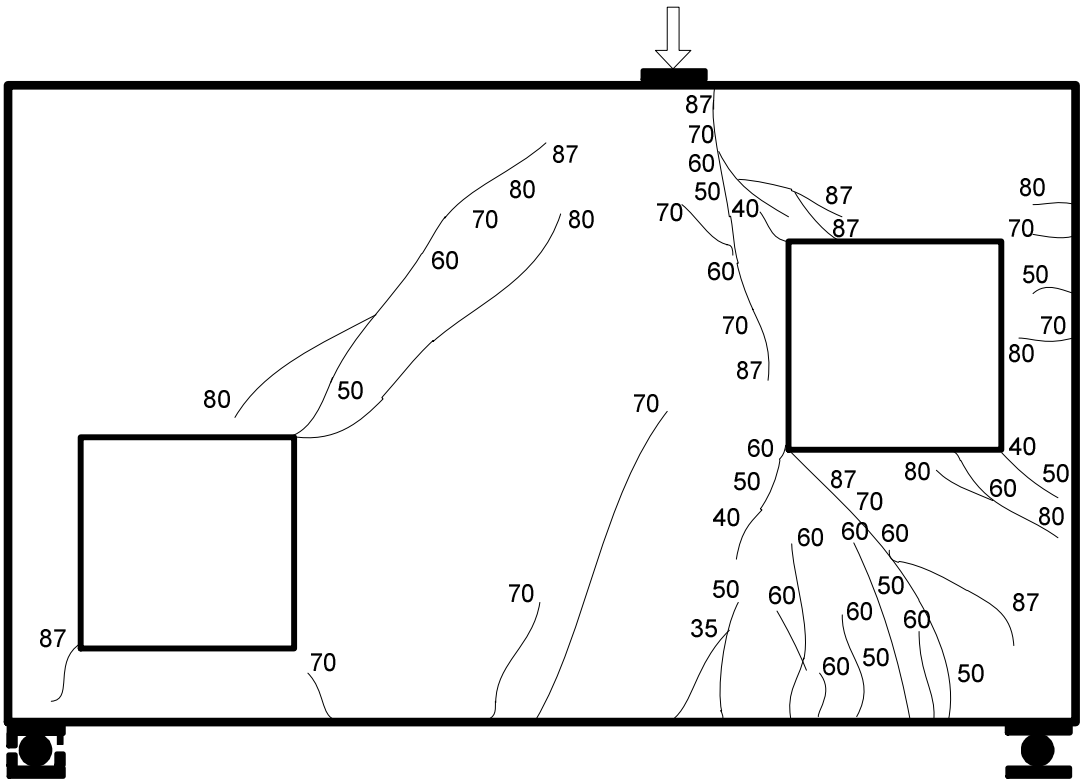

Figure 4.74 Overall cracking observed after testing of SFRC#3 specimen along front face (Numbers indicate load steps in kips)

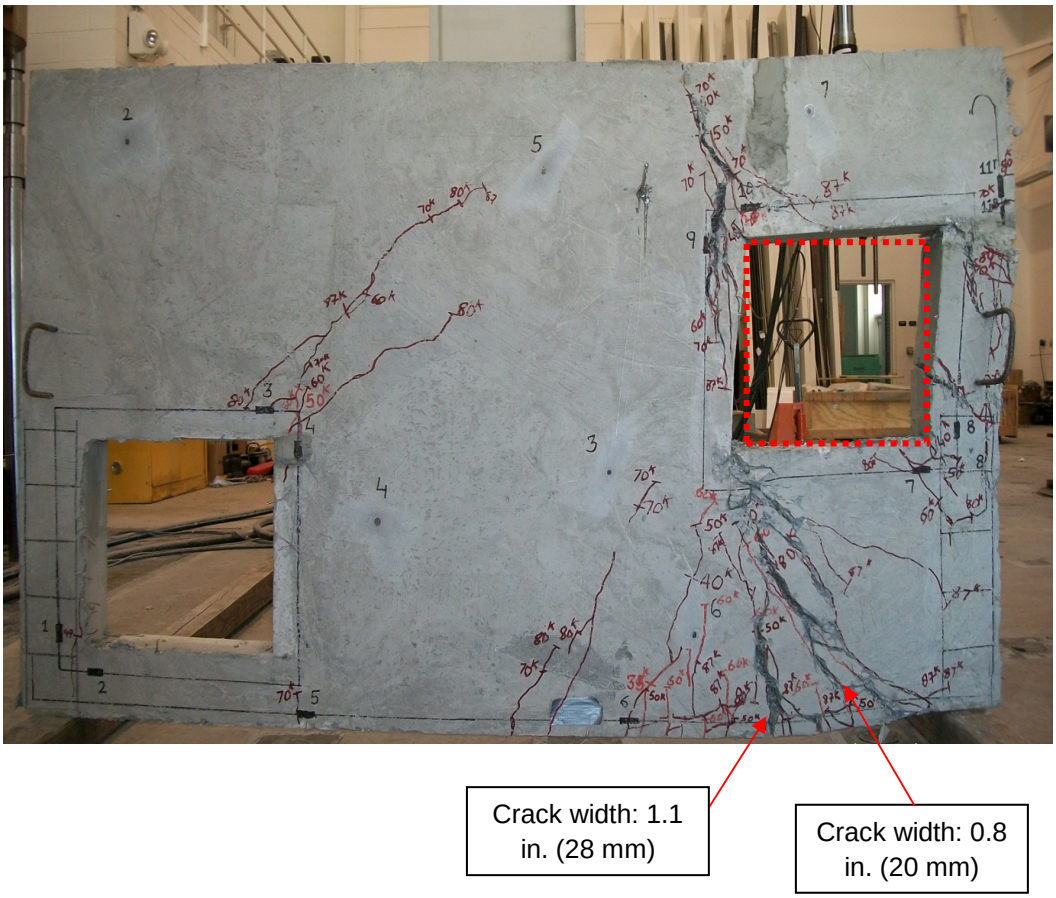

Figure 4.75 Overall state of SFRC#3 specimen after testing

4.6.2.2 Load-Deflection Response

As shown in **Figure 4.76** the load-displacement response of specimen was nearly linear up to a peak load of 87 kips (387 kN), which was more than 2.5 times the design load of 34.1 kips (152 kN). It should be noted that even though there were almost no steel reinforcement bars (except the longitudinal bars at the bottom, vertical bar near right top opening, steel cage at supports and bars around the opening) used as per STM, specimen reached more than 2.5 times the design load of the RC specimen. Further, it showed very gradual post-peak descending branch in the load-displacement response even without steel reinforcing bars, indicating significant contribution of steel fibers to the residual strength of the specimen. The boundary elements and steel reinforcement bars used to reinforce certain critical locations helped the specimen to achieve the design strength without premature local crushing and excessive cracking of concrete in addition to the sufficient residual strength. There is a sudden drop in the curve when deflection reaches 1.0 in. (25 mm), this was because at this stage crack were wide open, and as a result there was sudden decrease in load carried by the beam. However loading was further increased manually and was stopped at 1.6 in. (40 mm) deflection as the beam seemed unstable due to excessive deformation.

The load-displacement behaviors of all test specimens are compared in **Figure 4.77**. From the figure it's seen that initial stiffness of RC and SFRC#1 specimen is nearly equal, also stiffness of SFRC#2 and SFRC#3 was nearly equal to each other. The reason stiffness differ between these two pairs of specimens was attributed to the local deformation near the opening which affects the load deflection response because of the way it was measured. However it's important to note that unlike RC specimen deflection-hardening response was noticed for all SFRC specimens after peak strength was reached, followed by a gradual post-peak descending branch. This ductile behavior indicated a plastic redistribution of internal forces due to the addition of steel fibers and also due to the presence of reinforcing bars at certain critical locations which acted as ductile links.

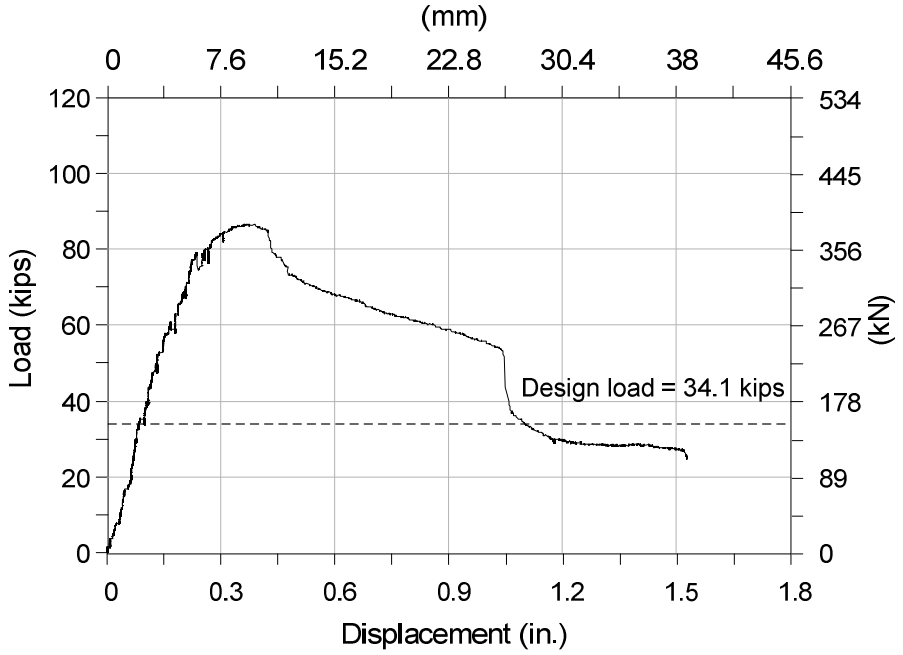

Figure 4.76 Load-deflection curve for SFRC#3 specimen

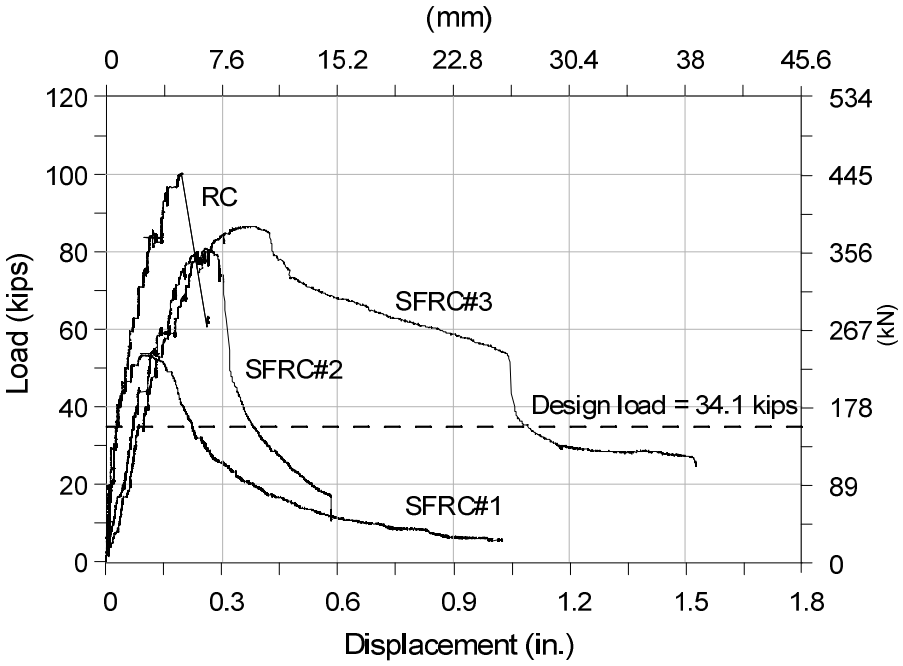

Figure 4.77 Load-deflection curves for all specimens

4.6.2.3 Concrete Strains

In total four LVDTs were installed to measure concrete strain, two at supports measuring strain in vertical direction and two in inclined direction pointing towards loading point. The inclined LVDTs measured the deformations on the axis with the compressive struts from the loading point. The response of LVDTs 1, 2, 3 was linear and strains (deformation/gage length) were measured as 1.215×10^{-4}, 12.89×10^{-4}, 1.515×10^{-4} at ultimate respectively (see **Figure 4.78**). Strain in LVDT 2 increased suddenly after 80 kips loading, this was because there was sever cracking at right corner of top right window. As the loading was increased further these cracks increased its width due to which top right opening appeared to be deformed, as a result the LVDT near the opening stretched. Also concrete near left support compressed significantly more after 40 kips (178 kN) and strain (deformation/gage length) recorded at ultimate was 9.392×10^{-4}.

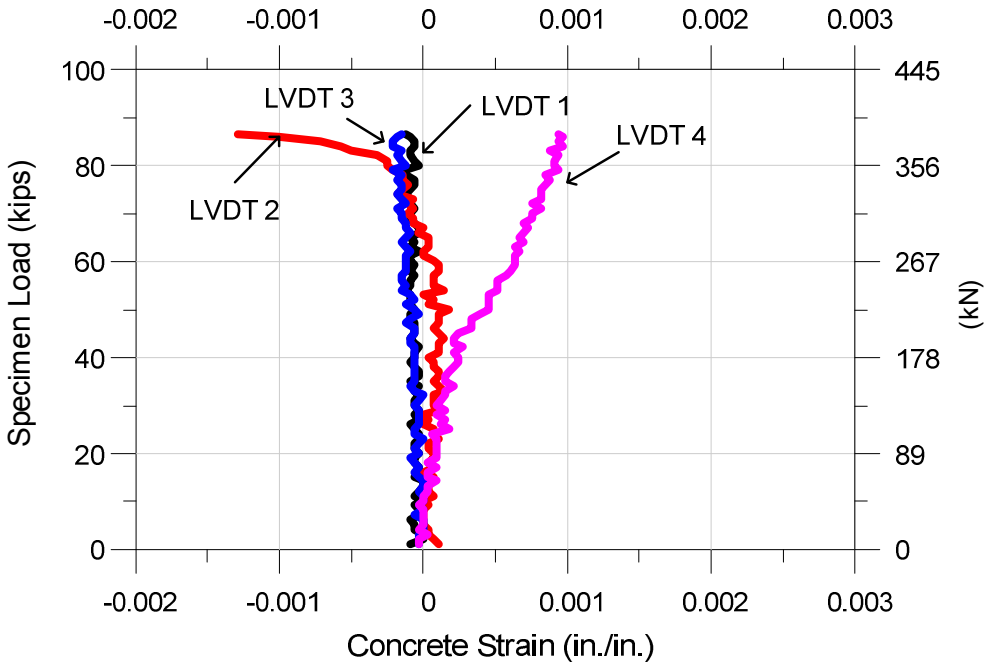

Figure 4.78 Plot of graph showing concrete stains in SFRC#3 specimen (compression shown as positive, tension shown as negative)

4.6.2.4 Reinforcing Steel Strain

The magnitude of strain in the reinforcement bar was determined by using uniaxial strain gauges installed on the surface of bars. In total 22 strain gauges were used, **Figure 4.69** shows the location of strain gauges (numbers in the figure). As there were two layer of reinforcement used, one strain gauge was installed in each layer; hence there were two strain gauges at a particular location. Stain in strain gauge number 1T, 3B and 8B were not recorded as they were damaged prior to testing.

Strains in almost all the strain gauges were linear up to 20 kips (89 kN). Strain gauge number 6T and 6B showed deviation from its linear behavior from 30 kips (133 kN) and started increasing linearly thereafter. This was because first crack appeared at this loading and propagated along same location where strain gauge was installed hence it experienced an exponential increase, however strain recorded at ultimate was 0.0035 in./in. Strain in 11B increased significantly after 80 kips (356 kN) loading and was recorded as 0.0158 in./in. at ultimate, this was because cracks along the vertical segment of top right opening was propagating towards extreme fiber of the beam resulting in increasing strain in the vertical bar placed next to the opening. Strain recorded at ultimate load in strain gauges 2T, 2B, 4T, 4B and 1B were very less and were 0.00021 in./in. , 0.000407 in./in. , 0.00053 in./in. , 0.00055 in./in. , 0.00009 in./in respectively.

Strain in 6T, 6B, 11T, 11B and 9B reached its yield limit of 2000 micro strains; however strain in all the other strain gauges were below this value. It's important to note that most reinforcing bars deformed the same amount at the same location which can be justified by looking at the strain gauge pair 5T, 5B and 6B, 6T which have nearly identical curves (see **Figures 4.79, 4.81**). However this is not the same for all the strain gage pairs such as 2T and 2B. This phenomenon is attributed to unequal force sharing by the reinforcing bars.

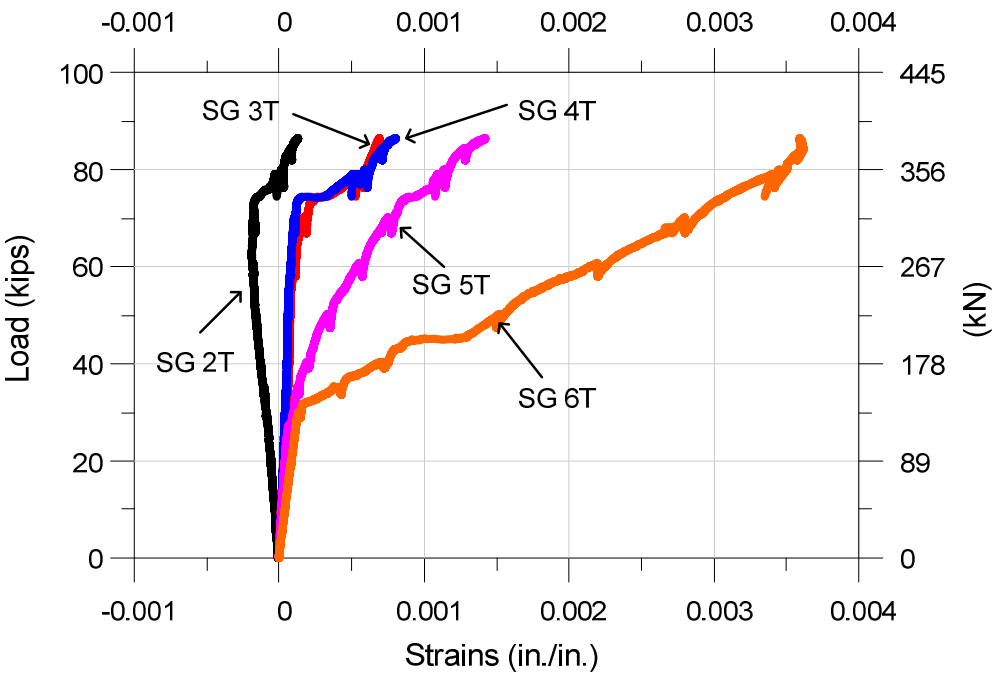

Figure 4.79 Reinforcing bar strain for SFRC #3 specimen (strain gauge 2T-6T)

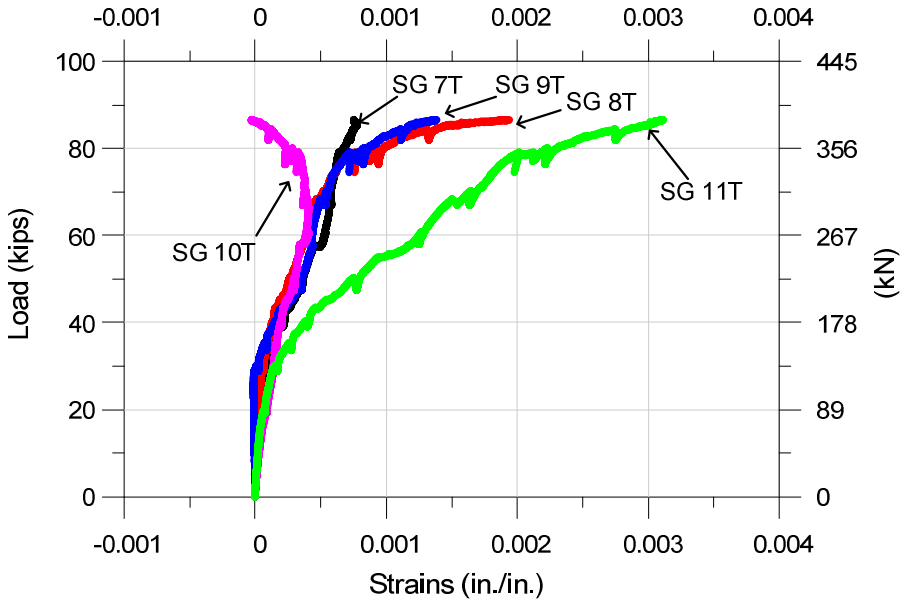

Figure 4.80 Reinforcing bar strain for SFRC#3 specimen (strain gauge 7T-11T)

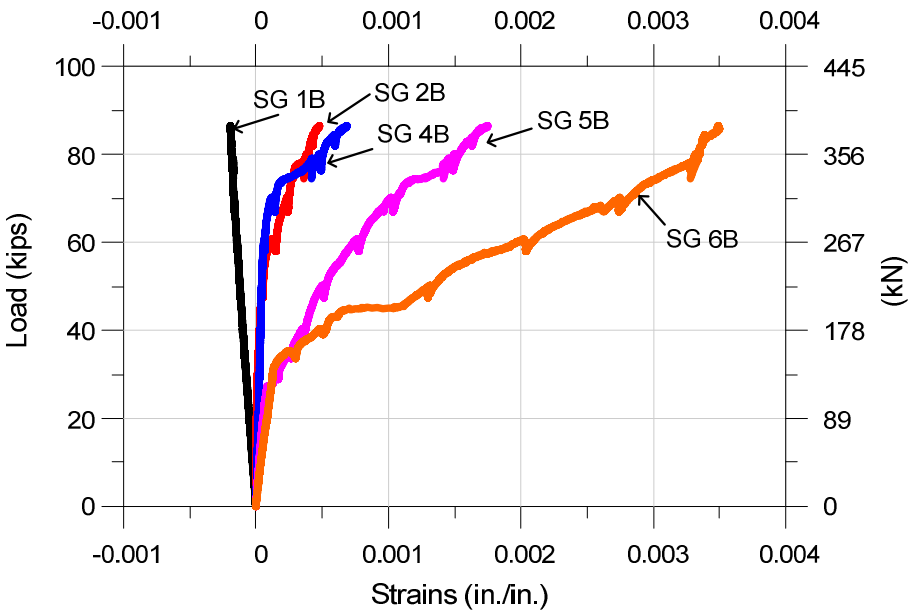

Figure 4.81 Reinforcing bar strain for SFRC#3 specimen (strain gauge 1B-6B)

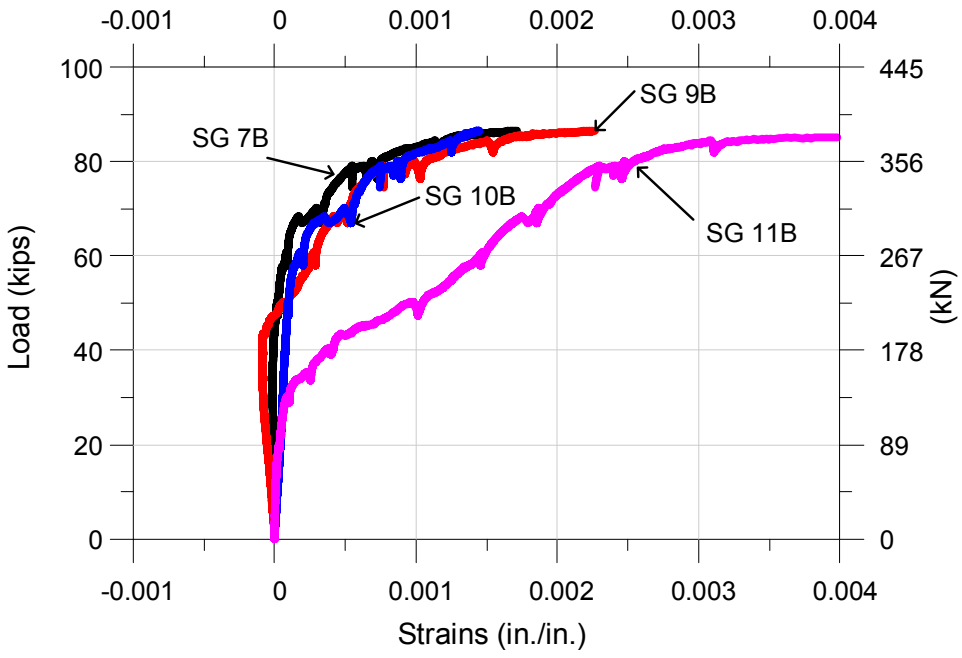

Figure 4.82 Reinforcing bar strain for SFRC#3 specimen (strain gauge 7B-11B)

4.7 Acoustic Emission Results

The propagation of crack in test specimens under the applied load was monitored by a non-destructive evaluation through acoustic emission (AE) technique. As discussed earlier in this study, a total of seven AE sensors were mounted on the concrete surface of test specimens using special glue. Each sensor had a radius of influence of 30 in. (750 mm). The location of an event (micro-cracking) inside the specimen is captured by three sensors using the principle of triangulation. Based on the measured time elapsed and the distance between two consecutive sensors for an event, the shear wave velocity for SFRC specimens was estimated as 1.1×10^5 in/s (2795 m/s). It is important to note that due to limited number of sensors available for testing location of these sensors were strategically decided to capture the activity in critical regions. It is due to the same reason that no activity was recorded at certain location in the specimens due to absence of sensors.

From the Acoustic Emission results it was revealed where the strain energy was released relative to the location of the test specimens. Time-versus-hits were synchronized with loading increments to determine the specific time when energy was released within the specimen. Because of the opening on the specimen AE was less effective between the piezoelectric sensors and concrete mass in the direction of the void by the opening. The width of compressive strut formed in the RC specimen was smaller as compared to that in the SFRC specimens (see Figure 3-87 and 3-88), indicating that the SFRC specimens dissipated energy over a wider area. It was observed that all the specimens dissipated almost equal amount of energy, however RC specimen dissipated energy through a large single crack propagation and due to the yielding of reinforcing bars. In contrast, the SFRC specimens dissipated energy through multiple fine cracks that branched out in random directions. This was because steel fibers served as a “link” that enabled the forces to be redistributed from one area to the next. This feature of steel fibers overcomes the weak tensile strength and the brittle nature of plain concrete. Furthermore, the cracking due to splitting of concrete compressive strut could be

delayed due to the superior tensile behavior of SFRC. To conclude, the SFRC specimens showed better crack distribution and smaller crack width as compared to the RC specimen. The coordinates of each sensor are given in **Table 4.3** to **4.5**. Following figures shows the location of AE sensors and activity recorded by them at various loading stages for all the tested specimens.

Table 4.3 Location of AE sensor on the surface of RC and SFRC#1 specimen

Sensor No	Coordinates	
	X (in.)	Y (in.)
1	8.25	8.5
2	29.25	26.25
3	39.5	6.25
4	49.5	17.5
5	48.25	40.0
6	56.75	6.25
7	63.75	34.25

Table 4.4 Location of AE sensor on the surface of SFRC#2 specimen

Sensor No	Coordinates	
	X (in.)	Y (in.)
1	2.25	3.5
2	2.75	32.75
3	1.25	17.75
4	39.75	8.0
5	33.25	41.0
6	16.0	2.0
7	3.0	34.25

Table 4.5 Location of AE sensor on the surface of SFRC#3 specimen

Sensor No	Coordinates	
	X (in.)	Y (in.)
1	8.25	5.5
2	45.25	28.25
3	28.25	31.50
4	40.12	7.75
5	51.75	39
6	59.25	4.10
7	72.25	28.25

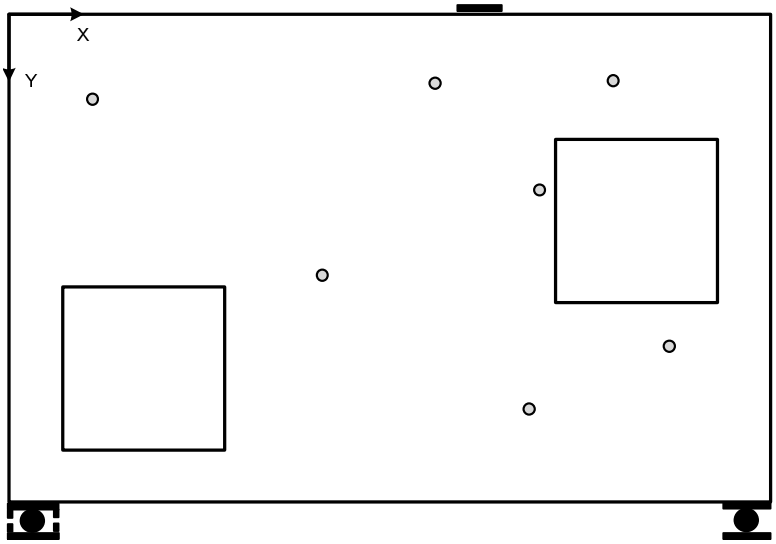

Figure 4.83 Location of AE sensors in RC specimen

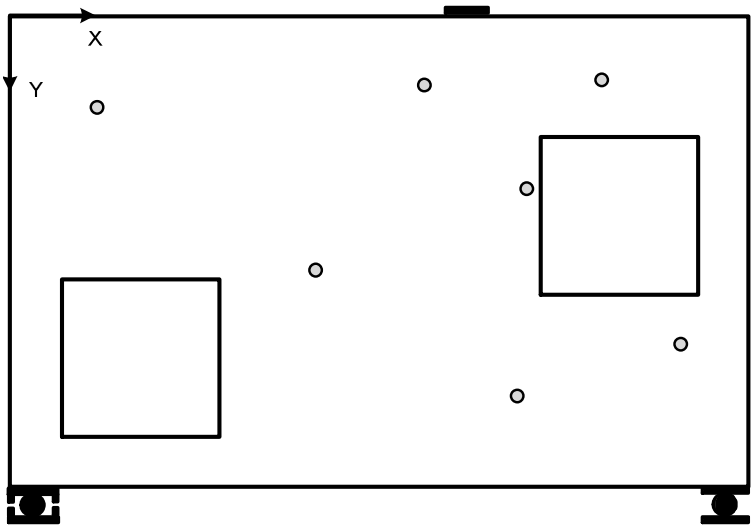

Figure 4.84 Location of AE sensors in SFRC#1 specimen

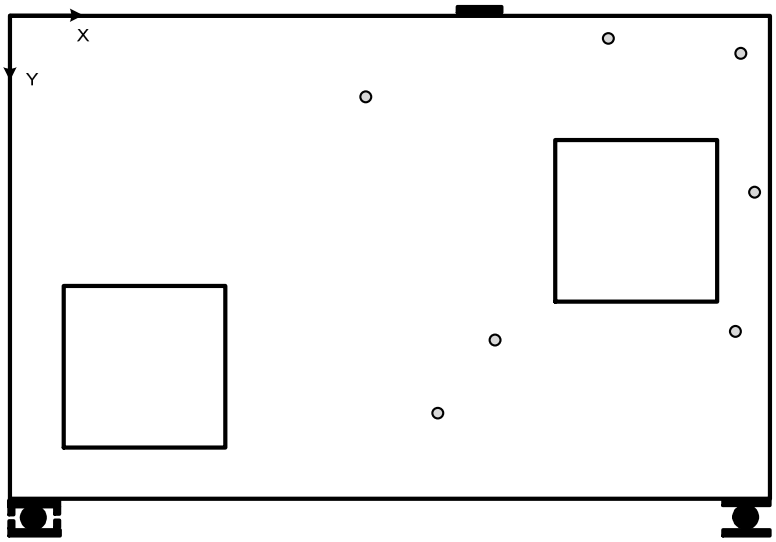

Figure 4.85 Location of AE sensors in SFRC#2 specimen

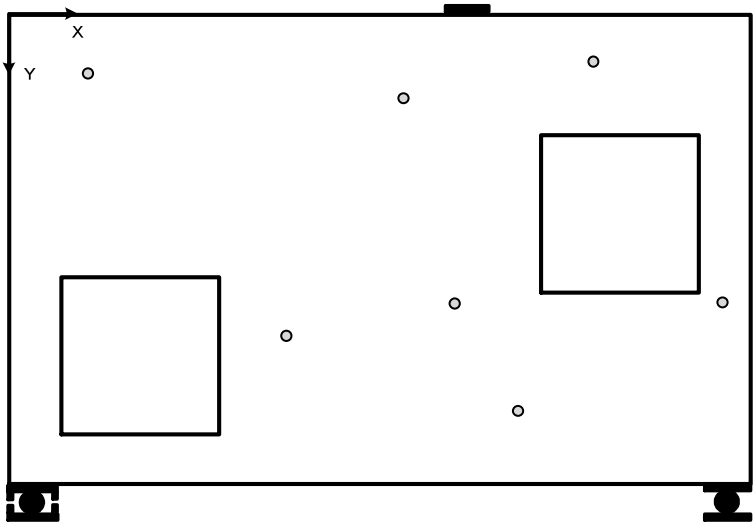

Figure 4.86 Location of AE sensors in SFRC#3 specimen

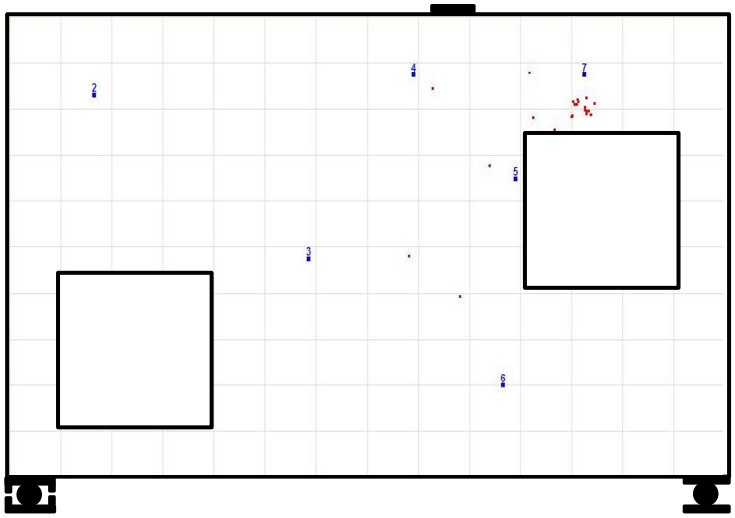

RC specimen

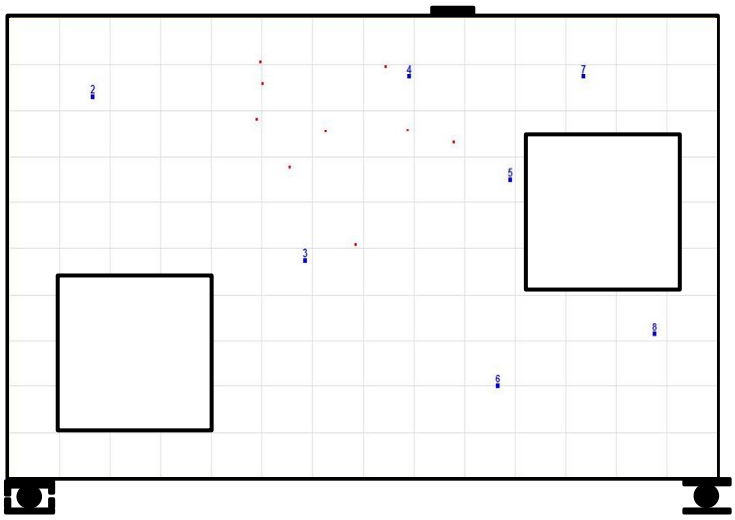

SFRC#1 specimen

Figure 4.87 Acoustic Emission cumulative events at 20 kips of RC (top) and SFRC#1 (bottom) specimens

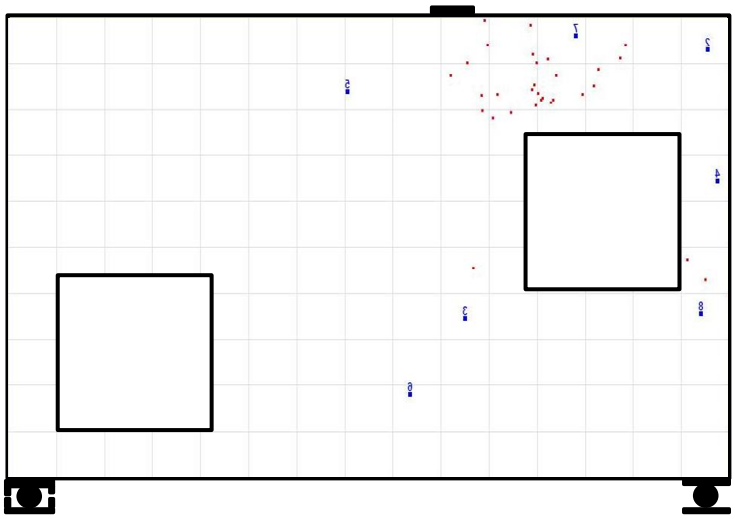

SFRC#2 specimen

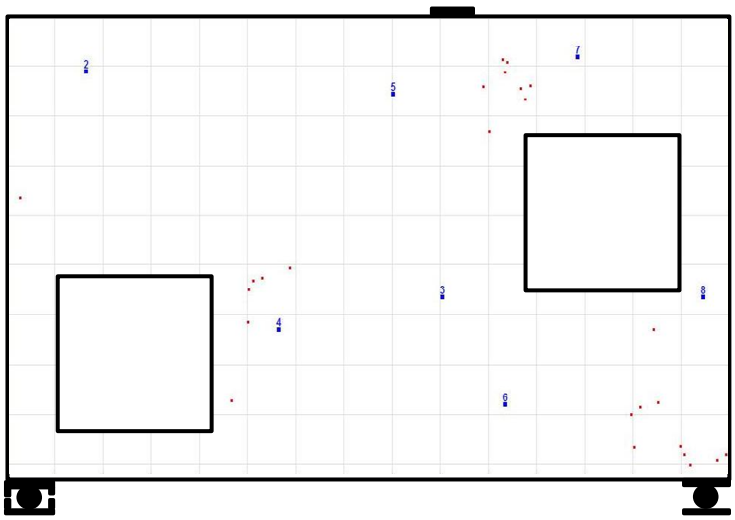

SFRC#3 specimen

Figure 4.88 Acoustic Emission cumulative events at 20 kips of SFRC#2 (top) and SFRC#3 (bottom) specimens

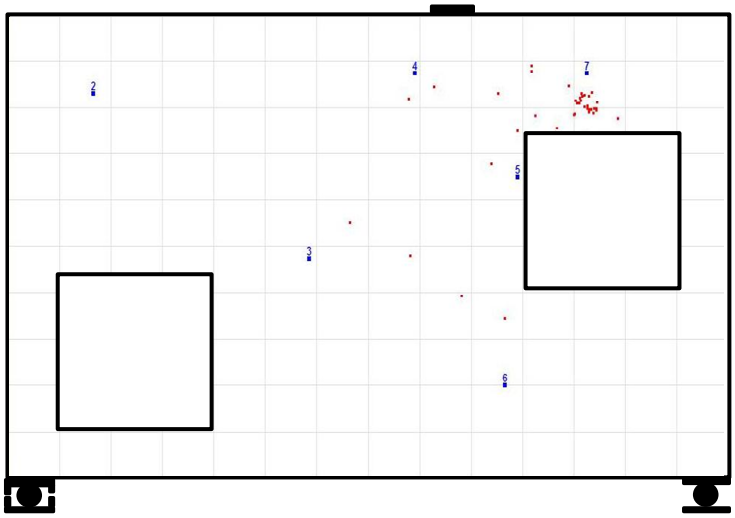

RC specimen

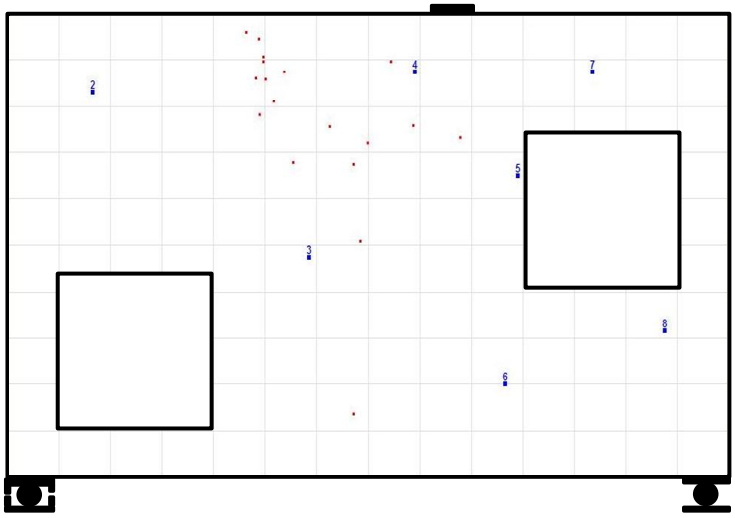

SFRC#1 specimen

Figure 4.89 Acoustic Emission cumulative events at design load of 34.1 kips of RC (top) and SFRC#1 (bottom) specimens

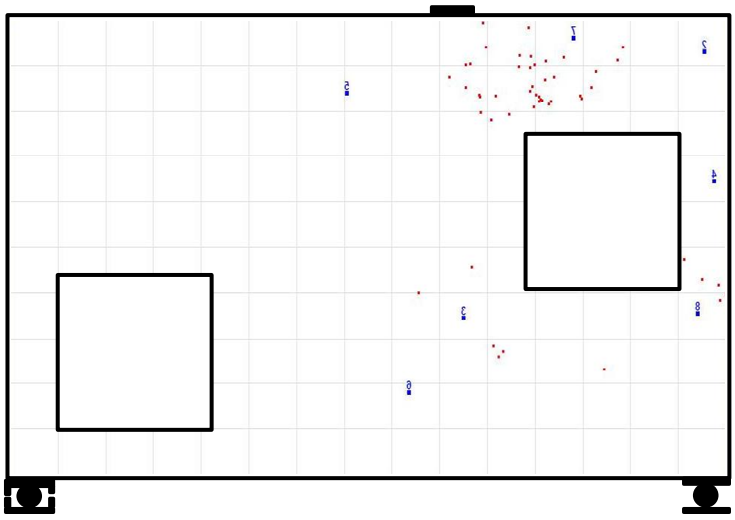

SFRC#2 specimen

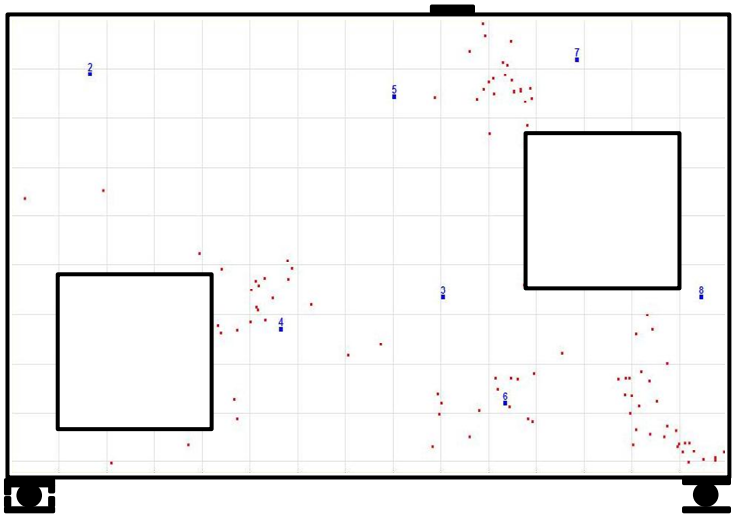

SFRC#3 specimen

Figure 4.90 Acoustic Emission cumulative events at design load of 34.1 kips of SFRC#2 (top) and SFRC#3 (bottom) specimens

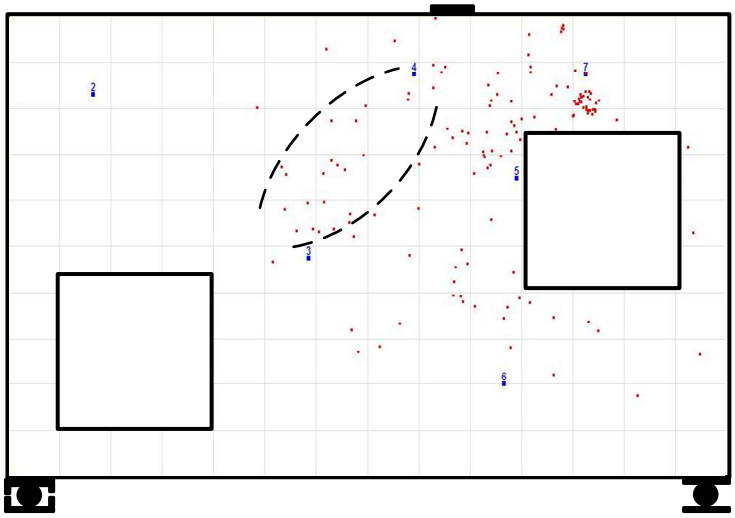

RC specimen

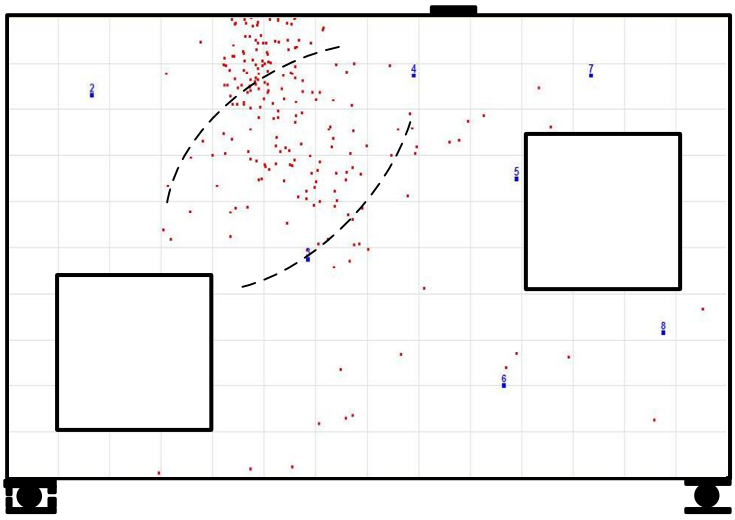

SFRC#1 specimen

Figure 4.91 Acoustic Emission cumulative events at 50 kips of RC (top) and SFRC#1 (bottom) specimens

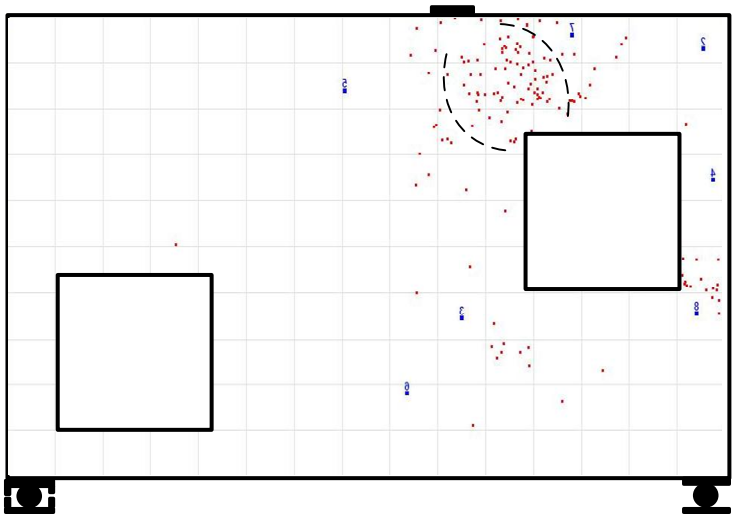

SFRC#2 specimen

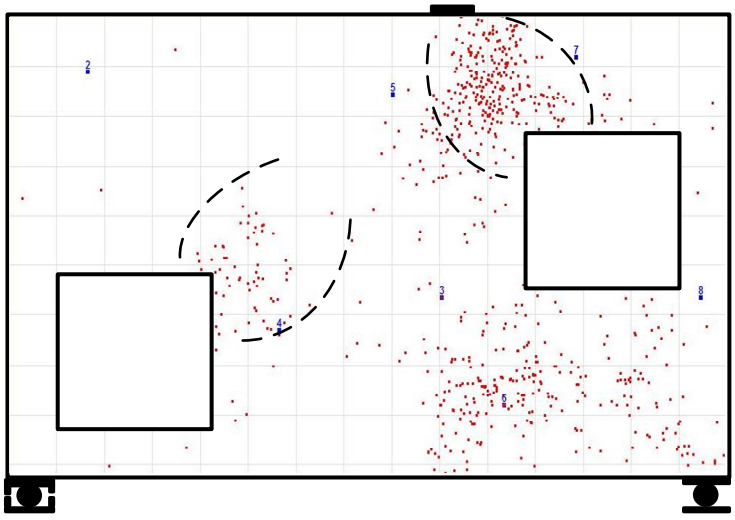

SFRC#3 specimen

Figure 4.92 Acoustic Emission cumulative events at 50 kips of SFRC#2 (top) and SFRC#3 (bottom) specimens

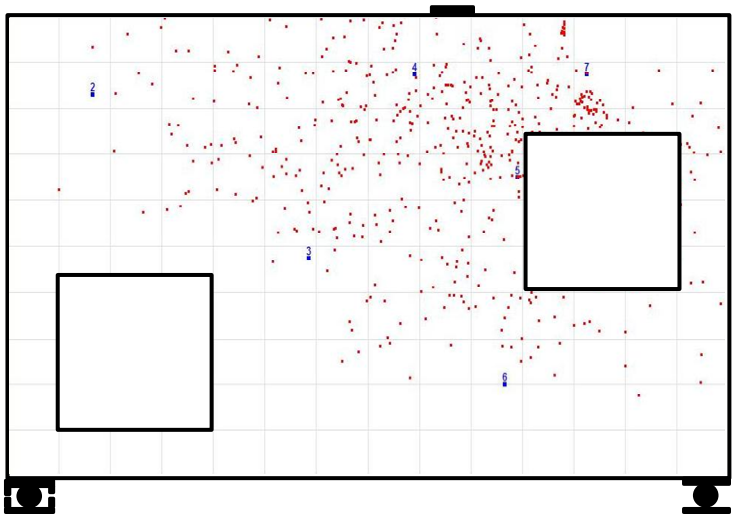

RC specimen

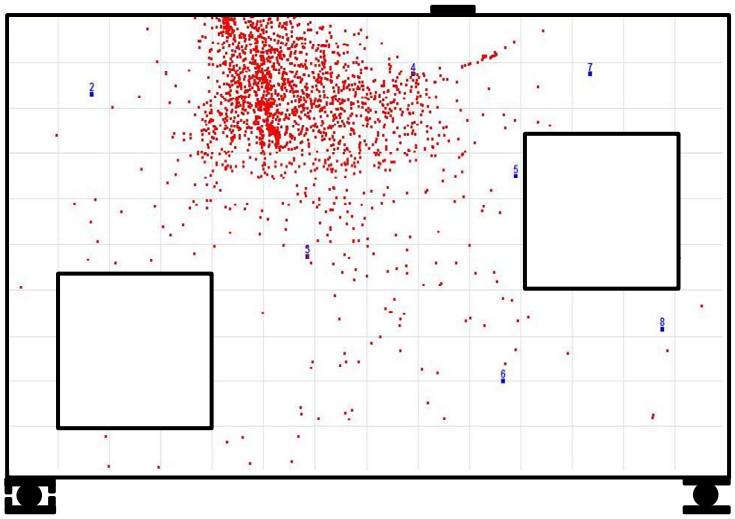

SFRC#1 specimen

Figure 4.93 Acoustic Emission cumulative events at 100 kips of RC (top) and 53 kips of SFRC#1(bottom) specimens

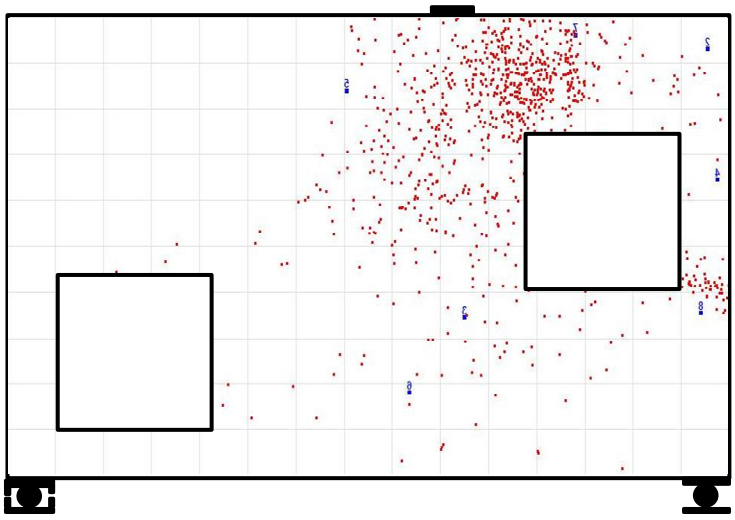

SFRC#2 specimen

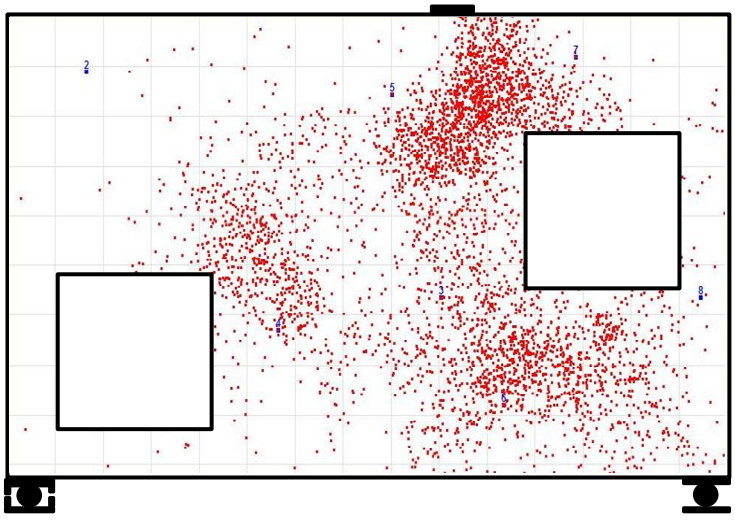

SFRC#3 specimen

Figure 4.94 Acoustic Emission cumulative events at 80 kips of SFRC#2 (top) and 87 kips of SFRC#3 (bottom) specimens

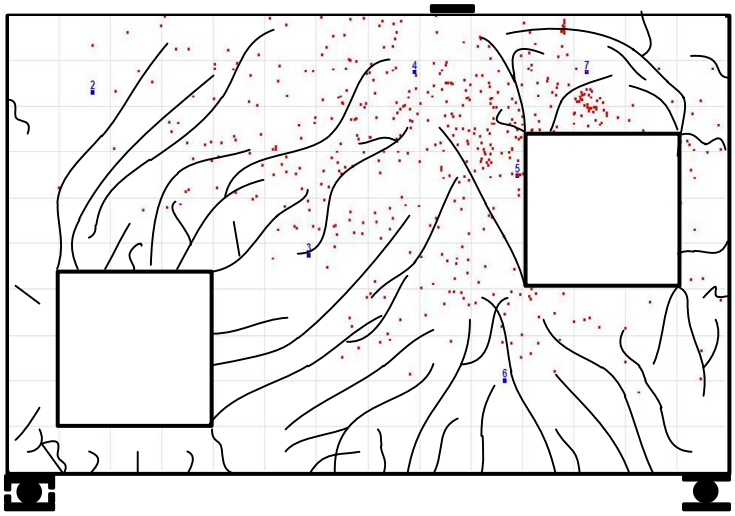

RC specimen

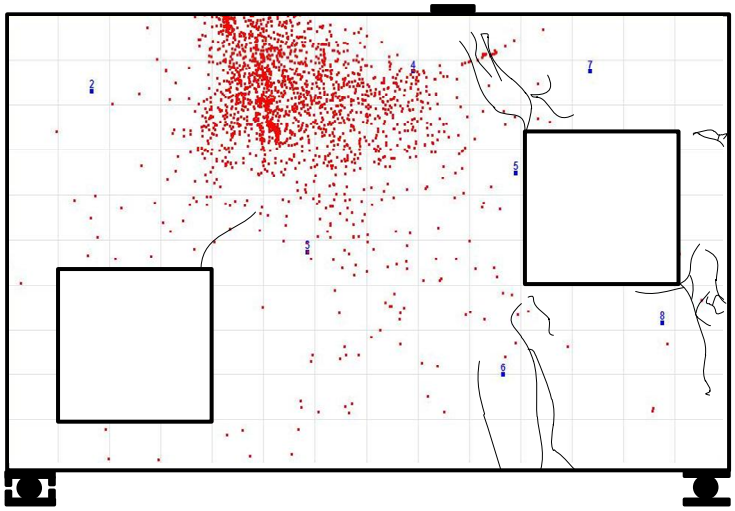

SFRC#1 specimen

Figure 4.95 Acoustic Emission cumulative events at 100 kips of RC (top) and at 53 kips of SFRC#1 (bottom) specimens with cracks superimposed

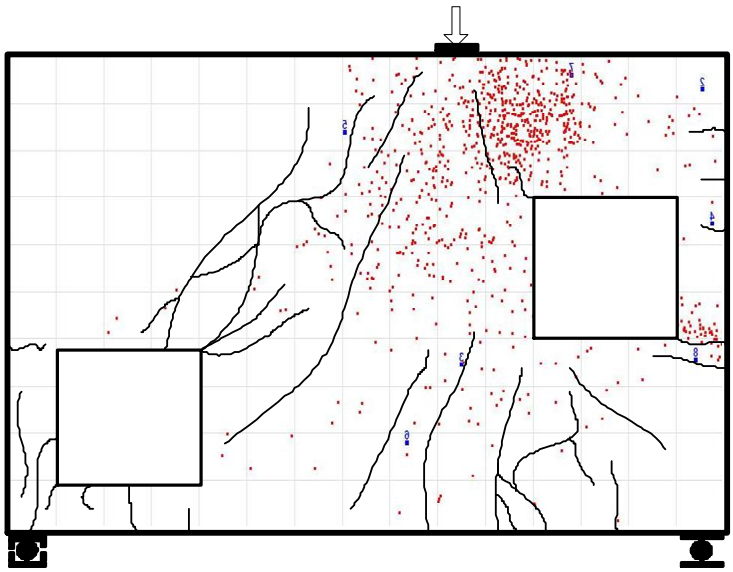

SFRC#2 specimen

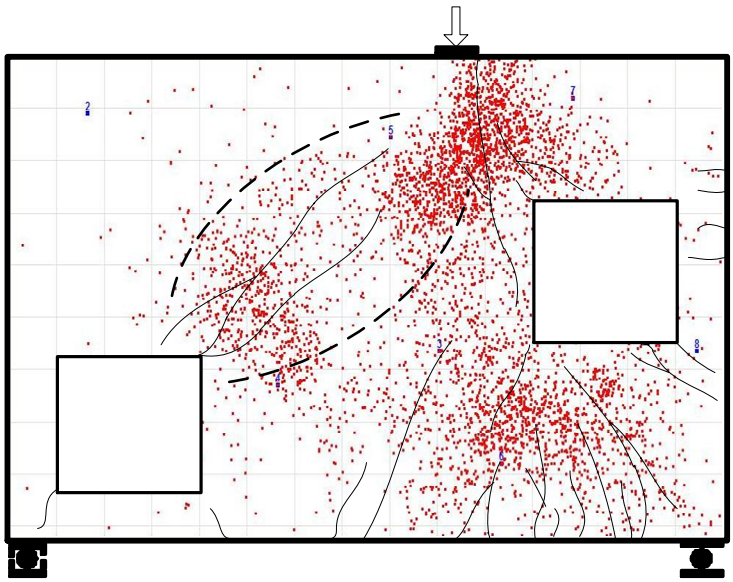

SFRC#3 specimen

Figure 4.96 Acoustic Emission cumulative events at 80 kips of SFRC#2 (top) and at 87 kips of SFRC#3 (bottom) specimens with cracks superimposed

CHAPTER 5

NONLINEAR ANALYSIS

5.1 Introduction

Until the advent of computers, the only way to find the answer to the engineering question "What would happen if I did this to my new design?" was to build a prototype and carry out the necessary tests. Today finite element software's allow designs to be assessed much more quickly and easily. Evaluating a complex engineering design by exact mathematical models, however, is not a simple process. This technology is growing rapidly and is becoming more popular among engineers. Modeling is often referred to as 'pre-processing' and viewing the results is often referred to as 'post-processing'. Pre-processing involves creating a geometric representation of a structure and defining its characteristic behavior in terms of its physical properties such as material, loading and support. There were two finite element software's used in this study namely VecTor2 and LUSAS. Further another computer program, Computer Aided Strut-and-Tie Analysis (CAST) was used to evaluate the performance of adopted strut-and-tie model adopted in the study based on actual material properties obtained from laboratory testing.

5.2 LUSAS Analysis

Modeling procedure in LUSAS involves creating a geometric representation of the structure; assigning attributes and outputting the information as a formatted data file suitable for processing by LUSAS Solver.

GEOMETRY:

Within LUSAS Modeller, a model is created as a graphical representation consisting of several known positions in 3D space and the connections between them. Collectively this is known as the geometry of the model. Geometry consists of points, lines, surfaces and volumes. A volume needs surfaces to enclose it and to define its boundary. Similarly a surface needs lines to form its perimeter and lines need points to define their ends. The shape of a surface between its boundary lines, and the shape of a line between its end points can be simple (straight lines, flat surfaces) or complex, depending on the manner in which it was created.

ATTRIBUTES:

It's another aspect of the behavior of parts of model, or the external factors which are imposed on it, are referred to as attributes. Within LUSAS Modeller, there are several types of attribute – each representing a particular type of behavior. For example materials, loading and support are all attributes, but are quite different from each other. Within each, there are further sub-divisions, for example there are isotropic materials, anisotropic materials, and orthotropic materials, among others. In each case an attribute is first created, and then subsequently attached to all or part of the model. This attachment process is known as assigning. Thus a material can be assigned to a line. Once assigned, the line takes on the properties of the material until further notice.

MESHING:

Points, lines, surfaces and volumes allow the exact smooth geometry of the problem to be defined. However, to solve the problem, the model must be broken down into nodes and elements. This process is known as meshing and the collective term for all the elements and nodes, once created, is the mesh. Special attributes, called mesh attributes, can be created and assigned to geometry in the same way as other attributes. They define the type and number of

nodes and elements that will be used to represent each part of the geometry. A consequential advantage of this approach is that the density of the mesh can easily be changed without rebuilding the geometry or reassigning any attributes. Simply modifying a mesh attribute automatically changes the mesh density in any part of the model where it is assigned.

5.2.1 Modeling Parameters

5.2.1.1 Concrete Model

The concrete model that has been used in this study is multi crack concrete model. It is a plastic damage contact model in which damage planes form according to a principal stress criterion and then develop as embedded rough contact planes (for more information see LUSAS user manual). The basic softening curve used in the model is controlled via a fixed softening curve or a fracture-energy controlled softening curve that depends on the element size. The former, a distributed fracture model, is applicable to reinforced concrete applications, while the latter localized fracture model is applicable to unreinforced cases. For the analysis in this study fixed softening curve was used for RC specimen were as fracture-energy controlled softening curve was used for SFRC specimens. For better performance of the damage evolution function employed in this model a completely continuous exponential softening curve, which has a smooth transition from undamaged to damaged states and from the pre-peak to the post-peak region is introduced. The model assumes that the material can soften, and eventually lose all strength in positive loading, in any one of the predefined cracking directions.

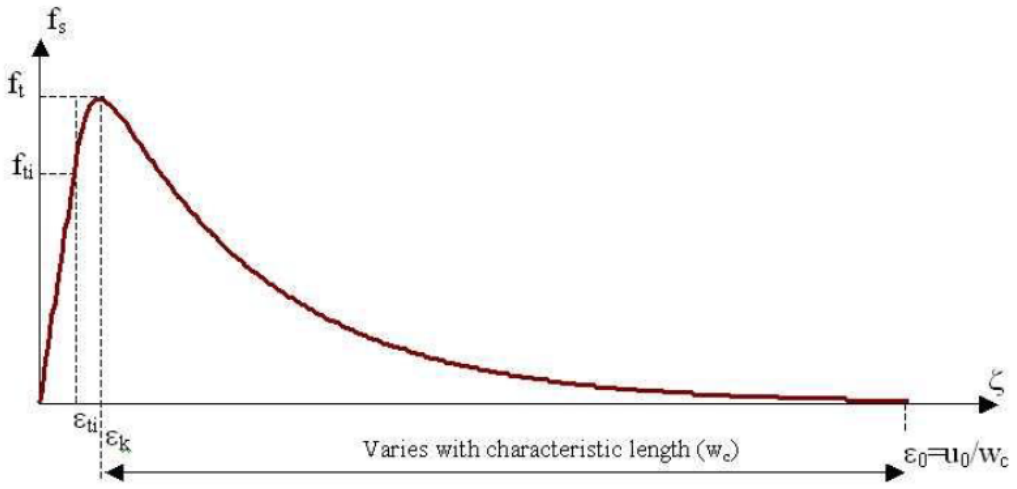

Figure 5.1 Damage evaluation function-softening curve. (LUSAS v14.6-3 user manual, 2011)

The function, which is illustrated in **Figure 5.1** is in terms of the fracture stress (f_s) and the strain parameter (ζ), has (as control parameters) the stress at first damage (f_{ti}), the associated strain (□), the uniaxial strength (f_t), the strain at peak stress (□$_k$) and the strain at the effective end of the curve as (□$_0$). For concrete that contains reinforcement (RC specimen), distributed fracture will be the dominant fracture state. In this case a value for the strain at the end of the tensile softening curve (□$_{t0}$) was specified and G_f (fracture energy per unit area) was set to zero. It is important to note that to ensure a valid shape for the softening curve any value entered should obey the following rule □$_{t0}$ > 1.5(f_t/E). For SFRC specimens the strains will tend to localize in crack zones. In this case by selecting mass concrete option the value for □$_{t0}$ is set to zero and fracture-energy per unit area, G_f is given a positive value. If the effective end of the softening curve parameter, □$_0$ is set to zero, it will be calculated from $5G_f / W_c$, where W_c is a characteristic length for the element. Fracture energy for SFRC specimens was calculated based on publication by Kazemi (2007).

5.2.1.2 Reinforcement Steel Model

The models available within LUSAS can be broadly divided into two families. The older models are based on classical continuum formulations in which the plastic strains are integrated according to a strict interpretation of the flow rules governing their evolution. Recent developments in numerical analysis have re-interpreted the classic laws in a search for greater numerical efficiency and have led to the concept of "consistency" of formulation (LUSAS v14.6-3 Theory manual, 2011). These methods have the advantage of improved stability for large load steps and quadratic convergence during iterations process.

The models available within LUSAS are as follows:

- Continuum Formulation
- ✓ Von Mises, Tresca, Mohr-Coulomb and Drucker-Prager.
- ✓ Stress resultant models for beams and shells.
- ✓ Models for sliding interfaces.
- Consistent Formulation
- ✓ Rate independent formulations, e.g. Hoffman, modified von Mises, Hill, von Mises.
- ✓ Rate dependent formulations, e.g. Uniaxial creep laws generalized to multiaxial states.

The model used in this study was consistent formulation (Hoffman, Hill, von-Mises).

5.2.1.3 Hardening Properties

There are three methods for defining nonlinear hardening. Hardening curves in LUSAS can be defined in terms of hardening gradient, plastic strain or total strain. A nonlinear hardening function may be approximated by using a series of straight line segments (see **Figure 5.2**). In this case hardening gradient data will be input as (C1, ep1), (C2, ep2) for each straight line segment LUSAS extrapolates the curve past the last specified point.

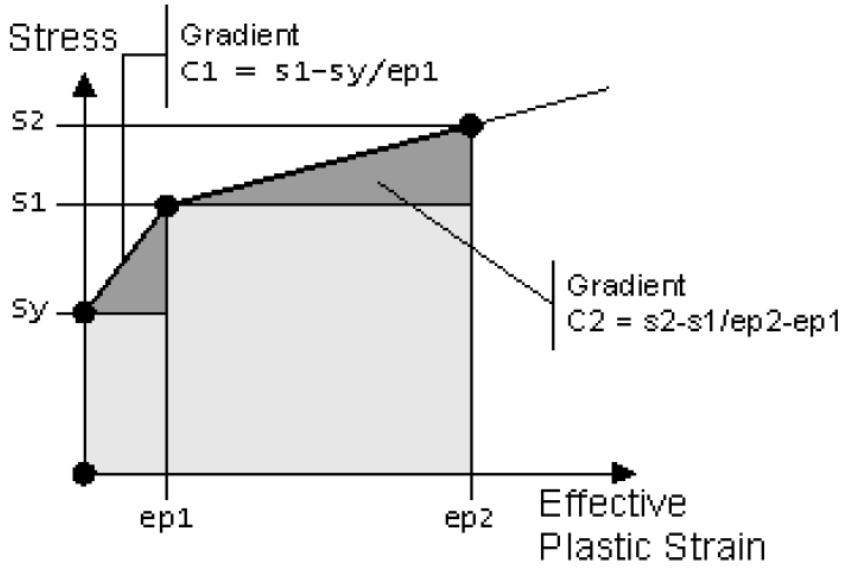

Figure 5.2 Definition of the nonlinear hardening law (LUSAS v14.6-3, 2011)

5.2.2 Elastic Analysis of Deep Beam

The use of FEA allows the designer to better understand the elastic stress fields in an unreinforced, uncracked member. Whereas the FEA can be useful to visualize the elastic flow of forces in the member, engineering judgment must be used for reinforcement design.

As a first step in the design process for SFRC specimens, a two-dimensional linear elastic finite-element analysis (FEA) was carried to establish the elastic stress fields in the structure at a design load of 34.1 kips (152 kN). Reinforcement bars were not included for this analysis also linear elastic properties were assigned to concrete. The specimen geometry used to carry out FEA analysis is shown in chapter 4 and the resulting contour plot is shown in **Figure 5.3**. The critical locations cited where those which had principal tensile stresses (see **Figure 5.3**) close to or greater than the peak flexural strength (f_P), of the SFRC materials (see chapter 3). The main focus while deciding the reinforcement layout for SFRC specimens was to use minimum reinforcement and also to strategically detail reinforcement bars so that they behave as a ductile link in order to transfer tensile stress which cannot be taken by steel fibers.

This analysis proved to be a powerful tool in quickly identifying the critical locations, some of them are shown in **Figure 5.3**.

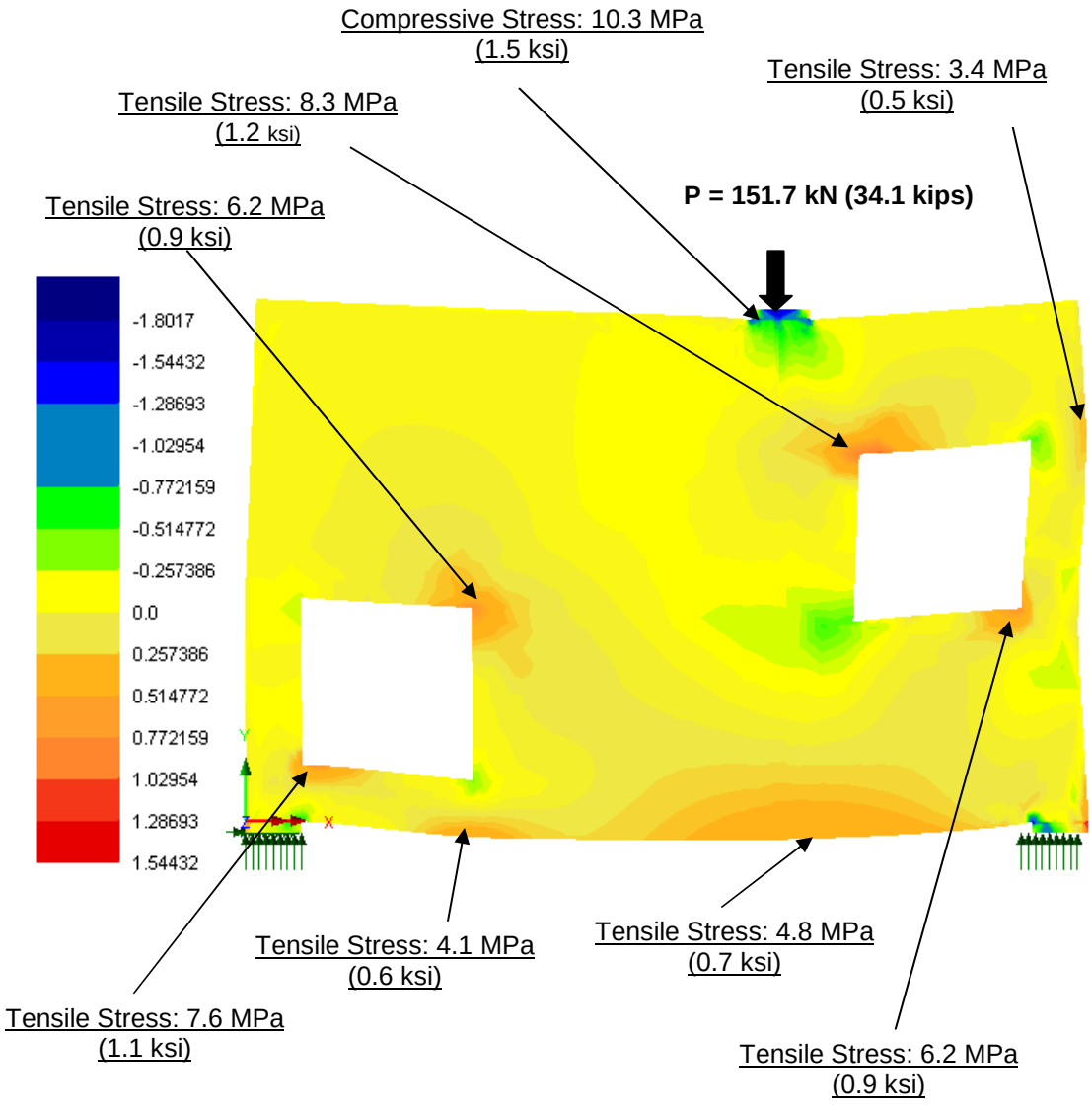

Figure 5.3 Elastic finite element analysis: contour of principal stresses at design load of 151.7 kN (34.1 kip)

5.2.3 Non Linear Analysis of Specimens

It is important to note that although developing truss models based on the elastic flow of stresses is very satisfying for some cases, it needs to be improved for others. Furthermore, the stress field in a body (and consequently its overall behavior) depends on the actual reinforcement layout and is thus not exclusively determined by its geometry and load pattern. This is justified because tensile forces carried by the reinforcing steel are necessary to ensure the internal equilibrium. Consequently, the reinforcement layout influences the resulting stress field within the body. A non linear finite element analysis of all the four specimens with material properties as determined from testing (see chapter 3) was carried out and was analyzed for stress flow, crack propagation and strain in the reinforcement at different loading stages. For SFRC#1 the solution was terminated at the load of 50 kips (222 kN) due to excessive flexural cracking and for RC, SFRC#2 and SFRC#3 it was terminated at 61.6 kips (274 kN), 83 kips (369 kN) and 60 kips (267 kN) respectively. These loadings was more than double the design load of 34.1 kips (152 kN), it is important to note here the contribution from the steel fibers as there was almost negligible amount of steel reinforcement (rebars) used in all SFRC specimens as compared to that required by the strut-and-tie model discussed by Breña and Morrison (2007) which was used in RC specimen. After analyzing the results it was observed that failure pattern in case of SFRC specimens were close to actual failure mode observed during testing, however brittle localized failure observer in case of RC specimen from testing was not captured from the analysis. Also it was observed that the ultimate loads of SFRC specimens from the analysis was comparable to that observed from testing, but in case of RC specimen there was large difference between the ultimate loads.

5.2.3.1 SFRC#1 Specimen

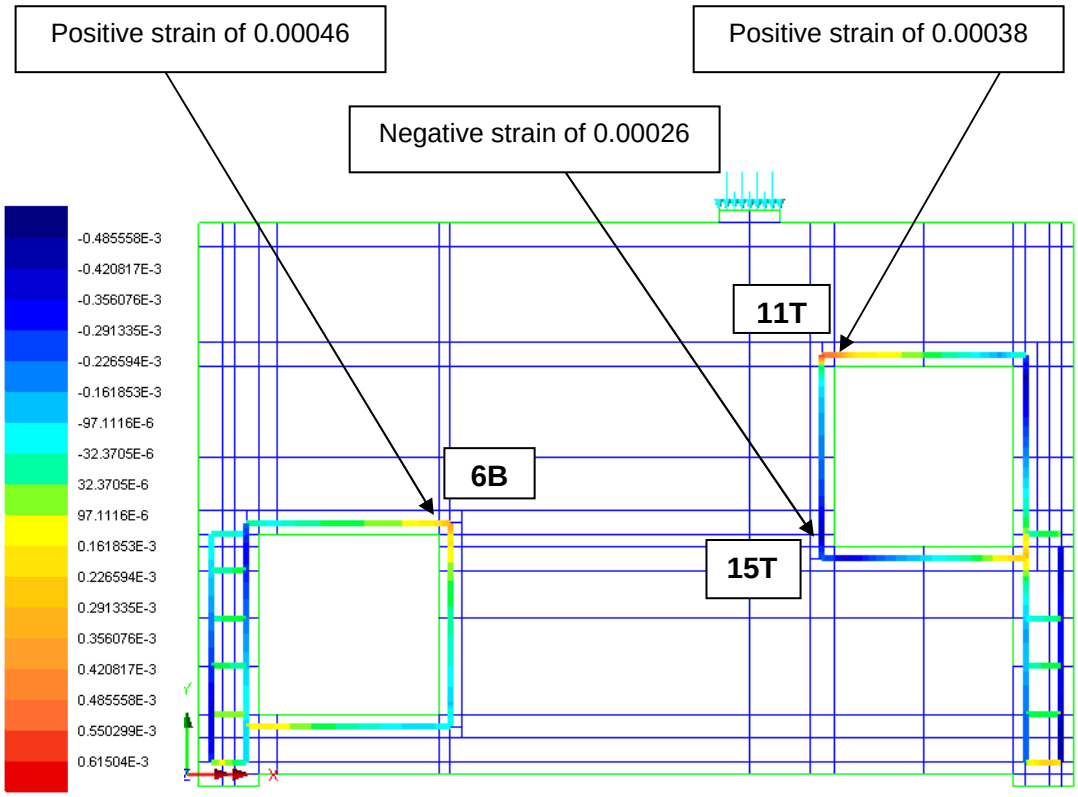

Figure 5.4 Non linear finite element analysis for SFRC #1: Contour of strain in rebars at ultimate load of 50 kip (222 kN)

Table 5.1 Comparison for reinforcement steel strain from large scale testing and LUSAS - SFRC #1.

Strain Gauge #	Strain at Design Load of 34.1 kips		Strain at ultimate Load	
	From Large Scale Testing	From LUSAS Analysis	From Large Scale Testing at 53 kips	From LUSAS Analysis at 50 kips
1T	-0.00003	-0.000022	-0.00005	-0.00004
2T	0.00023	0.00018	0.00062	0.00053
3T	¶	0.000073	¶	0.00012
4T	-0.00006	-0.000045	-0.00008	-0.000064
5T	0.00016	0.00028	0.00037	0.00048
6B	0.00019	0.00029	0.00039	0.00046
7B	¶	0.000075	¶	0.00016
8B	-0.00007	-0.00005	-0.00009	-0.00007
9B	-0.00006	-0.00006	0.000068	-0.00007
10B	-0.0002	-0.00012	-0.0003	-0.00024
11T	0.00019	0.00012	0.00042	0.00038
12T	-0.00007	-0.00007	-0.0002	-0.00018
13T	0.000093	0.000056	0.00076	0.00057
14T	-0.0002	-0.00017	-0.0004	-0.00036

Table 5.1 – *Continued*

15T	-0.0002	-0.00016	-0.0003	-0.00026
16T	0.00011	0.00018	0.00065	0.00045
17B	-0.0002	-0.0002	-0.0006	-0.0005
18B	-0.0002	-0.00027	-0.0005	-0.0007
19B	0.00021	0.00016	0.00037	0.00028
20B	0.00011	0.00018	0.00045	0.00045

Note: Positive values indicating tension where as negative values compression.

¶ Data not recorded as strain gauge was damaged; T: Top layer of bar, B: bottom layer of bar

Strain values in the rebars from testing and LUSAS analysis was compared at design load of 34.1 kips (152 kN) and their respective ultimate load (see **Table 5.1**). Since it was 2D analysis strain was recorded only at one location i.e. top and bottom layer had same value of strain. From laboratory testing of the specimen it was seen that none of the bar yielded at ultimate load of 53 kips (236 kN). Similar observations were made from the analysis also strain in the rebars from the analysis was found to be comparable to the strain observed during testing at various load stages. Also from LUSAS analysis it was observed that first cracking started at 27 kips (120 kN) from the bottom fiber of the beam, were as during laboratory testing it appeared to be starting at 30 kips (133 kN) from same location. However, overall LUSAS was precise in predicting crack location (see **Figure 5.5**) and also testing results such as strain in the reinforcement and deformed shape from the analysis was found to be in agreement with results obtained from testing.

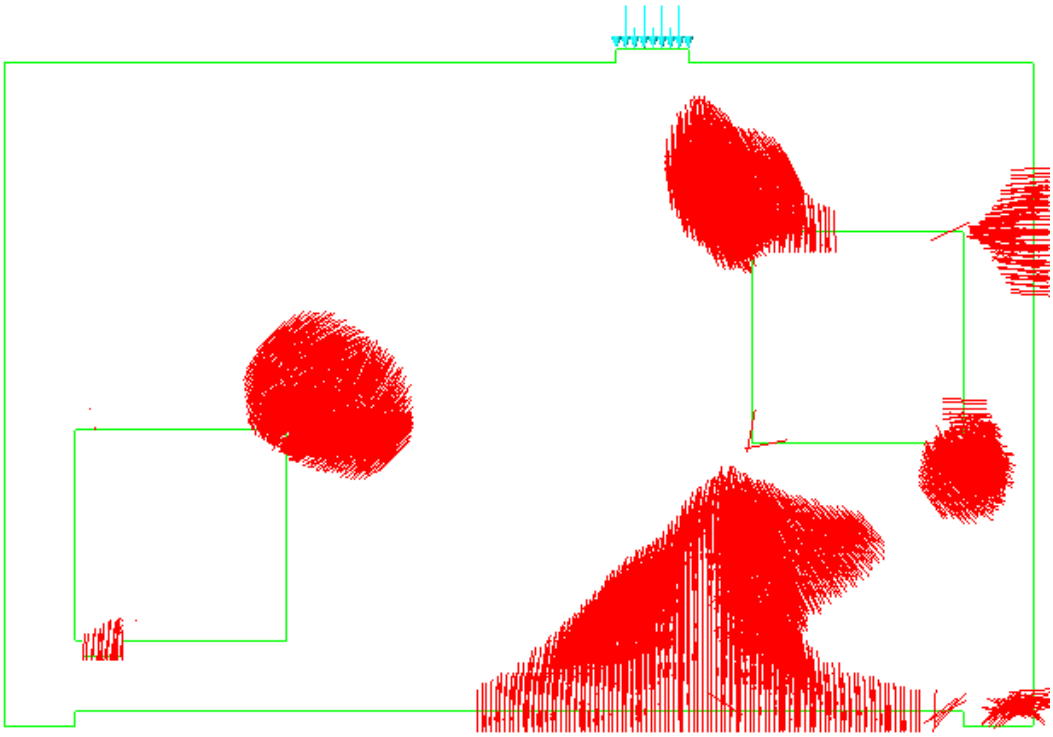

Figure 5.5 Non linear finite element analysis for SFRC #1: Cracking pattern at ultimate load of 50 kip (222 kN)

5.2.3.2 SFRC# 2 Specimen

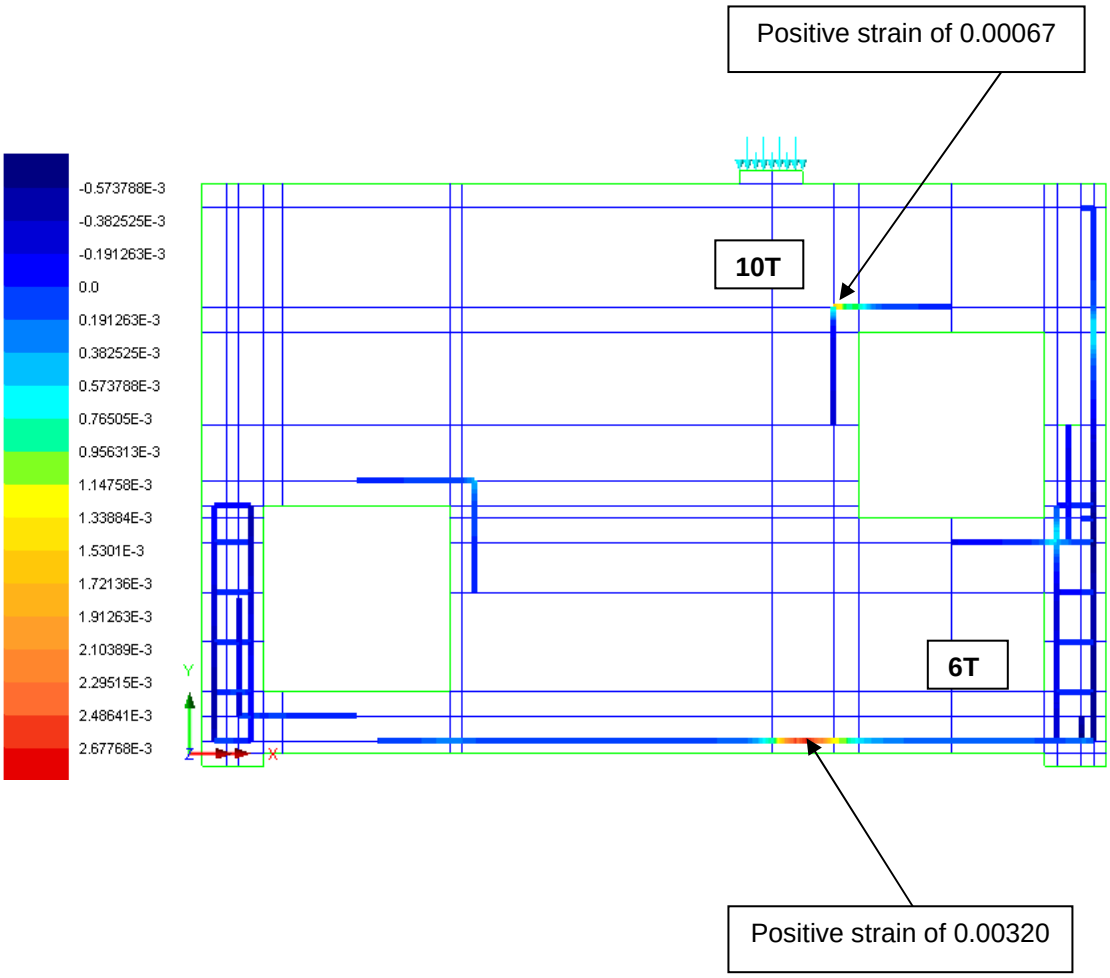

Figure 5.6 Non linear finite element analysis for SFRC#2: Strain in rebars at ultimate load of 83 kips (369 kN)

Table 5.2 Comparison for reinforcement steel strain from large scale testing and LUSAS - SFRC#2.

Strain Gauge #	Strain at Design Load of 34.1 kips		Strain at Ultimate Loads	
	From Large Scale Testing	From LUSAS Analysis	From Large Scale Testing at 80 kips	From LUSAS Analysis at 83 kips
1T	-0.00009	-0.000085	0.00092	0.00076
1B	¶	-0.000085	¶	0.00076
2T	0.00064	0.000046	0.00136	0.00100
2B	0.000070	0.000046	0.00188	0.00100
3T	0.000096	0.000087	0.00214§	0.0025§
3B	¶	0.000087	¶	0.00180
4T	¶	0.00006	¶	0.00160
4B	0.000065	0.00006	0.00188	0.00160
5T	0.000050	0.000058	0.00038	0.00026
5B	0.000061	0.000058	0.00037	0.00026
6T	0.00017	0.00014	0.00494§	0.00320§
6B	0.00023	0.00014	0.00326§	0.00320§
7T	0.000076	0.000072	0.00101	0.00090
7B	0.000052	0.000072	0.00103	0.00090

Table 5.2 – *Continued*

8T	0.00014	0.000096	0.00139	0.00124
8B	-0.00006	0.000096	0.00102	0.00124
9T	-0.000006	0.000045	0.00044	0.00028
9B	-0.00005	0.000045	0.00101	0.00028
10T	0.00036	0.00023	0.00098	0.00067
10B	0.0002	0.00023	0.0017	0.00067
11T	0.00018	0.00009	0.00217§	0.00084
11B	0.00022	0.00009	0.0021§	0.00084

Note: Positive values indicating tension where as negative values compression.
¶ Data not recorded as strain gauge was damaged.
§ Bar yielded, T: Top layer of bar, B: bottom layer of bar.

As mentioned earlier, nonlinear analysis for SFRC#2 was terminated at the loading of 83 kips (369 kN), this is because the program terminates the solution once there is excessive cracking in the structure due to which the solution cannot converge further. In this case it was terminated due to excessive cracking at horizontal segment of lower left window (see **Figure 5.7**). However during testing specimen reached to peak load of 80 kips (356 kN).

During analysis first cracking was observed at 32 kips loading, it was flexural crack starting from bottom fiber of the beam exactly below the loading point. This crack was observed at 35 kips during laboratory testing of the specimen. **Table 5.2** give the comparison between values of strain in rebar from laboratory test and nonlinear analysis by LUSAS. Strain gauge 6T and 6B were the first one to reached their yield limit of 2000 micro strain at the loading of 65 kips (289 kN) during testing. Although these strain gauges were also the first one to yield during

analysis, they reached 2000 micro strain at 68 kips (302 kN). Also the rebar with strain gauge number 3T reach its yielding limit of 2000 micro strain at 80 kips (356 kN) during testing, this value was reached at 78 kips during analysis (see **Table 5.2**).

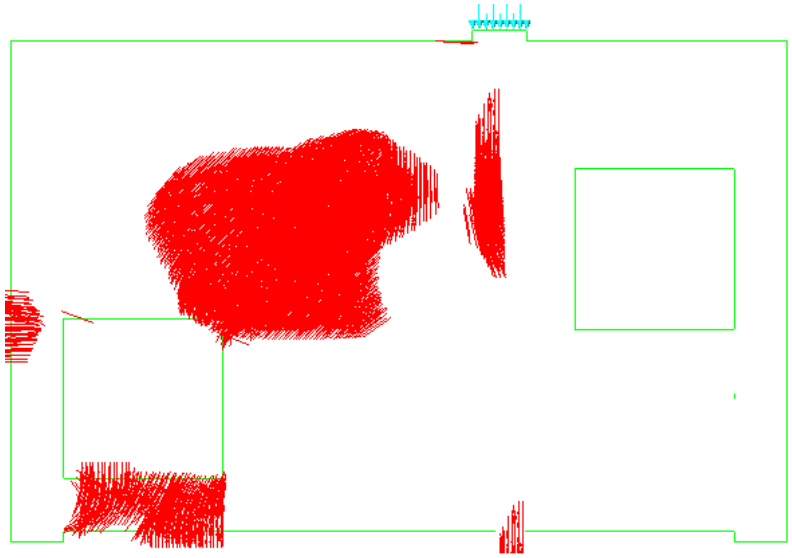

Figure 5.7 Non linear finite element analysis for SFRC#2: Cracking pattern at ultimate analysis load of 83 kips (369 kN)

Figure 5.8 Overall state of SFRC#2 after testing

5.2.3.3 SFRC# 3 Specimen

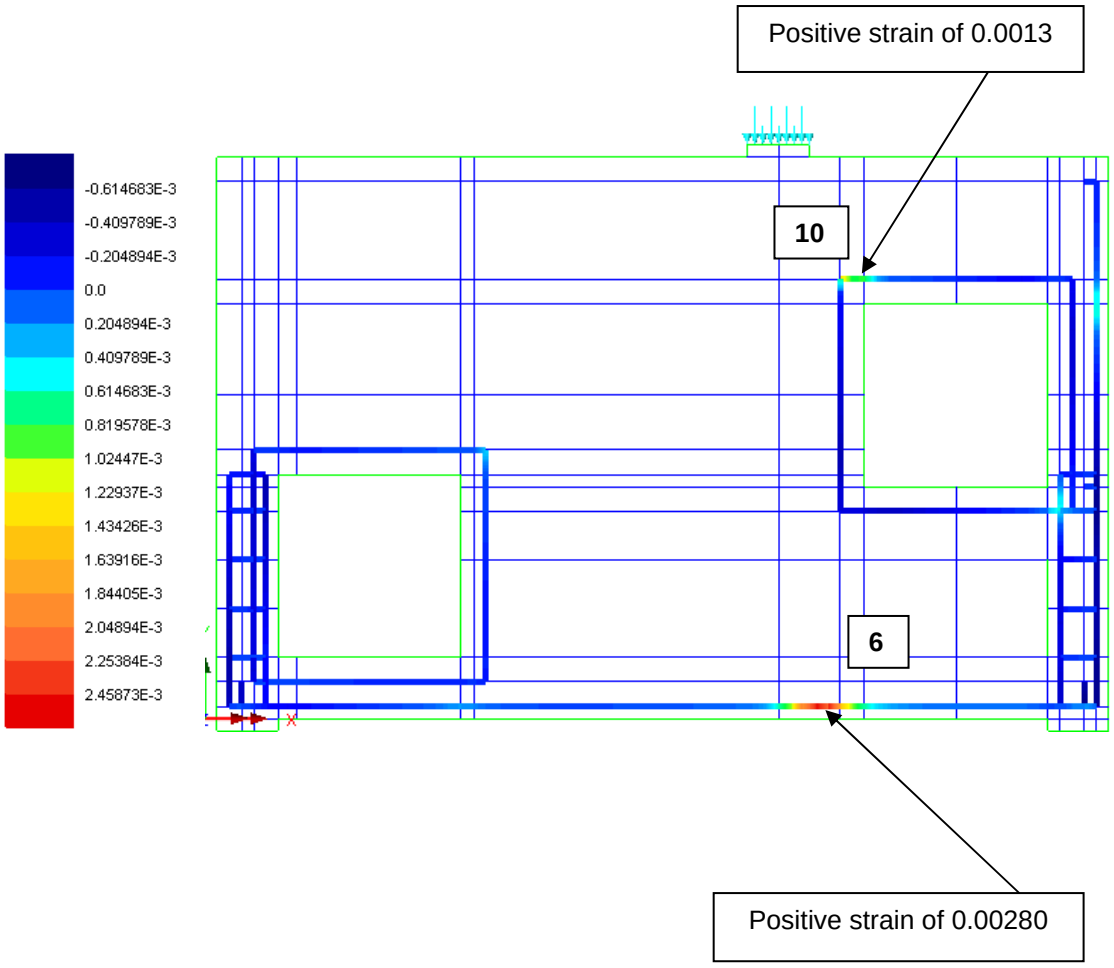

Figure 5.9 Non linear finite element analysis for SFRC#3: Strain in rebars at ultimate analysis load of 60 kips (267 kN)

Table 5.3 Comparison for reinforcement steel strain from large scale testing and LUSAS- SFRC#3.

Strain Gauge #	Strain at Design Load of 34.1 kips		Strain at Ultimate Load	
	From Large Scale Testing	From LUSAS Analysis	From Large Scale Testing at 87 kips	From LUSAS Analysis at 60 kips
1T	¶	-0.000073	¶	-0.00018
1B	-0.00008	-0.000073	-0.0002	-0.00018
2T	-0.0001	0.000023	0.00013	0.00011
2B	0.00002	0.000023	0.00048	0.00011
3T	0.000058	0.000054	0.00069	0.00054
3B	¶	0.000054	¶	0.00054
4T	0.000048	0.000043	0.00082	0.00058
4B	0.00003	0.000043	0.00069	0.00058
5T	0.00014	0.00024	0.00143	0.0011
5B	0.00027	0.00024	0.00176	0.0011
6T	0.00043	0.00029	0.00358§	0.00280§
6B	0.0003	0.00029	0.00349§	0.00280§
7T	0.00014	0.00014	0.00076	0.0010
7B	-0.00001	0.00014	0.00181	0.0010
8T	0.0001	0.0002	0.00206§	0.0013
8B	¶	0.0002	¶	0.0013

Table 5.3 – *Continued*

9T	0.000088	0.000062	0.00148	0.0012
9B	-0.00008	0.000062	0.0024§	0.0012
10T	0.00017	0.000065	-0.00005	0.0013
10B	0.000063	0.000065	0.00148	0.0013
11T	0.00028	0.00006	0.00318§	0.0010
11B	0.00025	0.00006	0.01580	0.0010

Note: Positive values indicating tension where as negative values compression.
¶ Data not recorded as strain gauge was damaged.
§ Bar yielded, T: Top layer of bar, B: bottom layer of bar

During testing this specimen was able to reach a peak load of 87 kips (387 kN) and the testing was stopped at deflection of 1.6 in. (40 mm). However from the analysis it was observed that the specimen was able to reach a peak load of 60 kips (267 kN), also there was crushing of concrete at right support and at loading point along with severe flexural crack once the specimen reached 56 kips (249 kN). First crack started at 31 kips (138 kN) during analysis from the bottom fiber of the beam below loading point. From laboratory testing this crack was seen at the load of 35 kips (156 kN). **Table 5.3** gives the comparison between values of strain in reinforcement bars from laboratory test and nonlinear analysis by LUSAS. Strain gauge 6T and 6B reached a value of 2000 micro strain at 58 kips (258 kN) as observed from testing, however during analysis strain at this location reached 2000 micro at 57 kips (254 kN). Values of strain in the rebar with strain gauges 9, 8 and 11 did not reached its yield limit of 2000 micro strain as the analysis was terminated at 60 kips (267 kN). Also crack pattern predicted from analysis was found to be similar to what observed from the overall state of specimen after testing (see **Figures 5.10** and **5.11**).

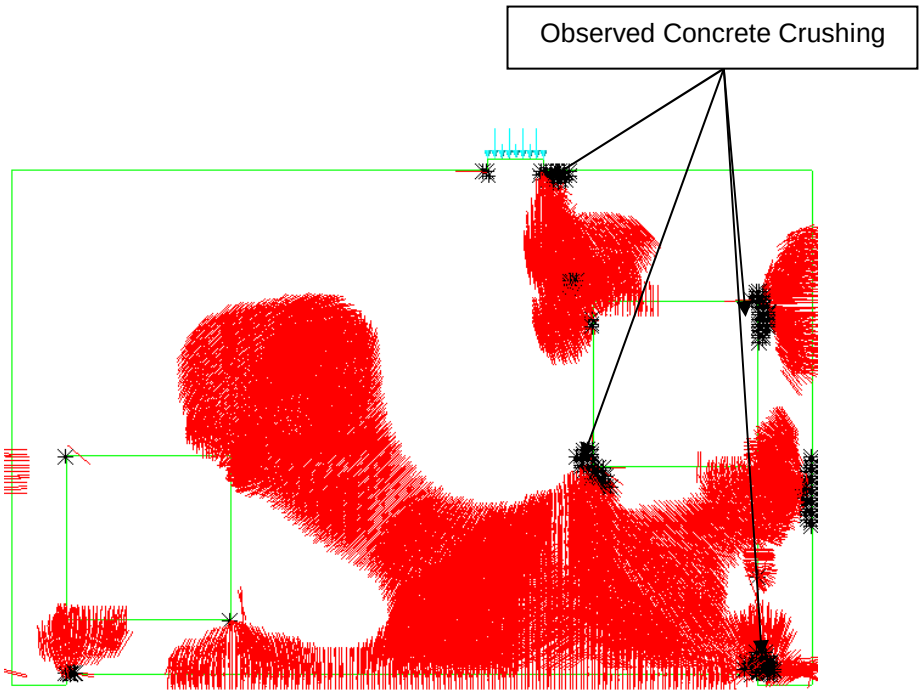

Figure 5.10 Non linear finite element analysis for SFRC#3: Cracking pattern at ultimate load of 60 kips (267 kN)

Figure 5.11 Overall state of SFRC#3 after testing

(a) (b)

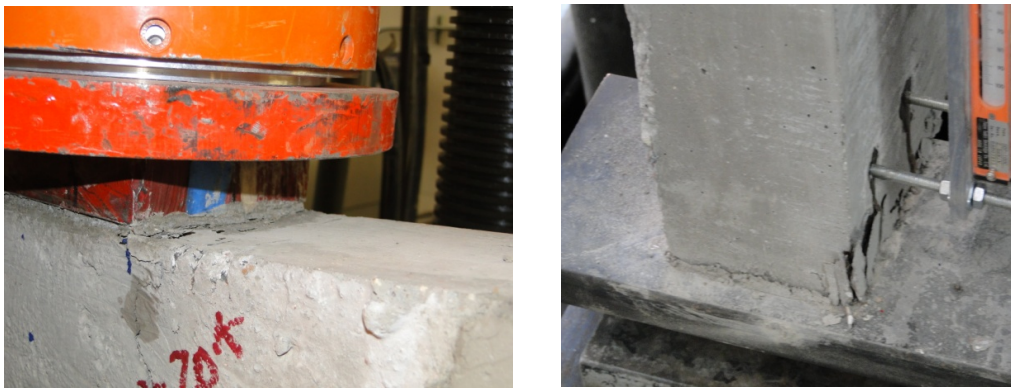

(c) (d)

Figure 5.12 Observed crushing of concrete in SFRC#3 during testing (a) corner of left window (b) corner of right window (c) at loading point (d) at right support

5.2.3.4 RC Specimen

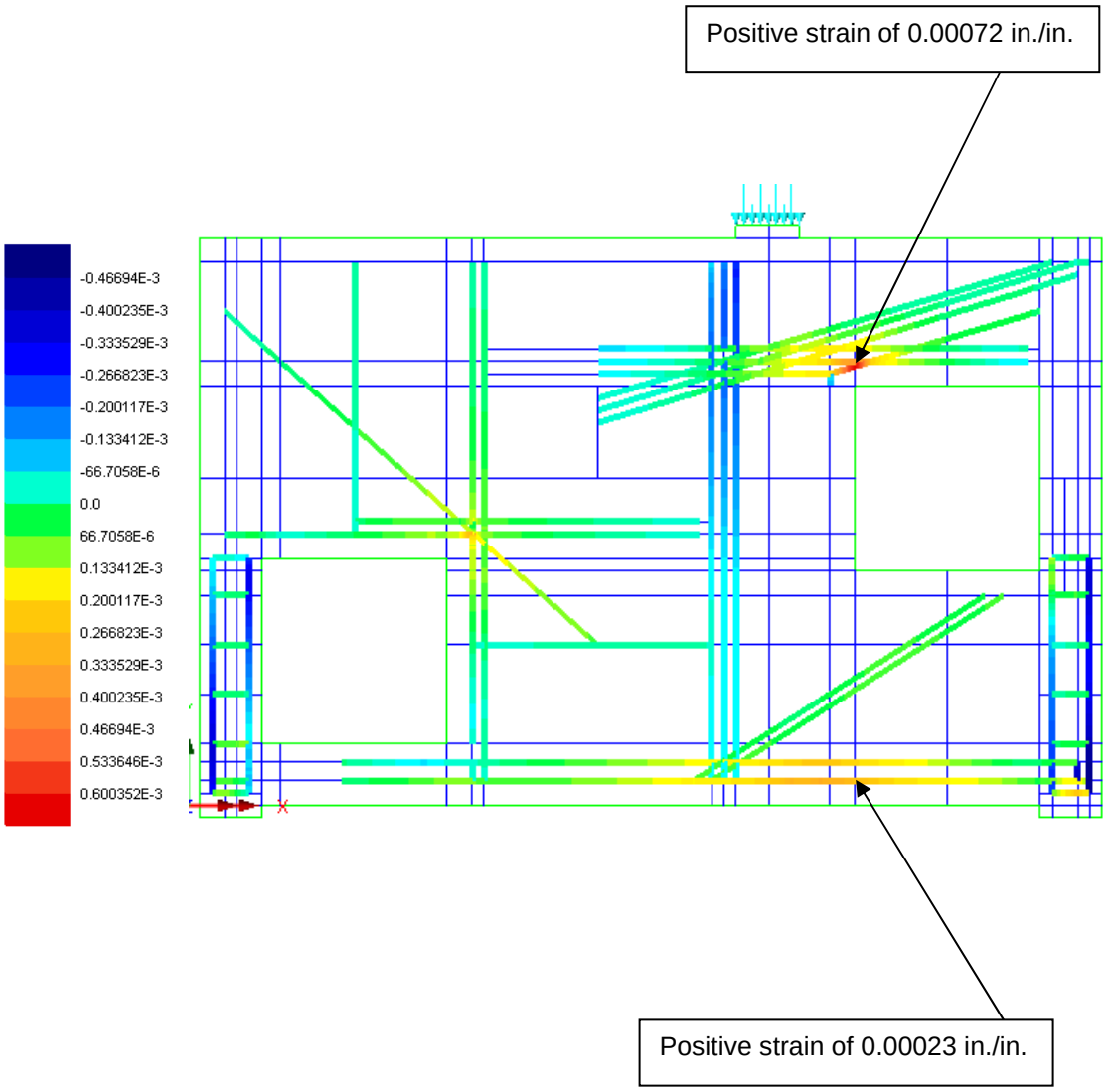

Figure 5.13 Non linear finite element analysis for RC: Strain in rebars at design load of 152 kN (34.1 kips)

Table 5.4 Comparison for reinforcement steel strain from large scale testing and LUSAS - RC.

Strain Gauge #	Strain at Design Load of 34.1 kip		Strain at Ultimate Load	
	From Large Scale Testing	From LUSAS Analysis	From Large Scale Testing at 100 kips	From LUSAS Analysis at 61.6 kips
1T	0.000039	0.000031	0.00163	0.00018
1B	0.000042	0.000031	0.00172	0.00018
2T	0.00025	0.000065	0.00221§	0.00032
2B	0.000043	0.000065	0.00196	0.00032
3T	0.00089	0.00023	0.00399§	0.00052
3B	0.00091	0.00023	0.0076	0.00052
4T	0.000039	0.000049	0.00266§	0.00028
4B	0.000048	0.000049	0.00258§	0.00028
5T	¶	0.000045	¶	0.00038
5B	¶	0.000045	¶	0.00038
6T	¶	0.000045	¶	0.00019
6B	¶	0.000045	¶	0.00019
7T	0.00036	0.00015	0.00144	0.00026
7B	0.00041	0.00015	0.00153	0.00026

Table 5.4 – *Continued*

8T	0.00039	0.00018	0.00154	0.00028
8B	0.00036	0.00018	0.00161	0.00028

Note: Positive values indicating tension where as negative values compression.
¶ Data not recorded as strain gauge was damaged.
§ Bar yielded, T: Top layer of bar, B: bottom layer of bar

Analysis for RC specimen was terminated at 61.6 kips (274 kN) due to instability deducted in structure and further load increment was not possible. As it was plain concrete, there was no post peak behavior assigned therefore hardening response was not notice after peak loading was reached. **Table 5.4** gives the strain values at design load and ultimate load both from testing and analysis. As analysis terminated at 61.6 kips (274 kN) none of the strain value reached 2000 micro strain. However highest strain recorded was in strain gauge no 3T.

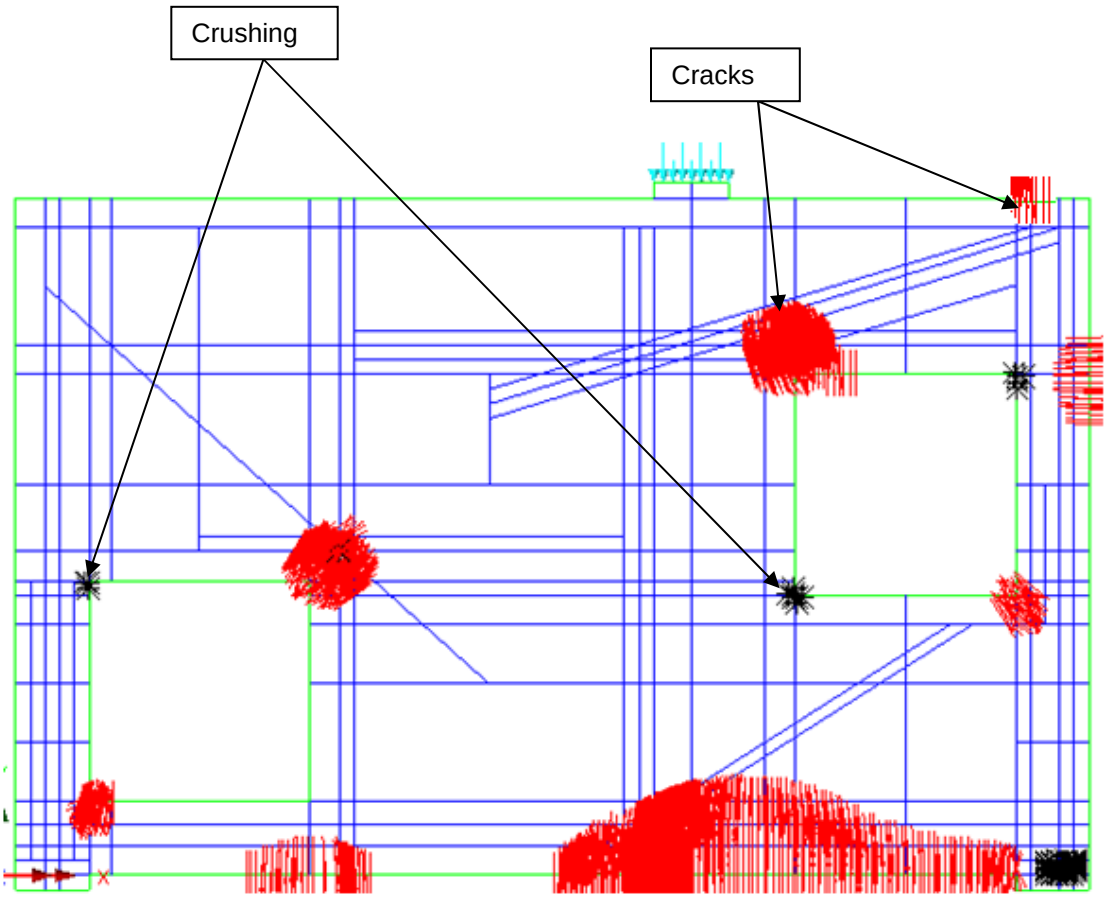

Figure 5.14 Non linear finite element analysis for RC: Cracking pattern at ultimate analysis load of 61.6 kips (274 kN)

5.3 VecTor2 Analysis

5.3.1 Introduction

A nonlinear finite element modeling of the deep beam was carried out using VecTor2, a two-dimensional nonlinear finite element analysis program for reinforced concrete structures developed at the University of Toronto over the past 20 years. VecTor2 is based on the Modified Compression Field Theory (MCFT) by Vecchio and Collins (1986), and the Disturbed Stress Field Model (DSFM) by Vecchio (2000). The use of VecTor2 for the numerical analysis of two-dimensional reinforced concrete membrane structures is facilitated by the pre-processor FormWorks (Wong, 2002). Augustus, the post-processor for VecTor2, (Bentz, 1996-2007), is used to observe the analysis results. VecTor2 is one of the most user-friendly among other finite element programs available today. VecTor2 is capable of modeling two-dimensional reinforced concrete membrane structures under monotonic, cyclic and reversed cyclic loading conditions. The post-cracking influences on concrete, such as compression softening, tension stiffening, hysteretic effects and dowel action of steel reinforcement are some of the behavior mechanisms that are considered by VecTor2. Most of the finite element modeling tools available for nonlinear analysis of reinforced concrete structures require definition of the failure mechanism or are dependent on empirical values obtained through similar experimental tests. VecTor2 on contrary performs analysis by using only the sectional, material and loading system details of the specimens necessary to define the structure. Further information about the program is given in “VecTor2 & FormWorks User’s Manual” by Wong and Vecchio (2002).

5.3.2 Modeling on VecTor2

The procedure of modeling a structure in VecTor2 starts with creating the geometry of the structure, selection of loading conditions and material behavior models. Then the regional properties, meshing options and restraint conditions of the structure are defined to simulate the

actual loading system. Further the element properties for concrete, reinforcement and bond regions are individually assigned to the model. The finite elements that are available in the VecTor2 library are simple and low-powered elements which have linear displacement functions leading to fewer suspicious and mostly accurate behavior results. Once the model is ready for analysis, VecTor2 starts an iterative secant stiffness procedure for the nonlinear analysis of the reinforced concrete structure under designated loading and restraint conditions. The results of an analysis by VecTor2 can either be obtained from the ASCII result files or simply by using the post-processor, Augustus. Most of the local and global member behavior can be observed using Previous studies have shown that using only the default material constitutive models in modeling the specimens have resulted in accurate results (Sagbas, 2007).

5.3.2.1 Concrete Model

The concrete element that has been used in this study is a four-node rectangular element, as shown in **Figure 5.15**. This is a plane stress rectangle with uniform thickness in the out-of-plane direction. This element having eight degrees of freedom allows translation at each node in x- and y-directions, and should be defined by a counter clockwise sequence.

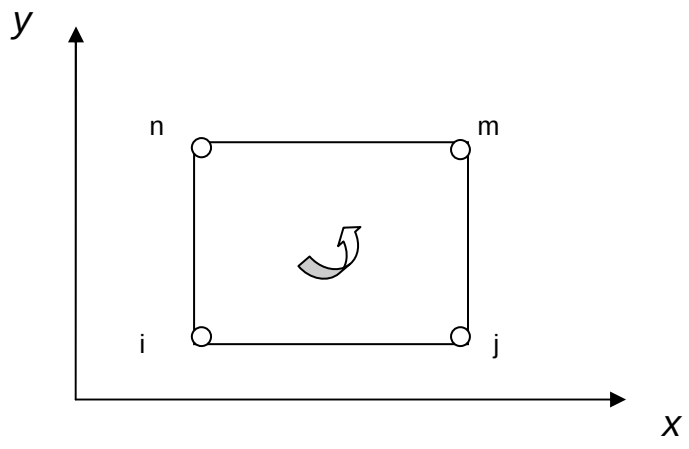

Figure 5.15 Rectangular concrete element (Wong and Vecchio, 2002)

5.3.2.1.1 Concrete Behavior Model

Different constitutive and behavioral models are available in VecTor2. The nonlinear behavior of the structure changes according to the model that has been selected. Therefore, it is extremely important for the user to have knowledge of all the models that are available and the effects of these models on the behavior of the structure. The material models assigned to the large scale specimen used in this study are discussed below. The Concrete pre-peak response was modeled using the default option. This is a simple compression curve model for concrete regions, and can be observed in **Figure 5.16**.The Hognestad Parabola can be used for concrete regions having a normal compressive strength. This model option computes the principal compressive concrete stress before the compressive strain reaches the peak compressive strain value, ε_p.

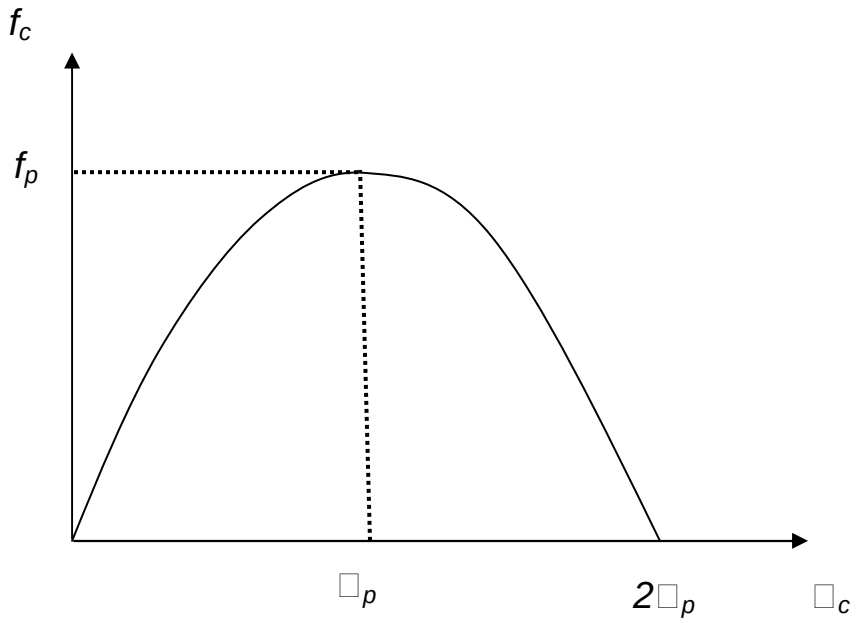

Figure 5.16 Hognestad Parabola for concrete pre-peak response (Wong and Vecchio, 2002)

The stress-strain relationship is symmetric about ε_p, diminishing to zero stress at zero strain and $2\varepsilon_p$. Note that the Hognestad parabola predefines the initial tangent stiffness, E_c, as follows: The Concrete Post-Peak Response was modeled using the "Modified Park-Kent" option, as illustrated in **Figure 5.17**. This is a modified "Park and Kent" model that accounts for the improved concrete compressive strength and ductility due to confinement. This option computes the principal compressive concrete stress after the compressive strain surpasses the peak compressive strain value, ε_p. The descending linear branch after the peak strain is followed by a plateau at a value of $0.2\,f`_c$.

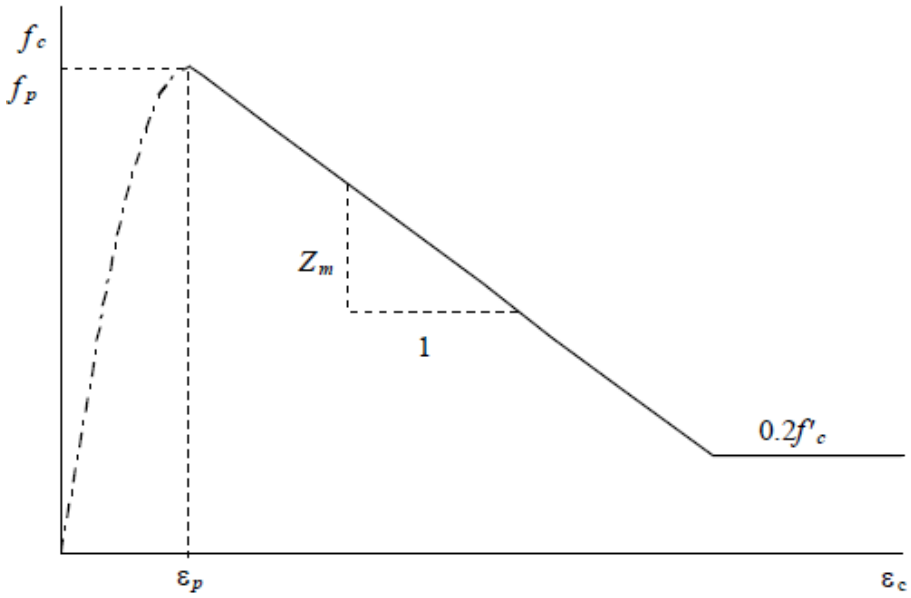

Figure 5.17 Modified Park-Kent for concrete post-peak response (Wong and Vecchio, 2002)

The Concrete compression softening models that are available in VecTor2 were developed from a series of panel and shell elements tested at the University of Toronto (Vecchio and Collins, 1992). The effect of concrete cracking on the compression strength and stiffness are taken into account by either strength-and-strain softened or strength-only softened models. From the four different models available in VecTor2, the default model, “Vecchio 1992-A (e1/e2-Form)” was assigned to the concrete material properties. Briefly, this is a strength-and-strain softened model in which both uniaxial compressive strength and strain values are softened. Concrete tension stiffening is the tensile resistance of cracked concrete arising from the bond with the reinforcement within the cracked regions. This phenomenon is especially important in finite element modeling. The coarseness of the element mesh has an important effect on simulating this behavior. The “Modified Bentz 2003” model, which is a rigorous adaptation of previous Bentz (2000) model, was selected to represent this behavior. This model incorporates the bond actions to the tension stiffening behavior, and accounts for two-dimensional stress conditions and for the placement of each type of reinforcement. The Concrete tension softening model considers the post-cracking behavior of concrete that has been described in many fracture mechanics approaches of concrete behavior after cracking. This is an important behavior to model especially for lightly reinforced concrete members. The default “linear” model, in which concrete tensile stresses are represented by a linearly descending branch, was selected for the modeling RC specimen in this study.

5.3.2.2 Reinforcement Model

All reinforcement was modeled using discrete bar elements. This option of modeling is recommended by VecTor when the area of interest is local stress-strain or the bond-slip response in the reinforcement. Reinforcement bars can be discretely represented with two-node truss elements which have nodal displacements in two directions and four degrees of freedom, as illustrated in **Figure 5.18.**

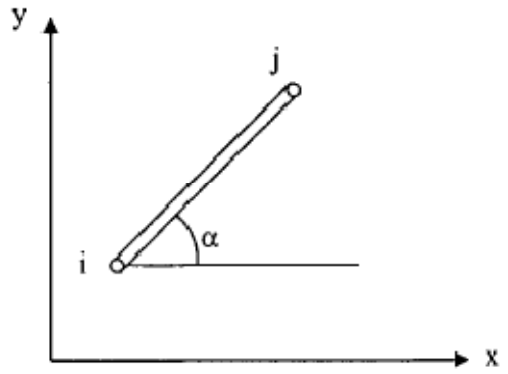

Figure 5.18 Truss element (Wong and Vecchio, 2002)

The model described in this section is the default option, “Seckin w/ Bauschinger Effect”, used for modeling purposes in this study. This is a formulation developed by Seckin (1981) for the hysteretic response of reinforcement which includes the Bauschinger effect. After the plastic prestraining, the local stress changes upon load reversal result in premature yielding of reinforcement. As shown in **Figure 5.19**, the monotonic stress-strain curve is followed by a linear unloading curve. As monotonic loading was applied to the specimen in this study only monotonic stress-strain curve was used as shown in the following figure.

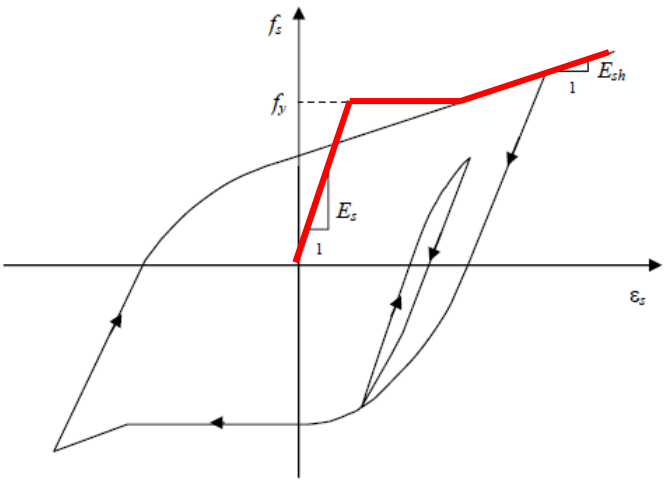

Figure 5.19 Seckin model for Hysteretic Response of reinforcement (Wong and Vecchio, 2002)

To stimulate post- peak response generated by steel fiber reinforced concrete different models discussed in VecTor2 user manual was investigated. However none of them showed expected response which was observed from laboratory testing. Therefore the model used for RC specimen (models discussed above) were also used to simulate analysis for SFRC specimens in order to capture the peak load and the corresponding failure pattern.

5.3.3 Modeling Results

5.3.3.1 Load-Displacement Response

The software has the capacity to give the load deformation curve, this curve was compared with testing data and resulted plots for all the specimen is given in **Figures 5.20** to **5.23**. Analysis was done by displacement control, the ultimate displacement seen from laboratory testing was used for this purpose. Looking at all the load-displacement curves it is seen that stiffness varies for each specimen, this is attributed to the method of measuring the load deflection response during testing. The true response is not shown as it is affected by local deformation near window. VecTor2 was unable to capture true load displacement response for SFRC specimens; this is because, software is not capable to produce the post peak response in case of SFRC (large deformation). Peak load from the analysis for RC, SFRC#1, SFRC#2 and SFRC#3 specimens was 119 kips (530 kN), 50 kips (222 kN), 49 kips (220 kN) and 94 kips (419 kN) respectively.

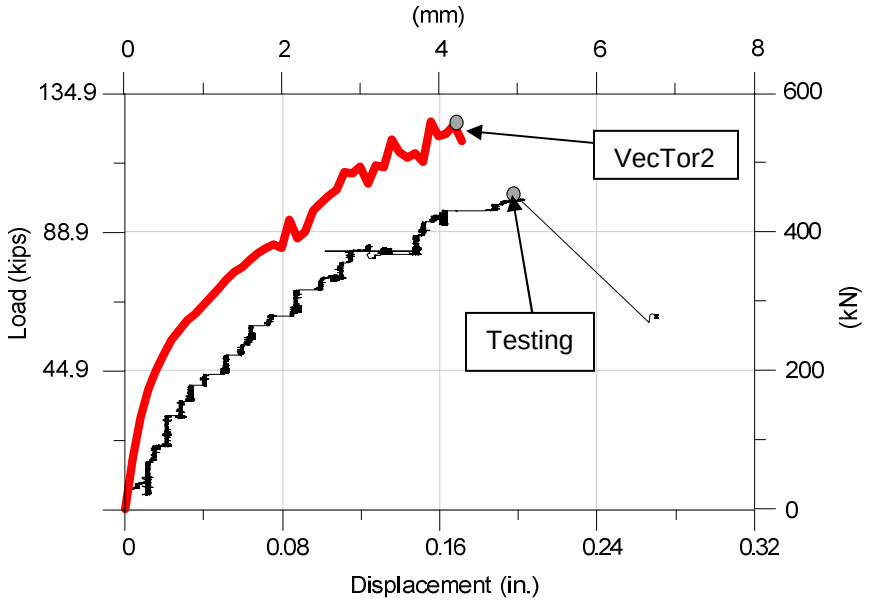

Figure 5.20 Load-Deformation curve (RC Specimen)

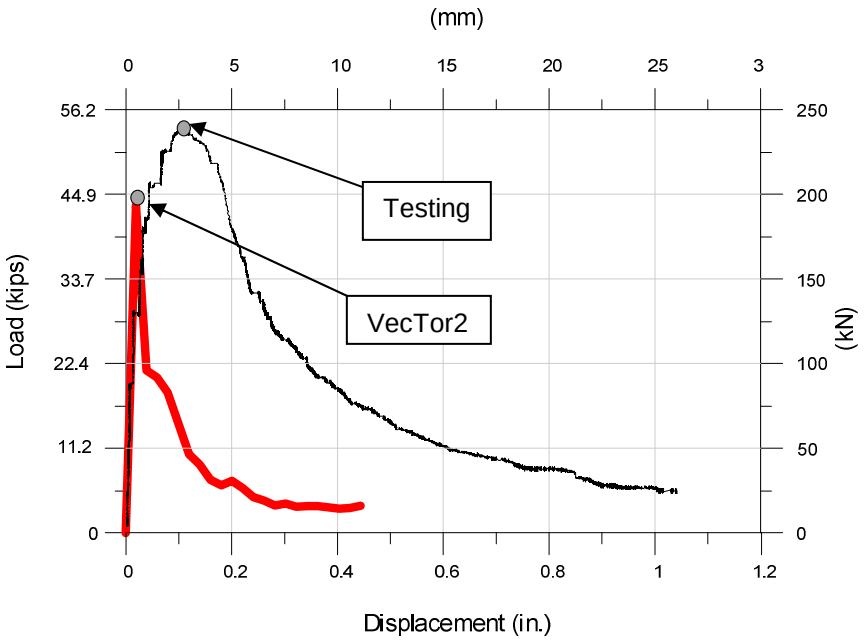

Figure 5.21 Load-Deformation curve (SFRC#1 Specimen)

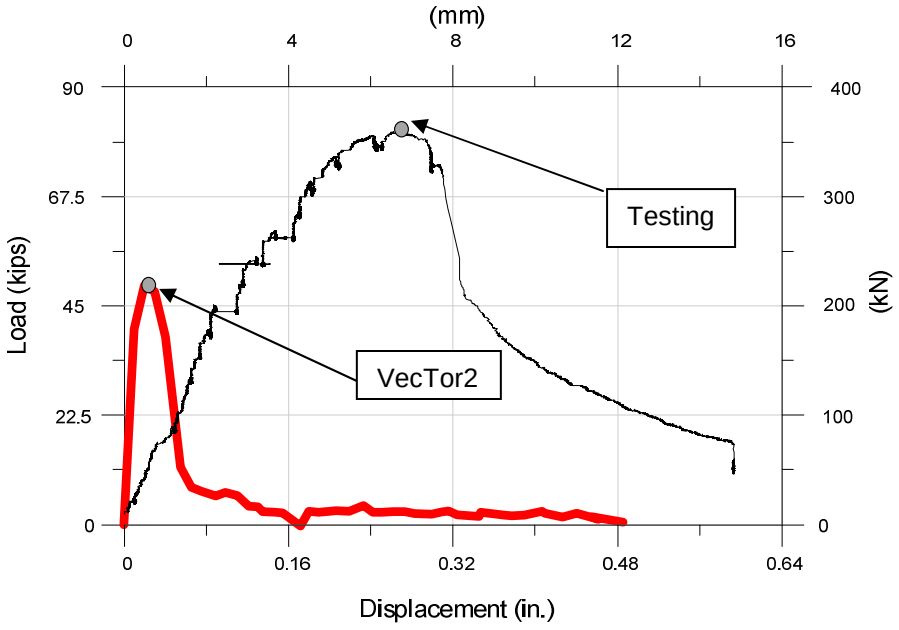

Figure 5.22 Load-Deformation curve (SFRC#2 Specimen)

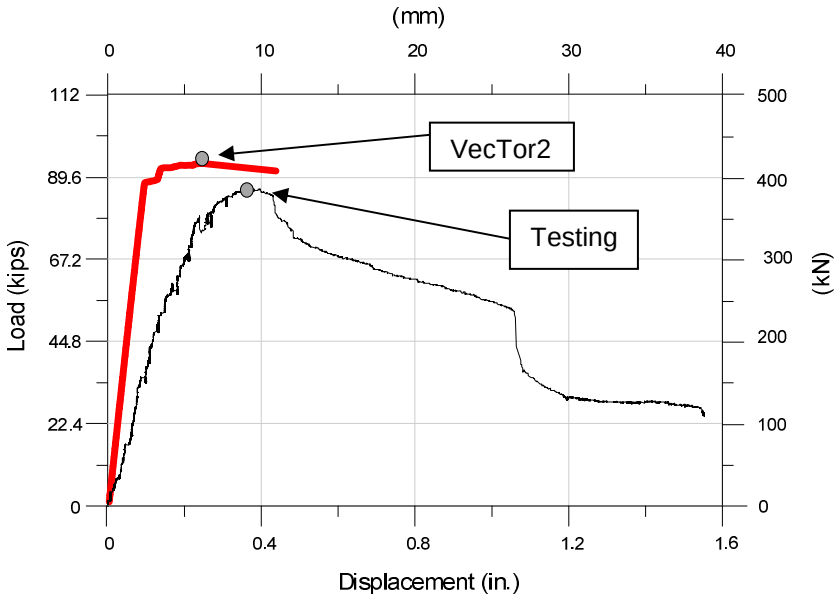

Figure 5.23 Load-Deformation curve (SFRC#3 Specimen)

5.3.3.2 Failure Pattern

As discussed earlier results was analyzed by using post-processor, Augustus. Combines view of cracking pattern and deformation was plotted to cite final failure mechanism. From the results it is seen that VecTor2 was able accurately capture the failure pattern in case of SFRC specimens, however the brittle localized failure observed during laboratory testing in case of RC was not captured. The reinforcement layout for all the modeled specimens is shown in **Figures 5.24** to **5.27**. As discussed earlier displacement control method of analysis was used. VecTor2 terminates the analysis once there is large displacement in the specimen in single increment. This is because the solution fails to converge and the stiffness matrix becomes negative. The final failure modes for all specimens with displacement magnification factor of 20X are shown in figures below**.** In RC specimen the analysis was terminated as there was sever cracking in horizontal segment of lower left window and also near right bottom corner of right window (see **Figure 5.29**). In case of SFRC#1 specimen no longitudinal reinforcement was used, from the analysis result it failed due to large crack propagating from bottom fiber towards loading point. The failure mechanism from the analysis was in agreement with the testing results and was due to excessive increase in crack width (see **Figure 5.31**). In case of SFRC#2 specimen failure mode predicted by VecTor was exactly same as observed from testing (see **Figures 5.34** and **5.36**), and was due to vertical crack extending thought the horizontal segment of lower left window also debonding observed during testing was captured by VecTor2. Similarly for SFRC#3 specimen VecTor was able to accurately capture the location of cracks.

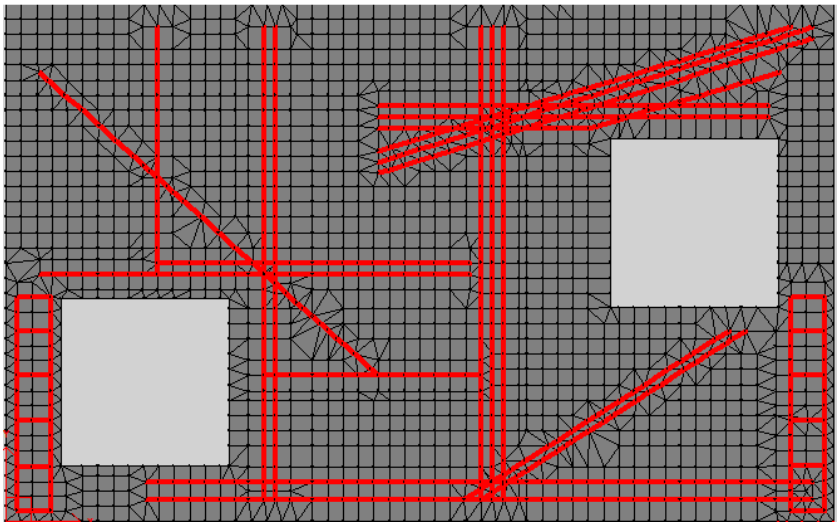

Figure 5.24 Reinforcement layout in VecTor – RC specimen

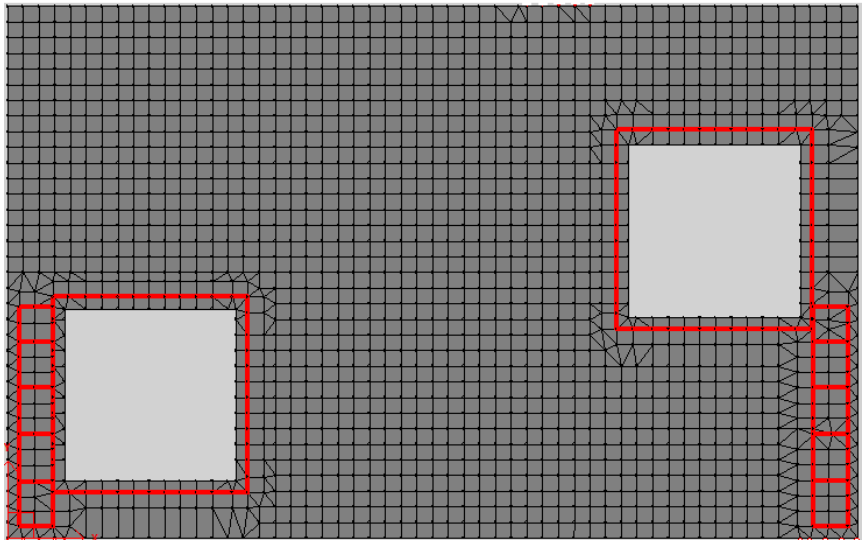

Figure 5.25 Reinforcement layout in VecTor – SFRC#1 specimen

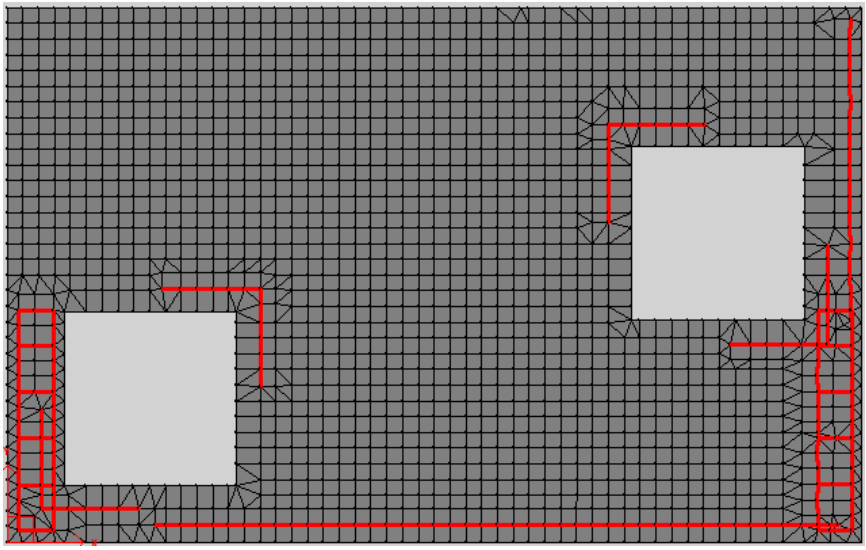

Figure 5.26 Reinforcement layout in VecTor – SFRC#2 specimen

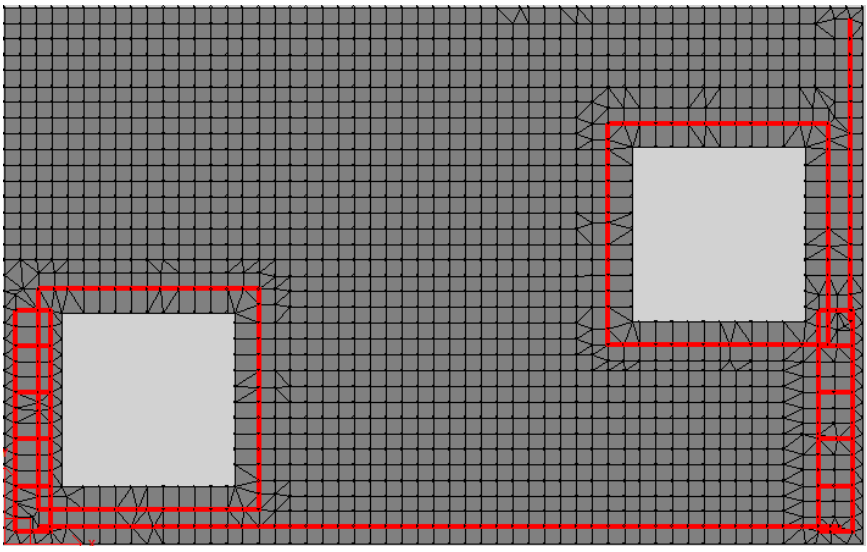

Figure 5.27 Reinforcement layout in VecTor – SFRC#3 specimen

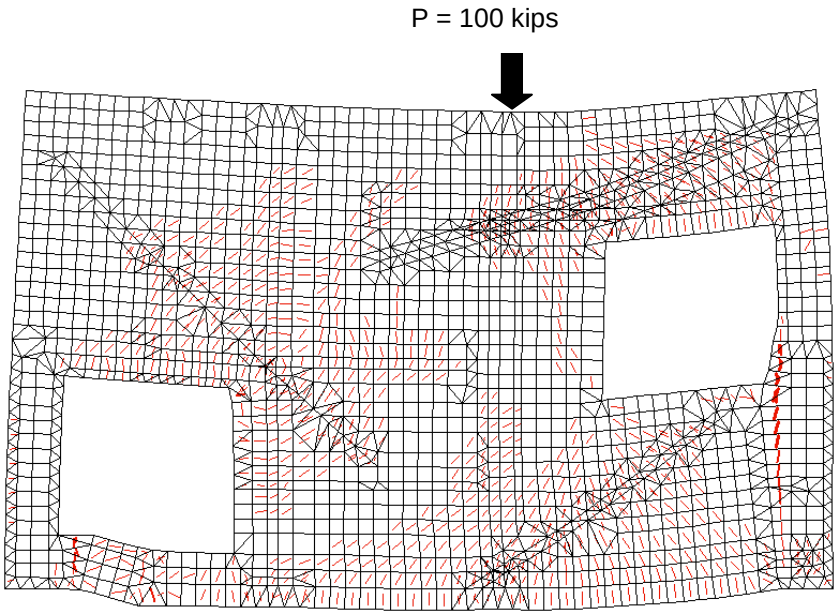

Figure 5.28 Cracking pattern predicted by VecTor2 – RC specimen

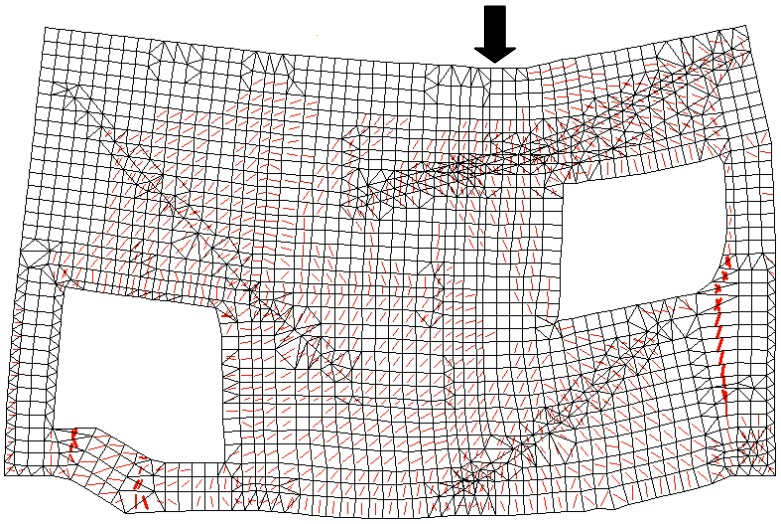

Figure 5.29 Failure mechanism predicted by VecTor2 – RC specimen (Displacement factor 20X)

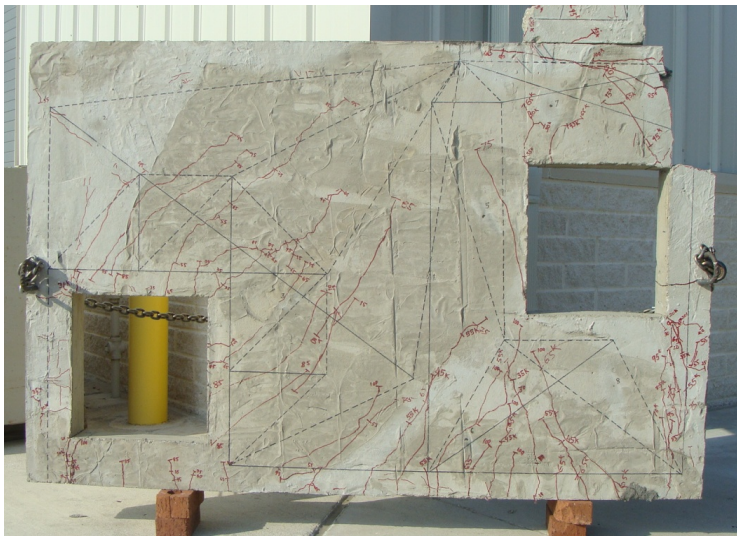

Figure 5.30 Overall state of RC specimen after testing

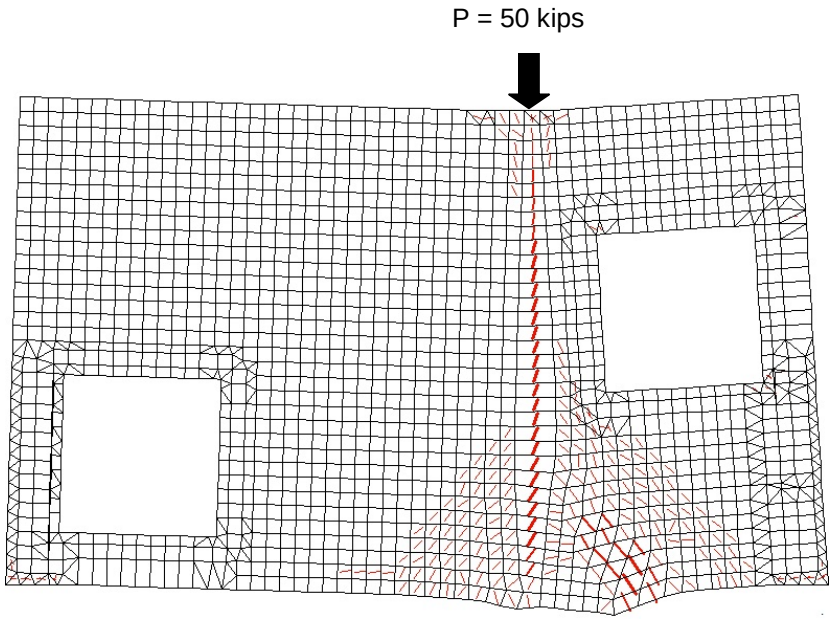

Figure 5.31 Cracking pattern predicted by VecTor2 – SFRC#1 specimen

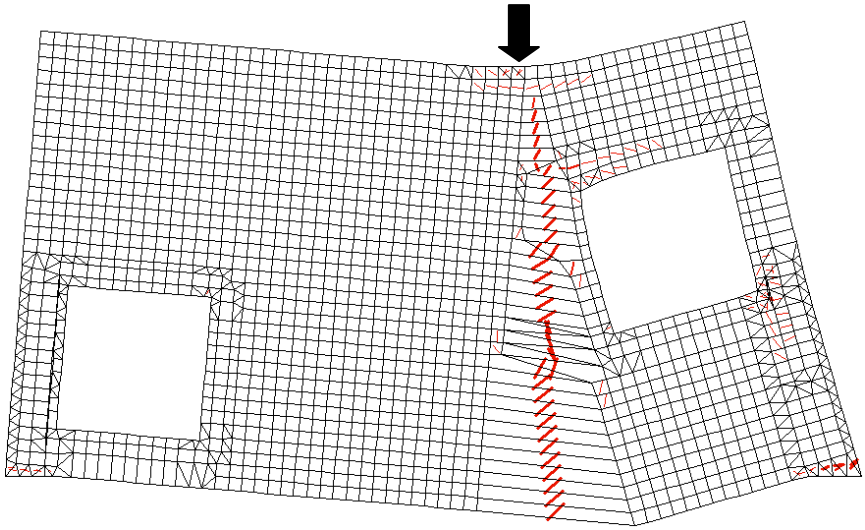

Figure 5.32 Failure mechanism predicted by VecTor2 – SFRC#1 specimen (Displacement factor 20X)

Figure 5.33 Overall state of SFRC#1 specimen after testing

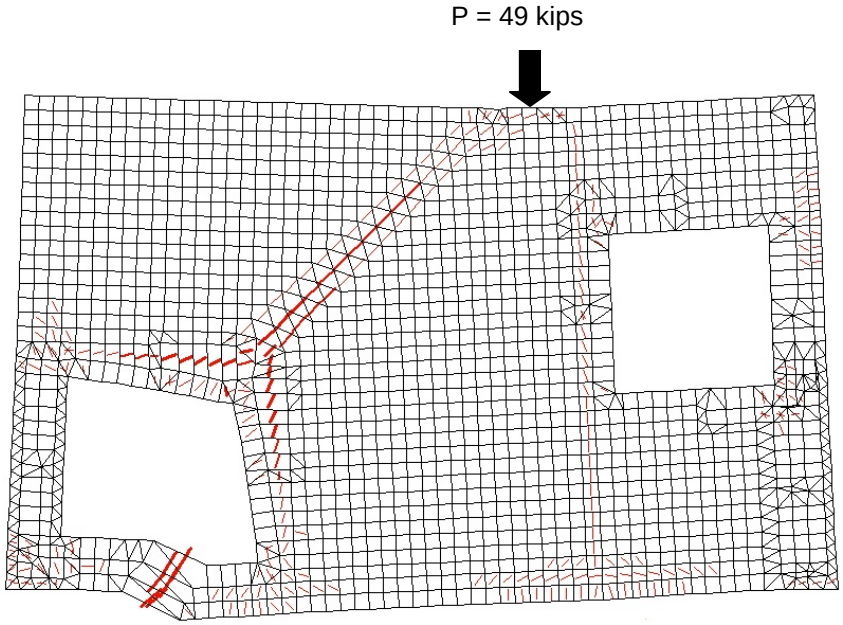

Figure 5.34 Cracking pattern predicted by VecTor2 – SFRC#2 specimen

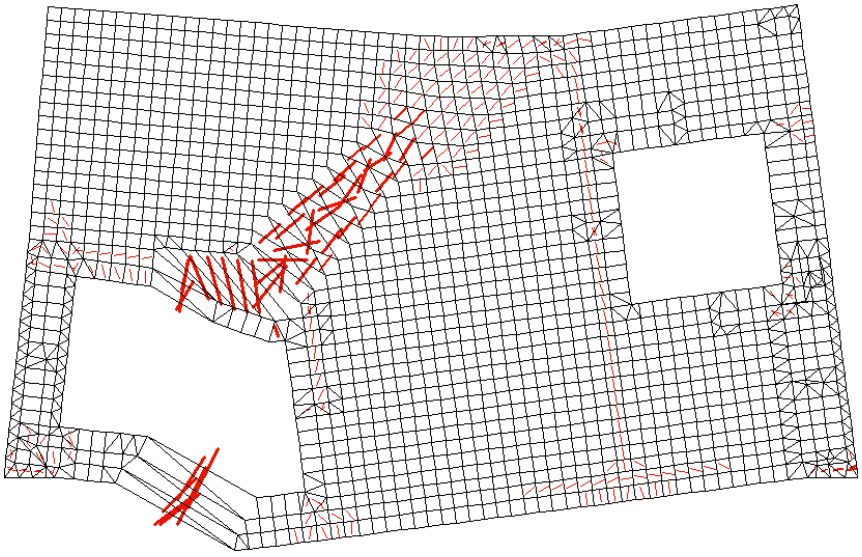

Figure 5.35 Failure mechanism predicted by VecTor2 – SFRC#2 specimen (Displacement factor 20X)

Figure 5.36 Overall state of SFRC#2 specimen after testing

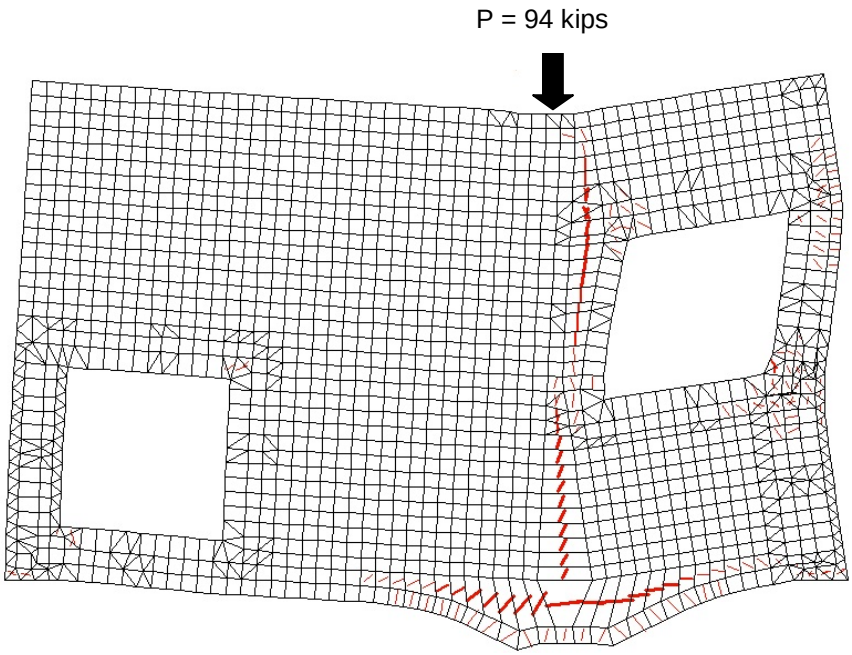

Figure 5.37 Cracking pattern predicted by VecTor2 – SFRC#3 specimen

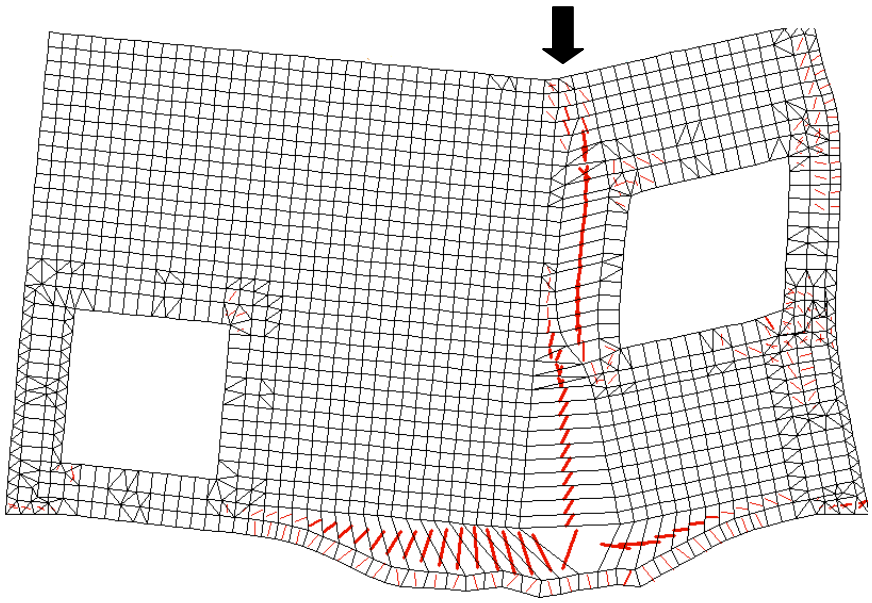

Figure 5.38 Failure mechanism predicted by VecTor2 – SFRC#3 specimen (Displacement factor 20X)

Figure 5.39 Overall state of SFRC#3 specimen after testing

5.4 Computer Aided Strut-and-Tie Analysis – RC Specimen

Strut-and-tie model discussed in this study was adopted from Breña and Morrison (2007). Expected strength based on analysis done by them was 47.7 kip (212 kN). However this model was tested for its capacity and design load on software developed by Tjhin and Kuchma at the University of Illinois at Urbana-Champaign (2002). The formulation of the model is presented in Appendix B and the output files for design calculations are presented in Appendix C. According to the analysis done by Breña and Morrison tie number 2 and 4 (see **Figure 4.2**) were suppose to yield at 47.7 kips (212 kN) load, however after testing it was found that only tie number 1 yielded at ultimate load of 83 kips (370 kN). This proves the fact that strut and tie model not only underestimates the strength of the structure but also cannot predict the failure mode.

The software can predict the capacity of system based on the input material properties. This feature was used to estimate the capacity using the provided steel reinforcement, concrete struts and nodal zones. Material properties obtained from testing were used for this purpose. The estimated capacity according to the software was 72 kips (320 kN) for the RC specimen. According to CAST, the failure would occur by yielding of the bottom tie. This mode of failure in strut and tie model is acceptable as it exhibits ductile behavior i.e. reinforcement bars yield before the failure which is contradiction of brittle failure of concrete strut.

During truss analysis in order to create stable strut-and-tie model stabilizers were induced by CAST (see **Figure 5.40**). Stabilizers are required to avoid ill-conditioned structure stiffness matrix in truss analysis. They do not have to be manually assigned to the model; they are identified by CAST and are not included in the dimensioning of STM Nodes. The numbers in parenthesis (O/S) shows the ratio of calculated to demand capacity. For any value greater than one, the actual force is greater than the model allows, therefore it has failed and is indicated by red region. Depending on the analysis (predicted strength based on the model or design strength) the program gives the tie that has analytically failed.

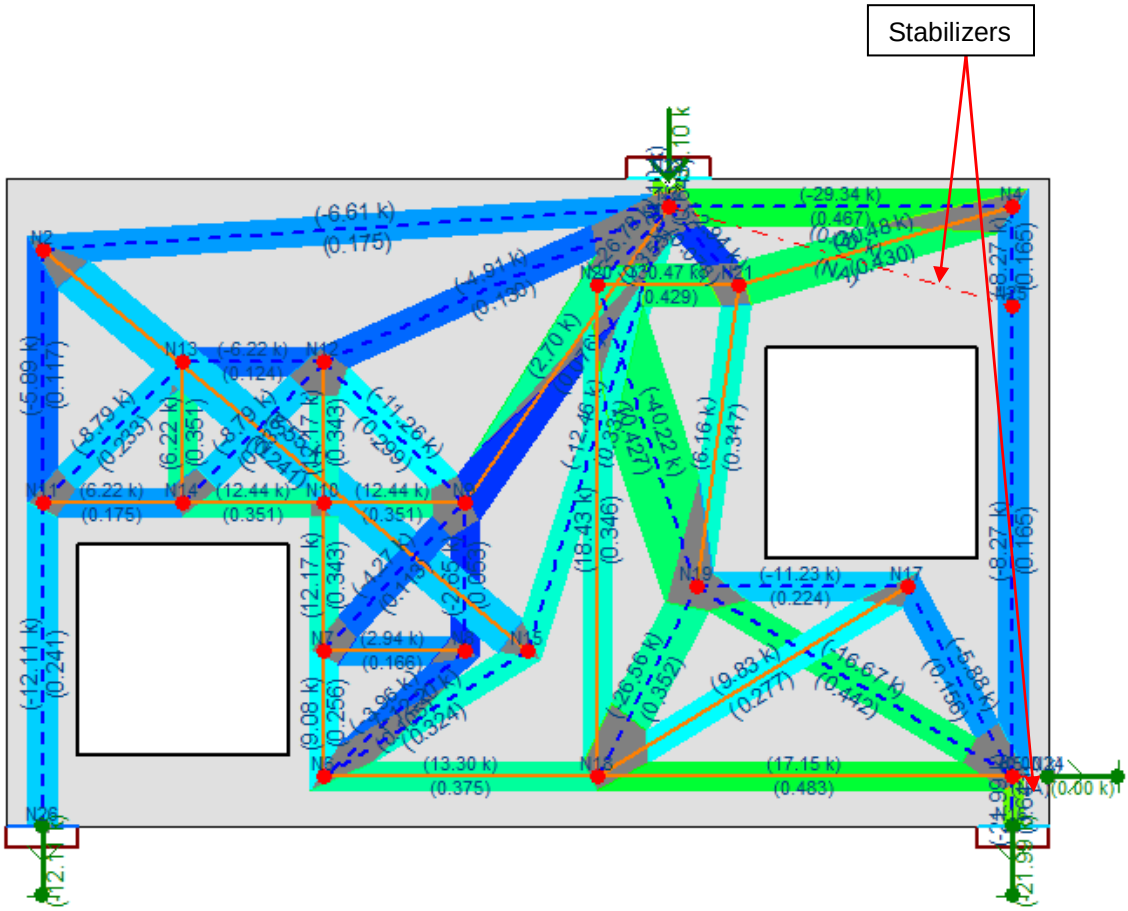

Figure 5.40 Strut and tie model analysis based on CAST at design load of 34.1 kip (unit less numbers indicate the ratio between demand and capacity of each member; O/S indicated)

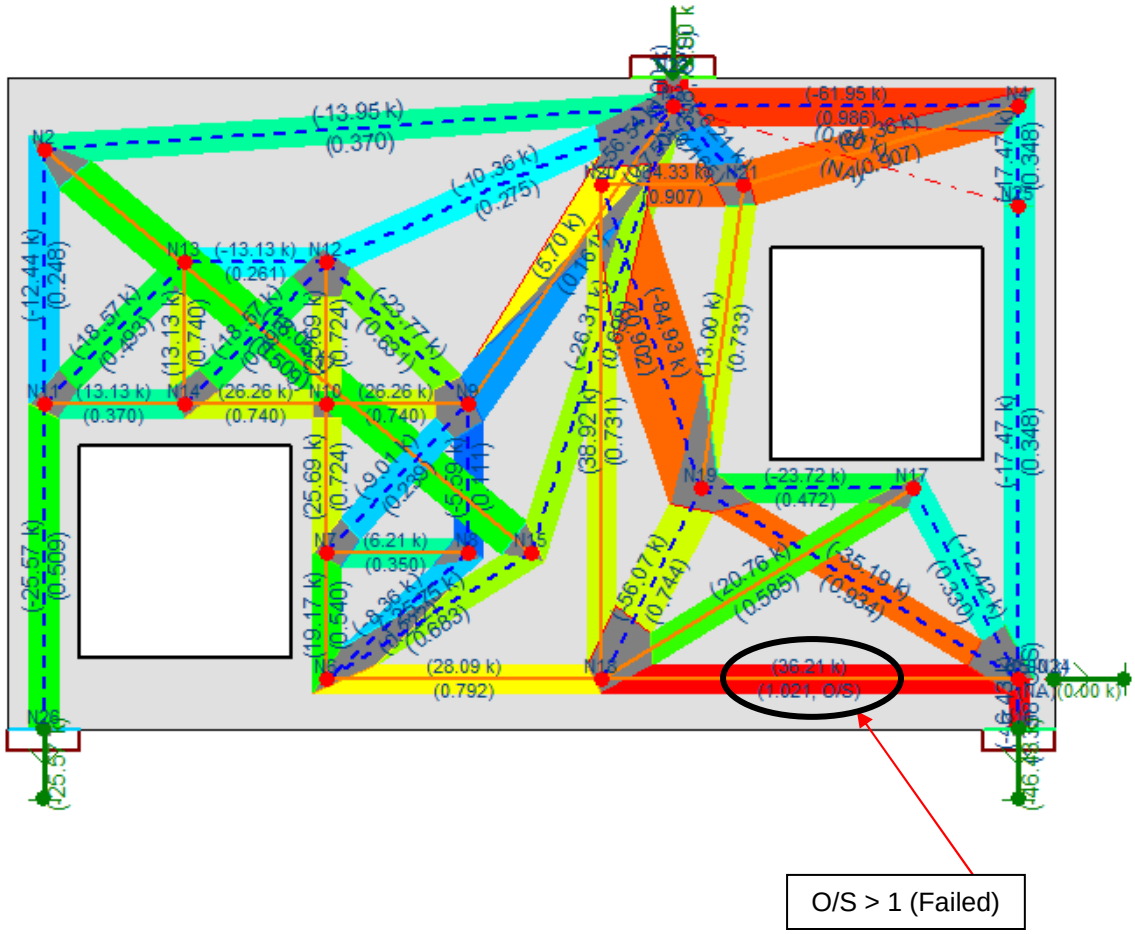

Figure 5.41 Strut and tie model analysis based on CAST at ultimate analysis load of 72 kips (unit less numbers indicate the ratio between demand to capacity of each member; O/S indicated over strength)

From the model in **Figure 5.41** it can be seen that O/S ratio exceeds it limit of 1 and CAST predicts tie will fail first. Concrete strut on top right corner of the beam has next higher ratio. Result from the lab test showed this tie yielded on 75 kips loading followed by yielding of tie T1. However when loading was tried to increase to 75 kips the region having next higher ratio exceed its limit of unity.

CHAPTER 6

SUMMARY, CONCLUSIONS AND RECOMMENDATIONS

6.1 Summary

Due to increase in population and industrialization the demand for land space is increasing rapidly as a result of which multistoried construction is gaining more popularity. Often in multistoried construction large open spaces without interior columns are required at bottom for business and parking etc. In order to provide such open spaces over large spans, structural elements such as deep beams are often used. These beams are also classified as deep walls if the extend to entire height of the floor. It is observed that forces in these structures can be effectively transferred through an arch mechanism to the supports (Muttoni, 2011). Past researches showed that these members have complex state of stresses, it becomes more complex when openings are provided in these structural members. These openings are generally provided for utility purposes such as passing duct, windows and doors. If these openings lie in between or obstruct the force transfer path (arch mechanism) it will adversely affect the performance of the structure. Muttoni (2011) suggested selecting an alternate force transfer mechanism to improve the performance. Therefore these members with significant geometric discontinuities and complex stress fields under loading require considerable analysis and usually complicated reinforcement detailing.

Strut-and-tie models (STMs) have typically been used to design deep beams. ACI 318-11 provide guidelines to design these members, however they do not provide any explicit design information when large openings exist in these members. Studies have shown that openings in these members significantly affect the load-carrying capacity (Ray, 1990). Based on limited

experimental studies (Maxwell and Breen, 2000; Chen et al. 2002; Kuchma and Park, 2007; Tan and Zhang, 2007; Ley et al., 2007; Breña and Morrison, 2007; Kuchma et al., 2008), it is inferred that STMs provide reliable, consistent and conservative results for deep beams with openings but fail to predict the ultimate load and failure modes. There is also concern on the early cracking under service load for members designed by STMs (Kuchma, 2008). Further, some tests have shown that large differences can occur between the calculated forces from STM and the actual instrumented experimental specimens (Breña and Morrison, 2007).

The concept of using small, discrete fibers as reinforcement for brittle materials has been known from thousands of years. There is evidence that the ancient Egyptians used straw to improve the cracking behavior of the sun-dried mud brick used in construction (Mansour et al., 2007). Shah and Rangan (1971) observed that the flexural toughness, enclosed area under the load-deflection curve, could be increased to five to fifteen times that of plain concrete when fiber contents of 0.5 to 1% were used, respectively. They also found that an increase in fiber content from 0.5% to 1.0% has been found to increase the direct tensile strength from 1.1 to 1.3 times that of plain concrete, and to increase the direct tension toughness from 1.8 to 2.7 times that of plain concrete.

This study investigated the effectiveness of using steel fibers in reinforced concrete members with significant geometric discontinuities, thus leading to complex stress fields under loading. The effectiveness was evaluated in terms of load-carrying capacity and ductility. Also accuracy of a few selected nonlinear computer programs (LUSAS, VecTor2, and CAST) to predict the failure modes and ultimate strengths of reinforced concrete and steel fiber reinforced concrete deep beams with openings was investigated. The studied deep beam specimens had two large openings which induced complex stress fields upon loading. Strut-and-tie model (STM) used in this study was also adopted in past by Breña and Morrison (2007).

Reinforced Concrete (RC) specimen was designed according to strut-and-tie model and had very complicated detailing. On the contrary SFRC specimens were designed based on a

simple procedure which starts from performing two-dimension elastic finite element analysis (FEA). In total three SFRC specimens were casted; the idea was to strategically locate the reinforcement bars at “critical locations” where high flexural demands (f_p) were identified from FEA. The reinforcement bars used in SFRC specimens served as “ductile links” to prevent the breakdown of the highly stressed regions before the fully plastic redistribution of internal forces through steel fibers. After testing of Specimen SFRC#1 the results were analyzed and further modifications in reinforcement layout was done. As discussed earlier while deciding the reinforcement layout synergetic interaction between fibers and reinforcement steel was kept in mind also there was constant motivation to use minimum amount of reinforcement steel in order to evaluate the performance of fibers. The efficiency of strut-and-tie model to predict the ultimate strength of the RC specimen was evaluated by using computer aid strut and tie (CAST) program (Tjhin and Kuchma, 2002).

All steel fiber reinforced concrete (SFRC) specimens which were designed based on FEA and the concept of ductile links performed very well as compared to RC which was designed based on strut-and-tie model. RC specimen reached almost 3 times the design load; however there was sudden release of energy as it failed due to unexpected localized brittle fracture, which can hardly be predicted by the strut-and-tie model. On the other hand, all the SFRC specimens which had much less conventional reinforcement steel as compared to RC specimen exhibited more controlled/ductile behavior and reached almost more than 3 times the deflection that that of the RC specimen.

SFRC#1 specimen failed when the longitudinal crack originating from the bottom fiber of the beam extended to the corner of the lower right opening; as a result beam could not carry any further load. This failure mode was expected as no longitudinal reinforcement was used at the bottom; however it reached almost 1.5 times the design load. Volume fraction of steel hooked fiber used in this specimen was 1.5%. Analyzing the specimen after testing also revealed that one-inch cover (centre of bar to face of formwork) used for the closed steel loops

around the openings was not sufficient to accommodate fibers, as very less fibers were observed after crack opened around the upper opening. For next specimen (SFRC#2) the cover was increased to two inches. Instead of using closed loops as those in SFRC#1, only 90 degree hooks were used, also longitudinal reinforcement was included at the bottom of the specimen but was not extended all the way into the support at one end, this was done as suggested by Breña and Morrison so as to allow the potential detrimental effects of apparently inadequate reinforcement detailing on the load carrying capacity. The final failure was in the bottom horizontal segment of lower left opening. Crack propagated along the section which the longitudinal bars did not pass through; also development length of 90 degree hooks was found to be insufficient as there was severe debonding of the bars observed; however the specimen reached almost 2.5 times the design load with almost negligible amount of reinforcement steel and 1.5% volume fraction of fibers. For the third SFRC specimen (SFRC#3) a few important modifications were made, one of them was that the volume fraction of fibers was reduced to 1% also the reinforcement layout of this specimen was based on the observed failure modes of the first two SFRC specimens . This specimen was reinforced with two layers of closed square loop reinforcement bars around the openings with two-inch cover and longitudinal reinforcement which extended into both the supports. The specimen sustained almost 2.5 times the design load and failure occurred due to excessive flexural cracking, excessive deformation was observed due to formation of plastic hinges at several locations. The sudden energy release of the RC specimen was mitigated in all the SFRC specimens, due to fiber bridging effect, as seen visually and measured by Acoustic Emission sensors. From the load-deflection response of all the specimens it was not able to compare the individual stiffness of the specimens because the way the deflections were measure did not indicate true behavior as it can be affected by local deformations near the openings. It is seen, however, from the presented load-deflection responses, that the SFRC specimens failed in a more ductile and controlled manner. This ductile behavior can be attributed to the fiber bridging effect which allows for effective internal

stress redistribution. Moreover the first cracking loads in case of all SFRC specimens were higher than that of the RC specimen due to the presence of steel fibers in hindering the prorogations of micro-cracks. **Table 6.1** shows the first cracking loads for all the specimens tested.

Table 6.1 First cracking load for all specimens

	RC		**SFRC#1**		**SFRC#2**		**SFRC#3**	
	(kips)	**(kN)**	**(kips)**	**(kN)**	**(kips)**	**(kN)**	**(kips)**	**(kN)**
First Cracking Load	20	89	30	133	35	156	35	156

Note: 1 kips = 4.45 kN

Two dimensional linear elastic finite element analyses done on LUSAS proved an effective tool in identifying critical locations where the stresses exceeded the capacity of the SFRC materials. All reinforcing steel used in SFRC specimens was based on critical locations identified by FEA. Also nonlinear FEAs of all the specimens were carried out by LUSAS with material models obtained from results of material testing. This was done to investigate the accuracy of predicting the failure modes and ultimate strengths of the RC and SFRC specimens by LUSAS. Another nonlinear FEA program used was VecTor2. This program proved to be a useful tool in analyzing the final failure modes of the SFRC specimens. Results of analysis indicated that the failure modes of all SFRC specimens was captured by either LUSAS or VecTor2, however the brittle localized failure observed during test of RC specimen was not captured by either program. The ultimate loads for all the specimens predicted by LUSAS and VecTor2 was found to be comparable from the experimental testing data with the exception of RC specimen. Strains in reinforcement steel recorded during testing were also found to be in good agreement with analyses results from LUSAS for all the specimens with few exceptions; however it is important to note that strain gauge data can be significantly affected by localized

behavior. Furthermore a strut-and-tie analysis of the model adopted for the study was done for the RC specimen by software developed by Tjhin and Kuchma called CAST (2002). The estimated capacity of the STM, considering the actual material properties, predicted by CAST was 72 kip (320 kN); however even this program was unable capture the failure mode observed from the test.

Acoustic emission (AE) technique proved to be a valuable tool in investigating the location of micro-cracking inside the specimens. AE results revealed that the SFRC specimens showed more wide spread micro-cracking than that of RC specimens. This behavior was because steel fibers serve as a “bridge” that enables internal stresses to be redistributed from one region to the next, which led to a more complete plastic mechanism upon failure.

6.2 Conclusions

1. Structural members with complex stress fields such as RC deep beams/walls with large openings designed by STMs generally show uncontrolled/unpredicted failure mode. Also their failure mode and force transfer path do not coincide with that predicted by STM;
2. Specimens using steel fibers carried more than twice the design load even though almost negligible amount of steel reinforcing bars were used;
3. Results from the experiments showed that failure in case RC specimen used in this study was very brittle and it is difficult to predict both the failure location and ultimate load;
4. SFRC specimens showed better serviceability than RC specimen in terms of limiting cracking under moderate loading;
5. For the design of SFRC members, two-dimensional linear elastic finite element analysis is an effective tool in locating highly stressed regions needed to be reinforced so that

the breakdown of these regions can be prevented before the fully plastic redistribution of internal stresses through the bridging effect of steel fibers;

6. Proposed material solution can almost completely replace conventional reinforcing bars by using steel fibers with volume fraction of 1.0%;
7. Volume of steel reinforcing bars used in Specimens SFRC#1, SFRC#2, and SFRC#3 are only 16%, 13%, and 18%, respectively, of that used in the RC specimen. Following table gives total weight of reinforcement (including conventional reinforcement bars and steel fibers) in all specimens;
8. The construction of RC members with complex stress fields is typically time-consuming and labor intensive; on the other hand, SFRC members are much easier to construct and take very less time due to less complicated detailing.

Table 6.2 Comparison for weight of steel used in all specimens

Specimen	**Weight of Steel Used**		
	Conventional Reinforcement Rebar (lb)	**Steel Fibers (lb)**	**Total (lb)**
RC	51.9	0	51.9
SFRC#1 (V_f=1.5%)	17.2	60.0	77.2
SFRC#2 (V_f=1.5%)	18.7	60.0	78.7
SFRC#3 (V_f=1.0%)	24.5	40.3	64.8

9. This study clearly shows that using SFRC and simple reinforcement detailing can ensure sufficient load-carrying capacity and ample ductility of structural concrete members with significant geometric discontinuities. Following table summarizes the results from testing and analysis for the specimen used in this study.

Table 6.3 Summary of results for all specimens

Specimen	Design Load		Ultimate Strength from Nonlinear Analysis						Ultimate Strength from Experiments	
			LUSAS		VecTor2		CAST			
	kips	kN	kips	kN	kips	kN	kips	kN	kips	kN
RC	34.1	152	61.6	247	119	529	72	320	100	445
SFRC#1	34.1	152	50	222	50	222	-	-	53	236
SFRC#2	34.1	152	83	369	49	218	-	-	80	356
SFRC#3	34.1	152	60	267	94	418	-	-	87	387

Note: 1 kips = 4.45 kN

6.3 Recommendations for future work

a) Deep beams with same geometry but with varying size and geometry of openings can be investigated.

b) Different location for the openings can be investigated to see the effect on load-carrying capacity of the specimens.

c) Different type of fibers can be used to see the effect on performance of beams.

d) Different volume fractions of fibers can be used to see the effect of varying dosage on load-carrying capacity of deep beam with openings.

e) Beam can be loaded at different locations along the thickness to see how the load is transferred and its effect on load-carrying capacity.

f) Effect of cyclic loading can be investigated.

g) Welded wire mesh (WWR) can be used as secondary reinforcement and fiber dosage can further be reduced to investigate its effect on load-carrying capacity of the specimen.

h) Develop a reliable and comprehensive design aid for engineers to design deep beams with openings using steel fiber reinforced concrete (SFRC).

APPENDIX A

NON-LINEAR MODELLING ON LUSAS

A.1 Introduction

A nonlinear plane stress analysis is carried on a model of deep beam with two web opening. The superposition of nodal degrees of freedom assumes that the concrete and reinforcement is perfectly bonded. It also assumes that self weight of beam is negligible compared with the applied load. The concrete section is represented by plane stress (QPM8) elements and the reinforcement bars are represented by bar (BAR3) elements. A nonlinear concrete cracking material model will be applied to plane stress elements and a von Mises plastic material will be applied to the reinforcement bars.

A.2 Specimen Layout

The beam is simply supported and is 74 inches (1875mm) long, 47 inches (1170mm) deep and 4.4 inches (117mm) thick. It has two square openings one at left bottom corner and other at right top corner. Size of the opening is 15x15inches (380mm).

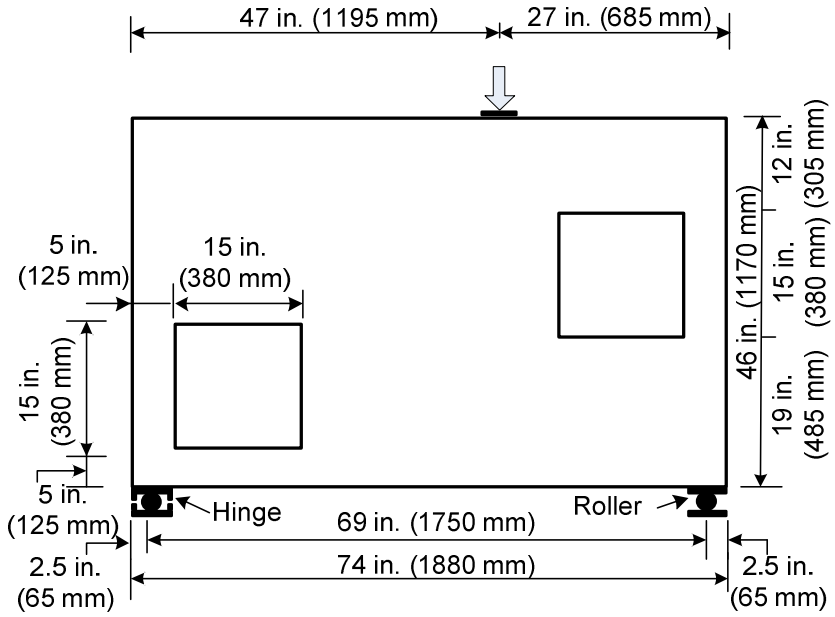

Figure A.1 Detailing of Deep beam with web opening

Step by step procedure for creating the model for specimen no 3 is discussed below, model for other specimens can be created similarly.

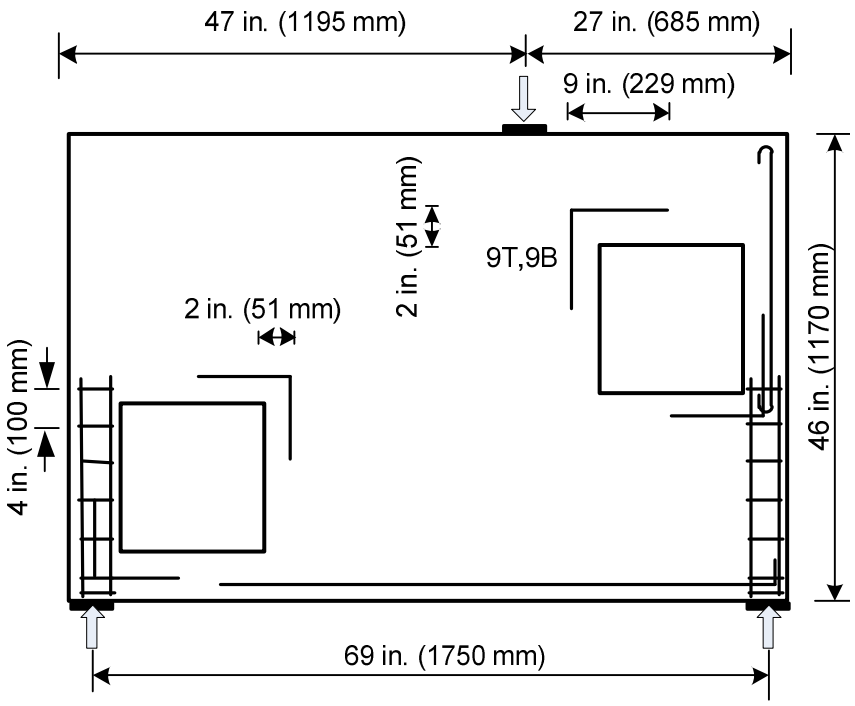

Figure A.2 Details of SFRC#2 specimen with reinforcement bars

All the reinforcement bars were standard no 3 bars. Concrete cover of 1 inch was used unless otherwise mentioned. Steel plate for both supports and loading are used to have a good load distribution and was assigned elastic steel properties from material library of LUSAS.

Unites used are kip, in, kslinch, s, F

A.3 Creating model

- Enter the file name as “Deep beam with web opening”.
- Use default working folder.
- Enter the title as Nonlinear concrete beam.
- Set the units as kip, in, kslinch, s,F.
- Select structural as user interface.

- Select the model startup template Standard.
- Select the Vertical Y axis option
- Click ok button.

Defining the Geometry:

➢ Geometry >Line>Coordinates….

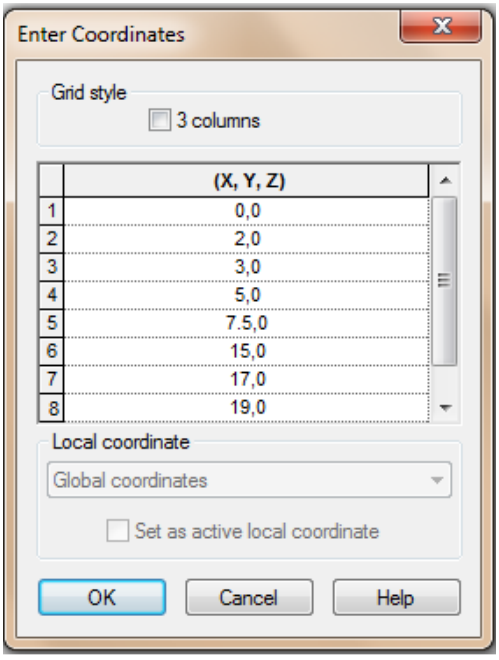

Figure A.3 Coordinates for model

Enter coordinates of (0, 0), (2, 0), (3, 0),(5,0)….. to define two Lines representing the bottom of the beam. Click the OK button to finish. Add more coordinates according to the geometry, it is better to have more lines at small spacing to have a better uniform mesh because in LUSAS mesh is assigned to lines.

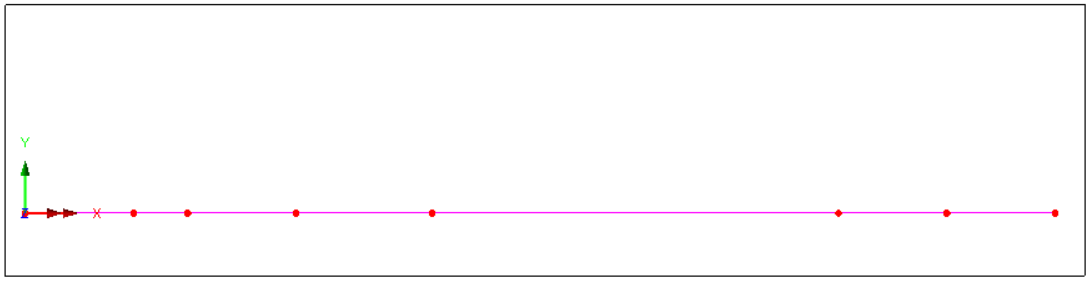

Figure A.4 Model after defining coordinates

- Select all lines just drawn by dragging a selection box around them.

➢ Geometry>Surface>By Sweeping…

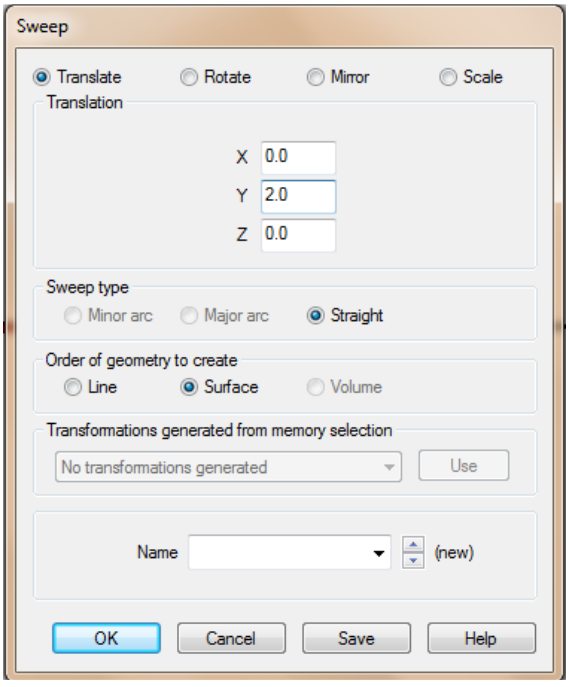

Figure A.5 Defining geometry by sweeping line.

Enter a translation value of 2 in the Y direction to create the Surface which represents the concrete cover from the face of the beam.

- Click the OK button.
- Select the upper Lines of the Surfaces just drawn as shown.

Enter different translation values in the Y direction to create various surfaces according to the geometry of the specimen. It is important to select topmost lines every time you create a new surface.

- Click the OK button.

The model should appear like this….

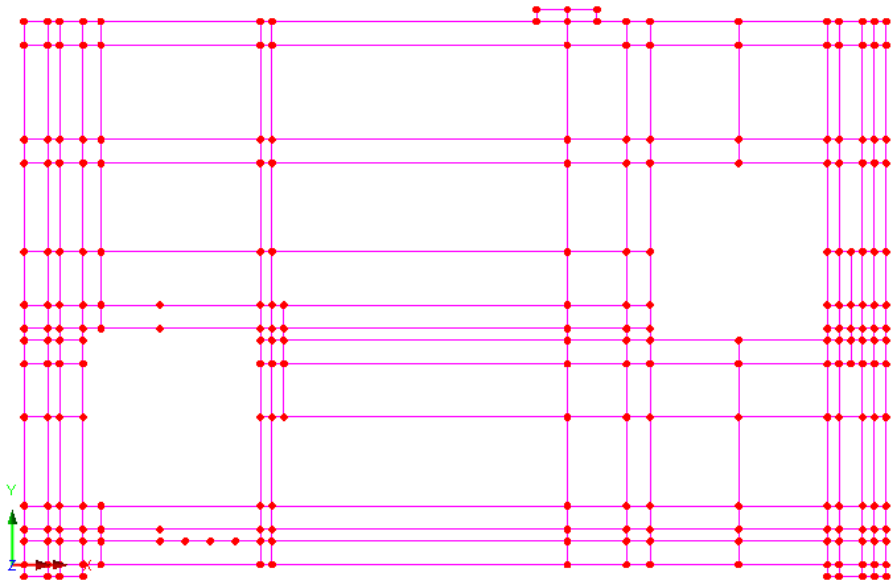

Figure A.6 Model after defining geometry

Defining Groups

To simplify the assignment of model attributes certain model features will be grouped together to allow selection by name in the Treeview as opposed to selection by cursor in the graphics window. The lines shown represent the reinforcement bars are and will be to be grouped together:

- Ensure the lines shown (reinforcement bars) are still selected as shown.

➢ Geometry>Group>New Group…

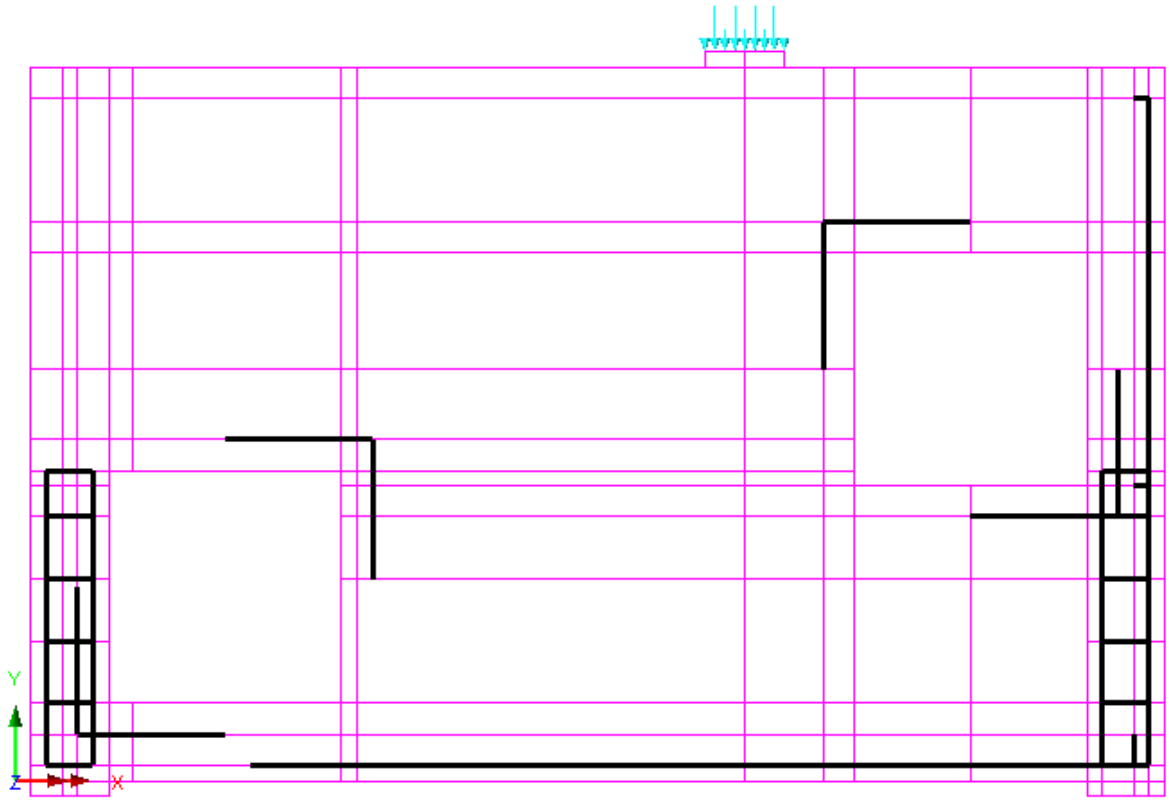

Figure A.7 Model with lines representing reinforcement bars selected

Enter Bars for the group name.

- Click the OK button to complete creation of the group.

The Surfaces representing the concrete are to be grouped together.

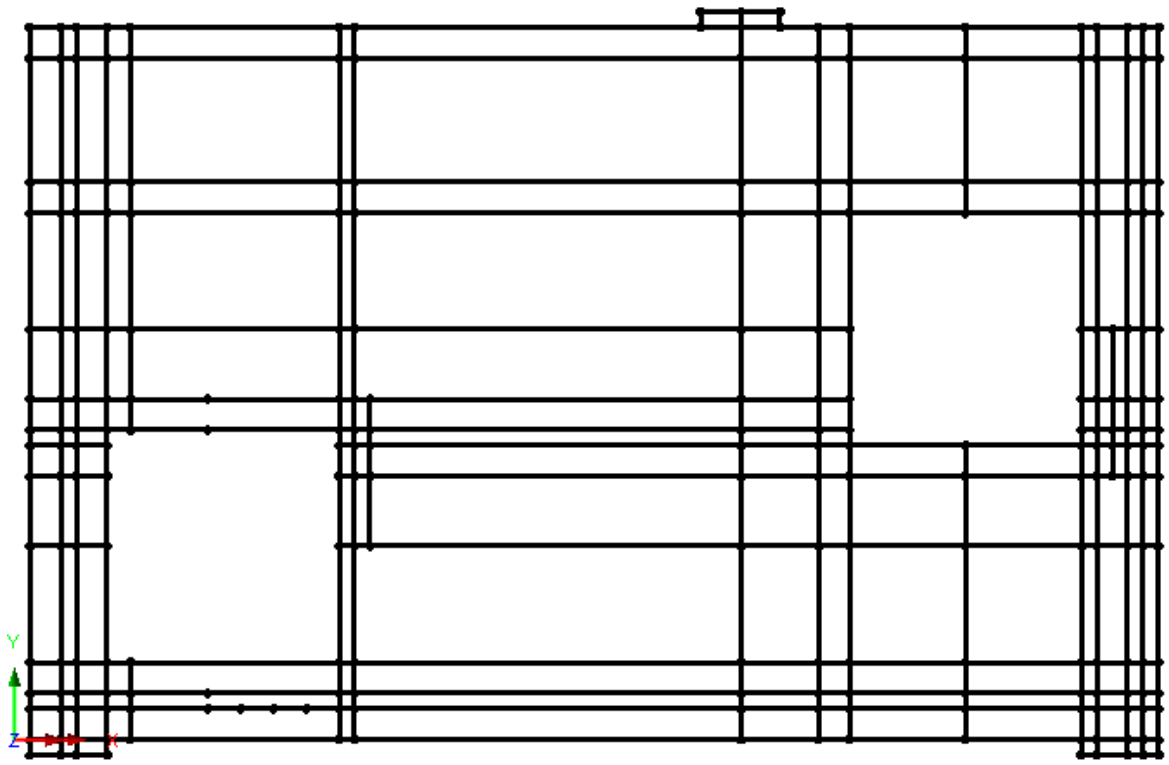

Figure A.8 Model with all surfaces selected

- Holding-down the S key, (and noting that the cursor changes to show the type of feature that will be selected) drag a box around the whole model to select only the Surfaces defining the concrete.

- Enter Concrete for the group name. Click the OK button to complete creation of the group.

Note. The model attributes will be defined but not assigned to the model straight away. They will be assigned to the model later by making use of the groups facility.

Defining the Mesh Reinforcement Bars

Separate mesh datasets need to be defined for the reinforcement bars and the concrete. For the reinforcement bars a uniform mesh is to be used. The reinforcement bars is modeled using Line meshes.

- Attributes>Mesh>Lines….

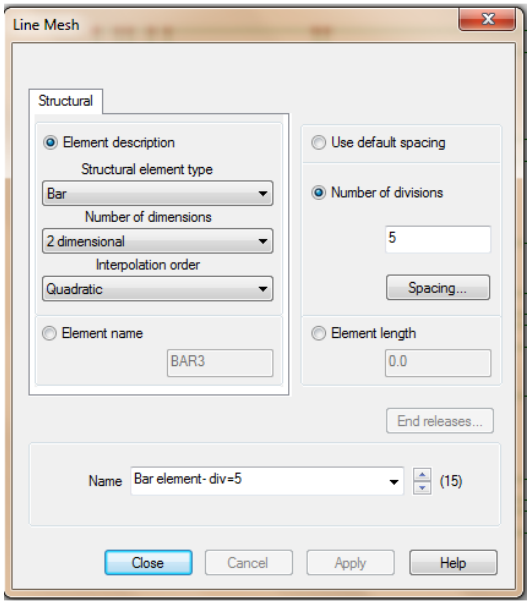

Figure A.9 Defining Mesh for bars

- Set Generic element type to Bar, Number of dimensions to 2 and Interpolation order to Quadratic.
- Ensure the Number of divisions is set to 5 (set this value according to the length of the line).
- Enter the attribute name as Bar Elements - Divs=5
- Select a Uniform transition ratio of first to last element of 5 and click OK
- Change the attribute name to Bar Elements - Divs=5
- Click the Apply button to create the attribute in the Treeview and leave the dialog visible in order to allow additional datasets to be defined.
- When defining all the mesh for reinforcement bar is finished click the OK button to finish.

Defining the Mesh Concrete

The concrete was modeled using a Surface mesh with Line mesh divisions to control the mesh density. The default mesh density of 4 divisions per line. A graded line mesh will be created for use on the Surfaces.

- Attributes> Mesh>Surface…

- Select Plane stress, Quadrilateral, Quadratic elements.
- Enter the attribute name as Plane Stress - Concrete
- Click the OK button to add the attribute to the Treeview.
- In the Treeview double click the Line mesh attribute name Divisions=2.
- The Line mesh properties dialog will appear.
- Click the Spacing button.
- Select Uniform transition ratio of first to last to first element of 2 and click OK.
- Change the attribute name to Divisions=2.
- Do this for all the vertical and horizontal lines in the model (change the values according to length of lines), it is very important to have a uniform spacing (in according to the length of line) to have a uniform mesh.
- Click the OK button to add the attribute to the Treeview.

Defining the Geometric Properties

- Attributes>Geometry>Line…..

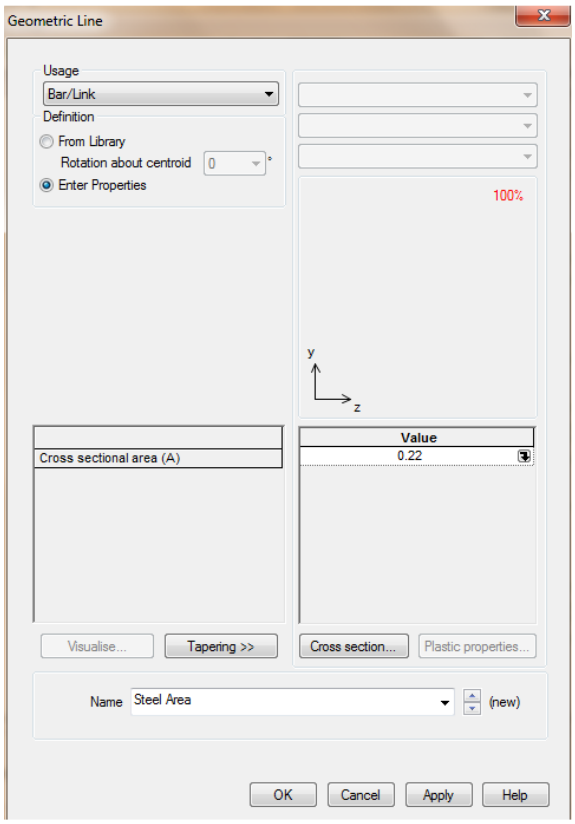

Figure A.10 Defining area for steel reinforcement.

- Select Bar/Link from the drop down list and enter a value of 0.22 for the total cross sectional area of the reinforcement.
- Enter the attribute name as Steel Area and click the OK button to add the attribute to the Treeview.

➢ Attributes>Geometric>Surface…..

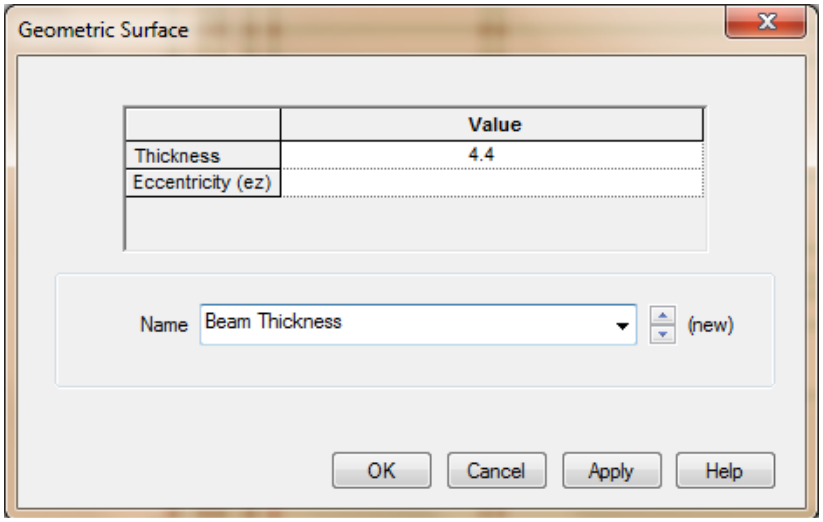

Figure A.11 Defining beam thickness

- Enter a value of 4.4 for the thickness. Leave the eccentricity blank.
- Enter the attribute name as Beam Thickness and click the OK button to add the attribute to the Treeview.

Defining the Material Properties

➢ Attributes>Material>Isotropic….

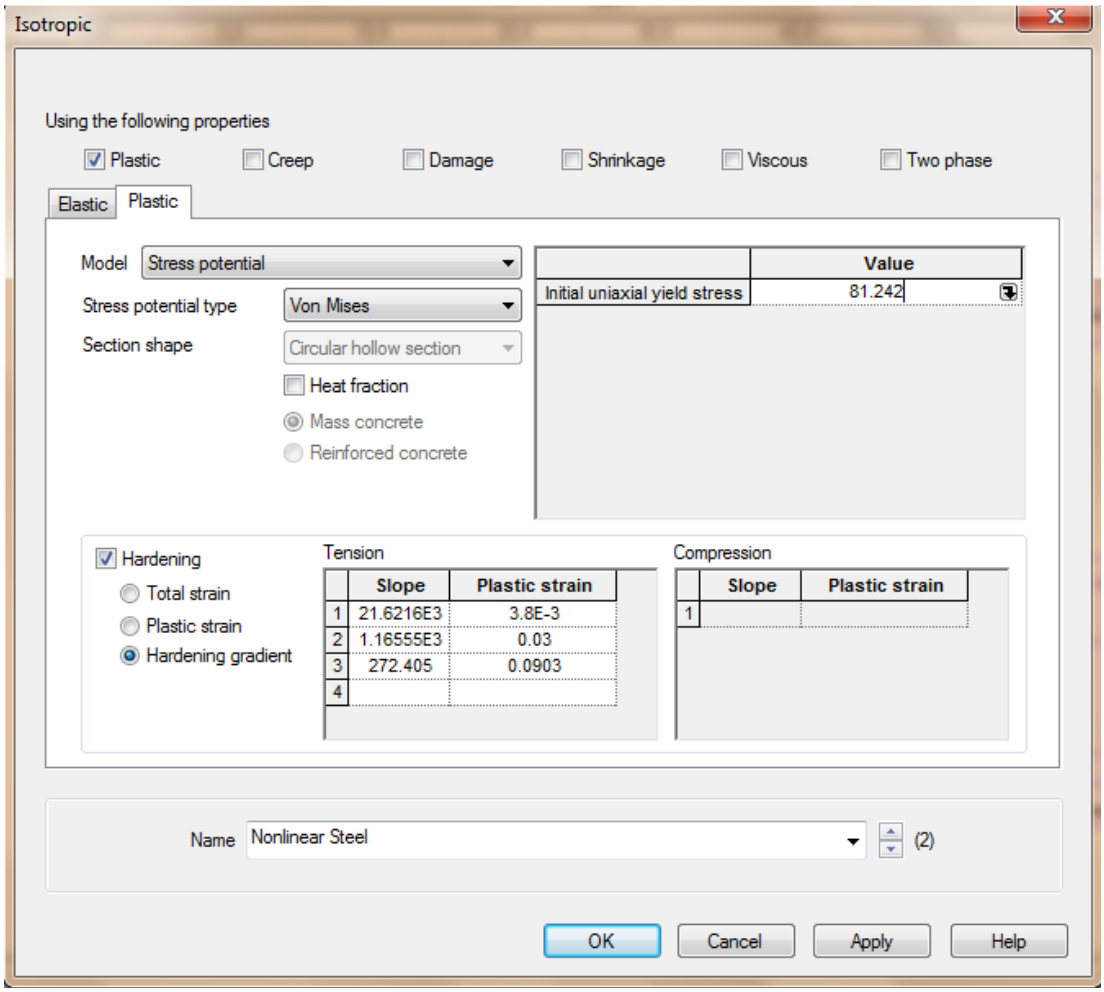

Figure A.12 Defining plastic material properties for steel.

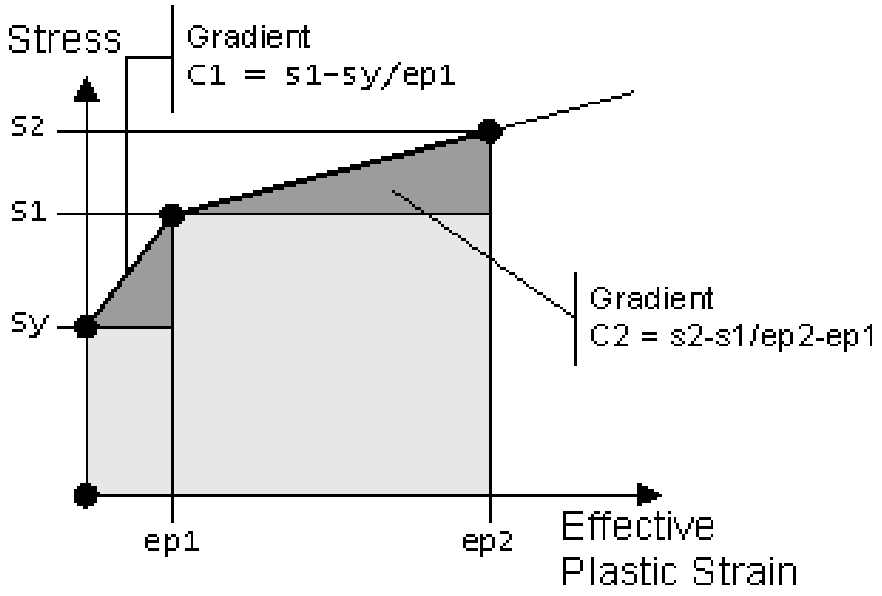

Figure A.13 Example of stress vs Strain curve for steel

Hardening gradient vs. Effective plastic strain requires specification of gradient and limiting strain values for successive straight line approximations to the stress vs. effective plastic strain curve. In this case hardening gradient data will be input as (C1, ep1), (C2, ep2) for each straight line segment. LUSAS extrapolates the curve past the last specified point.

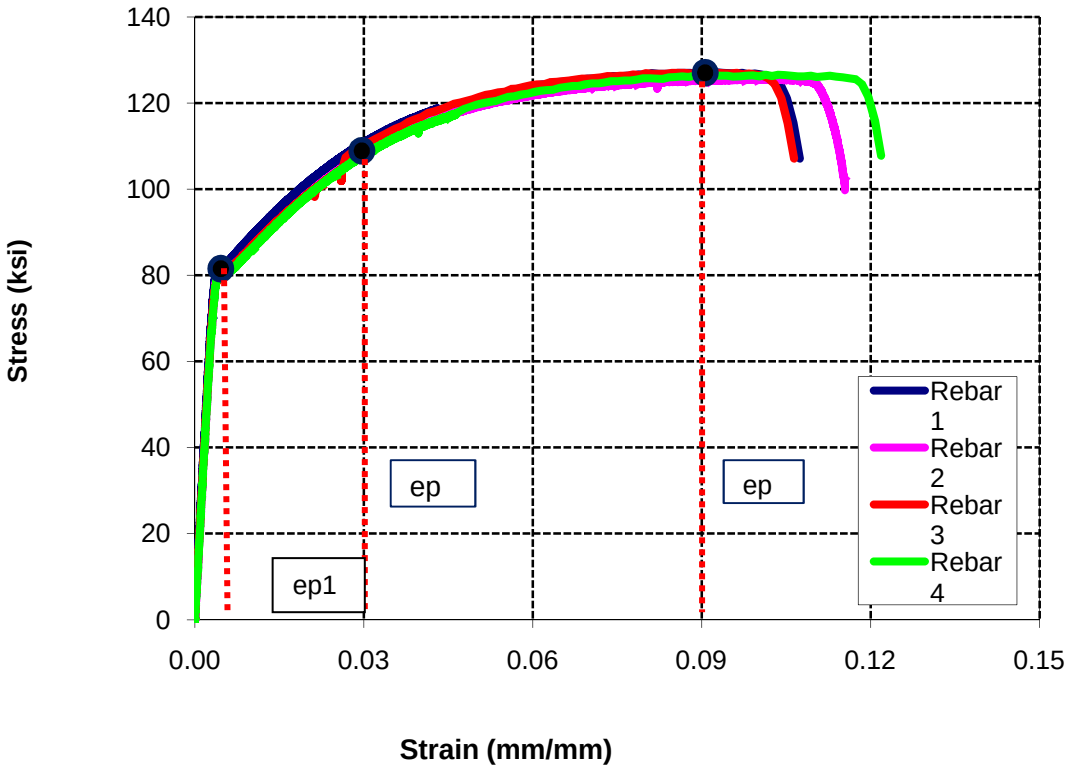

Figure A.14 Stress- Strain curve for hardening properties

Nonlinear steel properties will be defined for the reinforcing bar elements.

- Enter Young's modulus as 29E3 and Poisson's ratio as 0.3 in the Elastic tab and leave the mass density field blank.
- Click the Plastic option and enter an Initial uniaxial yield stress of 81.242 (from graph-see **Figure A.14**).
- Select the Hardening option, click the Hardening gradient button and enter a hardening Slope value of 21.6216×10^{3} with a Plastic strain of 3.8×10^{-3}, 1.16555×10^{3} with plastic strain of 0.03 and 272.405 with plastic strain of 0.09 (see **Figure A.13** and **A.14**)
- Enter the attribute name as Nonlinear Steel.
- Click the OK button to add the attribute to the Treeview.

Nonlinear concrete material properties will be defined for the Surface elements representing the concrete.

- Attributes>Material>Isotropic….

Enter a Young's modulus of 6.71E3, a Poisson's ratio of 0.2 and leave the mass density field blank.

- Click the Plastic option and from the drop-down list select the Concrete (model 94) entry.
- Select the Mass concrete option. (For RC specimen select Reinforced concrete tab)
- Enter a Uniaxial compressive strength value of 6.71 (see **chapter 3**).
- Enter a Uniaxial tensile strength value of 0.45 (from Direct Tensile Test see **chapter 3**).
- Enter Fracture energy per unit area value of 0.03015 (based on Kazemi (2007)). For RC specimen enter the value for strain at the end of softening curve.

- Enter the attribute name as Nonlinear Concrete.
- Click the OK button to add the attribute to the Treeview.

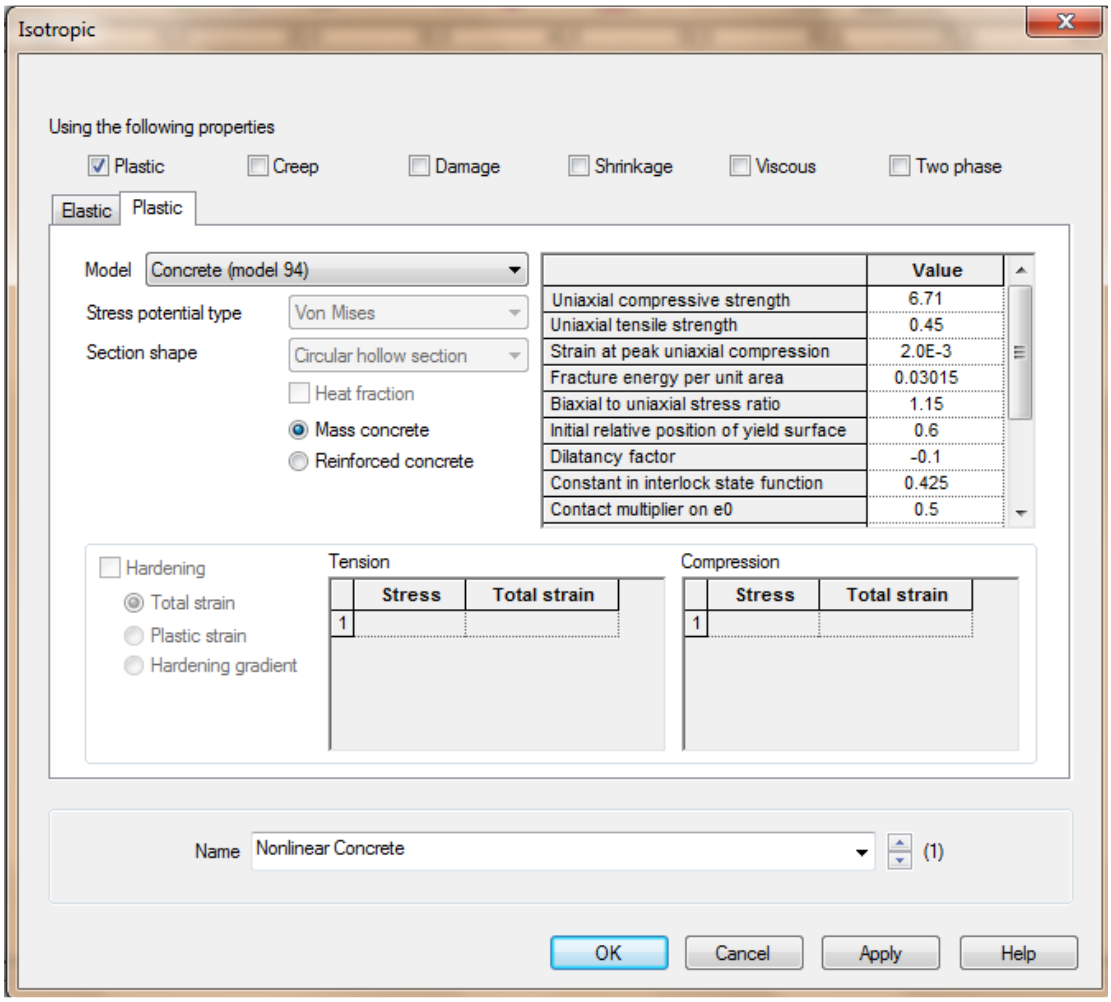

Figure A.15 Defining material properties for concrete

Assigning Attributes to the Bars

The various Line and Surface mesh, geometric and material attributes defined previously will now be assigned to the model using the groups that have been defined.

In the Treeview right-click the group name Bars. Select the Set as Only Visible option. The features in the group will be displayed.

- Select each line with length of 5 in.
- Drag and drop the Line mesh attribute Bar Elements - Divs=5 graded from the Treeview onto the selected Line. Do this for each bar with different lengths.
- Drag and drop the Line mesh attributes (for bars) from the Treeview onto the line by selecting them individually.
- In the Treeview double-click on the Mesh entry and select Show nodes.

The Line mesh divisions will be seen defined with the spacing as shown.

- Select all the Lines.
- Drag and drop the geometric attribute Steel Area from the Treeview onto the selected features.
- Drag and drop the material attribute Nonlinear Steel from the Treeview onto the selected features.

Note: The diagrams in this example show element nodes. To see these at any time you can go to the Treeview and double-click the Mesh layer. On the Mesh tab select Show nodes and click the Close button.

Assigning Attributes to the Concrete

- In the Treeview right-click the group name Concrete. Select the Set as Only Visible option.
- The Lines in the Bars group will be removed from the display and the Concrete group will be displayed.
- Select all the lines with length 2 and drag and drop mesh attribute Division=2.
- Do this for all vertical and horizontal lines, it is important to assign the line mesh attribute with same uniform spacing as the length of the line in order to have a good mesh i.e. divisions should go along with the length of line.

Press Ctrl and A keys together.

- Drag and drop the Surface mesh attribute Plane Stress - Concrete from the Treeview onto the selected features.
- A uniform mesh will be drawn and the model will look as seen in **Figure A.16**.

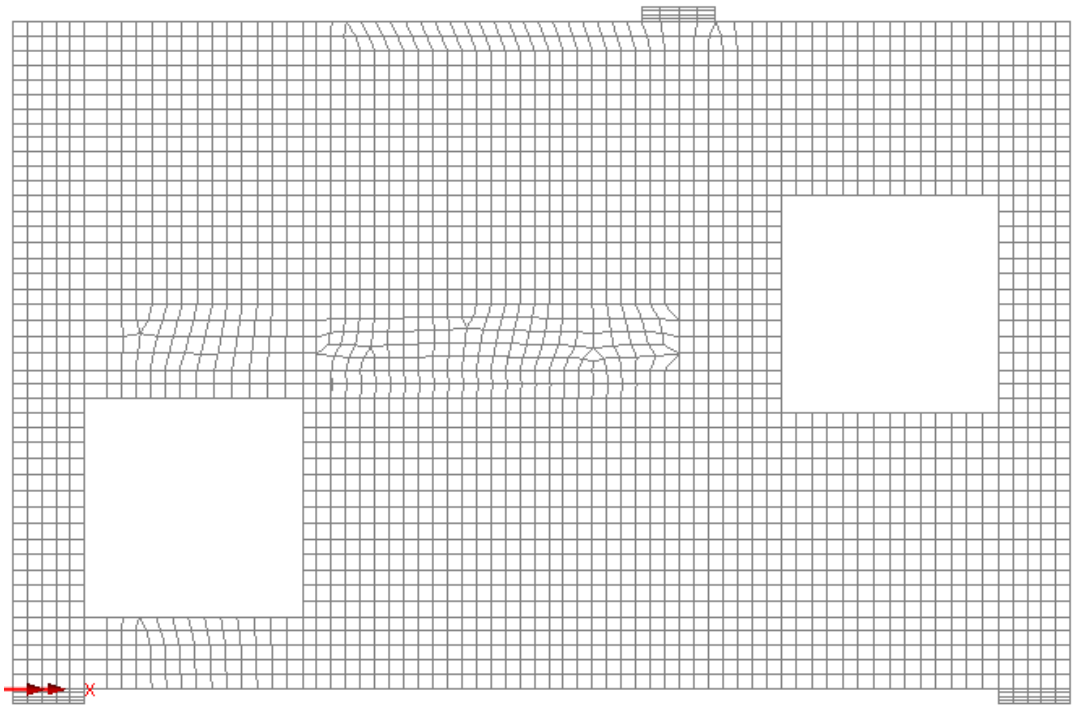

Figure A.16 Structure with assigned surface mesh

- Drag and drop the geometry attribute Beam Thickness from the Treeview onto the selected features.
- Select the fleshing on/off button to turn-off the geometric visualization. If at any time during the example you wish to visualize the geometry select this button.
- With the whole model still selected, drag and drop the material attribute Nonlinear Concrete from the Treeview onto the selected features. Ensure the Assign to surfaces option is selected and click OK.

Making all groups visible

- From the Treeview right-click the group heading name Deep beam with web opening.mdl. Select the Set as Only Visible option.
- Click Yes to act on sub groups as well.

All features in the model will now be displayed as shown.

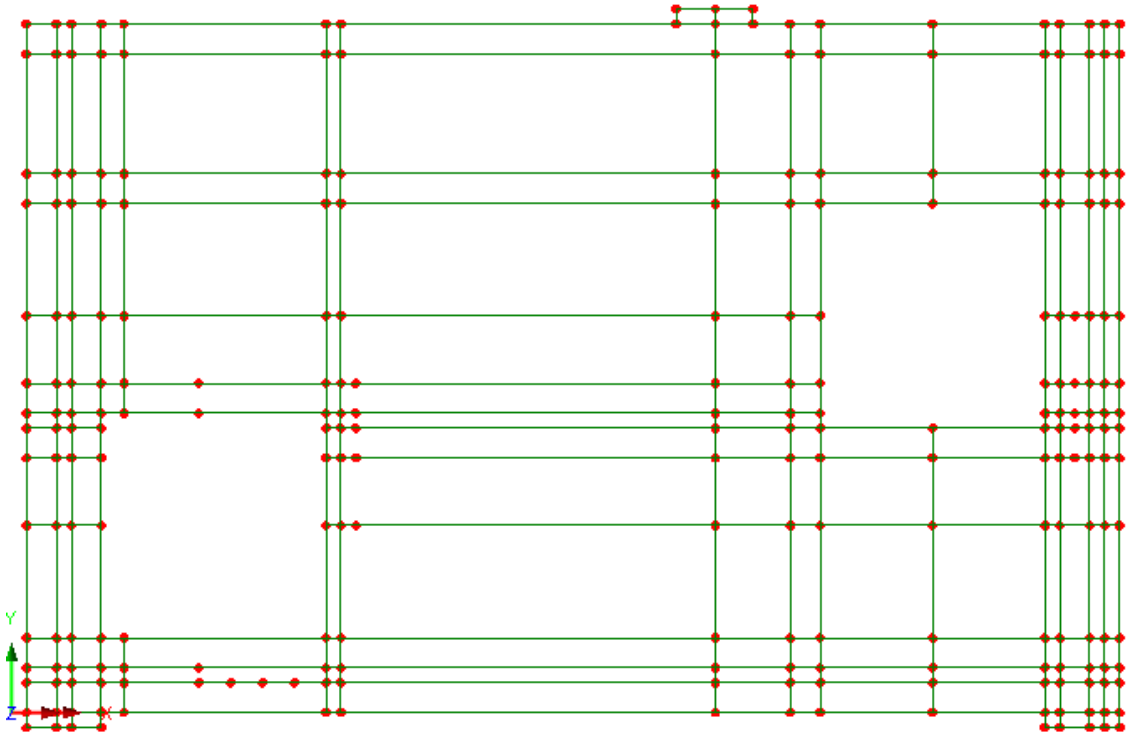

Figure A.17 Model with all features assigned

Supports

LUSAS provides the more common types of support by default. These can be seen in the Treeview. The beam is to be simply supported.

- Select the middle point of the lower left steel plate of the model as shown.
- Drag and drop the support attribute Pinned from the Treeview onto the selected point. Ensure the Assign to points and All loadcases options are selected and click OK.
- Similarly select middle point of lower right steel plate.
- Drag and drop Fixed in Y from the Treeview onto the selected point. Ensure the Assign to lines and All loadcases options are selected and click OK.

The model should appear like this,

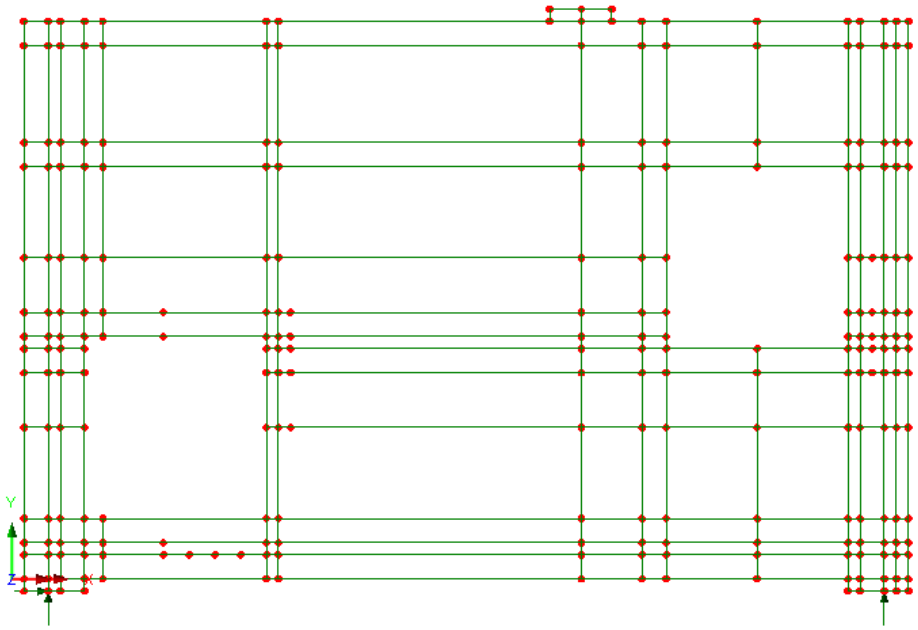

Figure A.18 Model with assigned support conditions.

Loading

- Attributes>Loading…

A single concentrated load is to be applied to the line at the steel plate at top of the beam. A unit load will be applied and the load factor in the nonlinear control will be used to control the magnitude of loading.

- With the Concentrated option selected click Next
- Enter a loading value of -1 in the component Concentrated load in Y Dir.
- Enter the attribute name as Point Load and click Finish.
- Select the lines on the top of the steel plate.
- Drag and drop the loading dataset Point Load from the Treeview onto the selected lines.
- Ensure the Assign to lines option is set and click OK to assign the load to Loadcase 1 with a factor of 1.

The beam should appear like this,

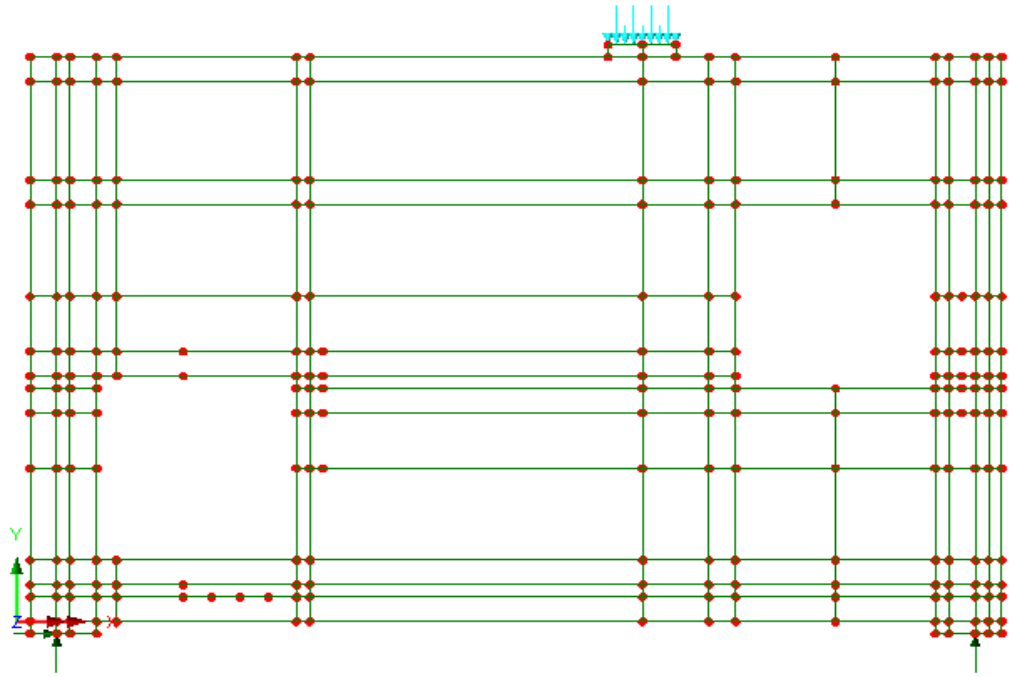

Figure A.19 Model with assigned loading

Nonlinear Control

- Nonlinear analysis control properties are defined as properties of a loadcase. The nonlinear analysis is to be terminated when the beam reaches the ultimate load observed from laboratory testing.
- Select the point shown.
- In the Treeview right-click on Loadcase 1 and select Nonlinear & Transient from the Controls menu.

Nonlinear Transient dialog box will appear,

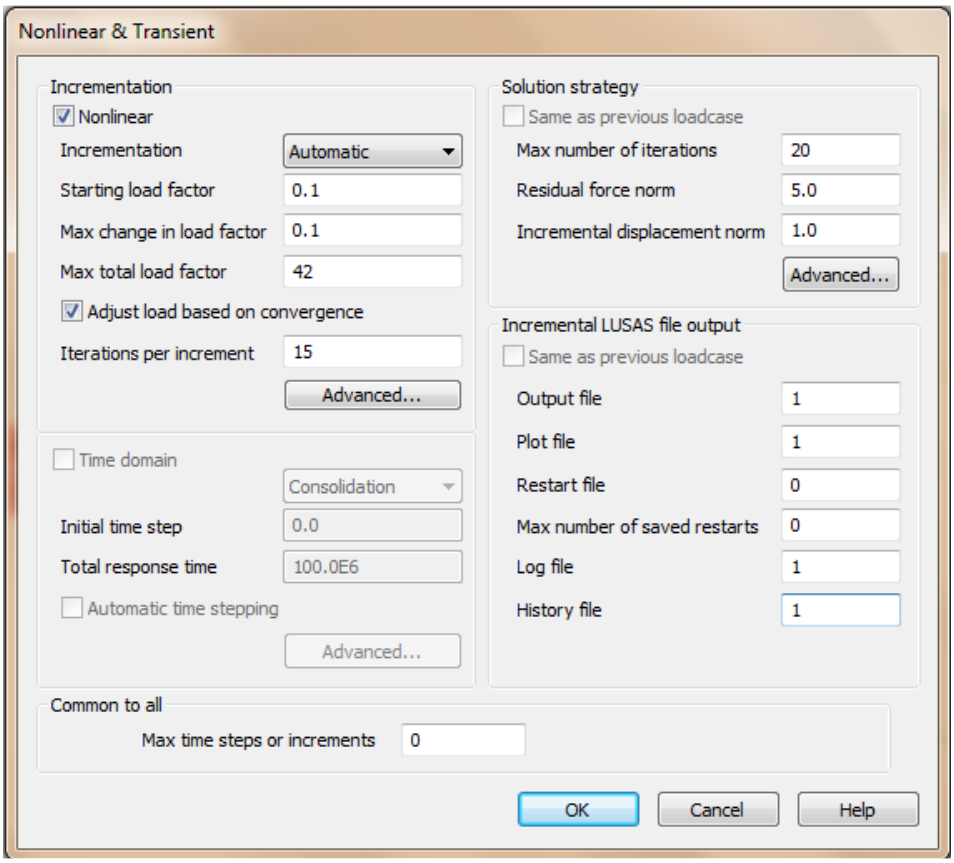

Figure A.20 Assigning nonlinear control

Select the Nonlinear option and set Incrementation to Automatic

- The initial load to be applied is the actual load applied to the model multiplied by the starting load factor. Set the Starting load factor to 0.1.
- Enter the Max change in load factor as 0.1 to restrict the second and subsequent load increment sizes to ensure sufficient points are obtained to observe the load deflection behavior of the beam.
- Change the Max total load factor to 42 as the solution is to be terminated at this loading.
- Change the number of desired Iterations per increment to 15.

Note: If the number of iterations on the previous increment is less than the desired number the next load increment will be increased (up to the maximum change in load increment) while if the number of iterations is less than the desired number the next load increment will be reduced.

- In the Solution strategy section of the dialog, ensure the Maximum number of iterations is set to 20.
- Leave the Residual force norm as 0.1 and the Incremental displacement norm to 1 so convergence of the solution at each load increment will be achieved when the out of balance forces are as less than 0.1% of the reactions and the iterative change in displacements is less than 1% of the displacements for that load increment.
- Click OK again to set the loadcase properties.

One additional setting is required for this analysis to ensure no element mechanisms are induced as the material yields.

- File >Model Properties….

- Select the Solution tab.
- Click on the Element Options button and select the Fine integration for stiffness and mass option.
- Click the OK button to return the Model Properties dialog.
- Click the OK button to finish.

Save the model

- File>Save…

The model is now complete and the model data is to be saved before an analysis is run using the LUSAS Solver. Save the model file.

Running the Analysis

With the model loaded:
A LUSAS data file name of Deep beam with web opening will be automatically entered in the File name field.

- Ensure that the options Solve now and Load results are selected.
- Click the Save button to finish.
- Click **=** button to run the analysis.

During the analysis 2 files will be created:

- Deep Beam with web opening.out this contains the statistics of the analysis, for example how much disk space was used, how much CPU time was used, and any errors or warning messages from LUSAS, and so on.
- Deep Beam with web opening.mys this is the LUSAS results database which will be used for results processing.

Results such as contour, cracking, crushing, strain in rebars etc. can be viewed from layers tab.

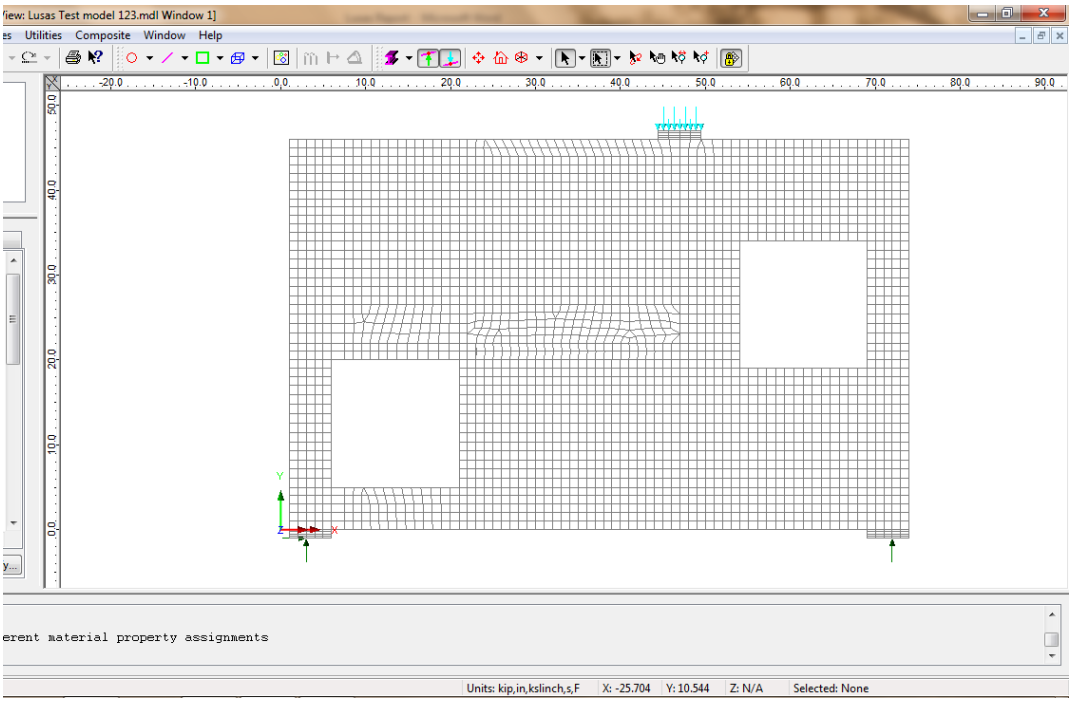

Figure A.21 User interface of LUSAS after analysis is completed.

Table A.1 Fracture energy for different SFRC specimens

	SFRC#1 (V_f=1.5%)		SFRC#2 (V_f=1.5%)		SFRC#3 (V_f=1.0%)	
Fracture Energy (G_F)	Ksi-in	J/m^2	Ksi-in	J/m^2	Ksi-in	J/m^2
	0.030150	5280	0.030150	5280	0.019206	3363.5

APPENDIX B

COMPUTER AID STRUT-AND-TIE ANALYSIS (CAST)

B.1 Design Procedure

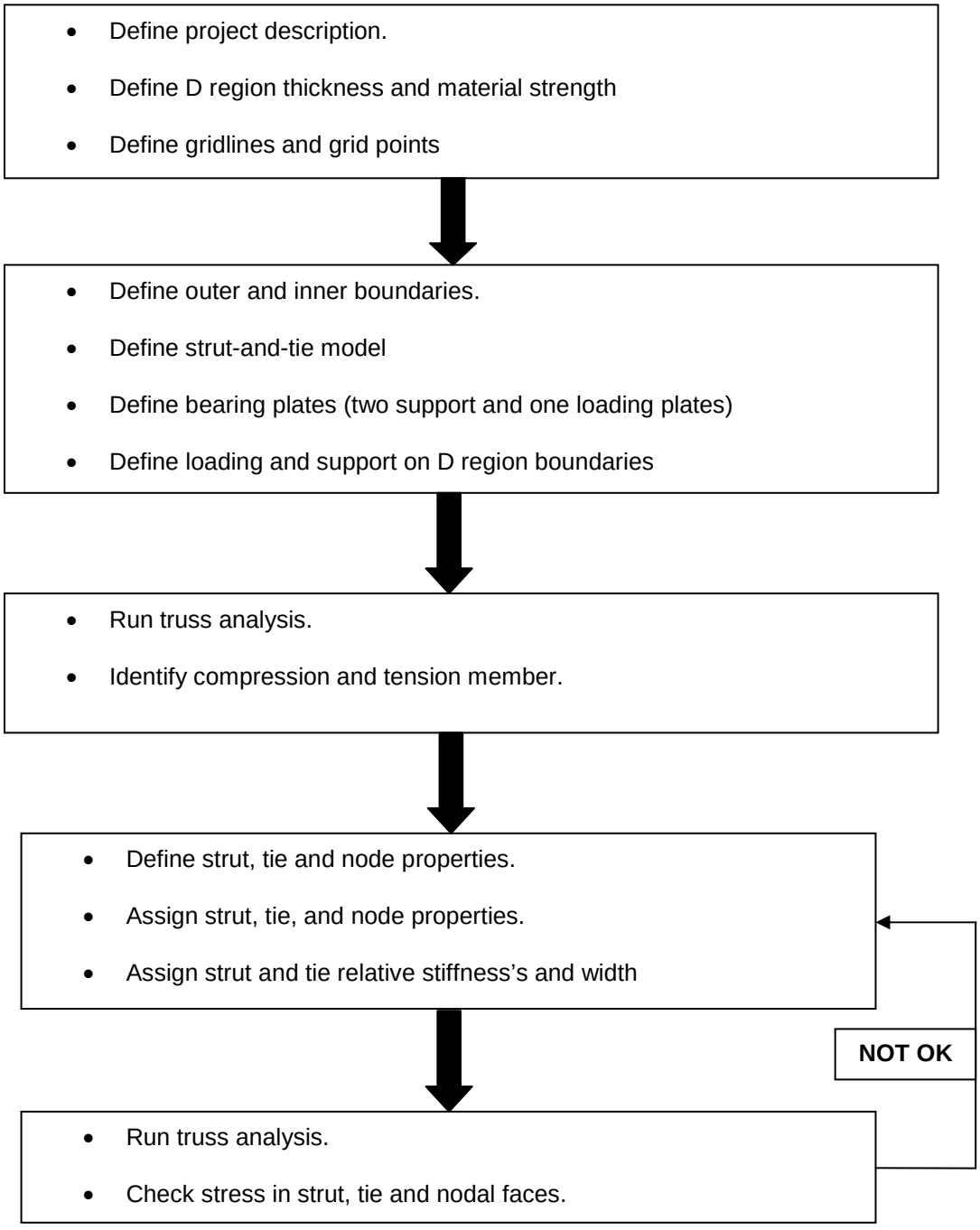

The coordinates of the strut-and-tie model was inserted and model was created by following the steps mentioned in the above flowchart.

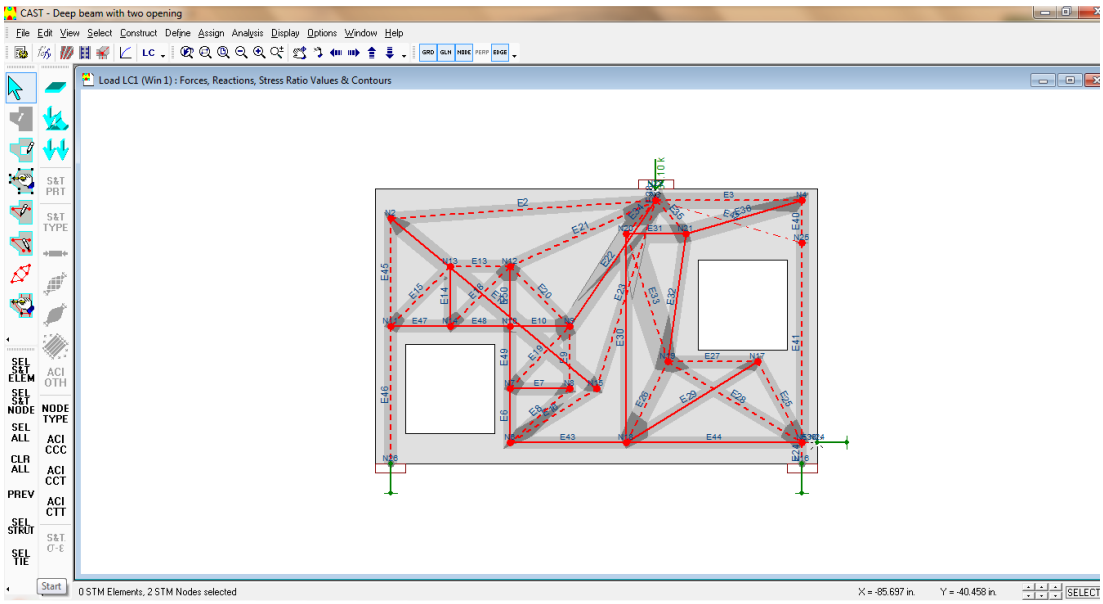

Figure B-1 User interface- CAST

Also material properties determined from chapter 2 was inserted in the model. Tensile strength for concrete was calculated as per ACI code as $7.5\sqrt{f_c}$

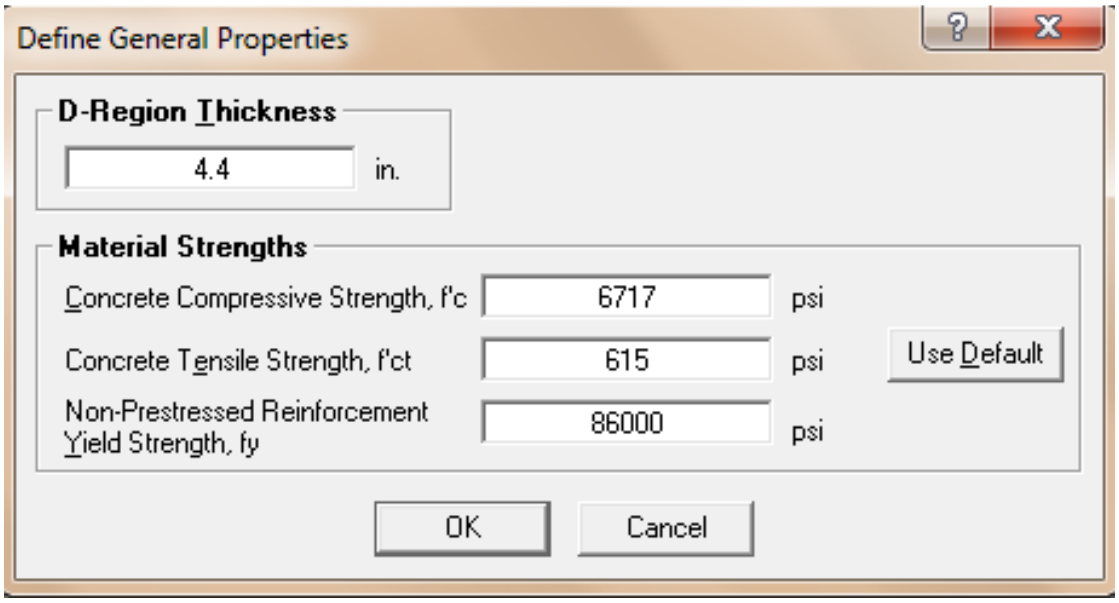

Figure B-2 General material properties dialog box – CAST

Primarily two type of concrete strut was used namely prismatic and bottle shaped. In built equation in CAST (ACI prismatic strut and ACI bottle shaped strut w/ steel) for strut calculation were used.

Nodes were either compression on all sides (C-C-C), tension on one side (C-C-T), or tension on more than one side (C-T-T). Accordingly, the strength-reduction ratios as recommended by ACI were used.

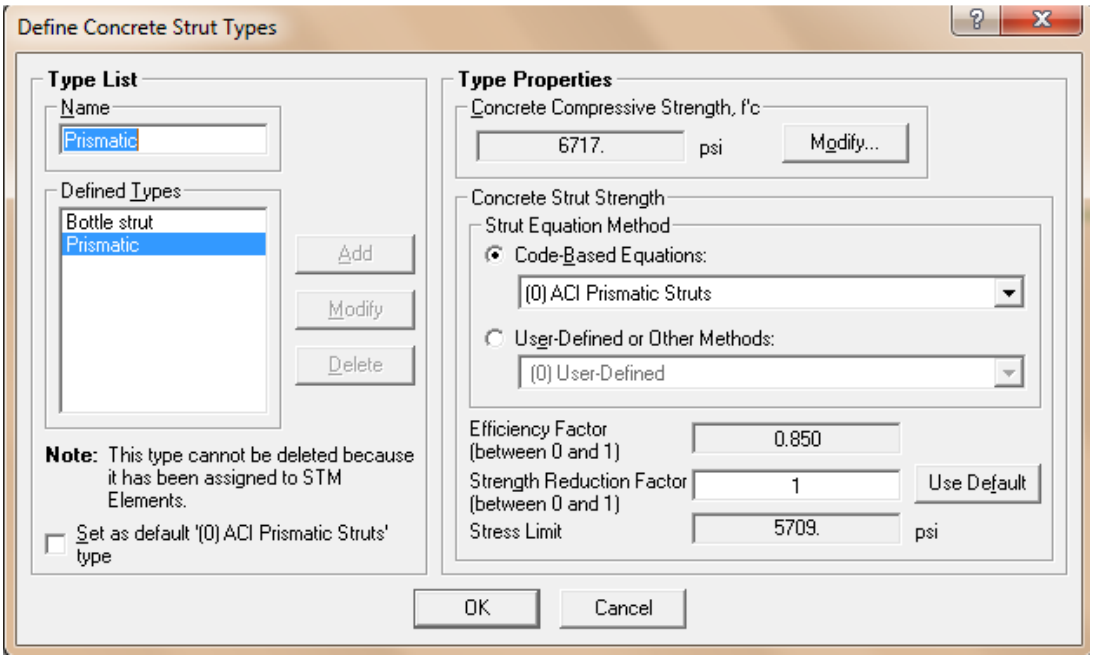

Figure B-3 Concrete strut types dialog box- CAST

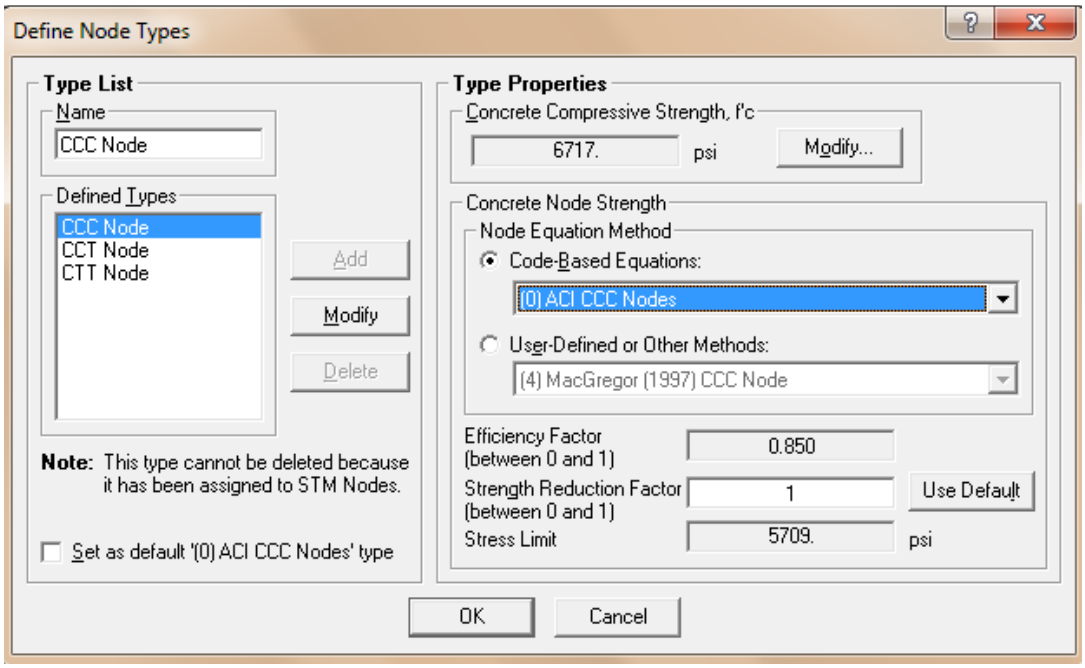

Figure B-4 Node types dialog box- CAST

Reinforcement steel tensile ties were defined as either a single tie, double tie or a triple tie. Since there was two No. 3 bars per layer for single tie 0.22 in^2, double tie 0.44in^2 and triple tie 0.66 in^2 steel area was used.

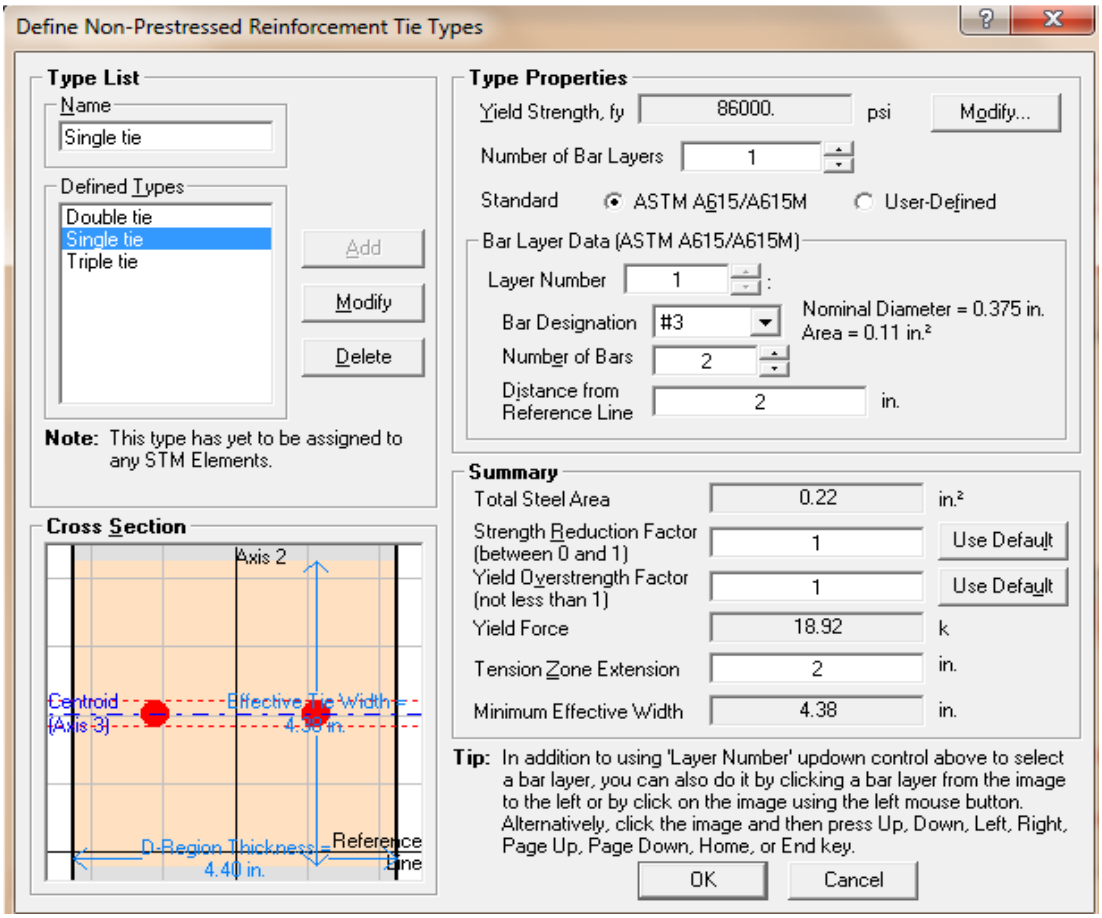

Figure B-5 Steel tie properties dialog box- CAST

APPENDIX C

DESIGN CALCULATION RESULTS AT ULTIMATE ANALYSIS LOAD - (CAST)

PROJECT NAME: Deep Beam with two opening
DESIGNER: Tarun Pareek
DATE: 10/23/2010
PROJECT NOTE: STRUT AND TIE ANALYSIS

C.1 CAST Output File for RC Specimen at ultimate analysis load of 72 kip

Table C.1 Results of stress and force in the element

ELEMENT ID	FORCE (k)	STRESS (psi)	STRESS LIMIT/YIELD (psi)	FORCE (k)
E32	13	59091	-	17.74
E36	64.36	73140	-	70.95
E34	-56.54	4284	5709	-
E41	-17.47	1985	5709	-
E3	-61.95	5631	5709	-
E10	26.26	59680	-	35.47
E13	-13.13	1492	5709	-
E14	13.13	59680	-	17.74
E15	-18.57	2110	4282	-
E16	-25.75	2926	4282	-
E17	18.05	41028	-	35.47
E18	-18.57	2110	4282	-
E19	-9.01	1023	4282	-
E2	-13.95	1585	4282	-
E20	-23.77	2701	4282	-
E21	-10.36	1177	4282	-
E22	5.7	12965	-	35.47
E23	-26.31	2990	4282	-
E24	-46.43	7756	5709	-
E25	-12.42	1411	4282	-
E26	-56.07	4248	5709	-
E27	-23.72	2696	5709	-
E28	-35.19	3999	4282	-
E29	20.76	47173	-	35.47

TableC.1 – *Continued*

E30	38.92	58971	-	53.21
E31	64.33	73100	-	70.95
E33	-84.93	3861	4282	-
E35	-6.21	706	4282	-
E38	-72	7756	5709	-
E39	0	NA	NA	
E40	-17.47	1985	5709	-
E42	0	NA	NA	
E43	28.09	63841	-	35.47
E44	36.21	82294	-	35.47
E45	-12.44	1413	5709	-
E46	-25.57	2905	5709	-
E47	13.13	29840	-	35.47
E48	26.26	59680	-	35.47
E49	25.69	58391	-	35.47
E50	25.69	58391	-	35.47
E6	19.17	43568	-	35.47
E7	6.21	28233	-	17.74
E8	-8.36	950	4282	-
E9	-5.59	635	5709	-

Table C.2 Results of stress ratio for each element

ELEMENT ID	STRESS RATIO	f'c RATIO	Beta RATIO
E32	0.733	NA	NA
E36	0.907	NA	NA
E34	0.75	0.638	0.75
E41	0.348	0.296	0.348
E3	0.986	0.838	0.986
E10	0.74	NA	NA
E13	0.261	0.222	0.261
E14	0.74	NA	NA
E15	0.493	0.314	0.37
E16	0.683	0.436	0.513
E17	0.509	NA	NA

Table C.2 – *Continued*

E18	0.493	0.314	0.37
E19	0.239	0.152	0.179
E2	0.37	0.236	0.278
E20	0.631	0.402	0.473
E21	0.275	0.175	0.206
E22	0.161	NA	NA
E23	0.698	0.445	0.524
E24	1.358	1.155	1.358
E25	0.33	0.21	0.247
E26	0.744	0.632	0.744
E27	0.472	0.401	0.472
E28	0.934	0.595	0.7
E29	0.585	NA	NA
E30	0.731	NA	NA
E31	0.907	NA	NA
E33	0.902	0.575	0.676
E35	0.165	0.105	0.124
E38	1.358	1.155	1.358
E39	NA	NA	NA
E40	0.348	0.296	0.348
E42	NA	NA	NA
E43	0.792	NA	NA
E44	1.021	NA	NA
E45	0.248	0.21	0.248
E46	0.509	0.433	0.509
E47	0.37	NA	NA
E48	0.74	NA	NA
E49	0.724	NA	NA
E50	0.724	NA	NA
E6	0.54	NA	NA
E7	0.35	NA	NA
E8	0.222	0.141	0.166
E9	0.111	0.095	0.111

Table C.3 Nodal results for STM

NODE ID	NODE FACE	FORCE	STRESS	STRESS LIMIT
		(k)	(psi)	(psi)
N23	E38	-72	7756	4924
N10	E10	26.26	2984	3693
	E48	26.26	2984	3693
	E49	25.69	2920	3693
	E50	25.69	2920	3693
N11	E15	-18.57	2110	4185
	E45	-12.44	1413	4185
	E46	-25.57	2905	4185
	E47	13.13	1492	4185
N12	E13	-13.13	1492	4185
	E18	-18.57	2110	4185
	E20	-23.77	2701	4185
	E21	-10.36	1177	4185
	E50	25.69	2920	4185
N13	E13	-13.13	1492	4185
	E14	13.13	1492	4185
	E15	-18.57	2110	4185
N14	E14	13.13	1492	3693
	E18	-18.57	2110	3693
	E47	13.13	1492	3693
	E48	26.26	2984	3693
N15	E16	-25.75	2926	4185
	E17	18.05	1368	4185

Table C.3 – *Continued*

	E23	-26.31	2990	4185
N16	E24	-46.43	7756	4924
N17	E25	-12.42	1411	4185
	E27	-23.72	2696	4185
	E29	20.76	2359	4185
N18	E26	-56.07	4248	3693
	E29	20.76	2359	3693
	E30	38.92	4423	3693
	E43	28.09	3192	3693
	E44	36.21	4115	3693
N19	E26	-56.07	4248	4185
	E27	-23.72	2696	4185
	E28	-35.19	3999	4185
	E32	13	1477	4185
	E33	-84.93	3861	4185
N2	E2	-13.95	1585	4185
	E17	18.05	1368	4185
	E45	-12.44	1413	4185
N20	E30	38.92	4423	3693
	E31	64.33	4873	3693
	E33	-84.93	3861	3693
	E34	-56.54	4284	3693
N21	E31	64.33	4873	3693
	E32	13	1477	3693
	E35	-6.21	706	3693
	E36	64.36	4876	3693
N24	E39	0	0	NA
N25	E40	-17.47	1985	4924

Table C.3 – *Continued*

	E41	-17.47	1985	4924
	E42	0	0	4924
N26	E46	-25.57	2905	4924
N3	E2	-13.95	1585	4185
	E3	-61.95	5631	4185
	E21	-10.36	1177	4185
	E22	5.7	432	4185
	E23	-26.31	2990	4185
	E34	-56.54	4284	4185
	E35	-6.21	706	4185
	E38	-72	7756	4185
	E42	0	0	4185
N4	E3	-61.95	5631	4185
	E36	64.36	4876	4185
	E40	-17.47	1985	4185
N5	E24	-46.43	7756	4185
	E25	-12.42	1411	4185
	E28	-35.19	3999	4185
	E39	0	0	4185
	E41	-17.47	1985	4185
	E44	36.21	4115	4185
N6	E6	19.17	2178	3693
	E8	-8.36	950	3693
	E16	-25.75	2926	3693
	E43	28.09	3192	3693
N7	E6	19.17	2178	3693
	E7	6.21	706	3693
	E19	-9.01	1023	3693
	E49	25.69	2920	3693
N8	E7	6.21	706	4185

Table C.3 – *Continued*

	E8	-8.36	950	4185
	E9	-5.59	635	4185
N9	E9	-5.59	635	3693
	E10	26.26	2984	3693
	E19	-9.01	1023	3693
	E20	-23.77	2701	3693
	E22	5.7	432	3693
NODE ID	NODE FACE	STRESS RATIO	f'c RATIO	Beta RATIO
N23	E9	0.172	0.095	0.111
	E10	0.808	0.444	0.523
	E19	0.277	0.152	0.179
	E20	0.731	0.402	0.473
	E22	0.117	0.064	0.076
N10	E9	0.172	0.095	0.111
	E10	0.808	0.444	0.523
	E19	0.277	0.152	0.179
	E20	0.731	0.402	0.473
	E22	0.117	0.064	0.076
N11	E9	0.172	0.095	0.111
	E10	0.808	0.444	0.523
	E19	0.277	0.152	0.179
	E20	0.731	0.402	0.473
	E22	0.117	0.064	0.076
N12	E9	0.172	0.095	0.111
	E10	0.808	0.444	0.523
	E19	0.277	0.152	0.179
	E20	0.731	0.402	0.473
	E22	0.117	0.064	0.076
N13	E9	0.172	0.095	0.111

Table C.3 – *Continued*

	E10	0.808	0.444	0.523
	E19	0.277	0.152	0.179
	E20	0.731	0.402	0.473
	E22	0.117	0.064	0.076
N14	E9	0.172	0.095	0.111
	E10	0.808	0.444	0.523
	E19	0.277	0.152	0.179
	E20	0.731	0.402	0.473
	E22	0.117	0.064	0.076
N15	E9	0.172	0.095	0.111
	E10	0.808	0.444	0.523
	E19	0.277	0.152	0.179
	E20	0.731	0.402	0.473
	E22	0.117	0.064	0.076
N16	E9	0.172	0.095	0.111
	E10	0.808	0.444	0.523
	E19	0.277	0.152	0.179
	E20	0.731	0.402	0.473
	E22	0.117	0.064	0.076
N17	E9	0.172	0.095	0.111
	E10	0.808	0.444	0.523
	E19	0.277	0.152	0.179
	E20	0.731	0.402	0.473
	E22	0.117	0.064	0.076
N18	E9	0.172	0.095	0.111
	E10	0.808	0.444	0.523
	E19	0.277	0.152	0.179
	E20	0.731	0.402	0.473
	E22	0.117	0.064	0.076
N19	E9	0.172	0.095	0.111
	E10	0.808	0.444	0.523

Table C.3 – *Continued*

	E19	0.277	0.152	0.179
	E20	0.731	0.402	0.473
	E22	0.117	0.064	0.076
N2	E9	0.172	0.095	0.111
	E10	0.808	0.444	0.523
	E19	0.277	0.152	0.179
	E20	0.731	0.402	0.473
	E22	0.117	0.064	0.076
N20	E9	0.172	0.095	0.111
	E10	0.808	0.444	0.523
	E19	0.277	0.152	0.179
	E20	0.731	0.402	0.473
	E22	0.117	0.064	0.076
N21	E9	0.172	0.095	0.111
	E10	0.808	0.444	0.523
	E19	0.277	0.152	0.179
	E20	0.731	0.402	0.473
	E22	0.117	0.064	0.076
N24	E9	0.172	0.095	0.111
	E10	0.808	0.444	0.523
	E19	0.277	0.152	0.179
	E20	0.731	0.402	0.473
	E22	0.117	0.064	0.076
N25	E9	0.172	0.095	0.111
	E10	0.808	0.444	0.523
	E19	0.277	0.152	0.179
	E20	0.731	0.402	0.473
	E22	0.117	0.064	0.076
N26	E9	0.172	0.095	0.111
	E10	0.808	0.444	0.523
	E19	0.277	0.152	0.179

Table C.3 – *Continued*

	E20	0.731	0.402	0.473
	E22	0.117	0.064	0.076
N3	E9	0.172	0.095	0.111
	E10	0.808	0.444	0.523
	E19	0.277	0.152	0.179
	E20	0.731	0.402	0.473
	E22	0.117	0.064	0.076
N4	E9	0.172	0.095	0.111
	E10	0.808	0.444	0.523
	E19	0.277	0.152	0.179
	E20	0.731	0.402	0.473
	E22	0.117	0.064	0.076
N5	E9	0.172	0.095	0.111
	E10	0.808	0.444	0.523
	E19	0.277	0.152	0.179
	E20	0.731	0.402	0.473
	E22	0.117	0.064	0.076
N6	E9	0.172	0.095	0.111
	E10	0.808	0.444	0.523
	E19	0.277	0.152	0.179
	E20	0.731	0.402	0.473
	E22	0.117	0.064	0.076
N7	E9	0.172	0.095	0.111
	E10	0.808	0.444	0.523
	E19	0.277	0.152	0.179
	E20	0.731	0.402	0.473
	E22	0.117	0.064	0.076
N8	E9	0.172	0.095	0.111
	E10	0.808	0.444	0.523
	E19	0.277	0.152	0.179
	E20	0.731	0.402	0.473

Table C.3 – *Continued*

	E22	0.117	0.064	0.076
N9	E9	0.172	0.095	0.111
	E10	0.808	0.444	0.523
	E19	0.277	0.152	0.179
	E20	0.731	0.402	0.473
	E22	0.117	0.064	0.076

APPENDIX D

NON-LINEAR MODELLING ON VECTOR2

D.1 Introduction

Program VecTor2, developed at the University of Toronto, have the capability of simulating the monotonic response of reinforced concrete structures. The programs employ the compatibility, equilibrium, and constitutive formulations of the Modified Compression Field Theory (MCFT). VecTor2 is applicable to concrete membrane structures. It employs a 4-noded (8 degree of freedom) constant strain element, which assumes a linear displacement field across the boundary of the element. A 3-noded, constant strain, triangular element is also available. Reinforcement is represented discretely by truss bar elements.

D.2 VecTor2 Model

Modeling in VecTor2 starts with creating the model in FormWork's workspace. The modeling of SFRC#2 specimen is discussed in this section. The dimension and geometry of this specimen was same as discussed in Appendix A. It is important to note that in VecTor2 geometry is defined in anticlockwise direction and should form a closed loop. **Figure D.1** shows the dialog box to define RC region, the coordinates are entered to snap the geometry of the specimen. After defining the geometry openings are created by entering its coordinates in voids and constrains tab (see **Figure D.2**). Reinforcements are defined as discrete truss element and are snapped to the geometry by defining its coordinates (see **Figure D.3**). Finally mesh is generated from create mesh tab and added to structure (see **Figure D.4**). Support conditions are defined by selecting individual nodes also a unit displacement is applied in downward Y axis direction to the nodes representing loading area. Model with all assigned features is shown in **FigureD.5**.

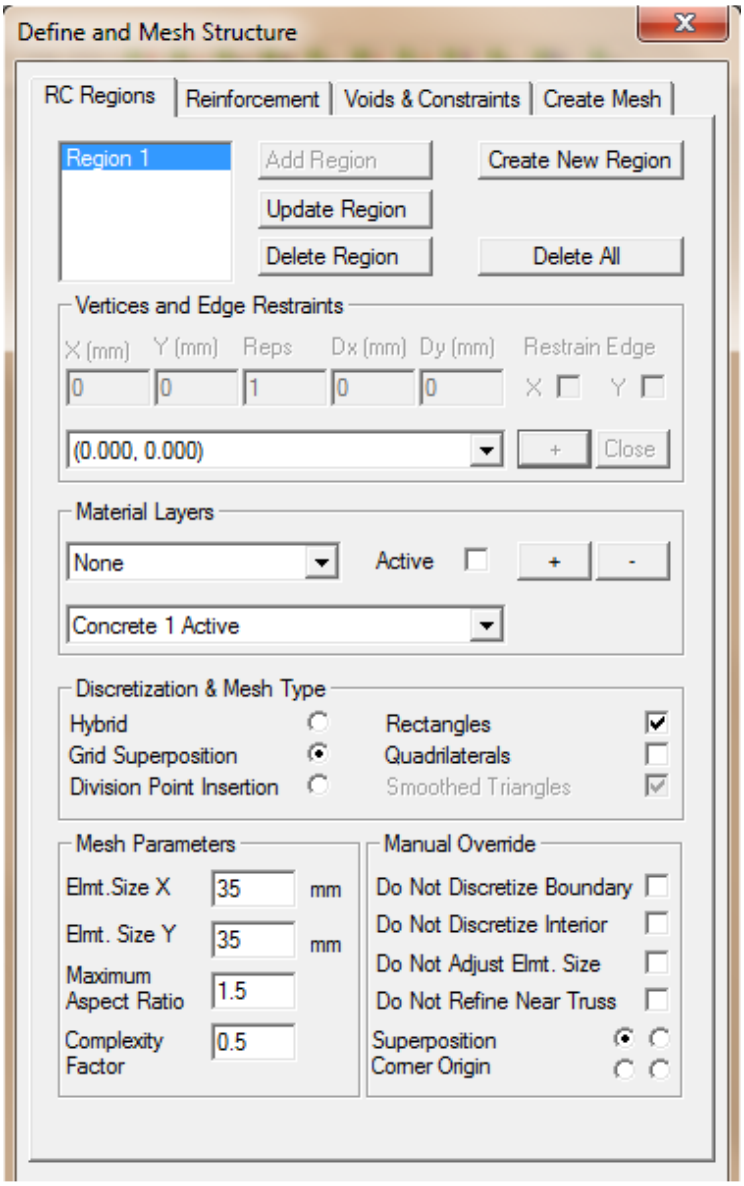

Figure D.1 Dialog box for defining RC region.

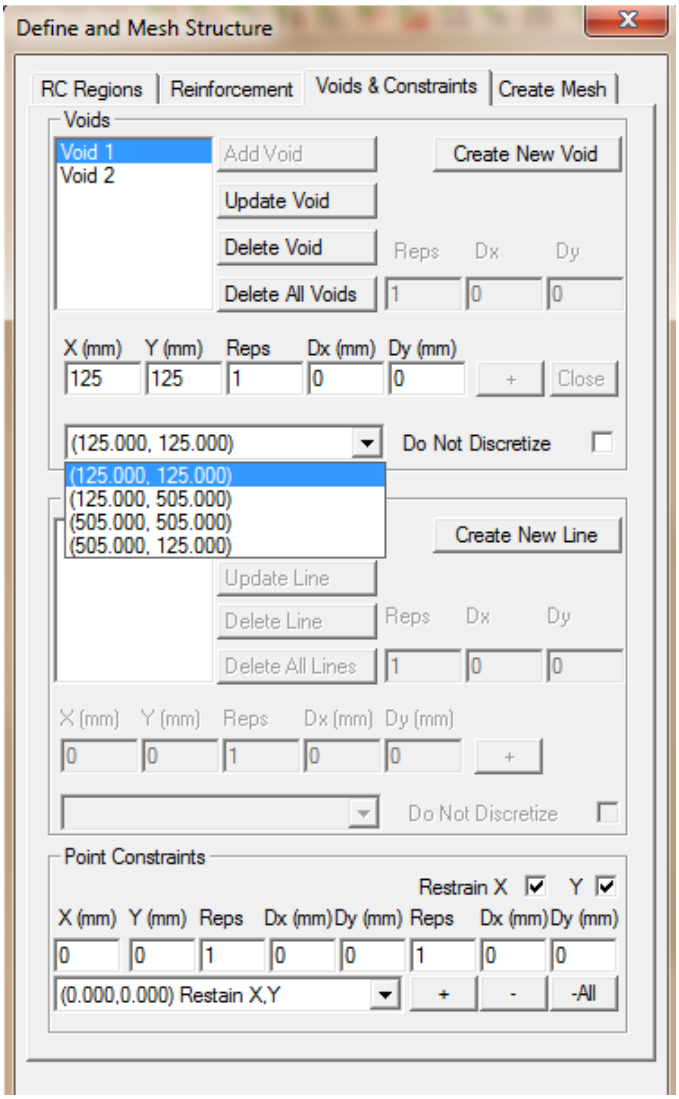

Figure D.2 Dialog box for defining openings in the structure.

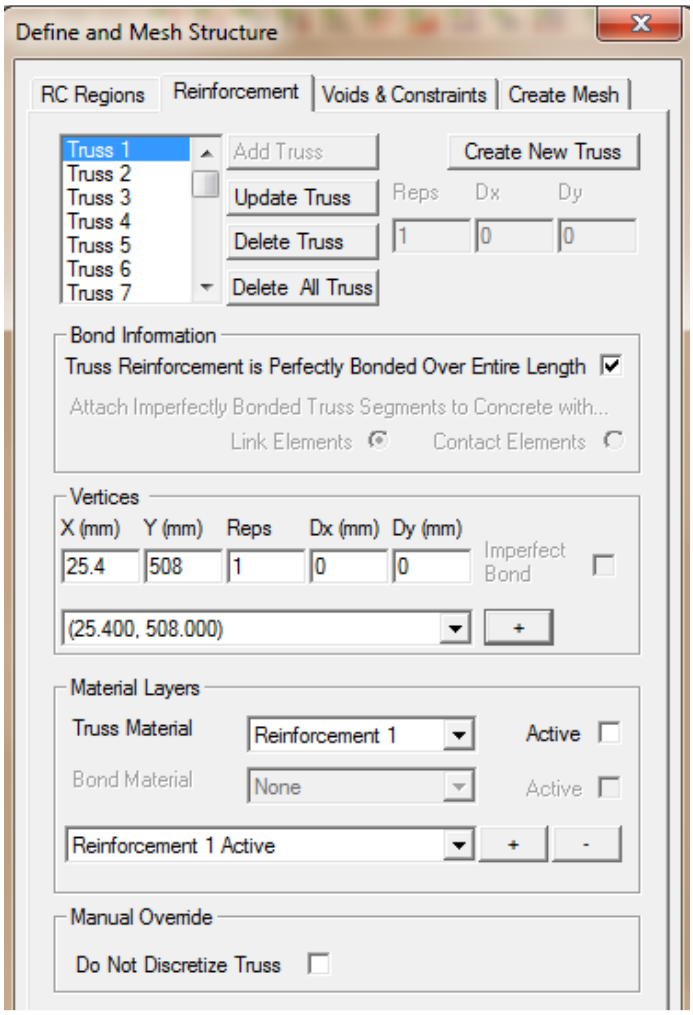

Figure D.3 Dialog box for defining reinforcement in the structure.

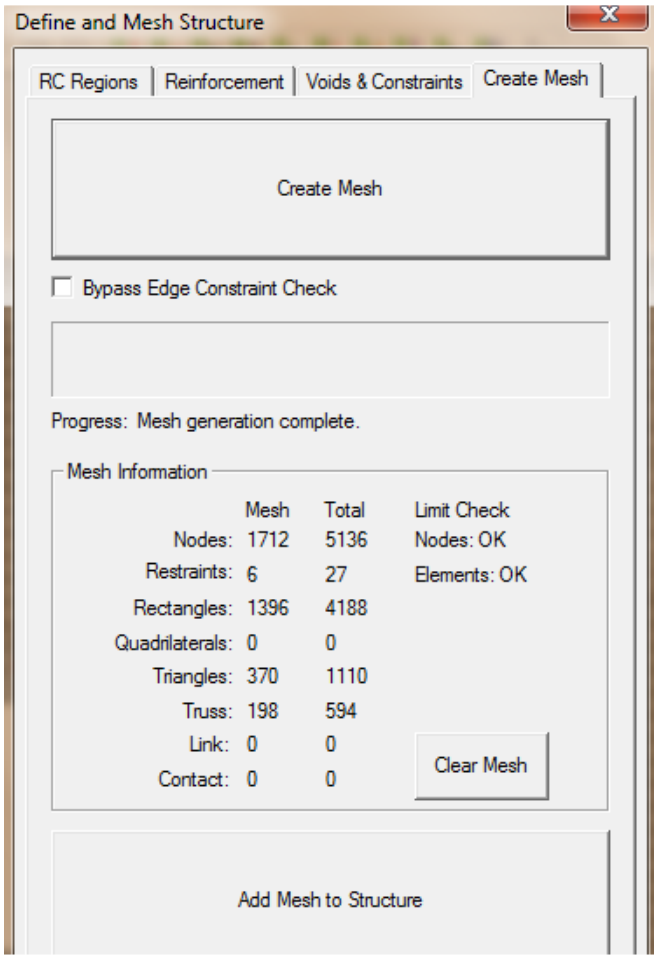

Figure D.4 Dialog box for defining and adding mesh to the structure.

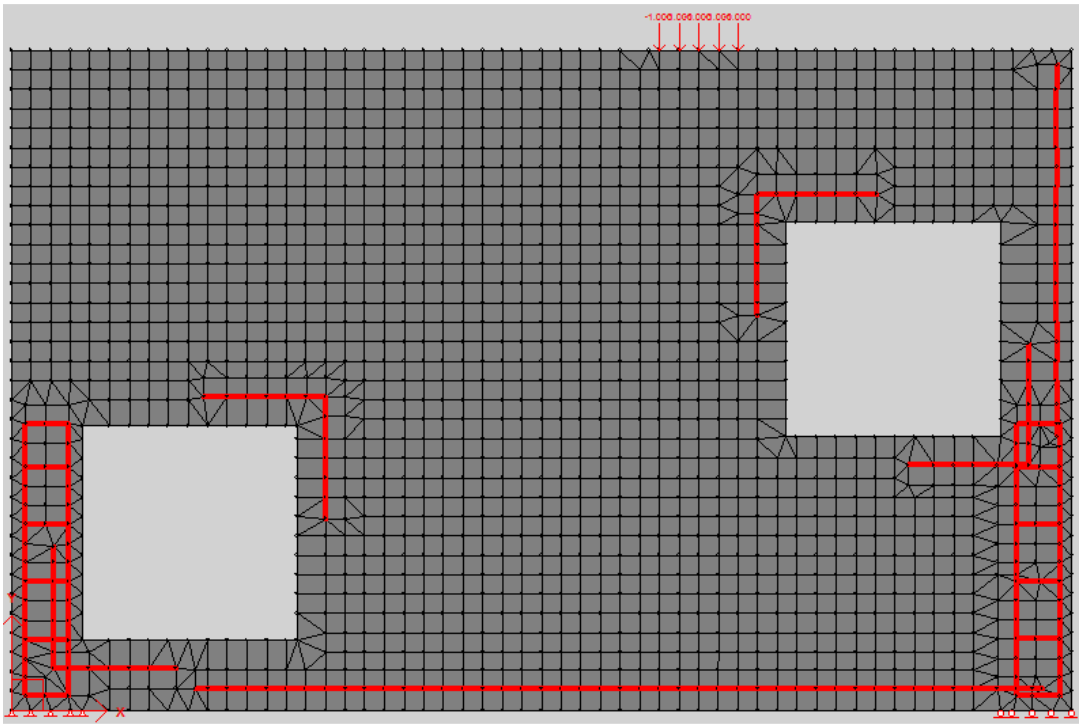

Figure D.5 Model with all features assigned.

After defining all the features in the model different concrete and reinforcement models are selected from “define job” tab (see **Figure D.6**). Further concrete and reinforcement steel properties are defined in their respective properties dialog boxes (see **Figure D.7, D.8**). The model selected for RC and SFRC specimens are same but their properties differ and are based on the material testing data from chapter 3. Based on the input concrete and reinforcement curves and from the defined material properties VecTor2 generates material responses. Once the model is ready with all input properties one last step before running the analysis is defining number of load stages and load increment (see **Figure D.9**). Since the analysis was displacement control the number of load stages were based on the displacement reached by the

large scale during laboratory testing. Results such as failure mechanism, cracking pattern, load displacement curve etc. can be viewed from AUGUSTUS (see **Figure D.10**).

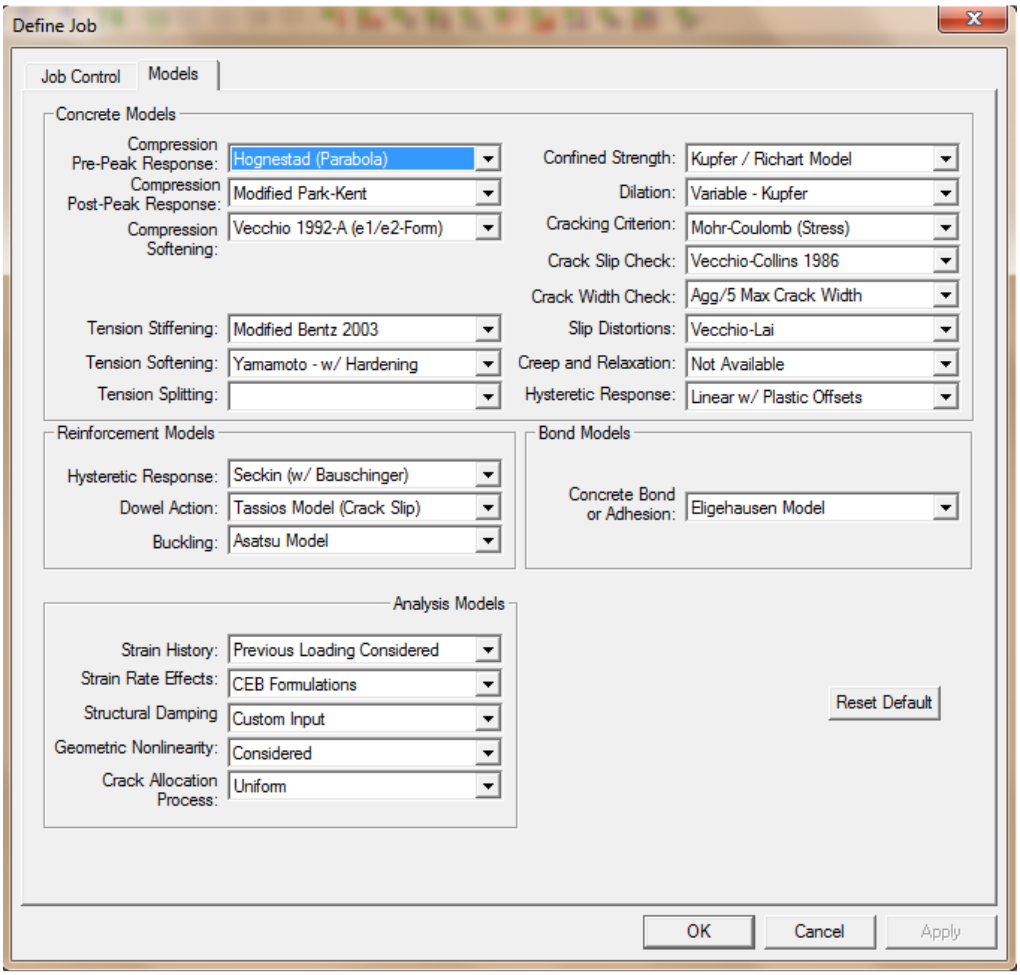

Figure D.6 Dialog box for defining concrete and reinforcement model.

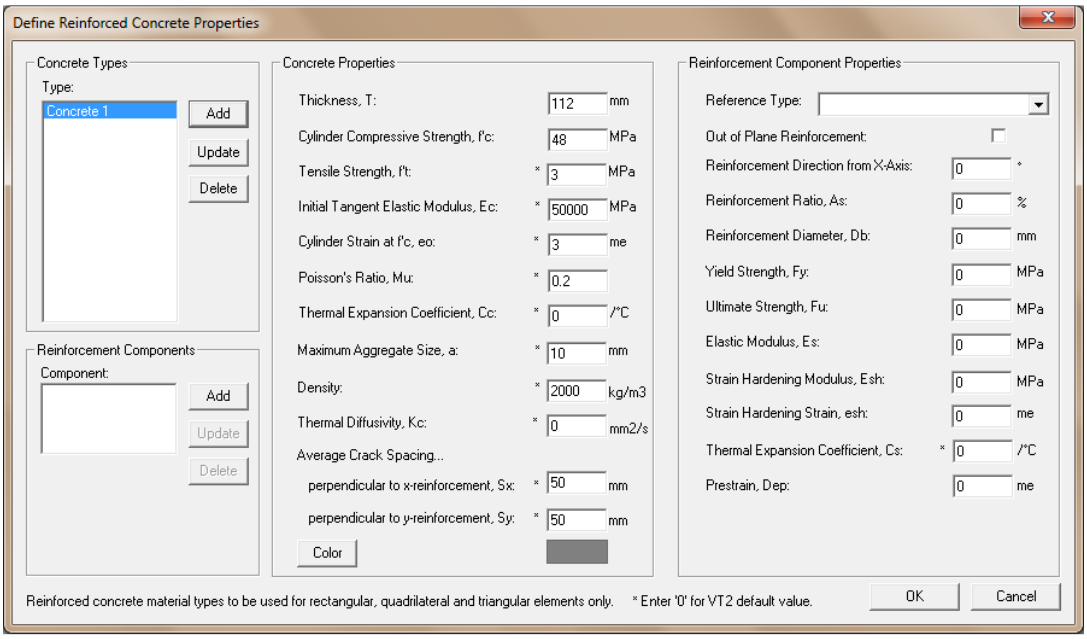

Figure D.7 Defining concrete properties

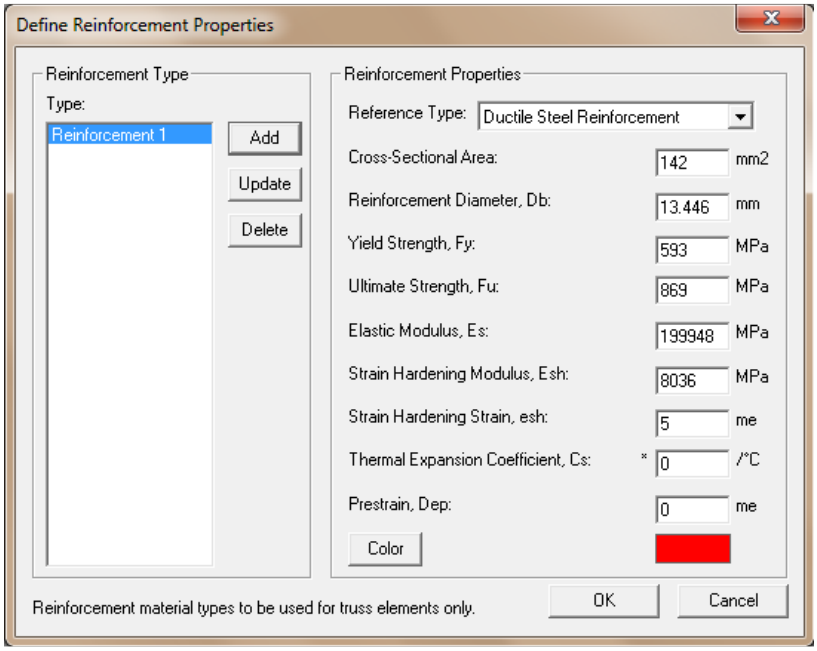

Figure D.8 Defining Reinforcement steel properties

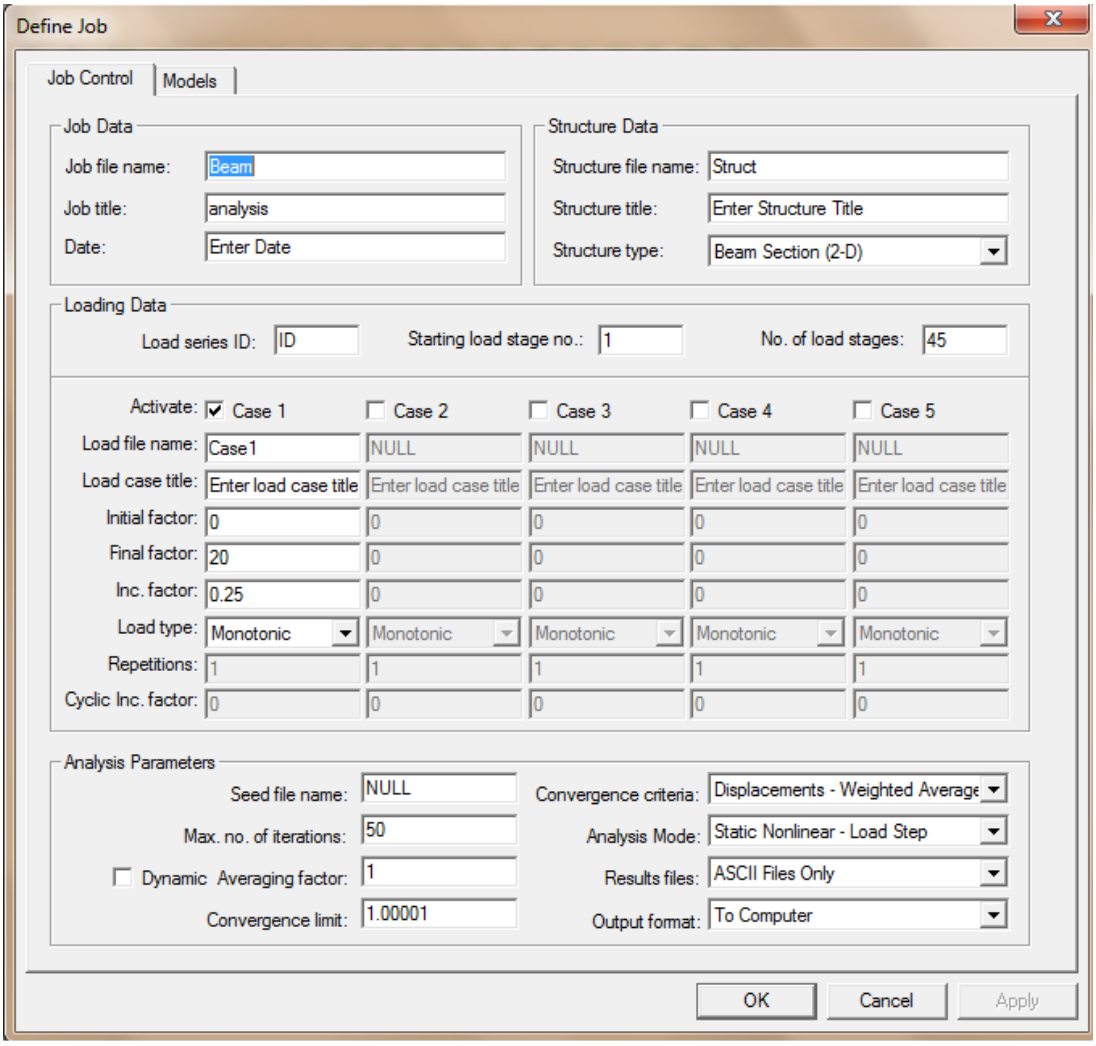

Figure D.9 Defining Job data

Once the analysis is complete the results can be seen from AUGUSTUS also a load verses displacement curve can be plotted by using respective parameters.

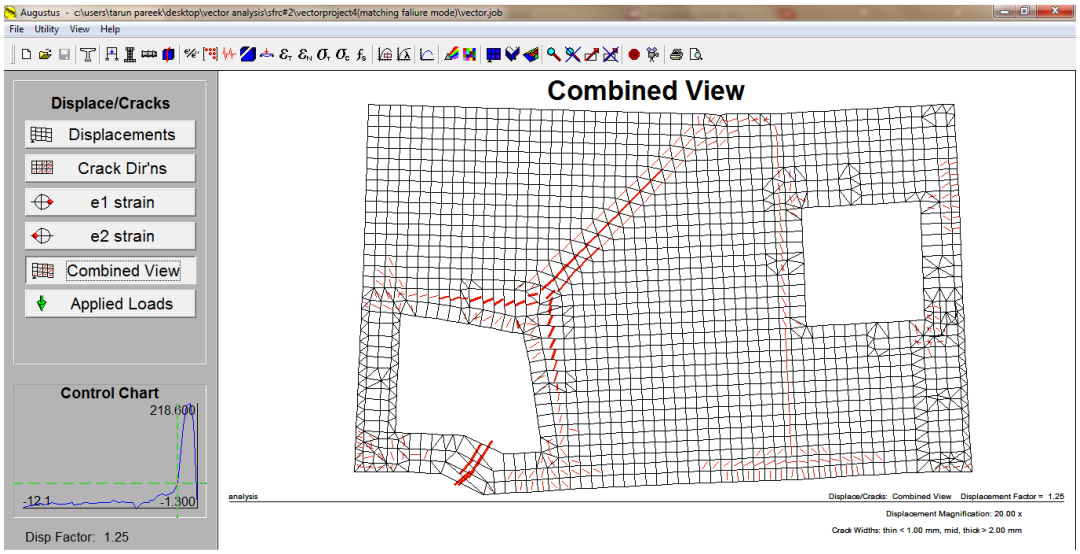

Figure D.10 User interface from AUGUSTUS showing failure mechanism

REFERENCES

ACI Committee 318 (2011), “Building Code Requirements for Reinforced Concrete and Commentary”, American Concrete Institute, Detroit.

ACI Committee 544 (1996), “Report on Fiber Reinforced Concrete (ACI 544.1 R-96),” American Concrete Institute, Farmington Hills, MI

ASTM C1609 – 10 (2010), “Standard Test method for Flexural Performance of Fiber-Reinforced Concrete (Using Beam with Third-Point Loading)”, ASTM International, West Conshohocken, PA, 2010, 9 pages

ASTM A370 – 11 (2011), “Standard Test Methods and Definitions for Mechanical Testing of Steel Products”, ASTM International, West Conshohocken, PA, pp. 191-195.

ASTM A615 – 09b (2009), “Standard Specification for Deformed and Plain Carbon-Steel Bars for Concrete Reinforcement”, ASTM International, West Conshohocken, PA, pp. 325-329.

ASTM C39 – 11 (2011), “Standard Test Method for Compressive Strength Cylindrical Concrete Specimens”, ASTM International, West Conshohocken, PA, pp. 22-28

ASTM C78 – 10 (2010), “Test Method for Flexural Strength of Concrete (Using Simple Beam with Third-Point Loading”, ASTM International, West Conshohocken, PA, pp. 40-42.

ASTM C617 - 11 (2011), “Standard Practice for Capping Cylindrical Concrete Specimens”, ASTM International, West Conshohocken, PA, pp. 324-328.

Al-Nahlawi, Khaled A., Wight, James K.,1992, “Beam Analysis Using Concrete Tensile Strength in Truss Models,” ACI Structural Journal, V. 89, No. 3, May-Jun., pp.284-289.

Ashour, A. F.; Chung, H. S.; and Yang, K. H., 2007, “Influence of Inclined Web Reinforcement on Reinforced Concrete Deep Beams with Openings,” ACI Structural Journal, V. 104, Sept-Oct., pp. 580-589.

Amiri, S., Masoudnia, R. and Pabarja, A.A., 2011, “The study of the effects of web openings on the concrete beams” Australian Journal of Basic and Applied Sciences, pp 547.

Bae, S.; Breen, J. E,; Ley, M. T.; Ridding, K. A.,; and Widianto., 2007, “Experimental Verification of Strut-and-Tie Model Design Method,” ACI Structural Journal, V. 104, No. 6, Nov-Dec., pp. 749-755.

Breña, S. F. and Morrison, M. C, 2007 “Factors Affecting Strength of Elements Designed Using Strut-and-Tie Models,” ACI Structural Journal, V. 104, No. 3, May-Jun, pp. 267-277.

Breña, S. F. and Morrison, M. C, 2008 “Authors’ Closure on the Discussion on Factors Affecting Strength of Elements Designed Using Strut-and-Tie Models,” ACI Structural Journal, V. 105, No. 2, March-April., pp. 236.

Casanova, P., Rossi, P., Schaller, I., 1997. “Can Steel Fibers Replace Transverse Reinforcements in Reinforced Concrete Beams?”, ACI Materials Journal, Vol. 94, No. 5, September- October, 1997, pp. 341-354.

Chao, S.H., Naaman, A.E., Parra-Montesinos, G.J., 2009. “Bond Behavior of Reinforcing Bars in Tensile Strain-Hardening Fiber-Reinforced Cement Composites”, ACI Structural Journal, Vol. 106, No. 6, November-December, 2009, pp. 897-906.

Chen, B. S., Hagenberger, M. J., and Breen, J. E., 2002 “Evaluation of Strut-and-Tie Modeling Applied to Dapped Beam with Opening,” ACI Structural Journal, V. 99, No. 4, July-Aug., pp. 445-450.

Colombo, S.; Main, I. G.; and Forde, M. C., 2003, “Assessing Damage of Reinforced Concrete Beam Using “b-value” Analysis of Acoustic Emission Signals,” Journal of Materials in Civil Engineering, ASCE, V. 15, No. 3, Jun., pp. 280-286.

CSA Committee A23.3, 1984 “Design of Concrete Structures (CAN3-A23.3-M84),” Canadian Standards Association, Rexdale, ON, Canada, pp. 281.

Daniel, J.I., 1991. “Fiber Reinforced Concrete”, Illinois: Portland Cement Association, pp. 48.

Darwish, I. Y. S.; and Narayanan, R., 1988, “Fiber Concrete Deep Beams in Shear,” ACI Structural Journal, V. 85, No.2, Mar-April, pp. 141-149.

Dupont, D.; and Vandewalle, L., 2003 “Shear Capacity of Concrete Beams Containing Longitudinal Reinforcement and Steel Fibers.” Ed. Banthia, N.; Criswell, M.; Tatnall, P.; and Folliard, K., Innovations in Fiber-Reinforced Concrete for Value, American Concrete Institute, Farmington Hills, MI.

Fanella, D.A. and Naaman, A.E., 1985. “Stress-Strain Properties of Fiber Reinforced Mortar in Compression”, ACI Journal, Vol. 82, No. 4, July-August 1985, pp. 475-483.

Flores, C. A., 2009, “Performance of large scale steel fiber reinforced concrete deep beam with single opening under monotonic loading”, Master Thesis, Department of Civil Engineering, The University of Texas at Arlington.

Hsu, L.S. and Hsu, C.T.T., 1994. “Stress-Strain Behavior of Steel-Fiber High-Strength Concrete under Compression”, ACI Structural Journal, Vol. 91, No. 4, July-August 1994, pp. 448-457.

Hube, M. A. and Mosalam K. M., Experimental and Computational Evaluation of Current and Innovative In-Span Hinge Details in Reinforced Concrete Box-Girder Bridges—Part 1: Experimental Findings and Pre-Test Analysis, Pacific Earthquake Engineering Research Center, PEER 2008/103, Jan. 2009.

Hibbeler, R.C., 2005, “Mechanics of Materials,” 6th Edition, Prentice Hall, 123.

Johnston, C.D., 2001. “Fiber-Reinforced Cements and Concretes”, Gordon and Breach Science Publishers, Ottawa, Canada, pp. 372.

Joint ACI-ASCE Committee 445, 2002, “Examples for the Design of Structural Concrete with Strut-and-Tie Models,” Strut-and-Tie Models, SP-208, K.-H. Reineck, ed., American Concrete Institute, Farmington Hills, Mich., pp. 445.

Kazemi, M.T., Fazileh, F., Ebrahiminezhad, M.A., 2007. “Cohesive Crack Model and Fracture Energy of Steel-Fiber-Reinforced-Concrete Notched Cylindrical Specimens”, ASCE Journal of Materials in Civil Engineering, Vol 19, No 10, October 2007, pp. 884-890.

Kuchma, D., Yindeesuk, S., Nagle, T., Hart, J., and Lee, H. H., 2008. “Experimental Validation of Strut-and-Tie Method for complex Regions,” ACI Structural Journal, V. 105, No. 5, Sep.-Oct., pp. 578-589.

LUSAS, Version 14.6-3, 2011.

Mansour, A., Srebric, J., and Burley, B.J., 2007. “Development of Straw-Cement Composite Sustainable Building Material for Low-Cost Housing in Egypt”, Journal of Applied Sciences Research, Vol. 3, No. 11, pp. 1571-1580.

Mansur, M. A.; and Ong, K. C. G., 1991, “Behavior of Reinforced Fiber Concrete Deep Beams in Shear,” ACI Structural Journal, V. 88, No. 1, Jan.-Feb., pp. 98-105.

Maxwell, B. S., and Breen J. E., 2000 “Experimental Evaluation of Strut-and Tie Model Applied to Deep Beam with Opening,” ACI Structural Journal, V.97, No.1 Jan.-Feb., pp. 142-149.

MacGregor, J. G.; Wight, J., 2002, “Reinforced Concrete Design: Mechanics and Design,” 4th Edition, Prentice Hall, pp. XXX.

Mehta, P. Kumar, Monteiro, Paulo J.M., 2006, “Concrete – Microstructure, Properties, and Materials,” 3rd Edition, McGraw-Hill, New York, p. 502.

Mindess, S., 1995. “Fiber reinforced concrete: Challenges and prospects”, Fiber reinforced concrete, 2nd University-Industry Workshop on Fiber Reinforced Concrete and Other Advanced Composites, N. Banthia and S. Mindess, eds. Toronto, pp. 1-11.

Mörsch, E., Concrete-Steel Construction, E.P. Goodrich, translation, McGraw-Hill, New York, 1909 pp. 368.

Parra-Montesinos, G. J., 2006, “Shear Strength of Beams with Deformed Steel Fibers”, Concrete International, V. 28, No. 11, Nov., pp. 57-66.

Park, J. W., and Kuchma, D., 2007 “Strut-and-Tie Model Analysis for Strength Prediction of Deep Beams,” ACI Structural Journal, V. 104, No. 6, Nov.-Dec., pp. 657-666.

Ray, S. P., 1990, “Deep Beams with Web Openings,” Reinforced Concrete Deep Beams, edited by F. K. Kong, Van Nostrand Reinhold, pp. 288.

Romualdi, J.P. and Batson, G.B., 1963. “The Mechanics of Crack Arrest in Concrete”, ASCE journal, Vol. 89, EM3, Paper 3558, June 1963, pp. 147-168.

Romualdi, J.P. and Mandel, J.A., 1964. “Tensile strength of concrete affected by uniformly distributed closely spaced short lengths of wire reinforcements”, ACI Journal, Proceedings, Vol. 61, No. 6, June 1964, pp. 657-671.

Ruiz, M. F.; and Muttoni, A., 2007, “On development of suitable stress fields for structural concrete,” ACI Structural Journal, V. 104, No. 4, Jul-Aug., pp. 495-502.

Sagbas, 2007, “Nonlinear finite element analysis of beam-column subassemblies”, Master Thesis, Department of Civil Engineering, University of Toronto.

Sahoo, D. R., Flores, C. A., and Chao, S.-H., 2012 "Behavior of Steel Fiber Reinforced Concrete Deep Beams with Large Opening ," ACI Structural Jounral (to be published).

Schlaich, J., Schäfer K., and Jennewein, M., 1987 “Toward a Consistent Design of Structural Concrete,” PCI Journal, V. 32, No. 3, May-Jun., pp. 75-150.

Shah, S.P. and Rangan B.V., 1971. “Fiber Reinforced Concrete Properties”, ACI Journal, Vol. 68, No. 2, February 1971, pp. 126-137.

Susetyo, J., 2009. “Fiber Reinforcement for Shrinkage Crack Control in Prestressed, Precast Segmental Bridges”, Ph.D Dissertation, University of Toronto, 2009, 532 p.

Tan, K. H.; and Zhang, N., 2007, “Size effect in RC deep beams: Experimental investigation and STM verification,” Engineering Structures, V. 29, pp. 3241- 3254.

VecTor2, Version 1.0, 2011.

BIOGRAPHICAL INFORMATION

Tarun Pareek was born on 1st June 1987 in Jaipur, capital of state Rajasthan in India. He received his Bachelor's Degree in Civil Engineering from Maharaja Sayajirao University of Baroda, India in May 2009. He completed his Master of Science degree in Civil Engineering (Structural Engineering) from University of Texas at Arlington in December 2011.

He was engaged in several on-site and off-site projects involving numerous designing and construction activities. His area of research interest includes large scale experimental testing of Reinforced Concrete and Fiber Reinforced Concrete. He is also a student member of American Society of Civil Engineers (ASCE), American Concrete Institute (ACI), Precast/Prestressed Concrete Institute (PCI), American Institute of Steel Construction (AISC).